

**Preparation for the accurate luminosity measurement by  
antiproton-proton elastic scattering and feasibility study for  
observation of  $h_c$  hadronic decay modes at the  $\bar{P}$ ANDA experiment**

Dissertation submitted  
for the award of the title  
"Doctor of Natural Sciences"  
to the Faculty of Physics, Mathematics, and Computer Science  
of Johannes Gutenberg University Mainz  
in Mainz

Anastasia Karavdina

Born in Novokuznetsk, Russia

Mainz, date .....

# Abstract

The  $\bar{P}$ ANDA experiment is one of the key projects at the future FAIR facility, which is currently under construction at GSI Darmstadt. Measurements will be performed with antiprotons using a fixed-target setup. One of the pillars of the  $\bar{P}$ ANDA program is hadron spectroscopy, in particular studies related to charmonium spectroscopy. The high number of expected collisions allows new discoveries and more accurate measurements of the properties of already known particles. The luminosity is a measure of how efficiently collision events are produced at particle accelerator facilities. Keeping track of luminosity allows monitoring the performance of the accelerator and thus promptly provides information for beam parameter adjustments to optimize the performance. In addition, precise luminosity data is crucial for absolute cross section measurements.

For the  $\bar{P}$ ANDA experiment the luminosity will be extracted by monitoring the scattered antiprotons from the  $p\bar{p}$  forward elastic scattering. The dedicated detector system, the Luminosity Detector, is currently under construction. The main part of this work describes in detail the developed reconstruction software and summarizes the simulation studies. The systematic uncertainties of the luminosity determination coming from the extraction method are expected to be below 0.1 %.

The largest uncertainty is coming from the model description of the elastic scattering. Depending on which experimental data is used, the systematic uncertainty even of the most accurate model varies between 1–10 %. The background is the second strongest contribution to the systematic uncertainty. According to simulation studies, the background contribution can be reduced down to the level of 1 %.

In a  $p\bar{p}$  experiment the non-vector charmonium states can be directly produced. Therefore, the fundamental properties such as mass and width of the non-vector states, e.g. of the singlet state of P wave charmonium  $h_c(P_1)$ , could be measured more accurately than it is currently done with  $e^+e^-$  colliders. The possible decay modes of the  $h_c(P_1)$  remain an open question. So far only few of them could have been observed. This work explores the feasibility of the measurement of  $h_c(P_1)$  hadronic decay modes by  $\bar{P}$ ANDA. To select the signal events in large background environment, a model dependent analysis is proposed. The expected signal efficiency is on the level of 40 %. The background can be suppressed by a factor  $10^6$ .

# Zusammenfassung

Das  $\bar{P}$ ANDA-Experiment ist eine der Säulen der zukünftigen Beschleunigeranlage FAIR, die an der GSI in Darmstadt entsteht. Für die Experimente werden Antiprotonen zum Einsatz kommen, die auf ein festes Target geführt werden. Der Schwerpunkt des  $\bar{P}$ ANDA-Physikprogrammes liegt auf dem Studium der starken Wechselwirkung im Energiebereich des Charm-Quarks, und hier im Bereich der Charm- und Charmonium-spektroskopie. Die zu erwartende Menge an Daten von  $\bar{P}$ ANDA ermöglicht sowohl neue Entdeckungen im Gebiet der Hadronphysik, als auch die Messung von Teilcheneigenschaften bereits bekannter Teilchen mit höherer Präzision als bisher.

Die Luminosität ist ein Maß für die Häufigkeit von Reaktionen an Teilchenbeschleunigeranlagen. Mit Hilfe der Messung der Luminosität können die Strahleigenschaften des Beschleunigers überwacht und gegebenenfalls unmittelbar angepasst werden. Außerdem ist die genaue Kenntnis der Luminosität für die Messung absoluter Wirkungsquerschnitte notwendig.

Die Luminosität des  $\bar{P}$ ANDA-Experiments wird durch die Messung elastisch gestreuter Antiprotonen unter Vorwärtswinkeln ermittelt. Das zugehörige Detektorsystem, der Luminositätsdetektor, befindet sich im Bau. Im Rahmen dieser Arbeit wurde die Rekonstruktionssoftware entwickelt und anhand ausführlicher Simulationsstudien getestet und charakterisiert. Es wird gezeigt, dass für die Extraktionsmethode eine systematische Unsicherheit besser als 0.1 % erreicht werden konnte.

Die größte systematische Unsicherheit kommt von der nur sehr ungenauen Kenntnis des hadronischen Anteils des elastischen Antiproton-Proton-Streuung. Je nachdem welche Daten welchem Modell zugrundegelegt werden, variiert dieser Wert sehr stark. Im besten Fall konnten abhängig von der betrachteten Schwerpunktsenergie Werte von 1–10 % erreicht werden. Den zweitgrößten Beitrag liefern Untergrundreaktionen. Studien zeigen, dass diese auf ein Level von 1 % reduziert werden können.

In  $p\bar{p}$ -Experimenten können neben Vektor-Zuständen vor allem auch Charmoniumzustände mit anderen Quantenzahlen direkt erzeugt werden. Dies bietet die Möglichkeit, die Eigenschaften des Charmonium-Singulett-Zustandes  $h_c(P_1)$  wie die Linienform in einem Energie-Scan-Experiment direkt zu untersuchen und genauer zu bestimmen, als das bisher in  $e^+e^-$ -Experimenten möglich war. Die meisten Zerfallskanäle dieses Zustandes sind bisher noch unbeobachtet; deshalb wurde für die vorliegende Arbeit eine Machbarkeitsstudie für die Messung hadronischer Zerfälle des  $h_c(P_1)$  mit dem  $\bar{P}$ ANDA-Experiment gewählt. Es zeigt sich, dass mit Hilfe eines modellabhängigen Ansatzes für die Analyse der Daten eine Rekonstruktionseffizienz vom 40 % erreicht werden konnte, während Untergrundreaktionen mit einem Faktor  $10^6$  unterdrückt werden.

# Table of Contents

<b>Chapter 1 Introduction</b>	<b>1</b>
1.1 Basic Forces in Nature . . . . .	1
1.2 Elementary Particles . . . . .	2
1.3 Hadron Physics . . . . .	3
<b>Chapter 2 The <math>\bar{P}</math>ANDA experiment of FAIR</b>	<b>7</b>
2.1 The $\bar{P}$ ANDA physics program . . . . .	7
2.1.1 Hadron spectroscopy . . . . .	7
2.1.2 Hadron structure experiments . . . . .	11
2.2 Facility for Antiproton and Ion Research . . . . .	14
2.3 High-Energy Storage Ring . . . . .	16
2.4 The targets . . . . .	18
2.5 Luminosity profile . . . . .	20
2.6 $\bar{P}$ ANDA detector . . . . .	22
2.6.1 Detector requirements . . . . .	23
2.6.2 Magnets . . . . .	24
2.6.3 Tracking system . . . . .	25
2.6.4 Electromagnetic Calorimeter (EMC) . . . . .	27
2.6.5 Particle Identification (PID) . . . . .	28
2.6.6 Luminosity Detector (LMD) . . . . .	31
<b>Chapter 3 The Luminosity Measurement</b>	<b>32</b>
3.1 Motivation . . . . .	32
3.1.1 Cross section measurements . . . . .	32
3.1.2 Precision measurements of resonance parameters . . . . .	33
3.2 Alternative methods for luminosity determination at fixed-target experiments . . . . .	34
3.2.1 COSY . . . . .	34
3.2.2 E760/E835 . . . . .	36
3.3 The luminosity determination at $\bar{P}$ ANDA . . . . .	38
3.3.1 Elastic $p\bar{p}$ scattering . . . . .	38
3.3.2 Models and their uncertainties . . . . .	41
3.3.2.1 Dual Parton Model (DPM) model . . . . .	41
3.3.2.2 E760 model . . . . .	45
3.3.2.3 Comparison of the models with the data from previous elastic $p\bar{p}$ scattering experiments . . . . .	48

3.3.2.4	KOALA experiment . . . . .	51
3.3.2.5	Model uncertainty caused by the momentum uncertainty . . . . .	52
3.4	The Luminosity Detector . . . . .	54
<b>Chapter 4</b>	<b>Extraction of the luminosity</b>	<b>59</b>
4.1	PandaRoot framework layout . . . . .	59
4.2	Hit reconstruction . . . . .	62
4.3	Track search . . . . .	63
4.3.1	Track Following . . . . .	63
4.3.2	Cellular Automaton . . . . .	64
4.3.3	Comparison of performance for track search algorithms . . . . .	67
4.4	Track fit . . . . .	74
4.4.1	Straight line fit with weighted hits . . . . .	74
4.4.2	Track fit with broken lines approach . . . . .	76
4.4.3	Results and comparison of track fit approaches . . . . .	77
4.5	Track filter . . . . .	80
4.5.1	Filtering of split tracks . . . . .	80
4.5.2	Filtering of background tracks . . . . .	81
4.6	Back propagation to the Interaction Point . . . . .	85
4.6.1	Assumption about the momentum of the antiproton . . . . .	85
4.6.2	Propagation of track parameters . . . . .	91
4.6.3	Tests of forward and backward propagation with GEANE . . . . .	94
4.7	Reconstruction of the Interaction Point . . . . .	99
4.8	Computing time for the track reconstruction . . . . .	102
4.9	Luminosity extraction . . . . .	103
<b>Chapter 5</b>	<b>Modules alignment</b>	<b>105</b>
5.1	Influence of misaligned modules on the track reconstruction accuracy . . . . .	106
5.2	Iterative and Non-Iterative Methods . . . . .	108
5.3	Introduction to Millepede . . . . .	111
5.4	Residuals and Global Parameters . . . . .	113
5.4.1	Position of hits in the frame of one LMD sector . . . . .	113
5.4.2	Constraining the internal alignment within Millepede . . . . .	116
5.5	Simulation test . . . . .	117
5.6	Limits for translation and rotation misalignment for high energy tracks . . . . .	119
5.7	Limits for translation and rotation misalignment for low energy tracks . . . . .	120
<b>Chapter 6</b>	<b>Background studies for the luminosity measurement</b>	<b>123</b>
6.1	Simplified simulation studies . . . . .	124
6.1.1	Parameterization of the magnetic field . . . . .	124
6.1.2	Forward extrapolation . . . . .	125
6.1.3	Simulated data . . . . .	127
6.1.4	Check for consistency: forward – backward extrapolation . . . . .	127
6.1.5	Tracks selection and suppression by cuts . . . . .	128
6.1.6	Backward extrapolation with <<wrong>> momentum . . . . .	129
6.2	Background studies with the DPM generator . . . . .	132
6.2.1	DPM validation on available data . . . . .	133
6.2.2	Simulation description . . . . .	136
6.2.3	Antiprotons from elastic scattering as a background source . . . . .	139
6.2.4	Background distribution . . . . .	141
6.2.5	Background reduction . . . . .	145

<b>Chapter 7</b>	<b>Simulation studies <math>p\bar{p} \rightarrow h_c \rightarrow 5\pi</math></b>	<b>158</b>
7.1	Charmonium as a framework for QCD tests . . . . .	158
7.2	Potential models . . . . .	159
7.3	Current status of $h_c(1^1P_1)$ meson . . . . .	163
7.3.1	Mass . . . . .	163
7.3.2	Width . . . . .	164
7.4	Construction of the analysis model . . . . .	167
7.5	Generation of datasets . . . . .	169
7.6	Analysis . . . . .	170
7.7	Results and Discussion . . . . .	172
<b>Chapter 8</b>	<b>Summary</b>	<b>181</b>
<b>Appendix A</b>	<b>Access to elementary particles in experiments</b>	<b>186</b>
<b>Appendix B</b>	<b>Overview of antiproton-proton experiments in the past</b>	<b>189</b>
B.1	Bubble chamber . . . . .	189
B.2	CERN . . . . .	190
B.3	Brookhaven National Laboratory . . . . .	191
B.4	Fermilab . . . . .	191
B.5	Proton antiproton elastic scattering . . . . .	195
<b>Appendix C</b>	<b>Extraction of the model parameters for <math>\bar{p}p</math> differential elastic cross section by the LMD</b>	<b>197</b>
C.1	Results for $P_{beam}=1.5 \text{ GeV}/c$ . . . . .	198
C.2	Results for $P_{beam} 15 \text{ GeV}/c$ . . . . .	199
C.3	Conclusion . . . . .	200
<b>Appendix D</b>	<b>Track extrapolation in a non-homogeneous magnetic field</b>	<b>201</b>
<b>Appendix E</b>	<b>Propagation of the covariance matrix of track parameters in a magnetic field</b>	<b>205</b>
<b>Appendix F</b>	<b>Fritiof model (FTF) versus DPM as a background model for the LMD</b>	<b>211</b>
F.1	DPM . . . . .	211
F.1.1	Dual Models and relativistic quantum strings . . . . .	211
F.1.2	Comment on comparison between DPM and the experimental data . . . . .	215
F.2	FTF . . . . .	216
F.3	Simulation description . . . . .	217
F.4	Generator (true) level . . . . .	217
F.5	Reconstructed tracks . . . . .	218
F.6	Estimation of background with FTF . . . . .	219
<b>Bibliography</b>		<b>221</b>



*Dedicated to the HIMster*  
The system which taught me how to be patient, but persistent  
calm, but exact  
and respect people, but remember my goals



# Chapter 1

## Introduction

### 1.1 Basic Forces in Nature

#### Macroscopic scale

In everyday life we experience two fundamental forces. The gravitational force that for instance keeps us on earth and binds the solar system together, and the electromagnetic force between electrically charged objects, which for instance holds electrons and protons together inside atoms. Both forces are mediated over a distance inversely proportional to the square of the distance between the objects. With the advent of quantum mechanics in the first decades of the 20th century, it was realized that the electromagnetic field, including light, is quantized and can be seen as a stream of particles (photons). In this picture, the electromagnetic force can be thought of as a force mediated from one object to another by photons. In a similar way the gravitational force is believed to be transmitted by particles called gravitons. However the gravitational force is weaker than the electromagnetic force by 40 orders of magnitude. Thus the gravitons have not yet been detected so far [1].

#### Microscopic scale

The electromagnetic force binds electrons to the nucleus, because the nucleus and the electrons carry electric charges. The nucleus itself is composed from protons and neutrons. E. Wigner [2] showed that there must be two distinct nuclear forces at play within the nucleus. There are a weak force that is responsible for the radioactive  $\beta$ -decay and a strong one that binds the protons and the neutrons together. Both of them act only over a very short range, of the size of the nucleus, hence they have no macroscopic analogue.

Since the middle of 20th century scientists have been trying to understand those microscopic forces with both theoretical as well as experimental approaches. This is

a particularly challenging task, due to the absence of experience with such kind of interactions in everyday life. However researchers managed to overcome this problem by construction of special experimental facilities, called particle accelerators, to enter the microscopic world and instruments, called detectors, which register phenomena happened there.

## 1.2 Elementary Particles

Elementary Particle physics aims to study the ultimate constituents of matter and the nature of the interactions between them. In current understanding, particles are excitations of quantum fields and interact following their dynamics. The set of fundamental fields and their dynamics are summarized in a theory called the Standard Model.

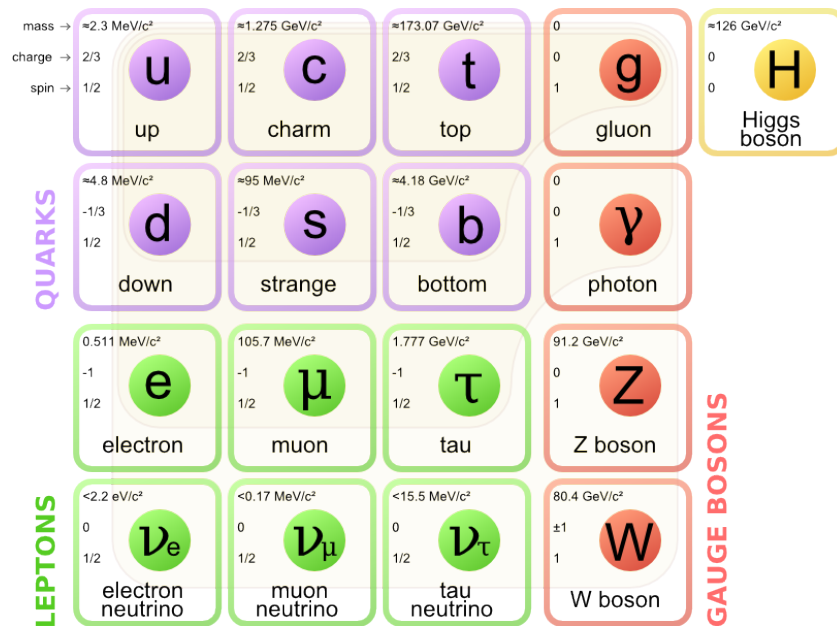


Figure 1.1: Standard Model of Elementary Particles [1]

The currently known elementary particles can be subdivided in two groups due to their different roles in the model (Fig. 1.1):

- (i) Matter is composed of fundamental fermions constituents (particles with  $\text{spin}=1/2$ ). There are *quarks* with third-integer in units of the elementary electric charges, *leptons*, carrying integral electric charges and electrically neutral *neutrino*. In addition to electric charge, quarks also carry another type of charge called *color*.
- (ii) These constituent can interact by exchange of fundamental *bosons*, which are the carriers of the quanta of the fundamental interaction or field. The bosons are characterized by integral spin.

The quarks have not been observed as free particles and seem to be permanently confined in objects called *hadrons*. Also quarks come in a variety of types or *flavors* (three with charge  $\frac{2}{3}e$  and three with  $-\frac{1}{3}e$ ) as do the leptons (three types of charged and of neutral leptons). The reason for quarks and leptons three generation ("copies") in flavors is not clearly understood yet.

The picture of fundamental interactions is a bit more clear. We know that some of them are *unified*. Therefore they are different aspects of one single interaction. The weak and the electromagnetic interaction appear to have the same intrinsic coupling of fermion constituents to the respective mediating bosons and they are different aspects of the *electroweak* interaction. The weakness of the weak interaction is explained by the short-range nature of its mediators, massive bosons  $W^\pm$  and  $Z^0$ . The mediator of the electromagnetic interactions is the massless photon. At energies high enough, well above a mass scale given by  $W^\pm$  and  $Z^0$  masses, both interactions have the same strength.

The weak bosons gain mass through the Higgs mechanism by interacting with the *Higgs* field. In the mechanism a Higgs field is added to the Standard Model gauge theory. The electroweak symmetry breaking triggers conversion of the longitudinal field component to the Higgs boson, which interacts with itself and the other fields and produces mass terms for the Z and W bosons. Fermions, such as the leptons and quarks in the Standard Model, can also acquire mass as a result of their interaction with the Higgs field, but not in the same way as the gauge bosons. The Higgs boson was predicted within Standard Model already a long time, until it was finally discovered in summer 2012 at CERN [3], [4].

### 1.3 Hadron Physics

A hadron is not a purely elementary particle, due to its internal structure. It contains quarks. The strong force is not only responsible for interactions between hadrons, but also for binding quarks into a hadron. Depending on the number of quarks in a hadron it can be categorized as *baryon* or *meson*. Baryons are made of three quarks (e.g. protons and neutrons). Mesons are made of one quark and one antiquark (e.g. the pion). In the Standard Model other types of hadrons are not forbidden, such as tetraquarks or, more generally, exotic mesons, and pentaquarks (exotic baryons), but so far only strong indication exist for tetraquark states, such as the  $Z_c(3900)$  [5].

The modern theory of the strong interaction is called Quantum Chromodynamics (QCD). The theory provides a dynamical basis for the quark-model description of hadrons. Interactions among the quarks are mediated by vector force particles called gluons, which themselves experience strong interactions. The nuclear force that binds protons and neutrons together in atomic nuclei emerges from the interaction among

quarks and gluons. Therefore the theory of QCD describes a wealth of physical phenomena, from the structure of nuclei to the inner workings of neutron stars and the cross sections for collisions of elementary particles at high energies.

Interaction mediated by 3 or 4 gluons makes the physics of QCD essentially different from the mathematically similar theory of Quantum Electrodynamics (QED). In QED, an electron's charge is partially screened by vacuum polarization of the surrounding cloud of virtual electron-positron pairs. The effect can be measured with a probe of wavelength, which is inversely proportional to the energy scale  $Q$ , and described by a scale dependence, or running, of the fine structure constant  $\alpha = e^2/4\pi$ . The fine-structure constant  $\alpha$  specifies the strength of the interaction between charged particles and photons and determines the magnitude of the fine structure (spin-orbit splitting) in atomic spectra. In QED at larger values of  $Q$  (at shorter distances), the effective charge increases as shown on the left panel of Fig. 1.2.

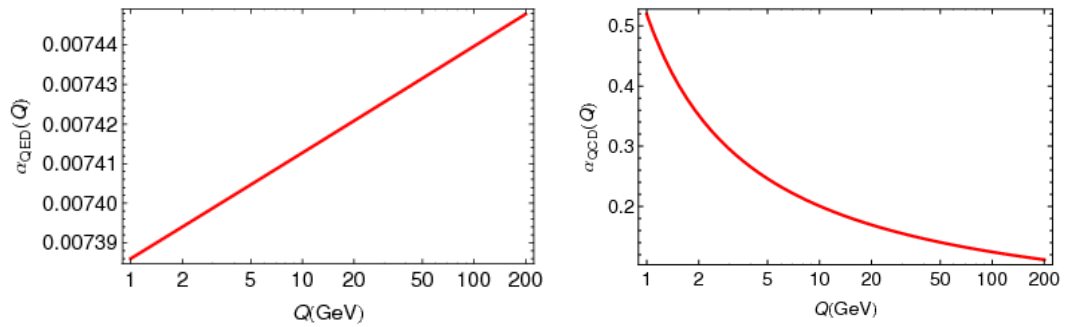


Figure 1.2: Coupling constant  $\alpha$  in QED (left) and in QCD (right) as a function of the energy scale  $Q$  [6]

In QCD gluons can fluctuate into further quark-antiquark pairs, and this vacuum polarization exerts a similar screening effect, tending to increase the effective color charge at short distances. This tendency is overcome by anti-screening effects that arise from the contributions of gluon loops to the vacuum polarization. The behavior of the strong-interaction analogue of the fine structure constant  $\alpha_s = g^2/4\pi$  depends on the number of quark flavors. In our six-flavor world  $\alpha_s$  decreases at large values of  $Q$  or short distances (right panel of Fig. 1.2). This property is called *asymptotic freedom*. Increasing of  $\alpha_s$  at small  $Q$  is believed to be responsible for the *confinement*. Due to the confinement, if a quark and an antiquark are separated by a large distance, the force between them does not fall off with distance, while the potential energy grows. This is the explanation of the empiric fact that quarks and gluons (the degrees of freedom in QCD) never appear as asymptotic states. The physically observed spectrum consists of color-singlet mesons and baryons. Therefore, although elementary quarks and gluons are the building blocks of Standard Model, in the detector we observe only hadrons.

The behavior of  $\alpha_s$  at large and small  $Q$  subdivides QCD in two different regimes. The

regime at large  $Q$  is called *perturbative*. Here asymptotic freedom governs the behavior of the particles, and their properties can be observed in great detail. In this case the measured properties are directly related to the quark and gluon degrees of freedom as they appear in the QCD Lagrangian. QCD is well tested at high energies, where the strong coupling constant  $\alpha_s$  is small and perturbation theory is appropriate.

In the low energy regime, QCD becomes a strongly coupled theory. This is the *non-perturbative* regime. At these energies, where quarks seem to be "dressed" with gluons and quark-antiquark pairs, the connection of the QCD Lagrangian to the microscopic description is inadequate. The individual quarks and gluons are making up the many-body system of hadron and can not be examined in isolation. The degrees of freedom of the QCD Lagrangian are not the degrees of freedom that are important in describing properties like the charge radius, magnetic moments, or the results of spectroscopy experiments in general. Since first-principle calculations using QCD are still not practical for many long-distance phenomena, a number of models motivated by the color structure of QCD have been proposed. Yet the quantitative description of hadron properties in terms of quarks and gluons remains a challenge.

One of the fundamental questions, which still have to be answered, is the origin of mass. While the Higgs mechanism explains the masses of the elementary particles, the mass-creation mechanism for hadrons, e.g. protons, is quite different. Through the Higgs mechanism light quarks acquire current masses of  $\sim 3\text{--}5\text{ MeV}$ . Thus the sum of the masses of three light quarks is around  $10\text{ MeV}$ , which gives only 2% of the contribution to the proton mass. The most part of the proton mass is believed to be arisen from the strong interaction by not very well understood mechanism [7].

Further progress in our understanding of the strong interaction requires high-precision data input from experiments in the non-perturbative regime. According to the methods and tools, experimental Hadron Physics is subdivided into several branches:

- Hadron Spectroscopy
- Hadron Structure
- Hadron Dynamics

Experimentally, studies of hadron physics can be performed with different probes such as electrons, protons, pions etc. Many recent experiments were using  $e^+e^-$  annihilation. There direct formation proceeds through an intermediate virtual photon. Therefore it is limited to the vector states ( $J^{PC} = 1^{--}$ ). Because electrons and positrons are point-like particles, their collisions are clean and suitable for precise measurements. However the limit of direct formation to the vector states implies a limited mass and width resolution for the non-vector states.

In  $p\bar{p}$  annihilation, thanks to the coherent annihilation of the three quarks in the proton with the three antiquarks in the antiproton, it is possible to form directly states

with any (non-exotic) quantum number combination via intermediate states with the appropriate number of gluons. Therefore achievement of an excellent mass and width resolution for all states is feasible. However, due to composite nature of hadron, these collisions contain a high level of hadronic background and therefore are more challenging to analyze.

At future  $\bar{P}$ ANDA experiment, an antiproton beam will be employed to perform measurements in hadron physics domain. The main part of this thesis is dedicated to studies for the luminosity measurement at  $\bar{P}$ ANDA experiment. The experiment with its physics program and the detector is introduced in the Chapter 2. As reviewed in Chapter 3, the LMD itself is a tracking system, which provides an independent luminosity measurement by registration of antiprotons scattered at small angles in proton-antiproton elastic scattering. The reconstruction of antiproton tracks, which is a subject of Chapter 4, was accurately checked in simulations to ensure good performance and robustness of chosen algorithms. Track reconstruction strongly relies on the exact knowledge of the LMD geometry and its alignment. The influence of a possible misalignment on the reconstruction accuracy and the method proposed to extract a misalignment from registered tracks are topics of Chapter 5. Due to the simplicity of the LMD as a detector, a background, mainly particles coming from inelastic interactions at IP, could be a problem. Dedicated simulations, which are based on our current knowledge of proton-antiproton inelastic interactions, were carried out and a background rejection scenario is discussed in Chapter 6.

The second part of the thesis discusses ideas and a fast simulation feasibility study of the charmonium state  $h_c$ . Search of decay modes of the  $h_c$  to light hadrons will be interesting, because just few of them were observed so far. At  $\bar{P}$ ANDA this search could be particularly challenging due to high cross sections of non-resonance production of such final states in  $\bar{p}p$  interactions. In Chapter 7 a model dependent analysis and a possibility to perform this measurement with a reduced  $\bar{P}$ ANDA set-up is explored.

# The $\bar{P}$ ANDA experiment of FAIR

$\bar{P}$ ANDA is a next generation hadron physics experiment planned for the future Facility for Antiproton and Ion Research (FAIR) at Darmstadt, Germany. It will use antiproton beams with a momentum between  $1.5 \text{ GeV}/c$  and  $15 \text{ GeV}/c$  interacting with various internal targets. The experiment has been designed to address open questions from all sub-fields of Hadron Physics. A comprehensive discussion on the  $\bar{P}$ ANDA physics program can be found in [8]. Here the physics program is discussed basically with an emphasis on the exploration of interactions between the hydrogen target and the antiproton beam ( $p\bar{p}$  interactions). Following this discussion, the experimental set-up is introduced.

## 2.1 The $\bar{P}$ ANDA physics program

### 2.1.1 Hadron spectroscopy

The spectrum of light, emitted by an excited atom, directly reflects the fact that atoms are composed of charged objects, nuclei and electrons, with an electromagnetic force holding them. Thus the spectrum of the system teaches us about its constituents and the forces that bind them together. This is equally true for the spectrum of hadrons.

In QCD the spectrum is a list of particles that are stable or at least sufficiently long-lived to be observed. Spectroscopy aims to answer questions about the structure of hadrons and their properties. Among others, past spectroscopy experiments led to the development of the quark model. A more precise description of strong interactions, especially dynamics at long-distance, shall be possible with improved experimental techniques. The goal of modern experiments is to reach as high statistics as possible. Significant number of registered interactions is needed to detect rare phenomena, in particular new forms of hadronic matter like multiquark states.

### Gluonic excitations (Glueballs)

Gluons are massless mediator particles of the strong interaction. However, they carry *color*, which is the charge of the strong interaction. It allows the formation of baryon-like bound states of gluons even if no quarks are present. Such a bound state is called a *glueball*. Glueballs made up from massless gluons would be massless without the strong interaction. Their predicted masses arise from the strong interaction. Thus glueballs offer a unique way to study the mass creation of strongly interacting particles.

However, glueballs are difficult to be identified because their masses (e.g. calculated from lattice QCD predictions [9]) overlap with these of mesons. And due to the fact that they have identical quantum numbers, interference between mesons and glueballs complicates their extraction and identification. Therefore an amplitude analysis of high statistics data is crucial here.

### Charmonium spectroscopy

A *charmonium* is a bound state of a charm quark  $c$  and an antiquark  $\bar{c}$ . Below the threshold for  $D\bar{D}$  production (3.73 GeV), the spectrum consists of eight states. Charmonium is a good system to test the assumptions of QCD. Unlike light-quark hadrons, the value of  $\alpha_s$  for charmonium is sufficiently small  $\sim 0.3$  to make perturbative calculations possible. Furthermore, the relatively small binding energy compared to the rest mass of its constituents allows  $c\bar{c}$  states to be described non-relativistically (with  $v^2/c^2 \approx 0.25$ ). Finally, the masses of the bound  $c\bar{c}$  states are well separated and narrow in width, as opposed to the light-quark resonances which have large, often overlapping, widths.

All eight states have been established, but not all of their properties have been measured with the same accuracy. This reflects the fact that it is easy to form vector mesons at an electron-positron collider, while other states need to be detected in the decay of a vector state. Only the Fermilab experiments E760 and E835 could achieve the formation of non-vector states. However, the beam time was limited and therefore decay channels with small cross sections could not be detected.  $\bar{P}$ ANDA can be considered as a successor of the Fermilab experiments, where both the intensity of the beam as well as detection techniques will be improved. This topic will be discussed in more detail in Chapter 7.

### Spectroscopy of X, Y and Z states

The XYZ states are unexpected resonances discovered during the last decade that contain a  $c\bar{c}$  pair and are above the open heavy flavor  $D\bar{D}^*$  threshold. The story began with the discovery of the X(3872) by the Belle Collaboration in 2003 [11] and its confirmation by BaBar and others [1]. The X(3872) has comparable branching fractions into  $J/\psi\rho$  and  $J/\psi\omega$  implying a violation of isospin symmetry. The most recent discovery in this context is the charged resonance  $Z_c^+(3900)$  by the BESIII Collaboration

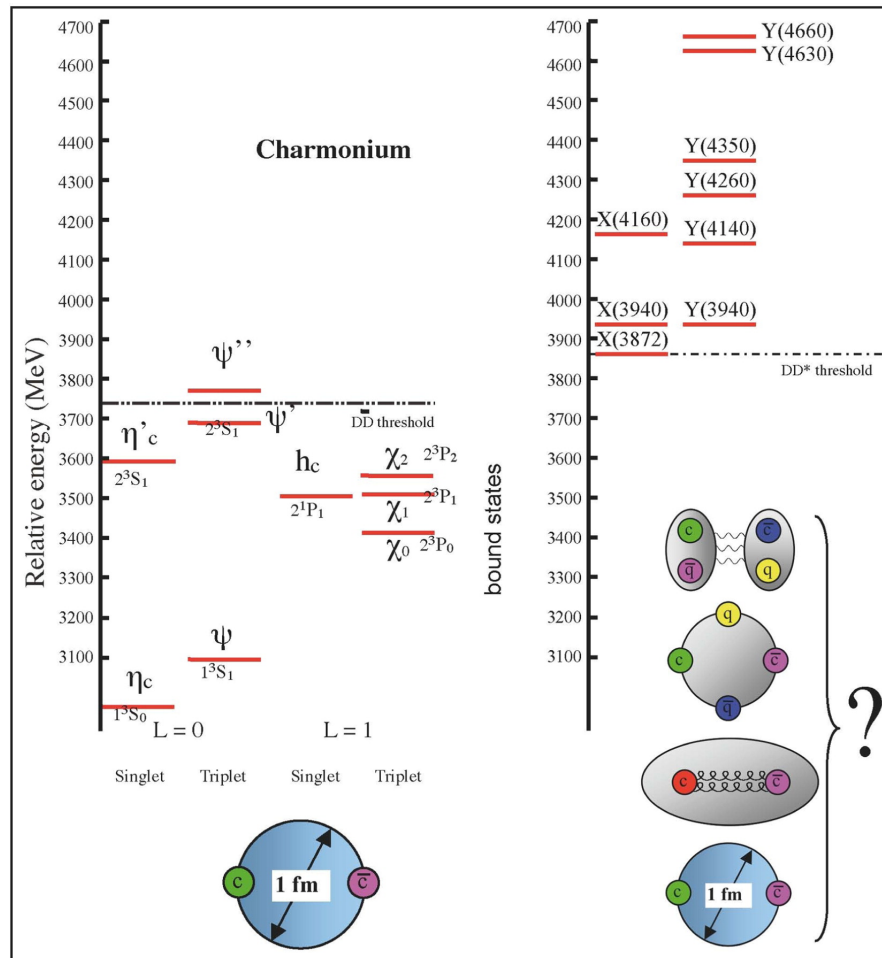


Figure 2.1: The established charmonium spectrum (left) and recently discovered X and Y states with unusual properties (right) [10]

in 2013 [5]. It decays into  $J/\psi\pi^+$ , which makes it a good candidate for a tetraquark state with constituents  $c\bar{c}u\bar{d}$ .

The most up to date list of the XYZ states in both the  $c\bar{c}$  (*charmonium*) and  $b\bar{b}$  (*bottomonium*) sectors is given in [12]. Many of these states are surprisingly narrow and place a serious gap in our understanding of the QCD spectrum. Various models proposed by theorists for the XYZ resonances include conventional quarkonium, quarkonium hybrids, quarkonium tetraquarks, meson molecule etc. So far none of the models has provided a compelling pattern for the XYZ states.

Additional hints will be given by future experiments like  $\bar{P}$ ANDA, which is going to measure in the center-of-mass energy range below 5.4 GeV. As can be seen in Fig. 2.1 masses of the charmonium as well as XYZ states lie within this energy range.  $\bar{P}$ ANDA will contribute to a better understanding or eventually a solution to the XYZ puzzle.

### Open charm spectroscopy

Open charm mesons (usually called D mesons) consist of charm and a light constituent. They are another example of very interesting objects in order to figure out the specific properties of the strong interaction. D mesons combine the aspect of the heavy quark as a static color source on one side and the aspect of chiral symmetry breaking and restoration due to the presence of the light quark on the other. Since a light quark and a heavy quark are bound together, such mesons can be seen as the hydrogen atom of QCD.

The quark model was capable of describing the spectra of D mesons with reasonable accuracy and even of making predictions, until the new resonances  $D_s(2317)$  and  $D_s(2460)$  were found at Belle, BaBar and CLEO. Since these new resonances did not fit well into the quark model, they triggered a large number of theoretical interpretations. Those range from models that predict the mass splitting of states due to chiral symmetry to those proposing tetraquark states or molecules. In order to distinguish between different models, the precise knowledge of the decay widths of the  $D_s$  states would certainly help. The current upper limit of a few MeV, given by the detector resolutions of previous experiments, is not precise enough to draw any conclusion [8].

### Baryon spectroscopy

Baryons are composed of three valence quarks plus any number of quark–antiquark pairs (sea quarks). So far all established baryons are 3–quark (qqq) configurations. The Particle Data Group identifies a baryon by its name and mass [1]. In this scheme, the name  $\Lambda$  or  $\Sigma$  is used for baryons having two light  $u$  or/and  $d$  quarks and one  $s$  quark. Particles with one light quark are called  $\Xi$ . Charmed baryons contain a charm  $c$  quark instead of the strange  $s$  quark. This is reflected in the suffix of the state name, e.g.  $\Lambda_c$ .

Baryons containing heavy quarks (like  $\Lambda$  or  $\Sigma$ ) provide an interesting laboratory for studying QCD. They combine two different regimes: the relatively slow motion of the heavy quark with the relativistic motion of the light quarks. The XYZ puzzle demonstrates our poor knowledge about the light quark dynamics and the urgent need of gaining a more accurate understanding. Any further explanations on already observed states or new predictions are dependent on that. A handful of exotic states have not been observed yet. This hints at the possibly inadequacy of the dynamical models. As discussed in [13], we can learn more on light quark dynamics from singly heavy baryons,  $Qqq$ , than from the light baryon sector,  $qqq$ .

The baryon spectroscopy of light–quark baryons is pursued intensively at electron accelerators. Whenever the baryons contain strange or even charm quarks, the data situation becomes extremely sparse. For instance the properties of  $\Xi$  resonances were not improved since the 1980's [14]. Data came from bubble chamber experiments with small statistic. While the mass of heavy baryons is measured as part of the discovery process, no spin or parity quantum numbers of the states have been measured exper-

imentally. Currently the expectation based on quark model are assigned as quantum numbers to the states. Such properties can only be extracted by studying the angular distribution of the particle decays, which are available only for the lightest and most abundant species. For excited heavy baryons the data sets are typically too small. This is the main reason for limited knowledge of radially and orbitally excited states. In contrast to ground states – whose properties are in good agreement with the quark model – the spectrum of excited states is much less clear. The assignment of some experimentally observed states with strange quarks to model configurations is only tentative and in many cases candidates are completely missing [1].

The  $\bar{P}$ ANDA experiment is well-suited for a comprehensive baryon spectroscopy program, in particular in the spectroscopy of (multi-)strange and possibly also charmed baryons. In  $p\bar{p}$  reactions, a large fraction of the inelastic interaction is associated with channels resulting in a baryon antibaryon pair in the final state. The requirement that the patterns found in baryon and antibaryon decays have to be identical reduces the experimental systematic uncertainties. A particular advantage of using antiprotons in the study of (multi-)strange and charmed baryons is that in antiproton-proton annihilations no additional production of extra kaons or D mesons is required for strangeness or charm conservation. The baryons can be produced directly close to the threshold, which reduces the number of background channels, for example compared to high-energy  $pp$  collisions [8].

### 2.1.2 Hadron structure experiments

Studying the internal structure of hadrons provides a way to probe Quantum Chromodynamics in the non-perturbative domain and can help to unravel the internal structure of the most elementary blocks of matter. The quark and gluon structure of hadrons can be best revealed with the help of electro-weakly interacting probes, such as photons and W, Z bosons. These probes are weakly coupled to quarks and "select" a well defined QCD operator. Such operator is expressed in terms of quark and gluon degrees of freedom of QCD Lagrangian. By measuring the reaction of a hadron to such a probe, one measures the matrix element of the well-defined quark-gluon operator over the hadron state revealing the quark-gluon structure of the hadron [15].

The phenomenon of asymptotic freedom, meaning that at short distances the interactions between quarks and gluons become weak, suggests that there are weak interactions as inherent property of QCD. This implies that if one manages to create a small size configuration of quarks and gluons it can be used as a new probe of hadronic structure. The possibility to create small size configurations of quarks and gluons is provided by *hard reactions*, for example by high energy lepton scattering on nucleon (protons and neutrons).

Traditionally, nucleon structure has been studied in two complementary ways. How-

ever, in both cases scattering processes of leptons on nucleons were used. Here it is necessary to distinguish elastic and inelastic scattering. In the elastic scattering initial and final particles are the same (left panel of Fig. 2.2). In the inelastic process lepton scatters on a hadron, but the hadron is "shattered" and emits many new particles (right panel of Fig. 2.2). Through elastic scattering the charge and magnetization distributions inside the hadron are studied via measurements of *form factors*. Generally form factors provide a distribution of hadron constituents in position space. Through Deeply Inelastic Scattering (DIS), momentum distribution of quarks and gluons can be studied and described via *parton distributions functions (PDFs)*. Form factors do not provide any

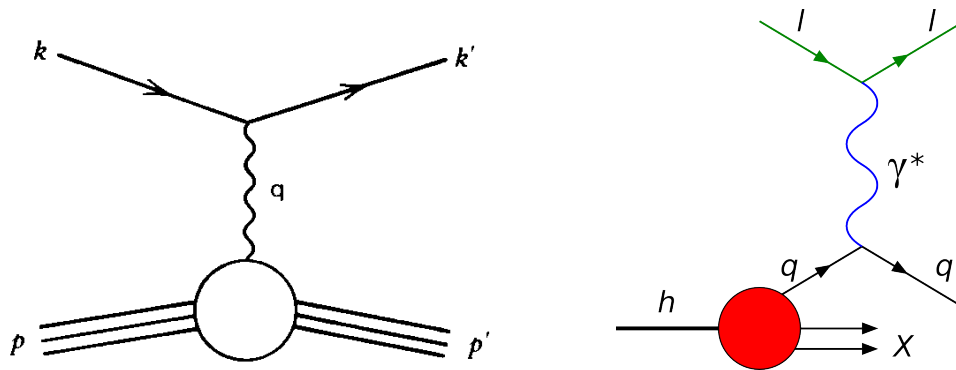


Figure 2.2: Elastic scattering (left) and deep inelastic scattering (right) [16]

information about the dynamics of the system, whereas parton distributions do not tell anything about the position of the constituents. A more complete picture can be gathered from the correlation between position and momentum spaces. These correlations are accessible through a new kind of functions that generalize PDFs and are therefore known as Generalized Parton Distributions (GPDs), where the correlation between the quark/gluon transverse position in a hadron and its longitudinal momentum is encoded.

The common important feature of hard reactions is factorization property. This gives the possibility to separate clearly the perturbative and nonperturbative stages of the interactions. Qualitatively speaking, the presence of a hard probe allows creation of small size quark, antiquark and gluon configurations whose interactions are described by means of perturbation theory due to the asymptotic freedom of QCD. This is the so-called "*hard*" part of a reaction. The non-perturbative stage (or "*soft*" part) of such a reaction describes how a given hadron reacts to this configuration, or how this probe is transformed into hadrons.

### Hard exclusive antiproton–proton annihilation processes

In the wide-angle Compton scattering process  $p\gamma \rightarrow p\gamma$ , the hard scale is related to the large transverse momentum of the final-state photon. The soft part of the process can be parameterized using GPDs. In  $p\bar{p}$  annihilations crossed kinematics cause an inverted process:  $p\bar{p} \rightarrow \gamma\gamma$ . Although it is not accurate for very low or very high energies, the factorization approach might be valid for  $p\bar{p} \rightarrow \gamma\gamma$  in exactly the energy regime where  $\bar{\text{PANDA}}$  operates [8]. The corresponding amplitudes, which parametrize the soft part of the annihilation process (i.e. the counterparts of GPDs), are called *Generalised Distribution Amplitudes* (GDAs). Measuring this reaction is a challenge since the two-photon final state suffers from a huge hadronic background. However, current results from Monte Carlo studies for  $\bar{\text{PANDA}}$  look very promising [10].

The factorization assumption is suitable for the description of further reactions, like  $p\bar{p} \rightarrow M\gamma$  where  $M$  is any neutral meson (e.g. a  $\pi^0$ ,  $\rho^0$ , etc) or  $p\bar{p} \rightarrow \gamma^*\gamma$ , where  $\gamma^*$  decays into an  $e^+e^-$  or  $\mu^+\mu^-$  pair. All these processes are planned to be studied at  $\bar{\text{PANDA}}$  [8].

### Electromagnetic form factors in the time-like region

The interaction of the electron with the nucleon can be described by the exchange of one photon with the space-like four momentum transfer  $q^2$ . The lepton vertex is described completely within QED. For the nucleon vertex, the structure of the nucleon is parameterized by two real scalar functions depending on one variable  $q^2$  only. These real functions are called *form factors*. The form factors are analytic functions of the four-momentum transfer  $q^2$  ranging from  $q^2 = -\infty$  to  $q^2 = +\infty$ . In electron scattering the form factors can be accessed in the range of negative  $q^2$  (space-like). The annihilation process allows to access positive  $q^2$  (time-like) starting from the threshold of  $q^2 = 4m_p^2$ . The unitarity of the matrix element requires that space-like form factors are real functions of  $q^2$  whereas for time-like  $q^2$  they are complex functions.

The  $\bar{\text{PANDA}}$  experiment offers an unique opportunity to determine the moduli of the complex form factors in the time-like domain. This can be achieved by measuring the angular distribution of the process  $p\bar{p} \rightarrow e^+e^-$  in  $q^2$  range from  $\sim 5(\text{GeV}/c)^2$  up to  $14(\text{GeV}/c)^2$ . It will then be possible to determine the magnetic form factor up to a  $q^2$  of  $22(\text{GeV}/c)^2$  by measuring the total cross section. Measuring the form factors is particularly difficult, because the expected background from  $p\bar{p} \rightarrow \pi^+\pi^-$  is about  $10^6$  times higher in the cross section. However according to current results from feasibility studies this measurement will be possible at  $\bar{\text{PANDA}}$  [17].

## 2.2 Facility for Antiproton and Ion Research

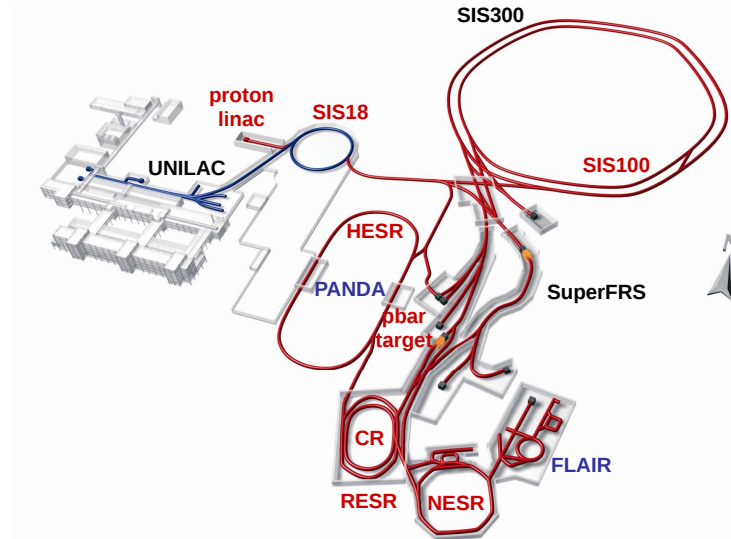


Figure 2.3: The accelerator complex at FAIR [18]

The Facility for Antiproton and Ion Research (FAIR) is an international accelerator facility which will use antiprotons and ions to perform research in different fields. They include nuclear, hadron and particle physics, atomic and anti-matter physics, high density plasma physics, and applications in condensed matter physics, biology and the bio-medical sciences. It is situated in Darmstadt (Germany) and it is currently under construction. FAIR will be based on an expansion of the GSI Helmholtz Center for Heavy Ion Research. Roughly 3000 scientists from more than 50 countries are already working on the planning of the experiment and the accelerator facilities.

An overview of the research center is given in Fig. 2.3. The already existing GSI accelerator complex will be used as the starting point of all future particle beams. In the following only the production of antiprotons will be discussed. The complete description of the facility can be found in [19].

### Production of Antiprotons

Antiprotons are usually generated in inelastic collisions of protons with target nuclei at rest. The process requires a minimum kinetic proton energy in the laboratory system above the antiproton production threshold of  $6m_p c^2 = 5.6 \text{ GeV}$ , where  $m_p$  is the rest mass of the proton (or antiproton) [20].

A proton linear accelerator (p-LINAC) will feed the Schwerionen Synchrotron (SIS) 18 4 times per second with a 70 MeV proton beam of 35 mA current. Roughly  $2 \times 10^{12}$  protons will be accumulated first, before being accelerated to a kinetic energy of 4 GeV [21]. Next protons are transferred to the SIS100, a normal conducting magnet synchrotron

of a total circumference of 1083.6 m. Several injections from the SIS18 are needed to accumulate roughly  $2 \times 10^{13}$  protons before being further accelerated to a final energy of 29 GeV. An additional acceleration to 90 GeV will be possible in a later stage of FAIR by the SIS300. Although the production yields increase with the proton energy, a kinetic energy of 29 GeV instead of 90 GeV is more favorable for several reasons. For example for protons at 29 GeV the maximum overall yield is already achieved for an antiproton energy around 3 GeV, which corresponds to a moderate magnetic rigidity of 12.7 Tm. For a kinetic energy of 90 GeV the maximum yield is around 9 GeV. Thus a beam transport system and storage rings with a much higher bending power of around 30 Tm would be required [20]. The high energetic protons from the SIS100 are shot as 50 ns long bunches on a nickel (or iridium) antiproton production target every 10 seconds, operating the target near melting temperatures [22]. The repetition rate is limited by the cycle length of the successive collector ring (CR). The remaining proton accelerator time is shared among experiments parallel to the antiproton production beam line.

### **Extraction of Antiprotons**

As a result of protons impinging on a solid state target, a large diversity of secondary particles is being produced. Momentum and angular distributions of the particles are range very widely. For a high antiproton collection efficiency, a combination of a magnetic horn and a momentum separation station is foreseen on the transfer way to the CR. Antiprotons will be accepted with a momentum of  $3.8 \text{ GeV}/c \pm 3\%$  while transverse emittance is expected to be cut to below  $\epsilon_{x,y} = 240 \text{ mm mrad}$  by that transfer beam line setup [20].

### **Collector Ring**

The collector ring (CR) provides full acceptance of those separated antiprotons. The major task is the collection of transported antiprotons, the cooling of the large phase space and the debunching of the beam within one cycle [23]. The Tab. 2.1 shows the key values of the beam parameters in the CR.

In the first years of physics runs, the pre-cooled beam will be directly fed into the High Energy Storage Ring (HESR). A later upgrade will involve the construction of the Recuperated Experimental Storage Ring (RESR) [24].

### **RESR**

The need for a high intensity beam requires an accumulation of antiprotons coming from the CR. The RESR will be located in the same hall as the CR. It is designed to accumulate within 3 hours up to  $10^{11}$  antiprotons at a momentum of  $3.8 \text{ GeV}/c$  [20]. During the accumulation the beam emittance is further reduced by stochastic cooling. In the operation as an antiproton accumulator, the designed final beam parameters for

values	at injection	at extraction
$p$ [GeV/ $c$ ]	3.8	3.8
$\Delta p/p$ ( $2\sigma$ )	3 %	0.1 %
$\epsilon_{x,y}$ [mm mrad]	240	5

Table 2.1: Antiproton beam parameters for the CR before and after debunching and cooling within a 10 s cycle [23]

the HESR are

$$\epsilon_{x,y} = 0.25 \text{ mm mrad} \left( \frac{N}{N_0} \right)^{4/5} \quad (2.1)$$

for the transverse emittance and

$$\frac{\Delta p}{p} = 3.3 \times 10^{-4} \left( \frac{N}{N_0} \right)^{2/5} \quad (2.2)$$

for the relative momentum spread. The beam quality depends on the number of accumulated antiprotons  $N$  and is given in respect to a reference particle number  $N_0 = 3.5 \times 10^{10}$  [25].

## 2.3 High-Energy Storage Ring

The High Energy Storage Ring (HESR), shown in Fig. 2.4, is an antiproton synchrotron and storage ring designed for the momentum range of 1.5 to 15 GeV/ $c$  [26]. The antiprotons are injected with a momentum of 3.8 GeV/ $c$  into the HESR, which is capable of accelerating or decelerating them. The advantage of a storage ring is that nearly all antiprotons that are produced can be used for experiments.

The desired beam quality and intensity will be prepared for two different operation modes. In the high luminosity (HL) mode a peak luminosity of  $2 \times 10^{32} \text{ cm}^{-2} \text{ s}^{-1}$  is expected. This mode is attained with  $10^{11}$  antiprotons and a target thickness of  $4 \times 10^{15} \text{ atoms/cm}^2$ . It should be available in the whole energy range of the HESR with a momentum spread  $\Delta p/p \leq 10^{-4}$ .

Higher requirements are necessary in the high resolution (HR) mode with an expected  $\Delta p/p \leq 4 \times 10^{-5}$  momentum spread. Here a peak luminosity of  $2 \times 10^{31} \text{ cm}^{-2} \text{ s}^{-1}$  can be attained with  $10^{10}$  antiprotons and a target thickness of  $4 \times 10^{15} \text{ atoms/cm}^2$ . High resolution beam is particularly beneficial for charmonium spectroscopy. Therefore this mode is requested up to 8.9 GeV/ $c$ .

In order to obtain an antiproton beam with a small momentum spread, the beam

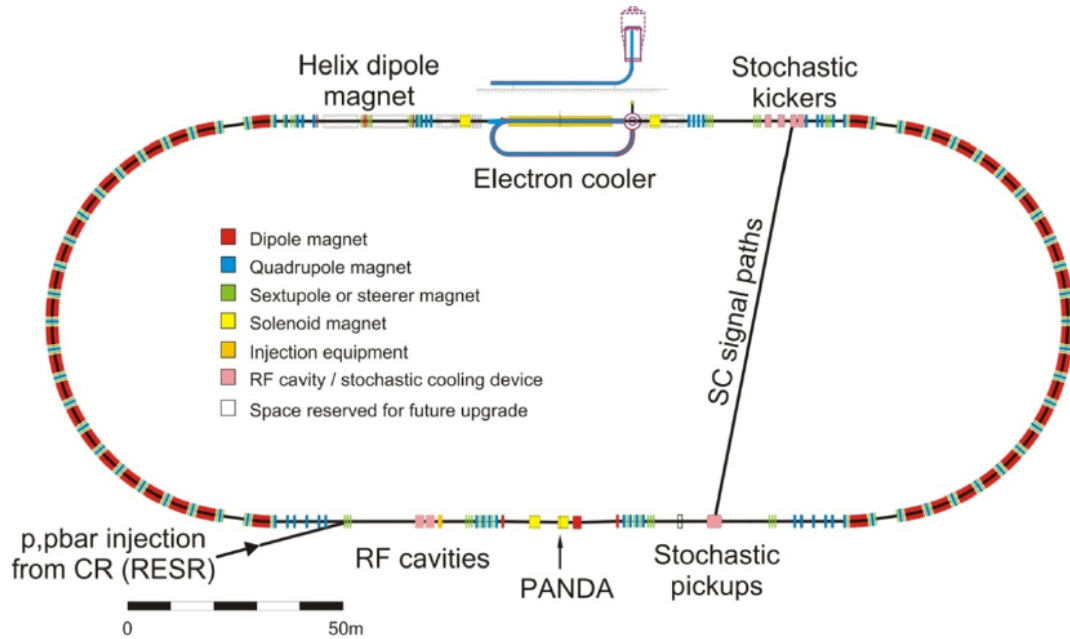


Figure 2.4: Layout of the High Energy Storage Ring [26]

must be cooled. *Cooling* is a process to shrink the size, divergence, and energy spread of charged particle beams without removing particles from the beam. Since the number of particles remains unchanged and the space coordinates and their derivatives (angles) are reduced, the phase space occupied by the stored particles is compressed. To accomplish these goals the current scenario foresees to apply electron cooling in the HR mode while a high bandwidth stochastic cooling system is utilized to provide the HL mode over the entire momentum range of the HESR [27].

*Stochastic cooling* uses the electrical signals produced by individual particles in a group of particles (called a *bunch*) to drive an electro-magnet device, usually an electric kicker, that will kick the bunch of particles to reduce the wayward momentum of that one particle. These individual kicks are applied continuously and over an extended time. Thereby the average tendency of the particles to have wayward momenta is reduced. This beam cooling method has the advantage of being capable to separately cool the transverse and longitudinal phase space. According to current detailed simulation studies, with this technique  $\Delta p/p \leq 8 \times 10^{-5}$  can be achieved after  $\sim 300$  s [28].

During *Electron cooling* the phase space of stored antiprotons can be compressed by aligning the antiproton beam with a cold dense electron beam. The velocity of the electrons is made equal to the average velocity of the antiprotons. The antiprotons lose energy by Coulomb scattering in the electron "gas". Energy loss is transferred from the antiprotons to the co-streaming electrons until some thermal equilibrium is attained. This results in a low antiproton beam emittance and a very narrow momen-

tum distribution. The compensation of heating requires cooling time constants in the order of seconds after an initial cool down. Stochastic cooling cannot provide adequate cooling rates, but according to the experience at lower energies, electron cooling is able to provide the required cooling times. The application of electron cooling in the HESR will require the extension of this technique to the MeV range. Feasibility studies have shown positive results [29]. Moreover a 2 MeV electron cooling system, which is well suited for the start up phase of HESR, is currently under commissioning at COSY.

The expected beam lifetime is restricted due to various effects. The most important ones are summarized in table 2.2. The relative loss rate

$$(\tau_{loss}^{-1}) = n_t \sigma_{tot} f_0 \quad (2.3)$$

is connected to the target thickness  $n_t$  and the reference particle's revolution frequency  $f_0$ . The inverse  $\tau_{loss}$  corresponds to the 1/e beam lifetime. For a target with a thickness of  $4 \times 10^{15}$  atoms/cm<sup>2</sup>, the dominating effect is the hadronic interaction. Revolution frequencies of 443 kHz, 519 kHz, 521 kHz were assumed for the distinct beam momenta with the corresponding hadronic cross sections  $\sigma_{tot}$ . As a consequence of the momentum dependent influence of the effects, the total expected beam lifetime ranges from 25 min at 1.5 GeV/c up to 118 min at 15 GeV/c beam momentum.

Process \ $P_{beam}$	1.5 GeV/c	9 GeV/c	15 GeV/c
Hadronic Interaction	$1.8 \times 10^{-4}$	$1.2 \times 10^{-4}$	$1.1 \times 10^{-4}$
Single Coulomb	$2.9 \times 10^{-4}$	$6.8 \times 10^{-4}$	$2.4 \times 10^{-4}$
Energy Straggling	$1.3 \times 10^{-4}$	$4.1 \times 10^{-5}$	$2.8 \times 10^{-5}$
Touschek Effect	$4.9 \times 10^{-5}$	$2.3 \times 10^{-7}$	$4.9 \times 10^{-8}$
Total	$6.5 \times 10^{-4}$	$1.7 \times 10^{-4}$	$1.4 \times 10^{-4}$
1/e lifetime	1540 s	6000 s	7100 s

Table 2.2: Upper limits for a relative beam loss rate ( $\tau_{loss}^{-1}/s^{-1}$ ) [26]

## 2.4 The targets

PANDA will use internal targets. These will be introduced at one Interaction Point (IP) into the HESR. The target inside a storage ring needs to be tuned in terms of size and thickness. Within the ultra-high vacuum of the storage ring, the target must be a very dilute and localized clump of matter. The overall area density of the target material corresponds to a mono-layer of atoms. In case of a gaseous target material, the use of even the thinnest window is prohibited. A solution for that can be realized by a

jet of nano- to micro-sized condensed matter particles (clusters, droplets or pellets) traversing the antiproton beam. Another basic requirements are a homogeneous volume target density and the absence of any time structure. At present, two different techniques for the internal target are being developed: a cluster-jet target and a pellet target, whose properties are presented in Tab.2.3.

	pellet target	cluster target
effective target thickness	$5 \times 10^{15}$ atoms/cm <sup>2</sup>	$1 \times 10^{15}$ atoms/cm <sup>2</sup>
target thickness adjustable	yes (reduced pellet rate)	yes (0-max)
volume density distribution	granular	homogeneous
size transverse to $\bar{p}$ beam	$\leq 3$ mm	2-3 mm
size longitudinal to $\bar{p}$ beam	$\leq 3$ mm	15 mm
target particle size	20 $\mu$ m	nm scale
mean vertical particle distance	2-20 mm	$\leq 10$ $\mu$ m
target material	H <sub>2</sub> , D <sub>2</sub> , N <sub>2</sub> , Ar heavier gases (opt.)	H <sub>2</sub> , D <sub>2</sub> heavier gases (opt.)

Table 2.3: Overview of the properties of the cluster-jet and the pellet targets [30]

The interaction point in a cluster-jet target can only be defined transversely through the focal size of the stored beam. Longitudinally, the reaction may take place anywhere along the intersection between the beam and the cluster stream, which typically will produce about 10 mm uncertainty for the vertex position. In contrast, a pellet target operated in a not too high frequency mode may allow to measure the interaction point with a precision up to 100  $\mu$ m using an optical pellet tracking system.

### Pellet target

The basic part of the pellet target is the triple-point chamber in which a jet of a cryogenic liquid is injected through a thin nozzle into a gas of the same element or helium close to triple-point conditions. Periodic excitations of the nozzle by a piezoelectric transducer impose jet oscillations along its surface. The axially symmetric jet disintegrates into drops downstream the nozzle when the perturbation amplitude becomes equal to the jet radius. The triple-point chamber ensures that an extremely regular drop flow can be produced under optimal conditions without disturbances from evaporation. The drops then pass through a thin injection capillary into the vacuum. They are cooled due to surface evaporation below the melting point, and a regular flux of frozen pellets is produced.

The position of individual pellets can be reconstructed by using a pellet tracking system based on optical detection devices. This can be done if there is one and only one

pellet in the beam region at the time of interaction. Unfortunately, even a small randomness in pellet occurrences leads to large variations in the target thickness. In order to reach the highest luminosity, a thick target with smooth time structure is required. This is incompatible with pellet tracking. Instead the high luminosity is obtained by simultaneously having many smaller pellets in the interaction region [30].

### **Cluster-jet target**

A disadvantage of a pellet target is the variation of the luminosity with the pellet flux. In this respect, clearly, a cluster-jet target with a homogeneous distribution of hydrogen atoms in the antiproton beam is better. The cluster-jet beam for the internal target in the HESR is produced by expansion of pre-cooled gas in a convergent-divergent Laval-type nozzle with micron-sized throat into vacuum. While passing through the nozzle, the gas adiabatically cools down and forms a supersonic stream of atoms or molecules. Under appropriate conditions, depending on the type of gas, condensation can take place and nano-particles, the so-called *clusters*, are created. The size of such clusters is strongly influenced by the experimental conditions such as the pressure and the temperature of the gas before entering the nozzle. Furthermore, the throat diameter and the shape of the supersonic part of the nozzle influences both the size of these particles and the total cluster yield. Cluster beams can travel over several meters of distance in a vacuum without changing their direction or shape. Also they have high densities.

The density achieved so far is below that of a pellet target, however, the expectations in current R&D are that the luminosity requirements for  $\bar{P}$ ANDA can be fulfilled. An additional advantage of a cluster-jet target is its homogeneous density profile. Thus, it is possible to focus the antiproton beam at highest phase-space density [30].

Both targets are connected to their source above the  $\bar{P}$ ANDA detector and to a dump below the  $\bar{P}$ ANDA detector by a thin pipe going through the whole detector and the magnet. A fixed cross with the beam pipe is installed at the interaction point. Beside hydrogen, internal targets of heavier gases, like deuterium, nitrogen or argon, will be available. For the dedicated Hypernuclear physics setup, even static primary and secondary targets are currently being developed [8].

## **2.5 Luminosity profile**

The quantity measuring the ability of a particle accelerator to produce the required number of events from the channel under study is called *luminosity*. It is the proportionality factor  $L$  between the number of events per second (event rate)  $dN/dt$  and the

cross section  $\sigma$  of a channel of interest:

$$\frac{dN}{dt} = L \cdot \sigma \quad (2.4)$$

Luminosity is not related to any particular reaction. It is a global characteristic of the experimental conditions and can be described in terms of the beam and target parameters. The incoming beam is characterized by the flux  $\Phi$ , i.e. the number of particles per second. The target is described by the density  $\rho_T$  and its length  $l$ . For a fixed-target experiment the luminosity is defined as:

$$L = \Phi \rho_T l \quad (2.5)$$

If the target parameters are constant, the time evolution of the luminosity follows the shape of the antiproton beam intensity. There are several options in order to provide constant luminosity. For instance, by increasing the target density to compensate of decreasing number of antiprotons in the beam. This can be achieved either by a constant increase of the target density or by increasing overlap of the beams by a shift of the target beam. Both scenarios require a fast feedback loop provided by a luminosity online monitoring system. It is expected that the luminosity can be kept constant at a 10% level [31].

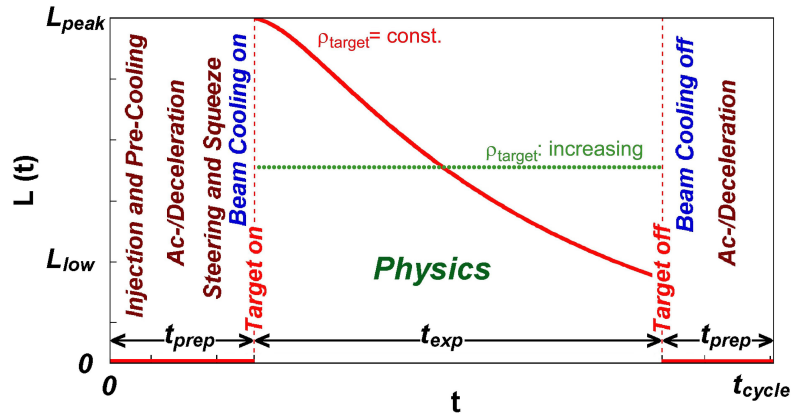


Figure 2.5: Typical operation cycles of the HESR with the RESR [26]

For successful physics experiments at HESR not the peak luminosity is important but the cycle average luminosity  $\bar{L}$ . For a constant target density it is given by:

$$\bar{L} = L_0 \cdot \frac{\tau \left[ 1 - \exp\left(-\frac{t_{exp}}{\tau}\right) \right]}{t_{exp} + t_{prep}} \quad (2.6)$$

$\bar{L}$  depends on the peak luminosity  $L_0$  at the beginning of the run, the experimental

data taking time  $t_{exp}$  and will be reduced by the beam lifetime  $\tau$  as well as the beam preparation time  $t_{prep}$ . Fig. 2.6 shows the expected average luminosity for a target with constants density of  $4 \times 10^{15}$  atoms/cm<sup>2</sup> and  $10^{11}$  antiprotons in the beam. Although the peak luminosity reaches the value close to  $2 \times 10^{32}$ cm<sup>-2</sup>s<sup>-1</sup>, the average luminosity is twice as low and around  $1 \times 10^{32}$ cm<sup>-2</sup>s<sup>-1</sup>.

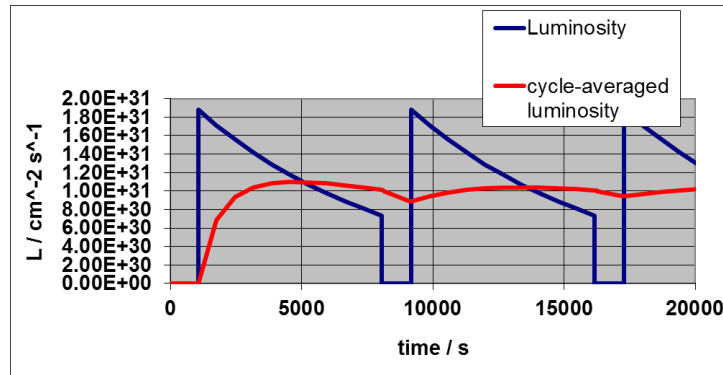


Figure 2.6: Difference between instant (blue) and time average (red) luminosity [31]

## 2.6 $\bar{P}$ ANDA detector

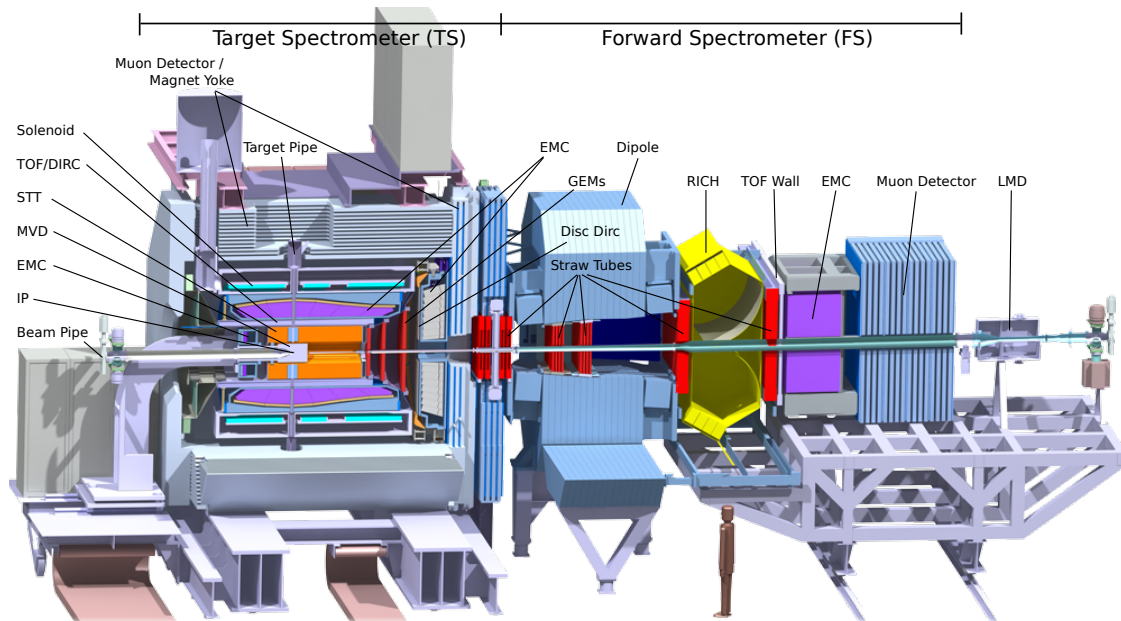


Figure 2.7: Artist's view of the  $\bar{P}$ ANDA experiment [32]

Fig. 2.7 shows the basic layout of the  $\bar{P}$ ANDA detector. It consists of a 4 m long Target Spectrometer (TS) with a 2 T superconducting solenoid magnet and Forward

Spectrometer (FS) with a 2 Tm resistive dipole magnet. Both are instrumented to detect charged and neutral particles emitted at large and backward angles (TS) and at angles between  $0^\circ$  and  $20^\circ$  (FS), respectively. The TS has an onion-shell like design surrounding the IP, which is very similar to the design of collider experiments. The FS is formed by an arrangement of subsystems along the beam axis in forward direction.

### 2.6.1 Detector requirements

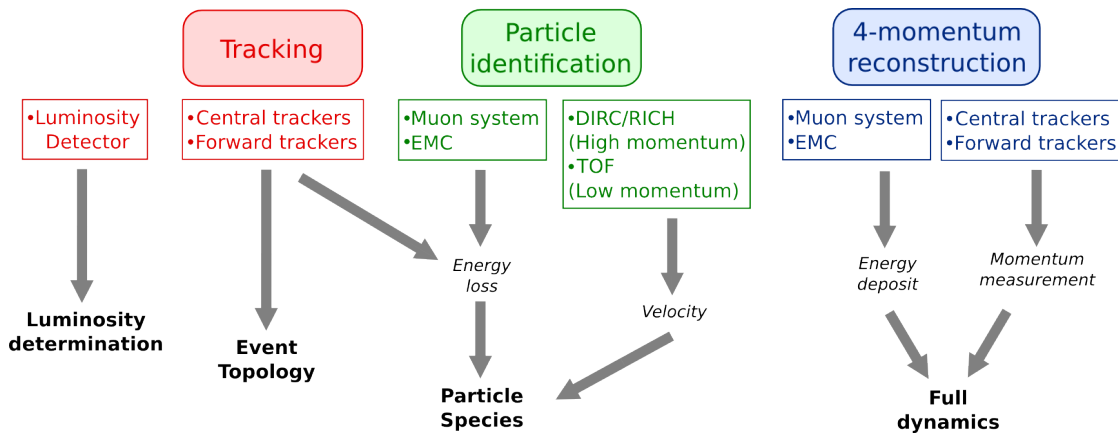


Figure 2.8: Basic detection concept [33]

To fully exploit the physics potential of the experimental conditions, the detector must provide a very accurate spatial resolution and a high reconstruction efficiency for a set of final states. Therefore, a multi-purpose detector is best suited. The design must also be compatible with different target systems.

For a complete event reconstruction the detection of both charged and neutral particles is required. Full  $2\pi$  azimuthal coverage and good PID are mandatory to identify multi-particle final states and to study correlations within the produced particles. The fixed-target setup implies a Lorentz boost with a  $\gamma$  factor ranging from 1.2 to 2.9. It corresponds to a large difference in the typical event topologies and a large dynamic range of emitted particles. Thus, the detector must be also suited to accurately track slow particles with momenta of about  $100 \text{ MeV}/c$  and to detect soft photons. Moreover, a very low material budget is needed to reduce multiple scattering effects.

The overall detection concept is shown schematically in Fig. 2.8. Most  $\bar{\text{PANDA}}$  subsystems serve several tasks at once. For example a very important task of the tracking system is the determination of secondary vertices (decay points) of short-lived particles. In this context, D mesons with mean decay lengths  $c\tau$  about  $0.1\text{--}0.3 \text{ mm}$  are of particular interest. These can be identified only by a vertex detector close to the Interaction Point (IP). However, the tracking system not only registers tracks of charged particles, but also measures their momenta and energy loss. Thereby the tracking sys-

tem contributes to an event topology (tracks and vertex) determination, to the particle identification and reconstruction of full dynamics. Neutral particles, especially those which do not necessarily decay into charged particles (photons, pions,  $\eta$ , etc., require dedicated detection systems for their registration and identification.

A main feature of  $\bar{P}$ ANDA is the need for the highly flexible trigger. Due to the similarity of interesting and background reactions in terms of the signatures, a sophisticated filtering strategy needs to be applied. It goes far beyond conventional hardware based trigger schemes. The concept of the  $\bar{P}$ ANDA data acquisition (DAQ) system bases on a trigger-less read-out. The detector's front-end electronics (FEE) and DAQ continuously sample and buffer data without any classical gated trigger signal. This approach principally allows to pre-analyze the data in an appropriate way before deciding to keep or reject a particular part of the data. Technically, this task puts a tremendous load on the DAQ system. The information allowing to effectively separate signal from background reactions has to be provided during data taking. Thereby it requires high-level reconstruction procedures in the online environment. The high intensity of the quasi-continuous beam will lead to an interaction rate up to 20 million antiproton annihilations per second. It represents a technical challenge in terms of high-rate capability for the detector components, the trigger and the data acquisition systems. The expected radiation level for the detector components will stay roughly one order of magnitude below the one of the LHC experiments [33]. The decision whether a certain fraction of the data stream should be written to the data storage or not is made by the online software trigger. This software package includes online reconstruction, event building and algorithms for data classification [34].

The  $\bar{P}$ ANDA apparatus will consist of tracking detectors (MVD, STT, GEM), electromagnetic calorimeters (EMC), a muon system, Cherenkov detectors (DIRC, RICH) and a time of flight (TOF) system. For high-precision spectroscopy and background suppression a relative resolution of particle momentum and energy on the percent level is required. In the following, the main components of the  $\bar{P}$ ANDA detector and their expected performance are described briefly.

## 2.6.2 Magnets

Appropriate magnetic fields are essential for a momentum reconstruction and subsequent particle identification of charged particles. The two large spectrometer magnets of  $\bar{P}$ ANDA are designed to provide an ideal combination of fields. A solenoidal magnetic field of 2 T around the interaction region and a dipole field of up to 1 T for particles emitted at forward angles below  $5(10)^\circ$ .

### Solenoid magnet

Fast and high-precision charged particle tracking can be achieved only with homo-

geneous magnetic field. Thereby the solenoid should provide a magnetic field of 2 T with a homogeneity of better than 2% in the region of the charged-particle detectors. This can be achieved by a superconducting solenoid with an inner radius of 90 cm and a length of 2.8 m. The coils of the magnet are placed outside the electromagnetic calorimeter in order to avoid dead material in front of it. The iron yoke is segmented to incorporate muon chambers in a range telescope arrangement. The cryostat for the solenoid coils contains two warm bores 100 mm in diameter, one above and one below the target position, to allow for insertion of internal targets.

### Dipole magnet

The forward direction is important for  $\bar{\text{PANDA}}$  because it is a fixed target experiment. Most of the particles will go forward due to momentum conservation. The magnetic field for the charged-particle tracking in the forward direction is provided by a dipole magnet with a one-meter gap and an aperture of more than 2 m. The magnet covers the entire angular acceptance of  $\pm 10^\circ$  in the horizontal direction and only  $\pm 5^\circ$  in the vertical direction to avoid a huge gap between the two poles. The magnet will be a conventional magnet with a maximum bending power of 2 Tm. It will deflect the antiproton beam by  $2.2^\circ$  at its maximum momentum of  $15 \text{ GeV}/c$ . This will be compensated by two correcting dipole magnets placed both upstream and downstream of the  $\bar{\text{PANDA}}$  experiment into the HESR ring.

### 2.6.3 Tracking system

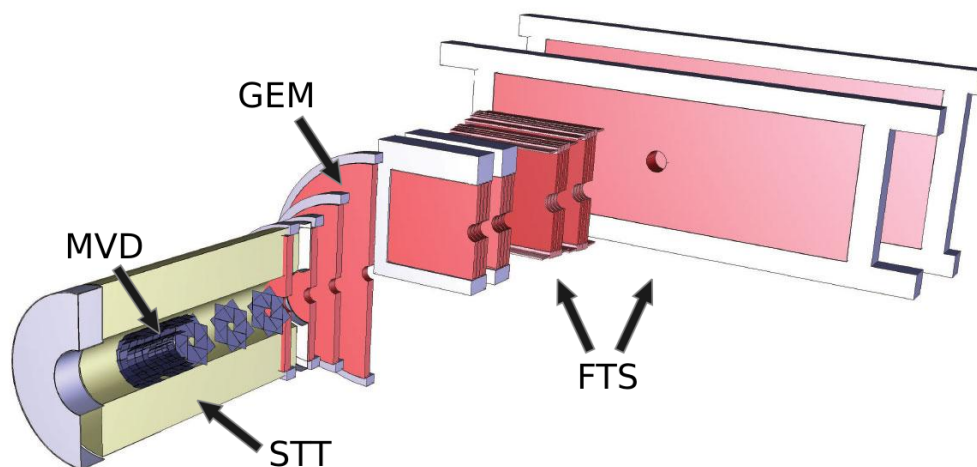


Figure 2.9: Tracking system of the  $\bar{\text{PANDA}}$  experiment

High resolution measurement of charged particle trajectories will be provided by three tracking systems in the TS (the Micro Vertex Detector, the Straw Tube Tracker

and the Gas Electron Multiplier Stations) and by the Forward Tracker system in the FS, as shown in Fig. 2.9.

### **Micro Vertex Detector (MVD)**

The MVD is the most inner sub-detector system in the target spectrometer, optimized for the detection of secondary decay vertices of short lived particles such as D-mesons and hyperon decays. It is based on radiation hard silicon pixel detectors with fast individual pixel readout circuits and silicon strip detectors. It consists of four barrel layers in the central part, with an inner radius of 2.5 cm and an outer radius of 13 cm, surrounding the beam pipe and of six detector discs arranged perpendicular to the beam. This ensures the best acceptance for the forward part of the particle spectrum. The vertex resolution is expected to be below  $35 \mu\text{m}$  in perpendicular to the beam line plane and below  $100 \mu\text{m}$  in the z-coordinate. Also the MVD will help to improve the transverse momentum resolution for tracks of charged particles. In addition it is capable of charged particle identification by measuring the energy loss  $dE/dx$  of slow particles. It contributes to the global particle identification decision up to a momentum of  $500 \text{ MeV}/c$  for kaons and up to  $1 \text{ GeV}/c$  for protons [35].

### **Straw Tube Tracker (STT)**

The STT is the main tracking detector for charged particles in the  $\bar{\text{P}}\text{ANDA}$  target spectrometer and consists of 4636 single straw tubes of 150 cm length, arranged in a large cylindrical volume around the IP. The basic module is a planar double-layer of tubes in order to resolve the left-right ambiguity of the track position with respect to the wire. The STT encloses the MVD (the inner tracking). It is followed in beam direction by a vertical setup of GEM disks for adding track points in the forward polar angle range, as discussed in the next section. The main tasks of the STT are the precise spatial reconstruction of the helical trajectories of charged particles in a broad momentum range from about a few  $100 \text{ MeV}/c$  up to  $8 \text{ GeV}/c$ . The expected resolution for charged tracks is  $\sim 150 \mu\text{m}$  in perpendicular to the beam line plane and  $\sim 1 \text{ mm}$  along the beam line. Also the particle momentum can be extracted from the reconstructed trajectory in the solenoidal magnetic field. Another important task for the STT is the measurement of the specific energy loss ( $dE/dx$ ) for particle identification. The PID information from the STT is needed in particular to separate protons, kaons and pions in the momentum region below  $1 \text{ GeV}/c$  [36].

### **Gas Electron Multiplier (GEM) Stations**

Particles emitted at angles below  $22^\circ$  are tracked by three planar stations placed approximately 1.1 m, 1.4 m and 1.9 m downstream of the target. Each station consists of double planes with two projections per plane. Double-sided read-out pad plane, which is located in the middle of each GEM-Disc, allows particle track position measurement

in four projections. The high number of projections per GEM-Disc ensures unambiguous determination of the particle trajectory position with a resolution of better than  $100\ \mu\text{m}$  [37].

### Forward Tracker Stations (FTS)

The FTS performs a tracks reconstruction and momentum analysis of charged particles deflected in the field of the  $\bar{\text{P}}\text{ANDA}$  dipole magnet. It covers an angular acceptance defined by the aperture of the magnet equal to  $\pm 10^\circ$  horizontally and  $\pm 5^\circ$  vertically with respect to the beam direction. The momentum acceptance extends above  $0.03 \cdot P_{\text{beam}}$ . The dependence on the beam momentum  $P_{\text{beam}}$  is introduced by scaling the field in the dipole magnet according to the beam momentum.

The FTS consists of three pairs of planar tracking stations: one pair is placed in front, the second behind the dipole magnet and, while the third pair is placed inside the dipole magnet gap. FTS is based on straw tube (10 mm in diameter) detectors of the type proposed for the STT. The detection planes are built of separate modules, consisting of 32 straws arranged in two layers. Each tracking station consists of four double-layers: the first and the fourth one contain vertical straws ( $0^\circ$ ) and the two intermediate double-layers – the second and the third one – contain straws inclined at  $+5^\circ$  and  $-5^\circ$ , respectively. The planned configuration of double-layers allows to reconstruct tracks in each pair of tracking stations separately, also in case of multi-track events [37].

### 2.6.4 Electromagnetic Calorimeter (EMC)

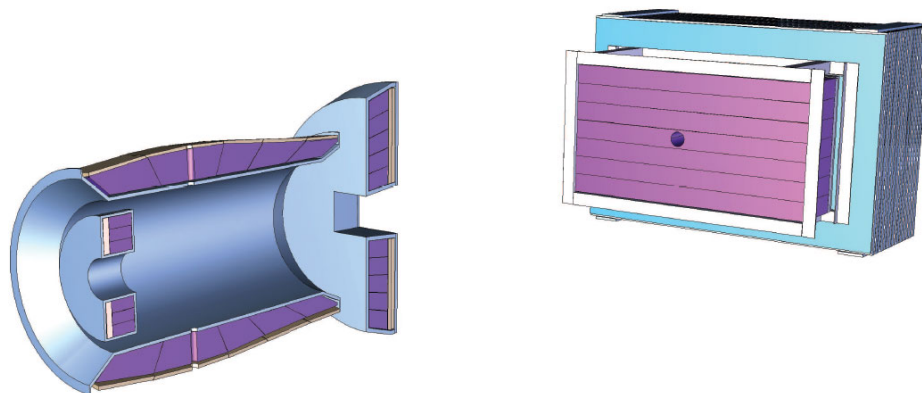


Figure 2.10: Electromagnetic Calorimetry in the  $\bar{\text{P}}\text{ANDA}$  experiment

The EMC identifies and absorbs  $e^+$ ,  $e^-$ , and  $\gamma$  particles. Combination of high count rates together with the proposed compact design of the target spectrometer requires a fast scintillation material with a small radiation length. In recent years lead tungstate

( $\text{PbWO}_4$ ) crystals have been investigated as a high density inorganic material. It can provide good energy resolution for photon and electron detection even at an intermediate energies. Crystals with a length of 20 cm (i.e.  $20 X_0$ ) are going to be used. Expected an energy resolution for photons and electrons is about  $1.54\%/\sqrt{E}[\text{GeV}] + 0.3\%$  in an energy range from a few MeV to 10 GeV. These crystals allow a pion/electron discrimination for momenta above  $0.5 \text{ GeV}/c$ . The EMC as shown in Fig 2.10 has a geometric coverage of  $\sim 96\%$ .

For the detection of photons and electrons in the FS a Shashlyk-type calorimeter with high resolution and efficiency is employed. The detection is based on lead-scintillator sandwiches read out with wave-length shifting fibres passing through the block and coupled to photo-multipliers. The lateral size of one module is  $110 \text{ mm} \times 110 \text{ mm}$  with a length of 680 mm ( $20 X_0$ ). A higher spatial resolution will be achieved by sub-dividing each module into 4 channels of  $55 \text{ mm} \times 55 \text{ mm}$  size coupled to 4 PMTs. To cover the forward acceptance, 351 modules, arranged in 13 rows and 27 columns at a distance of 7.5 m from the target, are required. With similar modules, based on the same technique as proposed for  $\bar{\text{PANDA}}$ , an energy resolution of  $4\%/\sqrt{E}[\text{GeV}]$  has been achieved [38].

### 2.6.5 Particle Identification (PID)

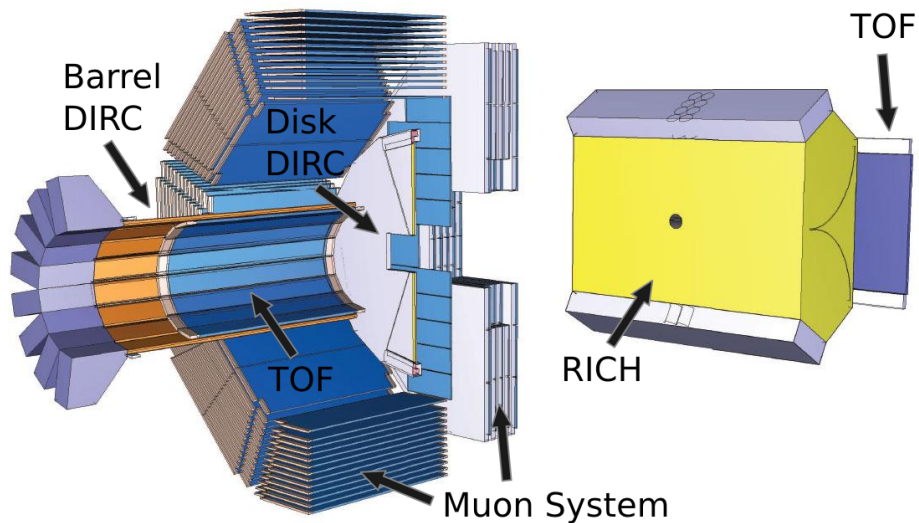


Figure 2.11: Particle Identification systems in the  $\bar{\text{PANDA}}$  experiment

The  $\bar{\text{PANDA}}$  detector is equipped with various particle identification systems providing the ability of classifying particle species over the whole kinematic range in addition to the  $dE/dx$  measurements from the tracking and information from the EMC.

### **Detector of Internally Reflected Cherenkov light (DIRC)**

Two DIRC sub-systems are going to be used. The Barrel DIRC is placed around the STT as main component for hadronic PID in the barrel section. It uses synthetic fused silica bars as Cherenkov radiators to provide a pion-kaon (and proton) separation for particle momenta up to  $3.5 \text{ GeV}/c$  at polar angles between  $22^\circ - 140^\circ$ . Another disc-shaped DIRC (Disc DIRC) is placed in the forward endcap of the target spectrometer. Pions and kaons with momenta up to  $4 \text{ GeV}/c$  and with polar track angles below the acceptance of the barrel DIRC down to  $10^\circ$  in horizontal and  $5^\circ$  in vertical direction are identified here.

The Barrel DIRC design is based on the BaBar DIRC [39] with several improvements, such as focusing optics and fast photon timing. It has a radius of 47.6 cm and 80 radiator bars with a length of 250 cm and a cross section of 1.7 cm x 3.3 cm in the baseline design. Five bars form one barrel section. Mirrors are attached to the bar in the downstream direction to reflect the photons towards the readout at the opposite end, where they are coupled out and focused via lenses into an expansion volume. This volume (with a depth of 30 cm) is filled with mineral oil. Micro-channel plate photomultiplier tubes (MCP-PMT) are attached to the backside of the volume with a pixel size of 6.5 mm and about 15.000 – 20.000 readout channels in total. For the PID process two spatial coordinates and the time of the detected photon are measured. With these 3D-patterns, PID likelihoods for different particle hypotheses are calculated. The expected performance of the Barrel DIRC is a single photon Cherenkov angle resolution of about 10 mrad and at least 20 detected photons per track at the complete angular range, providing at least  $3\sigma$  pion/kaon separation up to  $3.5 \text{ GeV}/c$  momentum [40].

The forward endcap Disc DIRC is a novel device. It consists of an octagonal disc with a diameter of 2 m, made of 20 mm thin synthetic fused silica. It is centered around the beam axis and divided into four optically independent segments. Cherenkov photons are internally reflected to the rim of the segments, where, behind dichroic mirrors for dispersion mitigation, they are collected by focusing light guide elements. As for Barrel DIRC three parameters are registered for each individual Cherenkov photon in the plate: time, angle and position. This sub-system will provide  $4\sigma$  pion-kaon separation up to a momentum of  $4 \text{ GeV}/c$  [41].

### **Aerogel Ring Imaging Cherenkov Counter (RICH)**

To enable the  $\pi/K$  and  $K/p$  separation in the forward region (polar angles of  $5^\circ - 22^\circ$ ) a RICH detector is proposed. The favored design is a dual radiator RICH detector. Two radiators, silica aerogel and freon ( $\text{C}_4\text{F}_{10}$ ) gas, with two different indices of refraction 1.0304 and 1.0137, provide a  $\pi/K/p$  separation in a broad momentum range from  $2 \text{ GeV}/c$  to  $15 \text{ GeV}/c$ . The total thickness of the detector is reduced to the freon gas radiator ( $5X_0$ ), the aerogel radiator ( $2.8X_0$ ), and the aluminum window ( $3X_0$ ) by using a lightweight mirror. The mirror focuses the Cherenkov light on an array of phototubes

placed outside the active volume [37].

### **Time of Flight System (TOF)**

A Time of Flight system called Scintillating Tiles (SciTil) between the Barrel DIRC and the EMC will be used for the identification of slow charged particles at polar angles from  $22^\circ$  to  $140^\circ$  which do not emit Cherenkov light in the DIRC. For optimal separation of most of the different types of produced particles ( $e, \mu, \pi^\pm, p, K^\pm$ ), the time resolution must be better than 100 ps. A fast and reliable timing detector will help in the global event building of the triggerless  $\bar{P}$ ANDA experiment with an average interaction rate of 20 MHz.

The SciTil consists of plastic scintillator tiles as the basic unit with a size of  $3 \times 3 \times 0.5 \text{ cm}^3$ . Two silicon photo multipliers are attached to different edges of each tile to spot as many photons as possible and to provide a relative timing. Four tiles share a common readout and form a quad module. One section contains 90 quad modules and 16 sections form the barrel TOF, with a total of 5760 scintillating tiles. Scintillating tiles are beneficial because they keep the material budget in front of the EMC small and yield 100 detected photons per tile. A first discriminator threshold provides excellent timing by triggering the first arriving photon. A second higher threshold distinguishes the event from noise counts. The time resolution of the SciTil can therefore be in the order of 100 ps.

In the FS a wall of slabs made of plastic scintillator and read out on both ends by fast photo-tubes serves as a time of flight counter placed at about 7 m from the target. Similar detectors are also placed inside the dipole magnet in order to detect low momentum particles which do not exit the dipole magnet. The time resolution is expected to be in the order of 50 ps thus allowing a good  $\pi/K$  and  $K/p$  separation up to momenta of  $2.8 \text{ GeV}/c$  and  $4.7 \text{ GeV}/c$ , respectively [42].

### **Muon Detection System**

Muons are identified at the outermost part of the detector as they pass the inner systems without major interactions. The Range System (RS) technique was chosen in  $\bar{P}$ ANDA for muons registration in a laminated iron absorber. Mini Drift Tubes (MDT) will be used as detectors with corresponding front-end electronics. The RS structure is a well-known solution for detecting muons when they are stopped by the absorber and when they cross the whole iron. In the first case, it is possible to roughly estimate the energy of the muons. The stopping power of iron is about  $1.5 \text{ GeV}$  per meter of absorber for relativistic muons with  $dE/dx = 2 \text{ MeV}/g$ . The kinetic energy of muons up to  $700 \text{ MeV}$  can be measured by the Muon System as a stand-alone. Adding information from the EMC the maximal detectable energy extends to  $\sim 900 \text{ MeV}$ . Above this energy muons will escape the system [43].

The solenoid magnet will be instrumented with 2600 MDTs of the muon system. Additional muon filters with 700 MDTs will be moved between the solenoid and the

dipole magnet (Fig. 2.11). Another range system (is not shown on Fig. 2.11) for measuring muons equipped with 900 MDTs will be installed at the downstream end of the FS. In the FS the Range System also serves as a coarse hadron calorimeter based on a track pattern. At energies of 3–15 GeV hadrons mostly produce a shower, while muons mostly undergo multiple scattering processes. As demonstrated in [43] the RS is capable to discriminate pions against muons with an efficiency above 90% for particles with a kinetic energy in the range of 500–1200 MeV.

### 2.6.6 Luminosity Detector (LMD)

Luminosity is an important parameter for many measurements at  $\bar{P}$ ANDA. It reflects the number of interactions, which happened between the antiproton beam and the target. There are many effects which could influence the luminosity behavior within one filling HESR cycle as well as the average luminosity. Therefore, it is crucial to measure the luminosity with high accuracy. A dedicated stand-alone and completely independent system, the Luminosity Detector (LMD), is developed for this purpose. The LMD is the most downstream detector in the  $\bar{P}$ ANDA setup. The requirement to measure elastically scattered antiprotons at small angles could only be fulfilled about 11 m downstream of the IP. There interacting particles with polar angles between  $3 \text{ mrad} < \theta < 9 \text{ mrad}$  are far from the non-interacting beam particles to be identified with a tracking station. Four detector planes with a radius of about 15 cm are equipped with in total 400 actively cooled high voltage monolithic active pixel sensors (HV-MAPS). They are placed retractable inside a vacuum box. The coverage of the full azimuth angle  $\phi$  is required to evaluate complex systematic effects by the accelerator beam and the complex magnetic field structure. The reconstructed tracks are propagated back to the IP to determine the shape of the cross section. A fit of the expected cross section to the angular distribution provides an absolute number for the time integrated luminosity with an excellent precision on the permille level. The accuracy finally depends on various parameters and is aimed at the result to be better than 5%. Moreover, instantaneous feedback for the target system and the Detector Control System (DCS) system is planned for steering and monitoring purposes.

# The Luminosity Measurement

Existing solutions, like the one chosen by experiment E835 at Fermilab, for the luminosity determination are not suitable for  $\bar{P}$ ANDA due to specific experimental conditions, such as the fixed-target experiment in the storage ring and the magnetic field around the IP. This led to the development of a new concept for the measurement and the dedicated device, Luminosity Detector (LMD), for this task.

Below, the conception of the luminosity measurement is discussed after an illustration of the importance of this quantity for experiments at  $\bar{P}$ ANDA. It is followed by the review of the  $p\bar{p}$  elastic scattering process, which is chosen as a reference channel for the luminosity determination in our case. Currently, the accuracy of the cross section of this process is the main limitation on the precision of the luminosity determination. A comparison between models and existing data is also presented here. The chapter is concluded by an overview of the LMD design, which is currently under construction at the Helmholtz-Institut Mainz.

## 3.1 Motivation

Keeping track of luminosity allows a monitoring of the performance of the accelerator and gives promptly the information for beam parameter adjustments to optimize this performance. Besides that, the precise knowledge of the luminosity is necessary for many measurements planned with the  $\bar{P}$ ANDA experiment. Below it is illustrated for two general cases.

### 3.1.1 Cross section measurements

The goal of a cross section measurement is to extract the probability that a certain process occurs. This is done by searching for events of the process and counting them.

In some cases a lot of effort is needed to ensure that all interesting events are counted or to even find any of these events. The main interest is the probability in order to compare the results between different experiments. Thus the number of found events always has to be normalized to the number of interactions in a data sample, *the absolute or time-integrated luminosity*. A cross section, which describes the probability of the process, is calculated as

$$\sigma = \frac{N_{obs} - N_{bkg}}{\varepsilon \cdot \int L dt} \quad (3.1)$$

where  $N_{obs}$  is the number of registered events,  $N_{bkg}$  the number of expected background events,  $\varepsilon$  the efficiency of the experimental set-up for extracting the events and  $\int L dt$  the luminosity integrated over the time of data accumulation. As it is clear from Eq. 3.1, the luminosity provides the needed normalization for the physics process under study. Moreover the errors on the luminosity determination will propagate to the accuracy of the cross section measurement and to the accuracy of parameters extracted from a cross section. E.g for the electromagnetic form factors it was shown that both  $G_E$  and  $G_M$  moduli of the complex form factors in the time-like domain can be extracted only if the luminosity is known with a precision of a few percents. Otherwise only the determination of the ratio between  $G_E$  and  $G_M$  is possible [17].

### 3.1.2 Precision measurements of resonance parameters

The example given above illustrates the necessity for the absolute measurement of the time-integrated luminosity. Sometimes an accurate knowledge of a *relative* time-integrated luminosity could be sufficient. e.g. the relative luminosity plays an important role for studying resonance formation rates with  $\bar{P}$ ANDA in energy scan experiments. The precise measurement of the width of a resonance in antiproton-proton annihilations was developed and successfully applied by the fixed-target experiments E760/E835 at Fermilab [44]. The improved complementary-scan technique [45] was based on the analysis of the excitation curves obtained by scanning the resonance twice: at constant orbit and at constant magnetic bend field. The precision was dominated by the statistical uncertainty.

The resonance parameters were determined by a maximum-likelihood fit to the excitation curve of the measured rate (Fig. 3.1). For each scan point (subscript  $i$ ), it was assumed that the average number of observed events  $\mu_i$  depends on the line shape of the investigated resonance (e.g a Breit-Wigner function  $\sigma_{BW_r}$ ) and on the center-of-mass energy distribution (the beam profile)  $B_i$ , as follows:

$$\mu_i = \mathcal{L}_i \left[ \varepsilon_i \int \sigma_{BW_r}(w) B_i(w) dw + \sigma_{bkg} \right], \quad (3.2)$$

where  $w$  is the center-of-mass energy,  $\varepsilon_i$  the extraction efficiency,  $\mathcal{L}_i$  the time-

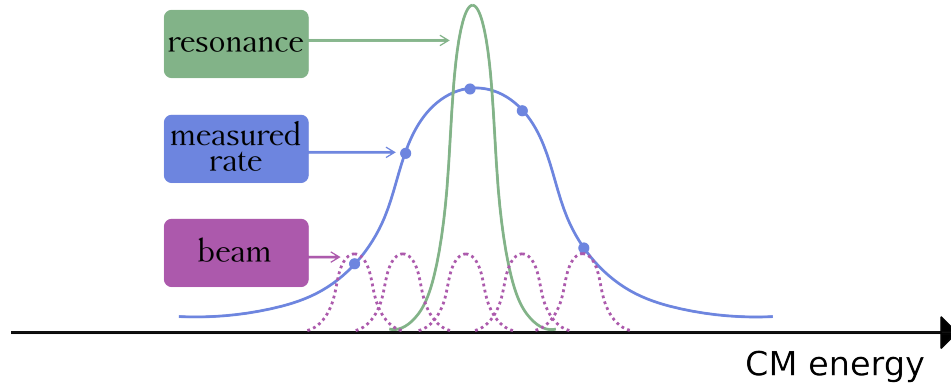


Figure 3.1: Illustration of energy scan experiments

integrated luminosity, and  $\sigma_{\text{bkg}}$  a function which describes the shape of the constant background. The integral is extended over the energy range of the measured resonance. The spin-averaged Breit-Wigner cross section for a spin- $J$  resonance of mass  $M$  and width  $\Gamma$  formed in  $\bar{p}p$  annihilations is

$$\sigma_{\text{BW}}(w) = \frac{(2J+1)}{(2S+1)^2} \frac{16\pi}{w^2 - 4m^2} \frac{(\Gamma_{\text{in}}\Gamma_{\text{out}}/\Gamma) \cdot \Gamma}{\Gamma^2 + 4(w-M)^2}; \quad (3.3)$$

$m$  and  $S$  are the (anti)proton mass and spin, while  $\Gamma_{\text{in}}$  and  $\Gamma_{\text{out}}$  are the partial resonance widths for the entrance (e.g.  $\bar{p}p$ ) and exit channel under study. The resonance mass  $M$ , width  $\Gamma$ , ‘area’ ( $\Gamma_{\text{in}}\Gamma_{\text{out}}/\Gamma$ ) and the background cross section  $\sigma_{\text{bkg}}$  were left as free parameters in the maximization of the log-likelihood function  $\log(\Lambda) = \sum_i \log P(\mu_i, N_i)$ , where  $P(\mu, N)$  are Poisson probabilities of observing  $N$  events when the mean is  $\mu$ .

This technique led to the most precise measurement of the width of the resonance  $\Psi(2S)$  ( $\Gamma_{\Psi(2S)} = 290 \pm 25$  (sta)  $\pm 4$  (sys) keV). This precision would not have been possible without the accurate normalization of each data point with respect to its integrated luminosity (see Sec. 3.2.2).

## 3.2 Alternative methods for luminosity determination at fixed-target experiments

### 3.2.1 COSY

The luminosity determination by using the accelerator and target parameters is based on Eq. 2.5. The beam current within a storage ring can be measured by the accelerator group directly. The target thickness cannot be established simply through macroscopic measurements.

When a charged particle passes through matter it loses energy through electromagnetic processes and this is also true inside a storage ring where a coasting beam goes through a thin target a very large number of times. The energy loss, which is proportional to the target thickness, builds up steadily in time and causes a shift in the revolution frequency in the machine which can be measured through the study of the Schottky spectra. Assuming that other contributions to the energy loss outside the target are negligible or can be corrected for, knowing the characteristics of the machine allows the effective target thickness to be deduced. This effect has been investigated with an internal proton beam of energy 2.65 GeV at the COSY accelerator using the ANKE spectrometer and a hydrogen cluster-jet target [46].

Most experiments with ANKE at COSY ran with a coasting beam without cooling, which offered the possibility to use the energy loss in the target as a direct and independent method for the luminosity determination. The energy loss  $\delta T$  per single traversal of the target, divided by the stopping power  $dE/dx$  of protons in hydrogen gas and the mass  $m$  of the target atom, yields the number  $n_T$  of target atoms per unit area which interact with the ion beam:

$$n_T = \frac{\delta T}{(dE/dx)m} \quad (3.4)$$

Over a small time interval  $\Delta t$ , the beam makes  $f_0 \Delta t$  traversals, where  $f_0$  is the revolution frequency of the machine. If the corresponding energy loss is  $\Delta T$ , Eq.3.4 may be rewritten as:

$$n_T = \frac{\Delta T}{f_0(dE/dx)m\Delta t} \quad (3.5)$$

In terms of the change in the beam momentum  $p$ ,  $n_T$  can be calculated as:

$$n_T = \left( \frac{1+\gamma}{\gamma} \right) \frac{\Delta T_0 \Delta p}{f_0(dE/dx)m p_0 \Delta t} \quad (3.6)$$

where  $T_0$  and  $p_0$  are the initial values of the beam energy and momentum, and  $\gamma = (1 - \beta^2)^{-\frac{1}{2}}$  is the Lorentz factor. In a closed orbit, the fractional change in the revolution frequency is proportional to that in the momentum:

$$\frac{\Delta p}{p_0} = \frac{1}{\eta} \frac{\Delta f}{f_0} \quad (3.7)$$

where  $\eta$  is the frequency-slip parameter. Putting these expressions together:

$$n_T = \left( \frac{1+\gamma}{\gamma} \right) \frac{1}{\eta} \frac{1}{(dE/dx)m} \frac{\Delta T_0}{f_0^2} \frac{\delta f}{\delta t} \quad (3.8)$$

Here  $\beta$ ,  $\gamma$ ,  $p_0$ , and  $T_0$  are determined from revolution frequency and nominal circumference of the accelerator.  $dE/dx$  is evaluated from the Bethe–Bloch formula. The frequency shift  $\Delta f$  is measured by analyzing the Schottky noise of the coasting proton beam and the  $\eta$ -parameter by studying the effects of making small changes in the magnetic field [46].

The result contains a contribution arising from the residual gas in the ring. The systematic correction for the residual gas effects lead to a systematic uncertainty of 4%. The uncertainty of the  $\eta$  determination added another 3% to the systematic uncertainty. Adding these errors quadratically, the total error in the target thickness determination at ANKE was 5%. The beam current  $n_B$  was accurate to 0.1%, therefore the determination of the luminosity via the beam energy-loss method was 5%, the same as for the target thickness.

This method is not limited to proton beams and therefore can easily be applied to any fixed-target experiment with an ion beam, including antiprotons, and thus is planned to be used at HESR too. It should be mentioned that at the HESR the antiproton beam will be cooled compensating for the energy loss and multiple scattering of the antiprotons in the target material (straggling). Therefore this method requires dedicated sessions of data taking and cannot be used for the luminosity determination in parallel to physics experiments at PANDA.

### 3.2.2 E760/E835

The luminosity can also be determined by measuring a *reference* channel with the well known cross section. In the most simple case, the number of events of the reference channel are counted and the luminosity can be extracted from Eq.2.4. The cross section of such a channel should be known with high accuracy and be relatively large to ensure a high amount of events from the reference channel during a short time for reliable instantaneous luminosity monitoring. In  $e^+e^-$  annihilation experiments the channel used for monitoring is typically Bhabha scattering ( $e^+e^- \rightarrow e^+e^-$ ) for which absolute cross sections can be calculated accurately from QED [1]. For hadronic reactions one does not have such an ideal channel for monitoring purposes. The only  $p\bar{p}$  cross section which is accurately known is that for elastic Coulomb scattering, but this is always accompanied by the contribution of the strong interaction, which is poorly known. Therefore to obtain the absolute luminosity one has to analyze the characteristic shape of the differential cross sections of this reaction (see Section 3.3.1).

The E760/E835 luminosity monitors were based on making absolute measurements of the differential cross section of  $p\bar{p}$  elastic scattering at extreme forward angles by measuring the energy of the recoil protons in dependence on the scattering angle as close as possible to the limiting polar angle  $\theta=90^\circ$  or  $\alpha=90-\theta=0^\circ$  [48]. As shown in Sec. 3.3.1, at such angles an accurate absolute normalization is possible. Another

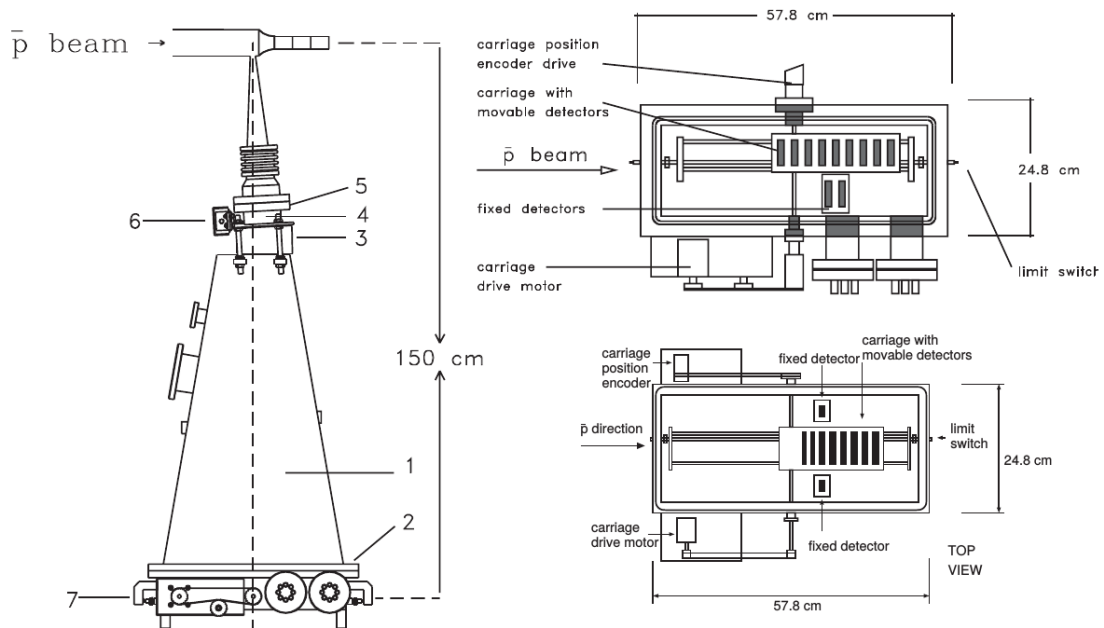


Figure 3.2: Schematic of the Luminosity Monitor. Left: assembly view; top right: the detector pan as used in E760; bottom right: the detector pan as used in E835 [47]

important advantage was that the recoil proton energies had a momentum of only a few MeV, thus the protons could be detected in solid state detectors of excellent energy resolution and stability.

The luminosity monitor (Fig. 3.2) consisted of a vacuum enclosure suspended just below the  $\bar{p}p$  interaction region at  $90^\circ$  to the  $\bar{p}$  beam. At its bottom there was a pan containing an assembly of five solid state detectors on a carriage. During the E760 running it was found that the antiproton beam orbit could occasionally undergo radial shifts of several mm. These shifts lead to errors in the luminosity measurements. Therefore for E835 the luminosity monitor was redesigned and contained detectors fixed left and right of the beam axis at  $\alpha_L = 3.496 \pm 0.005^\circ$  and  $\alpha_R = 3.511 \pm 0.005^\circ$ . The detectors were silicon surface barrier ( $500 \mu\text{m}$  deep) and Si-Li drift ( $3000 \mu\text{m}$  deep) of an area of  $\approx 1 \times 5 \text{ cm}^2$  each, deployed according to the expected maximum recoil energy at different recoil angles. The carriage could be moved such that the detectors sampled all recoil energies, from  $\alpha = 0^\circ$  to  $6^\circ$ . Displacement of the beam from the central orbit caused an asymmetry in the counts in the fixed detectors on different sides. For orbit displacements of an magnitude of  $< 1.5 \text{ mm}$  the asymmetry  $(L - R)/(L + R)$  was calculated to be less than 2% and no corrections were applied to the average luminosity. If the asymmetry was larger than 2%, the beam orbit was adjusted to its central value.

Both the instantaneous luminosity (integrated over 2 min) and the time-integrated luminosity (integrated over a whole run extending over several hours) were monitored.

The statistical error for the time-integrated luminosity was  $< 0.3\%$ . The systematic error was estimated as  $\sim 2.1\%$ , arising mostly from the uncertainties in the elastic scattering differential cross section parameterization [47].

### 3.3 The luminosity determination at $\bar{\text{PANDA}}$

The luminosity measurement foreseen for  $\bar{\text{PANDA}}$  is based on the experience of the E760/E835 experiments. As for Fermilab experiments,  $p\bar{p}$  elastic scattering will be exploited for this task. The main difference comes from the fact that the LMD at  $\bar{\text{PANDA}}$  will not register the recoil protons, but the scattered antiprotons at small angles. Nevertheless the theoretical description of the process is the same.

For a more accurate luminosity determination as well as in order to better suppress background events, the strategy for the measurement of the luminosity with the LMD is not only counting the events which hit the LMD, but also reconstructing of their scattering angles. Therefore differential counting will be done, i.e counting the number of scattered antiprotons versus the scattering angle  $\theta$ . The luminosity will be extracted by fitting the theoretical model from Eq. 3.9 to the differential counting rate.

#### 3.3.1 Elastic $p\bar{p}$ scattering

Proton-Antiproton elastic scattering can be described in terms of a Coulomb  $f_{coul}$  and a hadronic  $f_{had}$  amplitude. Usually the differential cross section is presented as a sum of three terms:

$$\frac{d\sigma_{el}}{dt} = \frac{\pi}{k^2} |f_{coul} e^{i\delta} + f_{had}|^2 = \frac{d\sigma_{coul}}{dt} + \frac{d\sigma_{had}}{dt} + \frac{d\sigma_{interf}}{dt} \quad (3.9)$$

with the following representation for each part:

$$\begin{aligned} \frac{d\sigma_{coul}}{dt} &= \frac{4\pi\alpha_{EM}^2 G^4(t) (\hbar c)^2}{\beta^2 t^2} \\ \frac{d\sigma_{had}}{dt} &= \frac{\sigma_T^2 (1 + \rho^2)}{16\pi (\hbar c)^2} e^{bt} \\ \frac{d\sigma_{interf}}{dt} &= \frac{\alpha_{EM} \sigma_T}{\beta |t|} G^2(t) e^{\frac{1}{2}bt} (\rho \cos(\delta) + \sin(\delta)) \end{aligned} \quad (3.10)$$

where  $\alpha_{EM}$  is the fine structure constant,  $G(t) = (1 + \Delta)^{-2}$  is the proton dipole form-factor with  $\Delta = |t|/0.71(\text{GeV}/c)^2$  and  $\delta$  is the Coulomb phase. Therefore  $\frac{d\sigma_{coul}}{dt}$  can be calculated very precisely. In contrary the physical quantities of the hadronic contribution, such as  $\sigma_T$  (total cross section),  $\rho$  (the ratio of the real part to the imaginary part

of the forward elastic scattering amplitude) and  $b$  (nuclear slope) must be determined experimentally [48].

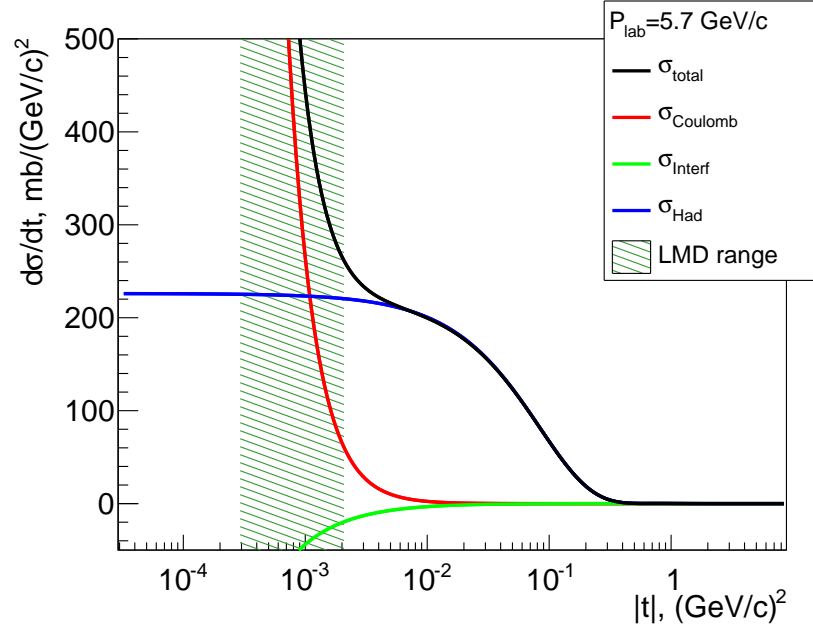


Figure 3.3: Differential cross section versus momentum transfer  $|t|$

Fig. 3.3 illustrates the contributions to the differential cross section according to Eq. 3.10 in case of the beam momentum  $p_{lab} = 5.7 \text{ GeV}/c$ . The Coulomb part of the differential cross section is dominating at small momentum transfer  $t$ . At large  $t$  the hadronic cross section  $\frac{d\sigma_{had}}{dt}$  is dominating. The accuracy of the hadronic cross section is limited due to sparse experimental data available for the determination of the  $b$ ,  $\rho$  and  $\sigma_T$  physical quantities. Therefore the region of small momentum transfers is preferred to omit the model dependencies and the resulting systematic uncertainties in the determination of the luminosity.

The scattering angle  $\theta_{cms}$  is directly related to the magnitude of the momentum transfer  $|t|$  by

$$|t| = |p_{\bar{p}} - p'_{\bar{p}}| = -2p_{cms}^2(1 - \cos(\theta_{cms})) \quad (3.11)$$

For a fixed target experiment with the momentum  $p_p = 0$  of the proton at rest the relation between the magnitude of the momentum transfer and the scattering angle  $\theta$  in the laboratory system is described by

$$|t| = 2p \sin(\theta/2) \quad (3.12)$$

For the  $\bar{\text{P}}\text{ANDA}$  detector it is not possible to measure the recoil proton at very small momentum transfers. Mainly because the energy of these very slow protons is too

small to exit the beam pipe or to pass the MVD or the STT. Measurement at higher momentum transfers, when energy is enough to go through the beam pipe, still would be complicated due to curling of the protons in the 2 Tesla solenoid field. And at much higher momentum transfers the Coulomb part of the differential cross section would not be visible in the data at any momentum of the beam.

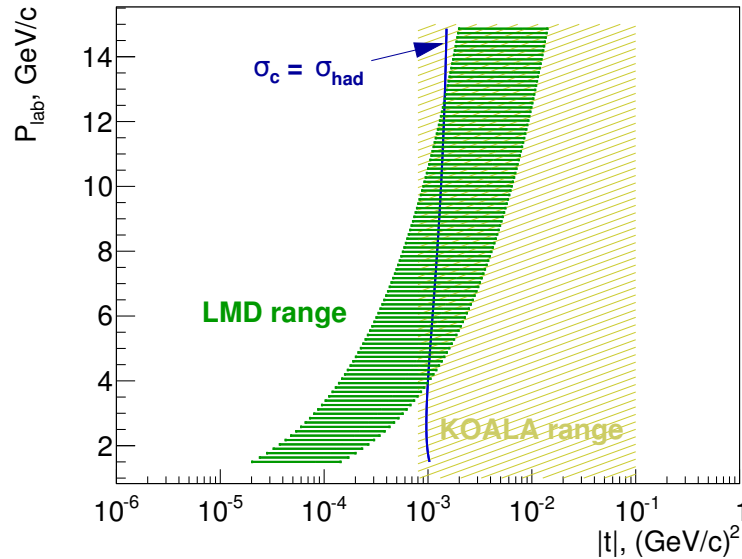


Figure 3.4: Region available for the luminosity measurement at  $\bar{\text{P}}\text{ANDA}$  (green) and range for the KOALA experiment in terms of momentum transfer  $|t|$

However it appears feasible to measure the forward scattered antiproton. The antiprotons scattered below 3 mrad are planned to be reused in the beam of HESR. Thus only larger angles can be used for the luminosity measurement. The LMD will be able to register scattered antiprotons with scattering angle  $\theta$  between 3 and 9 mrad<sup>1</sup>. Unfortunately in this angular range the Coulomb part is not dominating for large beam momenta. Fig 3.4 shows the range covered by the LMD in terms of  $|t|$  in dependence of the beam momenta of  $\bar{\text{P}}\text{ANDA}$ . The blue line on this plot indicates the  $|t|$  value at which the Coulomb part is equal to the hadronic part of the elastic scattering cross section. At higher  $|t|$  values the hadronic part becomes large than the Coulomb part. Already at  $P_{\text{beam}} \sim 3.5 \text{ GeV}/c$  the hadronic part contributes to the events registered by the LMD and for  $P_{\text{beam}} > 12 \text{ GeV}/c$  it dominates in the LMD measurement range. Therefore the uncertainties of the models for estimation of the hadronic part impact the accuracy of the luminosity extraction for the beam momentum values above  $3.5 \text{ GeV}/c$ .

<sup>1</sup>The upper bound is limited by size of the beam pipe.

### 3.3.2 Models and their uncertainties

The hadronic part of forward elastic scattering cannot be calculated from first principles. There are different ways to describe the differential cross section of this term. Currently there are two models available. One is called DPM model [49]. It is a part of the DPM background events generator in PANDARoot framework (in more details discussed in the following chapters). Another one is called the E760 model, because it was tuned and used in the E760 experiment for the luminosity extraction [50]. The last one is not implemented as a generator in the PANDARoot framework yet. Nevertheless, as shown by results of in the following, it is more accurate and most probably will be used for the luminosity extraction and the production of the simulation data in the future.

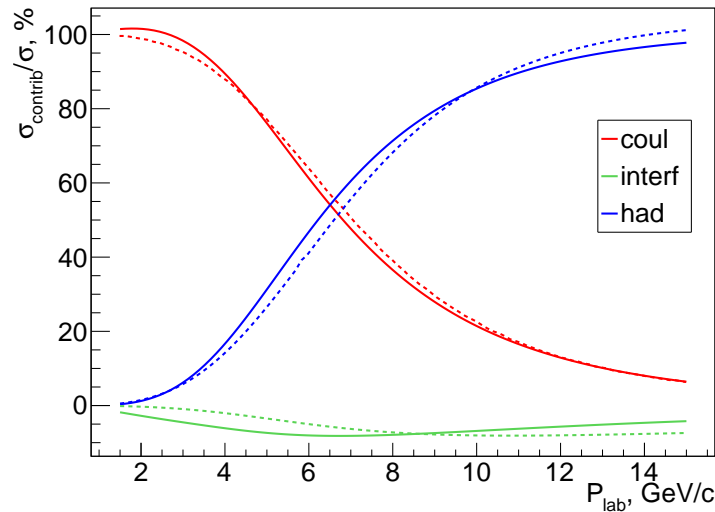


Figure 3.5: Contribution of the terms to the elastic  $p\bar{p}$  scattering cross section integrated in the scattering angle  $\theta$  between 3–9 mrad (solid line – estimation according to DPM elastic scattering model, dashed line – estimation according to E760 model)

Fig. 3.5 shows the contributions of the terms in Eq. 3.9 to the elastic scattering cross section integrated in the LMD range for the both models. These two models give only slightly different predictions concerning the relative contributions of different terms of elastic scattering. Therefore in estimations related to count rates in the LMD, e.g. radiation damage, the DPM generator is well suited too.

#### 3.3.2.1 DPM model

As discussed in [49], the description via Eq. 3.10 fails to describe the differential cross section behavior at large  $|t|$  values. A more complicated function is introduced for this

purpose in the DPM generator:

$$\frac{d\sigma_{had}}{dt} = A_1 \cdot [e^{t/2t_1} - A_2 \cdot e^{t/2t_2}]^2 + A_3 \cdot e^{t/t_2} \quad (3.13)$$

Parameters  $A_1, A_2, A_3, t_1, t_2$  were extracted from previous measurements at six different beam momenta. These fit results were taken to establish the momentum dependence of the parameters ( $t_1$  was kept fix at value 0.0899 for all momenta). All parameters follow the function:

$$x = c + a \cdot e^{-p_{lab}/d} \quad (3.14)$$

where  $x$  denotes  $A_1, A_2, A_3$  or  $t_2$  and  $c, a, d$  are constants extracted from the fit. The values used in the DPM code are indicated in Tab. 3.1 on the left.

In order to determine the uncertainty of the DPM model, the uncertainty of all parameters is needed. These are not provided in [49]. Also the parameters in the DPM generator software code and the values in [49] do not match. Therefore the fit of the beam momentum dependence for each DPM parameter was repeated. Comparison with the DPM parameters is presented in Tab. 3.1 and Fig. 3.6. The fit result is close to the parameter description used in the DPM code. The difference stays below 1%.

Parameter		DPM value	fit value
$A_1$	c	115.	$115.7 \pm 7.9$
	a	650	$656.9 \pm 31.9$
	d	4.08	$4.03 \pm 0.32$
$A_2$	c	0.0687	$0.0687 \pm 0.0087$
	a	0.307	$0.300 \pm 0.143$
	d	2.367	$2.406 \pm 1.184$
$t_2$	c	-2.979	$-2.978 \pm 0.096$
	a	3.353	$3.354 \pm 0.096$
	d	483.4	$471.4 \pm 132.9$
$A_3$	c	0.8372	$0.8411 \pm 0.1002$
	a	39.53	$40.07 \pm 51.97$
	d	0.765	$0.761 \pm 0.292$

Table 3.1: DPM parameters for the elastic scattering and their parameters for the momentum dependence

For the estimation of the model uncertainty, the error of each parameter has to be propagated via Gaussian error propagation. An uncertainty of function  $f(a, b)$  depen-

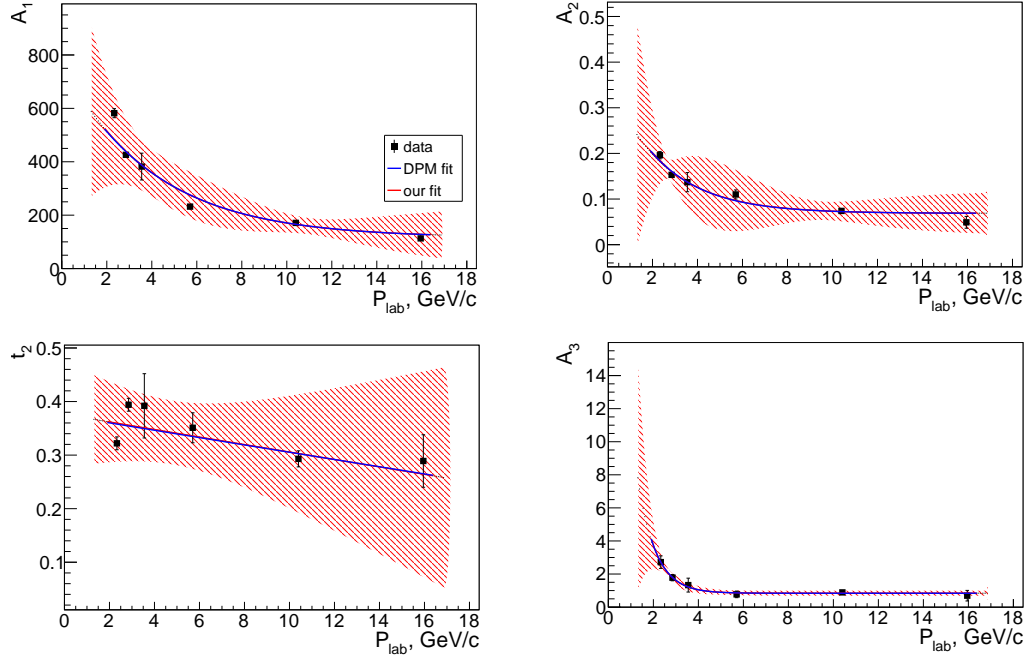


Figure 3.6: Momentum dependency of  $A_1$ ,  $A_2$ ,  $t_2$  and  $A_3$  parameters of the DPM model (points – the data, blue line – the momentum dependency as used in the DPM generator software, red line – fit results obtained in this work (Tab. 3.1), red band shows 0.95 Confidence Level of the fit)

dent on some measured parameters  $a$  and  $b$  has the following form:

$$\Delta f = \sqrt{\left(\left|\frac{\partial f}{\partial a}\right| \cdot \Delta a\right)^2 + \left(\left|\frac{\partial f}{\partial b}\right| \cdot \Delta b\right)^2} \quad (3.15)$$

This formula is applied to the parameters of the DPM model. Derivatives of the parameters are calculated from Eq.3.13:

$$\begin{aligned} \frac{\partial F}{\partial A_1} &= [e^{t/2t_1} - A_2 \cdot e^{t/2t_2}]^2 \\ \frac{\partial F}{\partial A_2} &= -2 \cdot A_1 \cdot e^{(t/2t_1+t/2t_2)} + 2A_1A_2e^{t/t_2} \\ \frac{\partial F}{\partial A_3} &= e^{t/t_2} \\ \frac{\partial F}{\partial t_1} &= A_1[-e^{t/t_1} + A_2 \cdot e^{(t/2t_1+t/2t_2)}] \frac{t}{t_1^2} \\ \frac{\partial F}{\partial t_2} &= A_1A_2[e^{(t/2t_1+t/2t_2)} - (A_2 + A_3) \cdot e^{t/t_2}] \frac{t}{t_2^2} \end{aligned} \quad (3.16)$$

The parameter errors  $\Delta A_1$ ,  $\Delta A_2$ ,  $\Delta A_3$  and  $\Delta t_2$  are estimated from the fit results as fit function uncertainties at 0.68 Confidence Level. For the fixed parameter  $t_1$ , an error  $\Delta t_1 = 0.01$  is assumed independent from the energy.

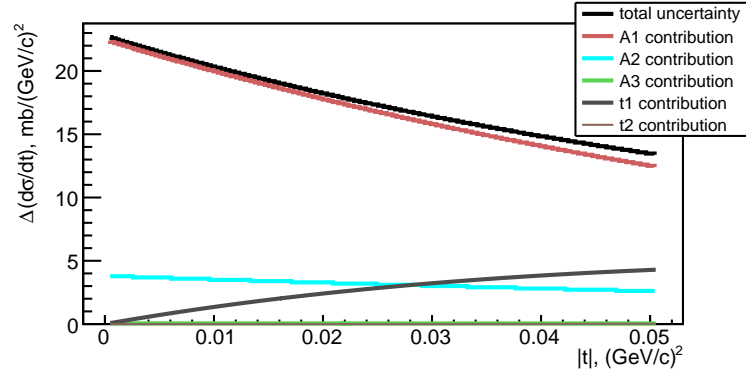


Figure 3.7: The uncertainty of the differential cross section of DPM model as a function of the momentum transfer  $|t|$  at  $P_{lab}$  15 GeV/c (maximum value  $|t|=0.05$  on the plot corresponds scattering angle of the antiproton  $\theta=15$  mrad)

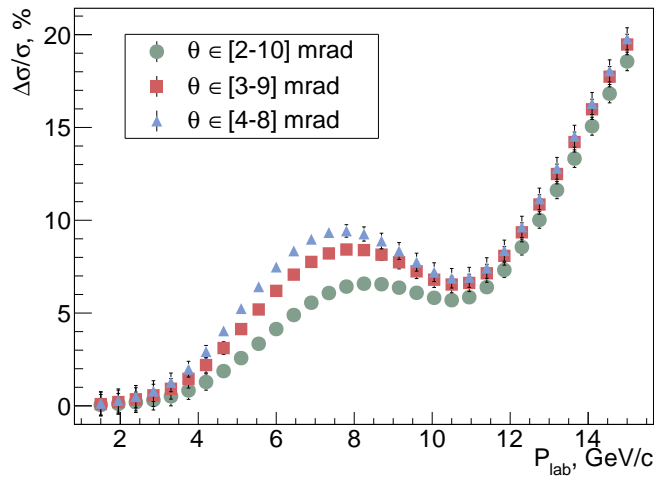


Figure 3.8: The relative uncertainty of the cross section integrated over different polar angles ranges in dependence on the beam momentum  $P_{lab}$  (for the DPM model)

Fig. 3.7 shows the uncertainty of the differential cross section in dependence on the momentum transfer at the beam momentum  $P_{lab}$  15 GeV/c. In addition the contribution to the uncertainty of each parameter to the total model uncertainty is plotted. The contribution from the parameter  $A_1$  dominates the model uncertainty. Contributions due to  $A_2$  and  $\Delta t_1$  parameters are already small and contributions due to  $A_3$  and  $t_2$  are

negligible. This is also valid for lower beam momenta.

Fig. 3.8 presents the uncertainty of the cross section integrated over different  $\theta$  ranges and normalized to the integrated elastic cross section in the same range. As one can see from this plot, at low energies, where the Coulomb part is dominating (e.g for  $P_{lab}$  below  $3.5 \text{ GeV}/c$ ), the expected uncertainty is below 2%. In the intermediate range (for  $P_{lab}$  between  $3.5$  and  $12 \text{ GeV}/c$ ), where both, the Coulomb and the hadronic parts contribute in the LMD range, the uncertainty of the model varies, but stays below 10%. And for high energies (for  $P_{lab}$  above  $12 \text{ GeV}/c$ ) the model uncertainty rises and goes up to 20%.

### 3.3.2.2 E760 model

The experiment E760 [50] used the parameterization given in Eq. 3.10 in order to describe the differential cross section  $\frac{d\sigma_{coul}}{dt}$  in dependence on the four-momentum transfer  $t$ . In the publication of its successor experiment E835 [47] the following dependence on the model parameters from beam momentum is given:

$$\begin{aligned}\sigma_T &= c + a \cdot p_{lab}^{-d}, \\ b &= c - a \cdot p_{lab}, \\ \rho &= c + a \cdot p_{lab}\end{aligned}\tag{3.17}$$

It is claimed in [47] that this parameterization is valid in the beam momentum range of  $2\text{--}8 \text{ GeV}/c$ . It led to a 2.1% systematic uncertainty in the luminosity determination (arises mainly from parameterization of  $\rho$ ). Momentum dependency for the accuracy of the determination is not indicated. However the value and uncertainty of each parameter was determined from experimental data at particular energies.

Parameter		E760 model	Fit to E760 data (fixed $\sigma_T$ )	Fit to E760 data (free $\sigma_T$ )
$\sigma_T$	c	34.48	$35.38 \pm 0.89$	$55.66 \pm 5.99$
	a	89.7	$89.6 \pm 0.4$	$758.1 \pm 1979.6$
	d	-0.7	$-0.72 \pm 0.03$	$-2.94 \pm 2.27$
$b$	c	13.64	$13.64 \pm 1.04$	$12.60 \pm 0.99$
	a	-0.2	$-0.21 \pm 0.19$	$0.019 \pm 0.178$
$\rho$	c	-0.12	$0.059 \pm 0.021$	$0.12 \pm 0.04$
	a	0.03	$-0.015 \pm 0.004$	$-0.029 \pm 0.007$

Table 3.2: E760 parameters for the elastic scattering and their parameters for the momentum dependence

The momentum dependence of the parameters was reproduced by fitting the parameters  $\sigma_T$ ,  $b$  and  $\rho$  values given in [50]. Again the extracted uncertainties of the fit parameters are propagated in order to get the uncertainty of the E760 model. As described in [47], the parameter  $\sigma_T$  was not used in the fit and fixed to the values obtained from the previous experiments. As shown in Tab. 3.2 and in Fig. 3.9 there is a significant discrepancy between the fit results and the  $\rho$  parameter extracted from the E760 experiment (Fig. 3.9, bottom left). In addition, also a fit was performed without fixing the values of the  $\sigma_T$  (to compare with the  $\sigma_T$ -free analysis in the [50]). In this case the discrepancy to the values from the E760 is even larger. However, the fit for parameters values from the  $\sigma_T$ -fixed analysis give a better agreement with E760 data for the differential elastic cross section published in [50]. For the further study the description of the momentum dependence of the parameters  $\sigma_T$ ,  $b$  and  $\rho$  are obtained from the fit with fixed  $\sigma_T$ . This model is referred as *E760-like* below.

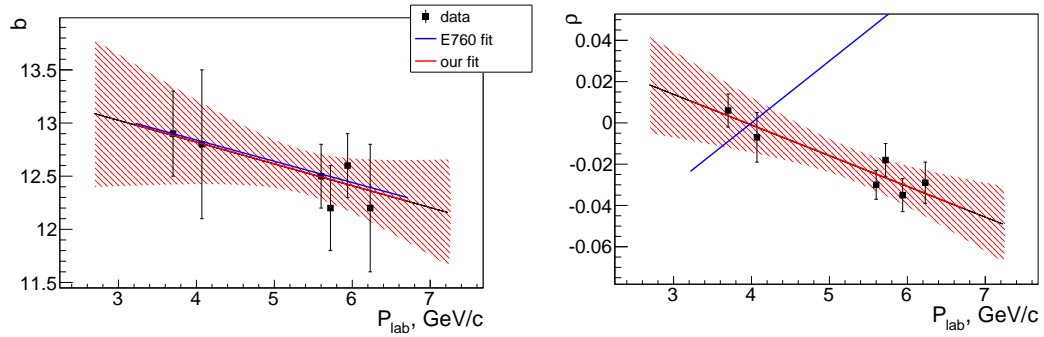


Figure 3.9: Momentum dependency of  $b$  and  $\rho$  parameters in the E760 model (points – the data, blue line – the momentum dependence as used in the E760 experiment, red line – fit results obtained in this work (Tab. 3.2), red band shows 0.95 confidence level of the fit)

With the assumption that the parameters are uncorrelated, the uncertainty for the differential cross section can be again obtained via Gaussian error propagation (Eq. 3.15) with the following derivatives:

$$\begin{aligned}
 \frac{\partial F}{\partial \sigma_T} &= \frac{2\sigma_T(1+\rho^2)e^{-b|t|}}{16\pi(\hbar c)^2} = \frac{2F}{\sigma_T} \\
 \frac{\partial F}{\partial b} &= \frac{-|t|\sigma_T^2(1+\rho^2)e^{-b|t|}}{16\pi(\hbar c)^2} = -|t|F \\
 \frac{\partial F}{\partial \rho} &= \frac{2\rho\sigma_T^2e^{-b|t|}}{16\pi(\hbar c)^2} = \frac{2\rho F}{(1+\rho^2)}
 \end{aligned} \tag{3.18}$$

The parameter errors  $\Delta\sigma_T$ ,  $\Delta b$ ,  $\Delta\rho$  and  $\Delta t_2$  are estimated from the fit results as a function uncertainty at 68 % Confidence Level. In Fig. 3.10 the uncertainty contribution

of each parameter to the total model uncertainty is shown at  $P_{lab}=15 \text{ GeV}/c$ . The contributions of  $\sigma_T$  and  $\rho$  dominate at small  $|t|$  and the contribution from the parameter  $b$  dominates at large  $|t|$ .

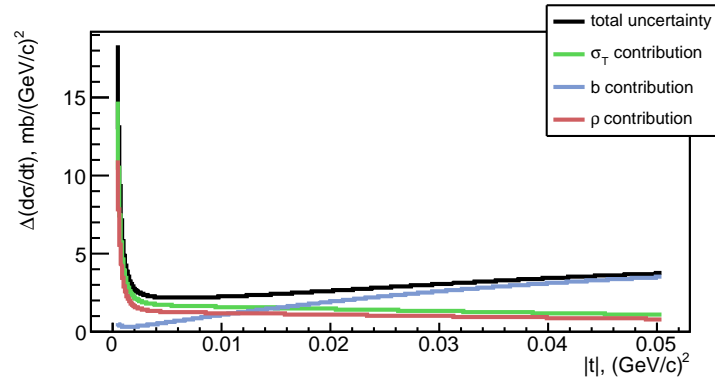


Figure 3.10: The uncertainty of the differential cross section of the E760-like model as a function of the momentum transfer  $|t|$  at  $P_{lab} 15 \text{ GeV}/c$  (maximum value  $|t|=0.05$  on the plot corresponds to the scattering angle of the antiproton  $\theta=15 \text{ mrad}$ )

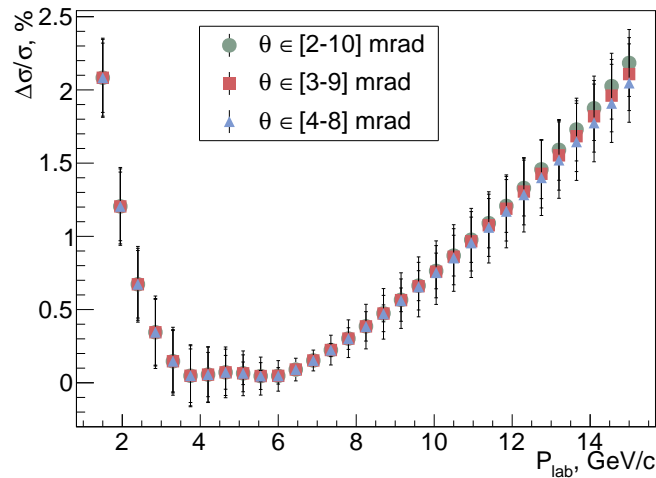


Figure 3.11: The relative uncertainty of the cross section integrated over different polar angles ranges in dependence of  $P_{lab}$  (for the E760-like model)

Fig. 3.11 presents the relative uncertainty of the cross section integrated over different  $\theta$  ranges and normalized to the integrated elastic cross section in the same range. The model uncertainty is around 2% at the beam momentum 1.5 GeV/c and goes down to 0.1% between 3–6 GeV/c. Afterwards it rises slowly and at the highest beam momenta ( $P_{lab} 15 \text{ GeV}/c$ ) goes up to 2%. In the range of 2–8 GeV/c beam momentum for which the model was originally provided, the model uncertainty is below 0.5%.

### 3.3.2.3 Comparison of the models with the data from previous elastic $p\bar{p}$ scattering experiments

In the Durham HepData base [51] 38 measurements of the differential  $p\bar{p}$  elastic scattering cross section are listed. The data is summarized in Appendix B. A short overview is presented in Fig. 3.12, where measurements are sorted by the beam momenta  $P_{lab}$  and the four-momentum transfer  $t$  ranges for all found past experiments. The data used for parameter determination of the DPM and E760 models are marked by different colors. In DPM only data with wide  $t$ -range (between  $10^{-2}$  and  $1$   $(\text{GeV}/c)^2$ ) is used. This is natural, since the DPM group aims to reproduce the differential cross section in a wide  $t$  range <sup>2</sup>.

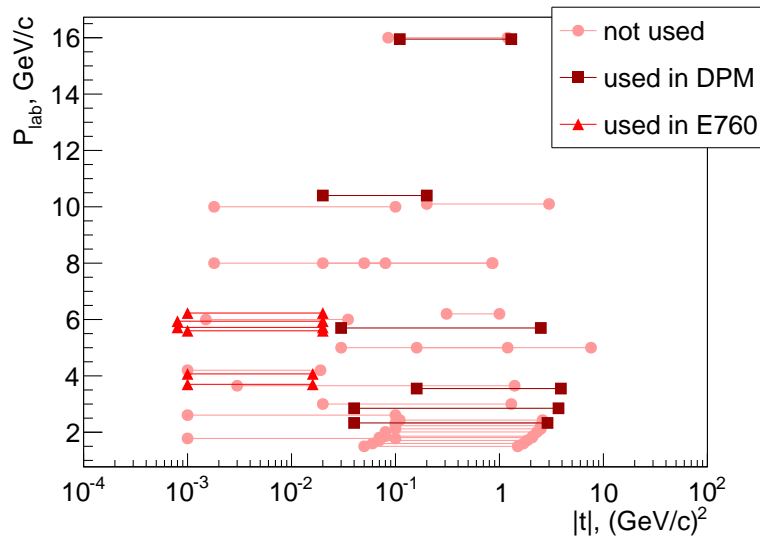


Figure 3.12:  $|t|$  ranges for previous  $p\bar{p}$  elastic scattering measurements

For the comparison of the DPM and the E760-like models with data, missing systematic errors are added to the data as suggested in [51]. A few examples of the comparison are provided in Fig. 3.13. For all energies, at large  $|t|$  the E760-like model rapidly decreases and predicts a vanishing differential cross section. The DPM model is more realistic and predicts non-zero values for large  $|t|$ . However, due to the large uncertainty of the DPM model, this prediction is rather inaccurate.

The  $|t|$  range, which will be available for the luminosity measurement at  $\bar{P}ANDA$ , is energy dependent. It varies between  $10^{-5}$ – $10^{-2}$   $(\text{GeV}/c)^2$  (see Fig. 3.4). Most of the experimental data are available at a relatively large  $|t|$  compared to the LMD  $|t|$  range (Fig. 3.12). Only a few measurements are available in the LMD range and are used to evaluate the relative systematic uncertainty between each model, the DPM model and

<sup>2</sup>For further parameter improvement it might be useful to combine data from different experiments, for example at  $P_{lab}$  8 GeV/c

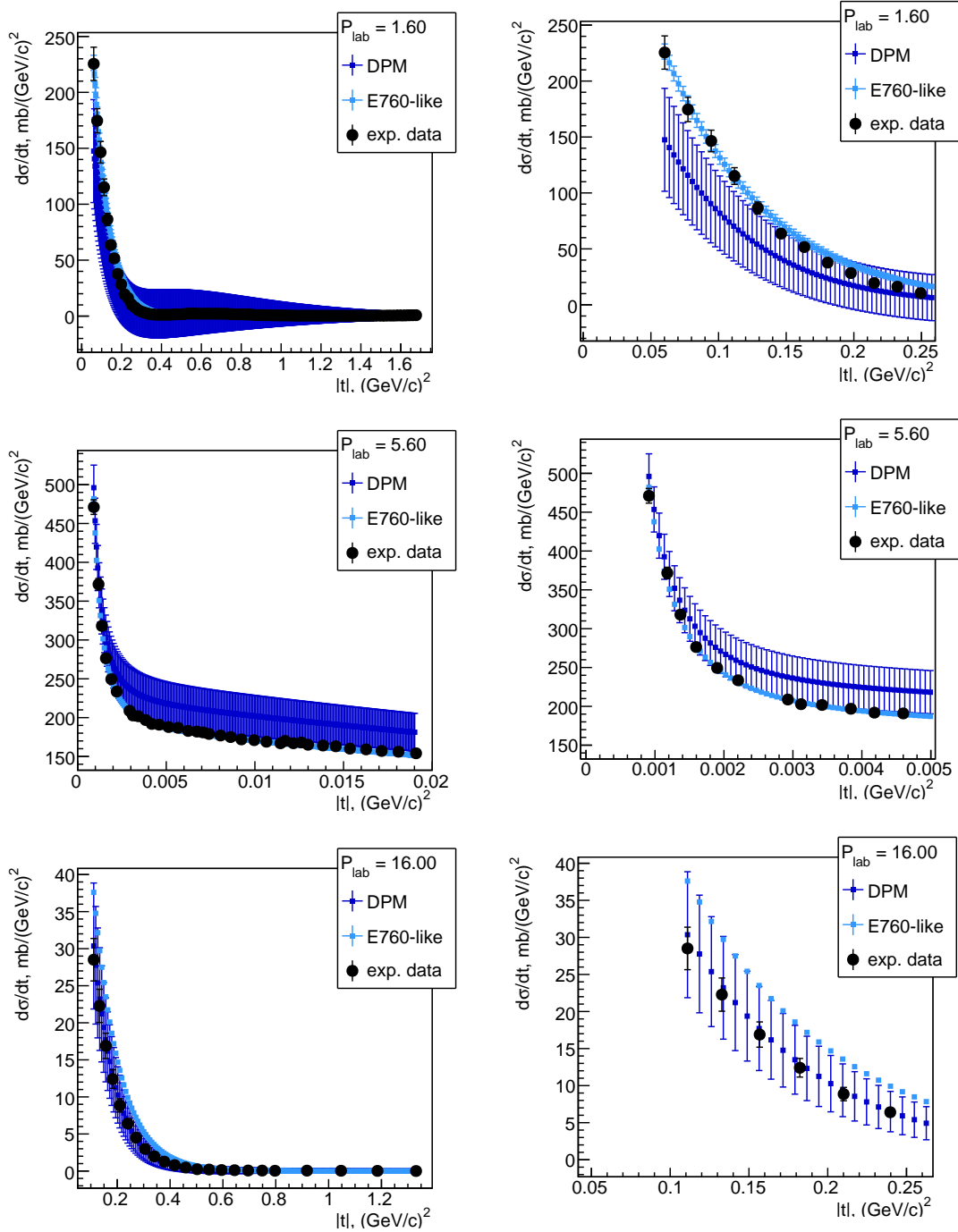


Figure 3.13: Comparison of the DPM and E760-like models with experimental data at  $P_{\text{lab}} 1.6 \text{ GeV}/c$  (top, data from [52]),  $5.6 \text{ GeV}/c$  (middle, data from [50]) and  $16 \text{ GeV}/c$  (bottom, data from [53]); right plot shows a zoom to small  $|t|$  values

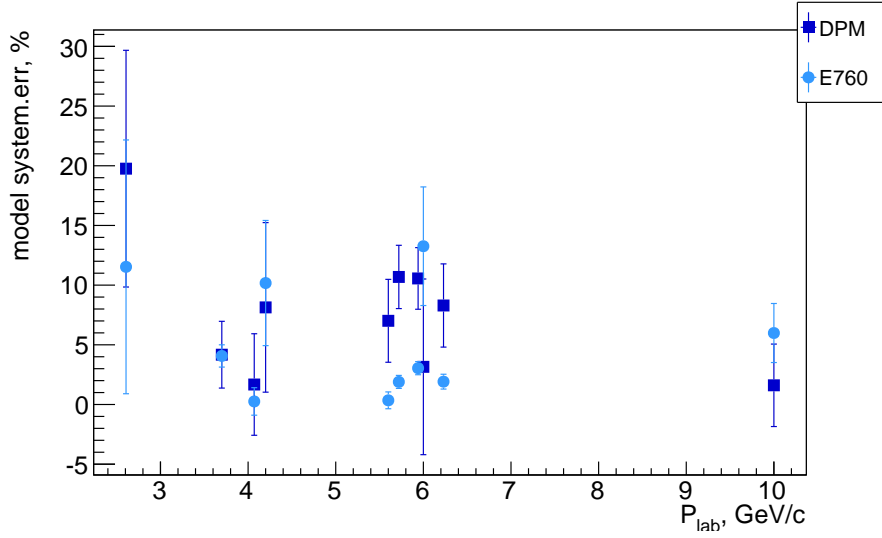


Figure 3.14: Discrepancy between the models and the experimental data available in the polar angle range  $\theta$  between 2–10 mrad

$P_{lab}$ , GeV/c	$\Delta_{LMD}^{had}$ DPM, %	$\Delta_{LMD}^{had}$ E760-like, %	Reference
2.607	$19.76 \pm 9.92$	$11.53 \pm 10.63$	[54]
3.7	$4.17 \pm 2.80$	$4.07 \pm 0.93$	[50]
4.07	$1.67 \pm 4.25$	$0.26 \pm 1.15$	[50]
4.2	$8.14 \pm 7.10$	$10.17 \pm 5.24$	[55]
5.6	$7.01 \pm 3.47$	$0.35 \pm 0.71$	[50]
5.72	$10.69 \pm 2.65$	$1.89 \pm 0.55$	[50]
5.94	$10.56 \pm 2.58$	$3.04 \pm 0.55$	[50]
6.0	$3.15 \pm 7.36$	$13.26 \pm 4.97$	[55]
6.23	$8.29 \pm 3.49$	$1.91 \pm 0.63$	[50]
10.0	$1.61 \pm 3.45$	$5.99 \pm 2.48$	[55]

Table 3.3: Discrepancy between the models and the experimental data available in the polar angle range  $\theta$  between 2–10 mrad

the E760-like model, and data. The discrepancy between a model and data is calculated as:

$$\Delta = \frac{\frac{d\sigma}{dt}(exp) - \frac{d\sigma}{dt}(model)}{\frac{d\sigma}{dt}(exp)} \quad (3.19)$$

The result is presented in Fig. 3.14 and Tab. 3.3 in terms of average discrepancy  $\Delta_{LMD}^{had}$

between the models and the data in the LMD  $t$ -range, where the hadronic contribution is dominating. The error bars on the plot include the model uncertainties as well as the experimental errors. It is no surprise that the E760-like model is in good agreement with the experimental data obtained by this experiment [50] with discrepancies of  $\sim 4\%$ . However, for data not used for the determination of the parameter functions of the E760-like model, the discrepancy is as large as 13%. The DPM model has discrepancies on the level of 10% for the E760 data. Only the data at 10 GeV/ $c$  beam momentum [55] the DPM model describes better than the E760 model. To conclude, the E760 model would be preferred for the luminosity extraction, because it was optimized for the region of small momentum transfers. However, new measurements in the low- $t$  region are desirable to confirm the model description at low energies, e.g. the description by the E760-like model. It would also be important to extend the measurements up to 15 GeV/ $c$  in order to cover the complete beam momentum range at  $\bar{\text{PANDA}}$  where up to now no data points exist.

### 3.3.2.4 KOALA experiment

Due to the limited acceptance of the detector, the LMD can only measure a small range of the momentum transfers  $|t|$ . The strong correlations between the fit parameters make it difficult to accurately determine the luminosity together with the unknown parameters of the hadronic part of the elastic scattering within such a small range of the  $|t|$  distribution (see Appendix C). These parameters will be measured by a dedicated Key experiment for  $\bar{\text{PANDA}}$  Luminosity determination (KOALA) before  $\bar{\text{PANDA}}$  starts data taking.

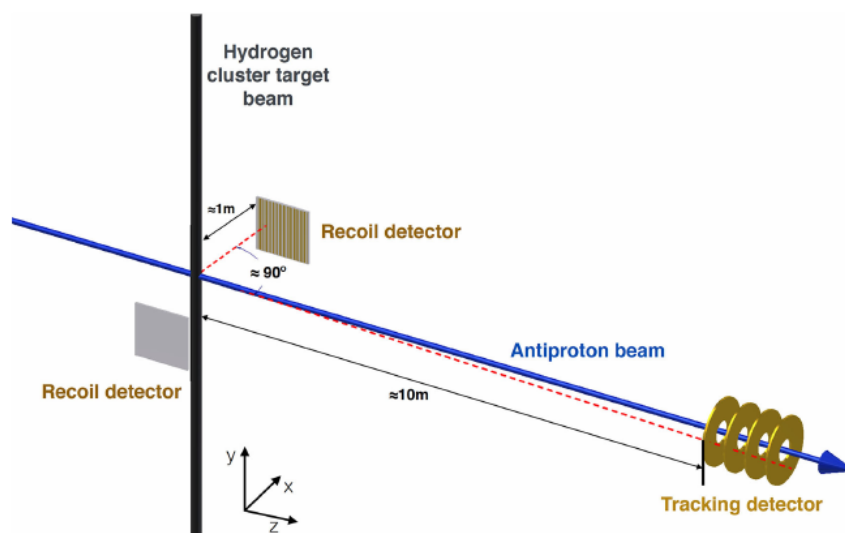


Figure 3.15: Sketch of the KOALA experiment at HESR [56]

The KOALA experiment at HESR, shown in Fig. 3.15, will measure antiproton-proton elastic scattering in a large range of the four momentum transfer  $|t|$  [56]. The  $|t|$  range available for KOALA is shown in Fig. 3.4 by the yellow band. The idea is to measure the scattered beam particles at forward angles by a tracking detector (a prototype of the LMD) and the recoil target protons near  $90^\circ$  by detectors which are able to measure the angle and the energy of the recoil protons. The recoil detector will measure both the kinetic energy and the polar angle of the recoil protons to achieve a strong background suppression. A coincidence between the recoil detector and the forward measurement will help to reach  $|t|$  values down to  $\sim 10^{-3} (\text{GeV}/c)^2$ . Simulations show that in such an extended  $|t|$  range, not only the luminosity, but also the parameters  $\sigma_T$ ,  $b$  and  $\rho$  can be determined with a precision better than 1% [56].

### 3.3.2.5 Model uncertainty caused by the momentum uncertainty

All models for the process of elastic scattering are energy dependent. In addition, in the experiment the beam momentum will be known only with limited accuracy. This can affect the systematic uncertainty of the model. Fig. 3.16 shows the resulting systematic uncertainty of the E760-like model in dependence on the beam momentum in the polar angle range  $\theta$  between 2–10 mrad, if the beam momentum deviates from the nominal beam momentum by 0.001%–10%. The systematic uncertainty introduced by the beam momentum deviations becomes significant for  $\Delta P = 10^{-2} \cdot P_{lab}$  and dominates the systematic uncertainty for  $\Delta P = 10^{-1} \cdot P_{lab}$ . In the last case the uncertainty increases up to  $\sim \pm 5\%$ .

From the HESR we expect an uncertainty of the beam energy value of  $\sim 0.1$  MeV in the charmonium region, which gives  $\Delta P/P_{lab} \sim 10^{-5}$ <sup>3</sup>. At such values the introduced systematic uncertainty is very small and stays below 0.005%.

---

<sup>3</sup>at beam momentum  $\sim 5$  GeV/c

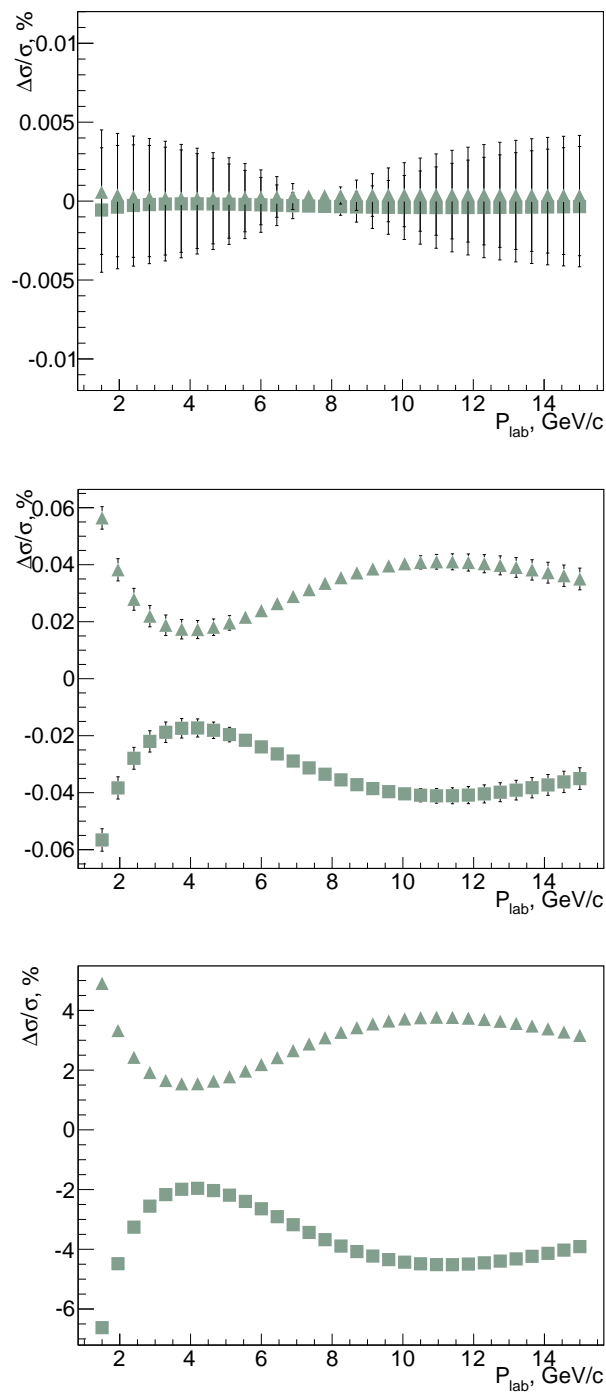


Figure 3.16: The uncertainty of the E760-like model for  $P = P_{lab} \pm \Delta P$  with  $\Delta P = 10^{-5} \cdot P_{lab}$  (top),  $\Delta P = 10^{-3} \cdot P_{lab}$  (center),  $\Delta P = 10^{-1} \cdot P_{lab}$  (bottom). Squares indicate  $P = P_{lab} - \Delta P$ , triangles  $P = P_{lab} + \Delta P$

### 3.4 The Luminosity Detector

The goal for the measurement of the absolute time-integrated luminosity at  $\bar{P}$ ANDA is to be better than 5%. Currently the accuracy is limited by the model uncertainty. Nevertheless, the registration and reconstruction of the scattered antiproton tracks should be performed with high accuracy to ensure that no significant uncertainty is introduced there.

During the design phase of the luminosity detector, a significant effort was made to ensure a reliable system with an optimal resolution building on current technologies. Extensive simulation studies were performed to make sure that the design will work in the experimental environment. The developed reconstruction algorithms were verified in these studies. The software algorithms together with the simulation results are presented in following chapters. The detector construction has just started and it is not part of this work. Therefore, only the main features relevant for understanding of the simulation results are discussed below. For more information the interested reader is referred to the LMD Technical Design Report [32].

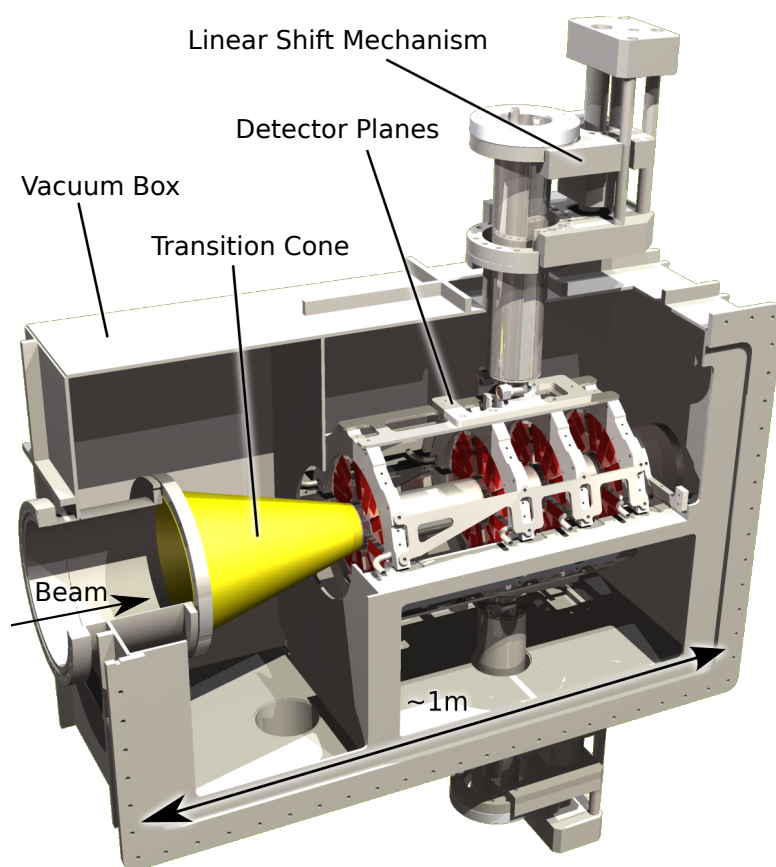


Figure 3.17: The Luminosity Detector at  $\bar{P}$ ANDA

The LMD is the most downstream detector in the  $\bar{P}$ ANDA setup, starting from 10.5 m behind the IP. It consists of 4 detector planes, where the first plane is placed at  $z=11.24$  m and the following 3 in distances of 20 cm, 10 cm and 10 cm with respect to each other (Fig. 3.17).

To minimize the multiple scattering effect on elastically scattered antiprotons, which should be registered in the LMD, the detector is operated in a vacuum box. Antiprotons, elastically scattered at small angles, go inside the beam pipe and pass only a transition foil before being detected in the sensitive material of the LMD. The transition foil is a cone made of a laminate of a robust foil (polyimide or boPET) and a conducting aluminum foil. The cone plays two important roles. First of all it is shielding the sensors from the electromagnetic fields of the intense non-interacting antiproton beam. And the smoothly changing diameter of the cone minimizes distortion of the stored beam in the HESR, to avoid a rapid change of the conductivity of the beam pipe. Secondly the beam pipe vacuum of up to  $10^{-9}$  mbar is separated from the detector vacuum which is expected to be orders of magnitudes worse due to the outgassing of various detector components.

The detector planes consist of 400 thinned HV-MAPS produced as individual  $2 \times 2$  cm<sup>2</sup> squares. HV-MAPS is a technology which combines biased silicon pixel detectors with smart diodes. Fig. 3.18 shows a block scheme of a smart diode. Starting from a p-

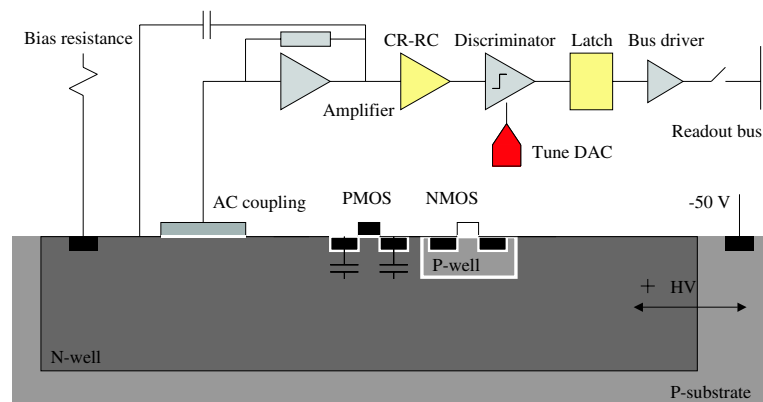


Figure 3.18: Block scheme of one smart diode [32]

substrate, isles of n-wells are doped into the substrate. The depletion region of the pn-junction is further increased by the application of a reverse bias voltage of typically 50–60 V. The thickness of the region is below  $10 \mu\text{m}$  and a charged particle passing this region will generate about  $\sim 700$  electron-hole pairs. The electric field collects electrons in the n-well where charge sensitive electronic is implemented. In a readout chain charge collection is followed by an amplifier with a shaping time of  $1 \mu\text{s}$ . Shaping is implemented on each diode to reduce noise. The shaped signal of each diode is connected by a metal layer with its own discriminator outside of the sensitive area

where digitization is performed.

In the final HV-MAPS design a pattern of smart diodes will be placed on one  $2 \times 2 \text{ cm}^2$  sensor. Space of about  $50 \mu\text{m}$  around the active area has to be reserved for a guard ring to reduce edge effects of the electric field of the depleted regions. Moreover, digitization of the signals requires accurate timing and a large number of metal layers. Therefore a special region along one side of the sensor of about  $500 \mu\text{m}$  width is used to implement that part of the readout chain. Smart diodes are  $70 \times 70 \mu\text{m}^2$  large n-wells and are placed with a pitch of  $80 \mu\text{m}$ .

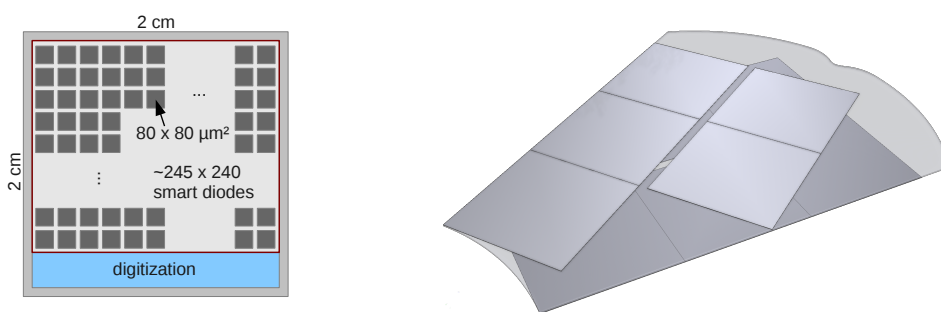


Figure 3.19: (left) Simplified layout of the HV-MAPS design; (right) Arrangement of 10 HV-MAPS on one CVD diamond

Since the HV-MAPS technology consumes power, the heat has to be conducted from the sensitive area to a liquid cooled support structure. As a rigid solution polished diamond plates produced in a CVD process were chosen. In that way the best heat conductivity is combined with the shortest radiation length.

To ensure as close to  $2\pi$  as possible acceptance around the beam pipe, a design of partially overlapping sensors was chosen, where 10 sensors are grouped on one module of a plane. On each side of the CVD diamond 5 sensors are arranged as illustrated in Fig. 3.19 (right). Sensors will be glued in groups of 3 and 2 along one side of the edge of the diamond. The same arrangement is chosen for the back side of the CVD diamond. What remains uncovered is a rhomb between the two groups as well as a small insensitive area next to the beam pipe. Some area is covered by sensors on the front as well as on the back side. This allows for precise alignment of the sensors of one module. However it also requires special treatment during hit reconstruction (see Chapter 4).

Although the HV-MAPS will be thinned down to  $50 \mu\text{m}$ , the total radiation length of a sensor module is expected to be  $\sim 0.37\%$ , which would correspond to a  $\sim 350 \mu\text{m}$  thick silicon sensor. The total material budget of one detector plane is illustrated in components by Fig. 3.20. The thickness of resin as an adhesive material between polyimide and aluminum traces as well as the glue between CVD diamond, sensors and the flex

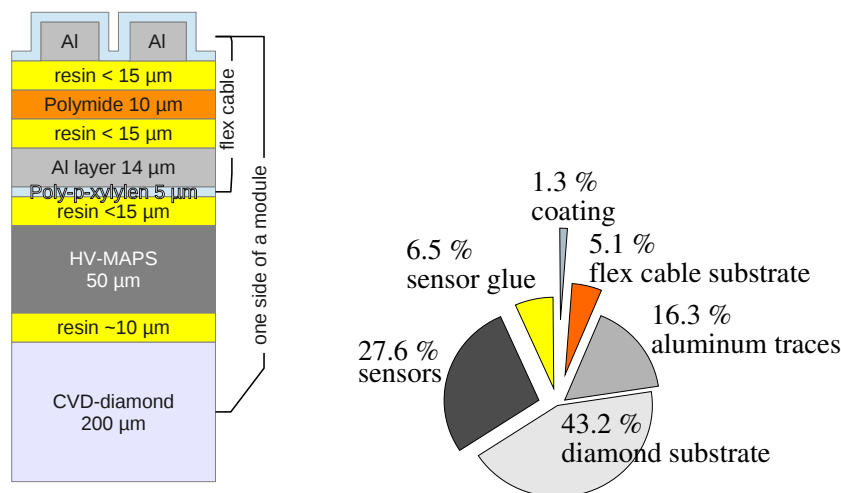


Figure 3.20: Components of one half of a double sided module and the corresponding thicknesses; The pie chart shows the relative contributions

cable depends on the production process and is still matter of ongoing studies. The thickness of the CVD diamond will be reduced if possible.

The support structure (half plane, Fig. 3.21) is made by CNC machines out of aluminum with an embedded cooling pipe. They are produced by melting aluminum around an already bent stainless steel pipe in a mold. The support structure does not only cool the heat produced by the HV-MAPS but also the heat from front-end electronics, which have to be placed in vacuum next to the sensors.

During the injection or acceleration phase, the beam conditions could be very bad, such that the sensors of the LMD are in danger to be hit by the primary beam. Thus it was decided to construct the sensitive area retractable: The plane array was divided into 2 halves. Each half is attached to one linear shift mechanism driven by a stepper motor with sub-micrometer precision and can be retraced by  $\sim 10$  cm.

A precise positioning of the HV-MAPS on the CVD support module, the modules within the cooling frame, and the support structures (half planes) among each other within one detector half are subjects of dedicated studies. Currently an accuracy of  $\pm 200 \mu\text{m}$  seems to be achievable.

No detector can be built without detailed simulation studies. Basic ideas are tested with simple geometrical models. In parallel, the technical work on the design is done and a more sophisticated simulation model is introduced to give feedback for the optimization of the design. As soon as a suitable design is found, performance studies are carried out and further input for the design optimization is given.

A realistic software model of the detector together with a well understood reconstruction software (Chapter 4) allows us to monitor important parameters like resolution and efficiency during the design optimization. The need of retractable halves of

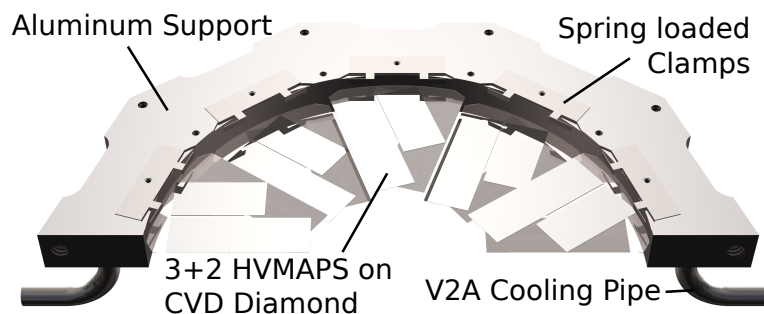


Figure 3.21: Half plane acting as a cooling and support structure of 5 modules. The aluminum structure contains a stainless steel pipe for cooling liquid

the LMD requires a fast and efficient alignment scenario. As a possible solution a software alignment method based on reconstructed tracks was proposed. In Chapter 5 it is shown that this alignment method can deal with the expected misalignment scales. The performance was also checked during detailed background studies (Chapter 6). It was shown that secondaries produced in non-sensitive parts of the LMD (such as the cooling structure or the vacuum box) can be suppressed after the track reconstruction and thus a change of materials is not needed.

# Extraction of the luminosity

For the determination of the luminosity, the differential cross section in dependence of the scattering angle has to be extracted from data. The data reconstruction includes several necessary steps: finding and fitting of the tracks of the elastically scattered antiprotons and backtracking them to the interaction point in order to get rid of the influence of the magnetic field.

A complete simulation of the  $\bar{\text{P}}\text{ANDA}$  detector components and their response to the passage of particles has been developed within the PandaRoot framework [57]. It is designed that way that the same reconstruction and analysis algorithms will work on the simulation output as well as on data. This chapter gives an overview of the framework and describes all procedures related to the track reconstruction in the luminosity detector and related performance studies.

## 4.1 PandaRoot framework layout

The software framework is a collection of software packages and tools for the description of the single detector components and the simulation of physics reactions. The layout is organized such as to allow the re-use of well known programs and tools, common to particle and nuclear physics simulations. One basic concept of the framework is its modularity, the possibility to switch algorithms and procedures at any point in the chain of processes. Hence a set of interfaces and data input/output are provided to connect all these tools properly.

Almost all experiments at the future FAIR facility are using the following features of organization of their software packages:

- *External Packages* with the commonly used packages as Geant3 and Geant4 (propagation of particles through matter written in Fortran [58] and C++ [59]), VMC

(Virtual Monte-Carlo [60]), ROOT (Plotting, fitting, graphics etc. [61]), Pythia [62] and auxiliary tools

- *FairRoot* handling the framework (data I/O, interfaces, infrastructure). The task is to provide all steps of the data processing up to the physics analysis stage. Data is stored in a ROOT file, using ROOT objects handling with chains, trees and branches.
- *DetectorRoot* detector framework (detector simulations and data reconstruction). For the Panda experiment such framework is called *PandaRoot*.

The PandaRoot framework user should add detector class implementations for the transport model and reconstruction tasks, which are processing the data. A typical chain of generating and processing of simulated data contains the following ingredients:

1. Event Generator:

The event generator produces in each event a set of particles according to the investigated physics reaction or detector studies. Particles are defined by their type and four-momentum, point of origin and time. Those properties are randomly distributed by the selected model. In PandaRoot for this purpose several generators are available. The "BOX" generator provides a uniform distribution for all variables. It also has possibility to choose a certain variable range. A generator for single-channel generation is called EvtGen [63]. And the DPM [64] generator provides the full description of all antiproton-proton reactions.

2. Transport Code (VMC):

The particle transport through matter is simulated by Geant [58],[59]. The Virtual Monte-Carlo interface (VMC) allows to switch between the different Geant versions as well as to introduce other packages. Each sub-detector has its own geometry description (usually in ROOT format) and definition of the active and passive elements. For all materials in which particles can interact according to physical processes, such as ionization, showering or Cherenkov emission, they react with the detector material and loss of energy is estimated. Interaction of particle with the detector material (e.g position and energy loss) is saved in each event. This data is called MCHits and it is accessible for the analysis of the performance of the reconstruction steps.

3. Digitization:

All Monte-Carlo data is processed to model the detectors response. The threshold, efficiency and amplification can be adjusted according to the measurements of real detector response. The digitized data formats in the simulation must be the same as those obtained in a real implementation (a prototype detector or even the final setup). This data is called DigiHits and is used as input information for reconstruction of the events.

4. Local Reconstruction:

The digitized data is subject of a local reconstruction procedure which associates DigiHits to information with a physical meaning, like a 3D space point, a total energy loss or a Cherenkov angle. For tracking sub-systems during this step track reconstruction is done, which usually includes track search and track fit.

5. Global Reconstruction:

At this stage, locally reconstructed information is sorted to produce valuable input for further analysis. This sorting procedure can include assignment between reconstructed data from different subsystems as well as merge of local information to improve reconstructed parameters (i.g two parts of one charged particle track in neighboring subsystems). Particle identification at Panda is performed globally, taking into account information from all sub-detectors.

6. Physics Analysis:

The analysis tools have to deal with a collection of information based on four-momenta, positions and the identity of the reconstructed particles in a unified way. Particle combination, selection mechanisms and manipulation tools (like boosting between lab and center of mass frame) are provided. Furthermore, a set of fitters is available to fit the four momenta and positions of particles (e.g. from a decay) under different types of constraints.

For the luminosity measurement, only information from the luminosity detector is essential. This means only locally reconstructed information is used and steps 5 and 6 are not needed. Fig. 4.1 shows the reconstruction chain in the LMD step by step, starting with hit reconstruction up to back propagation of tracks to the interaction point. In the following sections each step is discussed in detail.



Figure 4.1: Track reconstruction chain for the luminosity detector

## 4.2 Hit reconstruction

Charged particle going through the sensor creates an excitation in this solid-state material. The sensors of the luminosity detector have a pixel structure with a size of  $80\ \mu\text{m}$ . The digitized data contains the information about the position of the charge collected at the pixel. First of all, pixels are combined to clusters. The central position of the channel with the highest charge yield in a cluster gives an uncertainty on the coordinate position [65]:

$$\sigma_{digi} = d/\sqrt{12} = 23\ \mu\text{m} \quad (4.1)$$

A better resolution ( $\sigma_{digi} \sim 15\ \mu\text{m}$ ) for clusters with two or more pixels can be obtained by using the center of gravity as position of the cluster, which utilizes the digital charge measurements as weight. The average position is calculated by:

$$x = \frac{\sum_i q_i x_i}{\sum_i x_i} \quad (4.2)$$

with charge  $q_i$  deposited at a pixel with coordinate  $x_i$ . In the design of HV-MAPS it is not possible to measure the deposited charge due to the very small active layer thickness. The simulation shows that the fraction of events where a single cluster contains more than one fired pixel is below 40%. Therefore one cannot achieve a significant improvement in spatial resolution even if a measurement of the charge deposit would be possible.

For pixels, the x and y coordinates are defined in the local sensor frame. To obtain the hit (3D point) in the global frame, the x and y coordinates are recalculated in the global frame and the z position of the sensor in the global frame is added as the z coordinate of the hit. All corrections due to sensor and module alignment (Chapter 5) are applied during this step.

As it was mentioned in Chapter 3, in order to achieve the full acceptance in angle  $\phi$  both sides of the planes will be equipped with sensors. Some of those sensors overlap and a charged particle can hit pixels on both sides. These hits on different sides of the diamond wafer do not contain any new information and are merged together for simplicity of the usage in the track search procedure. To be merged, hits should fulfill the following conditions: both hits must come from different sides of the same module and the difference in x(y) coordinate  $\delta x(\delta y)$  should be smaller than  $\sigma_x(\sigma_y)$ , which is determined by pixel resolution and set to  $\sim 30\ \mu\text{m}$ . The drawback of sensors overlapping is a 38% larger radiation length compared to the single sided areas. The non-uniform material budget (overlapping and non-overlapping areas) is taken into account in the track fit procedure (Section 4.4).

## 4.3 Track search

Nowadays, tracking systems usually measure up to hundred hits per track, which demands quite complicated pattern recognition algorithms, but makes track reconstruction more robust against loss of hits in a track. In case of the LMD, there is only a small number of hits per track and all of them have to be used. Two different algorithms were developed for the track search. Their performance was studied in events with multiple tracks per event hitting the LMD.

### 4.3.1 Track Following

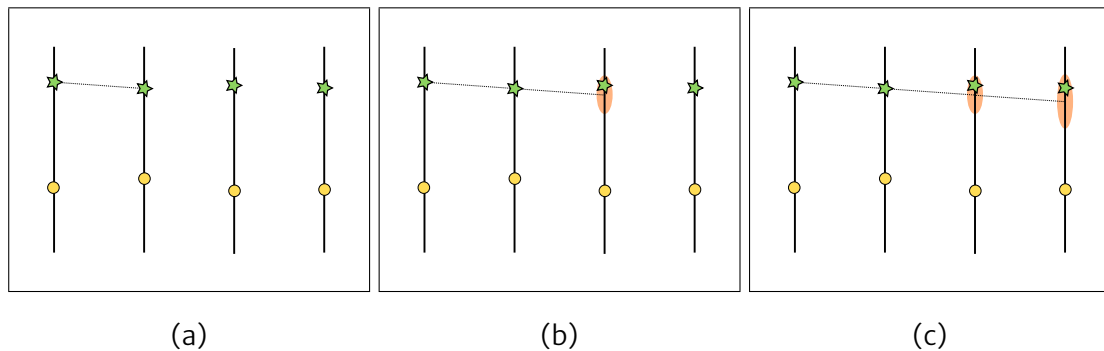


Figure 4.2: Track Following algorithm

(a): A track candidate seed between two first planes

(b): Search for a hit within corridor on the next plane

(c): Enlarged corridor for a hit search on the last plane

As it is clear from the name, Track Following (TF) is a simple routine which follows the track. Here a track candidate seed is built by two points of neighboring planes (Fig.4.2 a) and then propagated to the next plane (Fig.4.2 b). If the difference between the hit on the next plane and the track line is less than a certain distance (corridor), the hit is attached to the track and the track candidate is propagated to the last plane, where it is looking for the nearest hit once again (Fig.4.2 c). This procedure is repeated until all track candidate seeds between the first two layers are checked.

Sometimes it can happen that a hit on one layer is missed (broken sensor or error during hit reconstruction). To make the reconstruction possible in this case a special missing plane algorithm was implemented. It takes combinations between the first and the third (and the second and the third) layers as a track candidate seed and also allows for further track candidate propagation in case the hit on one of the planes was not found within the corridor [66].

### 4.3.2 Cellular Automaton

The second algorithm implemented for track search is the more sophisticated Cellular Automaton (CA), which was originally developed for the HERA-B experiment [67] and is used in many other experiments like ALICE [68], CBM [69], etc.

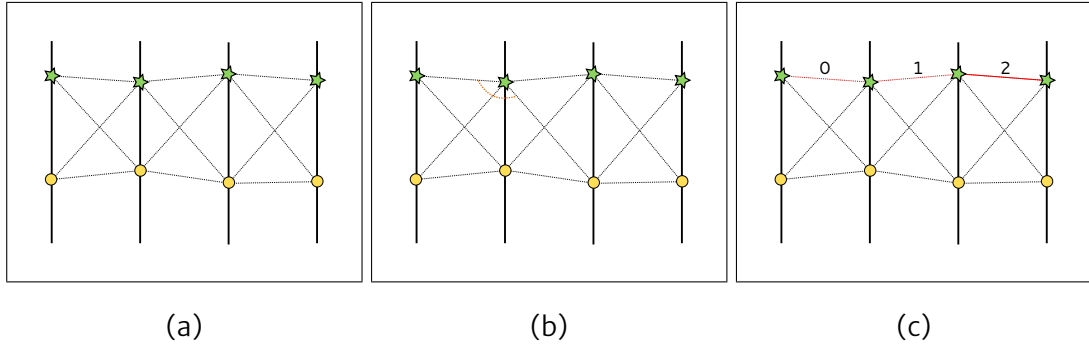


Figure 4.3: Cellular Automaton algorithm  
(a): All possible cells are built  
(b): Search for neighboring cells  
(c): Cells arranged during evolution by number of neighbors

This algorithm deals with cells: segments between two hits on different planes (Fig.4.3 a). The cell state defines the place of the segment in an optimizing sequence (e.g. track candidate). In the beginning all cell states are set to zero because each segment can, in principle, initiate the optimal sequence.

The cell state is updated accordingly to number of neighboring cells, which it has. Two cells are called neighbors, if they can form a straight line together, e.g. if they satisfy following rules:

- They share one point on a common plane
- the breaking angle  $\alpha$  between the two cells is such that  $(1 - \cos\alpha) < \delta\psi_{\max}$

The parameter  $\delta\psi_{\max}$  is not exactly zero. Due to multiple scattering a particle is scattered while going through the material of the planes. And due to the pixelation the coordinate of a pixel is always defined in the middle of the pixel. So between planes separated by a distance  $z_p$  ( $\sim 10$  cm), hits could be relatively shifted by the pixel size  $d_{\text{pixel}}$  ( $80 \mu\text{m}$ ). One can assume that the breaking angle  $\alpha$  is roughly the sum of the multiple scattering angle and the angle due to pixelation:

$$\alpha = \theta_{MS}^{\text{space}} + \alpha_{\text{digi}} \quad (4.3)$$

where  $\alpha_{\text{digi}} \sim \frac{d_{\text{pixel}}}{z_p} \sim 8 \times 10^{-4}$ ,  $\theta_{MS}^{\text{space}} \sim \sqrt{2} \cdot \theta_{MS}$  and  $\theta_{MS}$  is calculated according to

multiple scattering estimation [1]:

$$\theta_{MS} = \frac{13.6 \cdot 10^{-3}}{\beta p} \frac{X}{X_0} \left(1 + 0.038 L n\left(\frac{X}{X_0}\right)\right), \quad (4.4)$$

with the radiation length of a sensor  $\frac{X}{X_0}$  and the momentum  $p$  of the particle. For small angles, the approximation  $\delta\psi_{\max} = (1 - \cos\alpha) \sim \frac{\alpha^2}{2}$  can be used. Table 4.1 shows the estimation of the  $\delta\psi_{\max}$  parameter for different beam momenta. However, this simple estimate does not work in all cases. Due to the non-uniform material budget within one module, it has overlapping sensors and holes between the sensors. Thus the breaking angle between cells corresponding to one track can be different from the average multiple scattering angle, e.g. if the track goes through the hole between the sensors on one plane, but is scattered in such way that on the next plane it will go through sensors on both sides.

$P_{beam}, \text{ GeV}/c$	$\theta_{MS}^{space}, \text{ rad}$	$\delta\psi_{\max}$
15	$4.4 \cdot 10^{-5}$	$8 \cdot 10^{-7}$
11.91	$5.5 \cdot 10^{-5}$	$8 \cdot 10^{-7}$
8.9	$7.4 \cdot 10^{-5}$	$9 \cdot 10^{-7}$
4.06	$1.7 \cdot 10^{-4}$	$1 \cdot 10^{-6}$
1.5	$5.2 \cdot 10^{-4}$	$2 \cdot 10^{-6}$

Table 4.1: Estimation of  $\delta\psi_{\max}$  values for tracks with different momenta

Therefore the influence of  $\delta\psi_{\max}$  on the track reconstruction was studied with simulated data. The tracks were generated with the BOX generator uniformly within  $\theta$  range between 2 to 11 mrad and in the  $\phi$  range between  $-0.35$  and  $0.3$  rad, which corresponds to one sensor module of the LMD. After reconstruction, the number of missed and fake tracks was counted. A missed track is a track which is lost during reconstruction and a fake track is a track which is reconstructed out of a mixture of hits from different tracks<sup>1</sup>. Fig 4.4 shows the dependence of the number of events with missed and ghost track versus the breaking angle  $\delta\psi_{\max}$  for the simulation of antiproton tracks with momentum of  $1.5 \text{ GeV}/c$ . According to this result,  $\delta\psi_{\max}$  was chosen slightly larger than is was estimated ( $2 \times 10^{-6}$ ) and set to  $5 \times 10^{-6}$ . For momenta above  $1.5 \text{ GeV}/c$ , the estimated values work quite well and they are used during the reconstruction.

The evolution process in the Cellular Automaton is divided into *forward evolution* and *backward pass*. During forward evolution the automaton takes each cell and looks for its leftward neighbors. If there is such a neighbor and its state is equal to the cell's state, the cell's state will be increased by one. When the automaton completes a loop over

<sup>1</sup>The more detailed determination of missed and fake tracks is given in Section 4.3.3

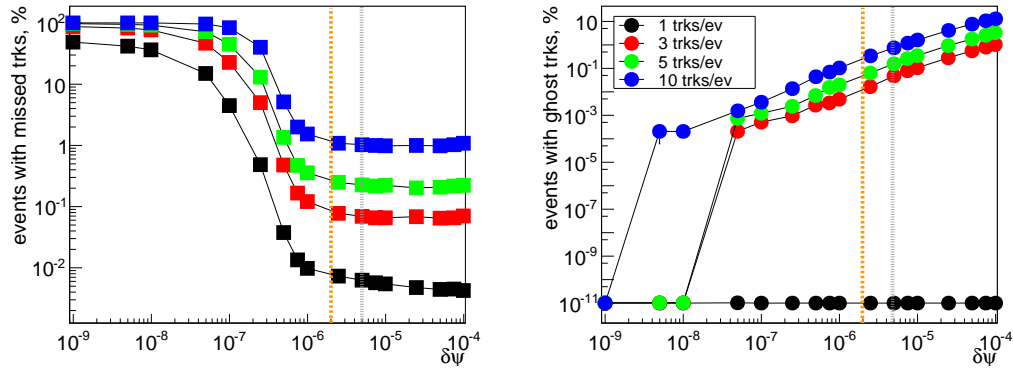


Figure 4.4: Influence of  $\delta\psi_{max}$  parameter on number of missed (left) and fake (right) tracks for simulation with  $P_{beam} = 1.5 GeV/c$  (orange dashed line is the estimated value, gray dashed line is the chosen value)

all cells, their previous states are simultaneously replaced by the increased ones. This process is iteratively repeated until there are no neighboring cells with the same states. At the end of the forward evolution, the state of each cell is equal to the length of a track candidate that can be traced leftwards starting from this cell (Fig.4.3 c). The backward pass starts with investigating the set of cells that have the highest state. These cells are considered as the first segments of track candidates. For each cell the automaton performs a loop over the cell's leftward neighbors looking for the best prolongation of the track candidate. To be a prolongating one a cell must have a state lower by unity. If such a cell is found, the automaton assigns it to the track candidate, looks for its leftward neighbors and so on. The candidate tracing stops when a segment with the state of zero is assigned to the candidate.

### 4.3.3 Comparison of performance for track search algorithms

The main goal of any track search algorithm is to find all tracks correctly with a minimal number of missed tracks and a minimal number of fake tracks. For the LMD a significant amount of missed tracks as well as fake tracks could lead to changes in the shape of the distribution of the reconstructed  $\theta$  angles. It could cause difficulties and systematic error in extraction of the luminosity by fitting the theoretical model to this distribution.

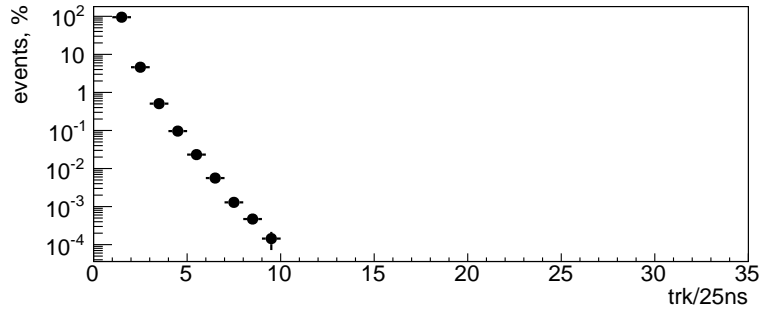


Figure 4.5: Multiplicity of events within one readout time frame at  $P_{beam}=1.5 \text{ GeV}/c$

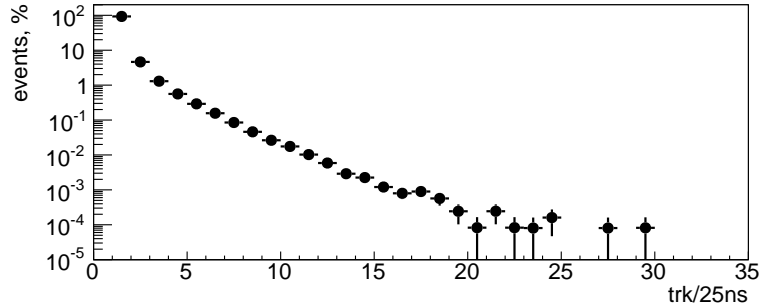


Figure 4.6: Multiplicity of events within one readout time frame at  $P_{beam}=15 \text{ GeV}/c$

Elastic  $p\bar{p}$  scattering is a process with naturally low track multiplicity. Due to the kinematic constrains, only the scattered antiproton can reach the LMD from this process. However, particles from inelastic  $p\bar{p}$  interactions can reach the LMD too. And secondary particles can also leave tracks in the LMD. The last two processes could produce higher track multiplicities than just 1 track per event. The multiplicity depends on the interaction rate. Due to different total  $p\bar{p}$  cross section, the interaction rate is different for different beam momenta, e.g. at  $P_{beam}=15 \text{ GeV}/c$  the interaction rate is 10 MHz and at  $P_{beam}=1.5 \text{ GeV}/c$  it is 25 MHz. According to the current design, the readout cycle (time resolution) of the LMD DAQ is expected to be 25 ns [32]. Fig. 4.5 and Fig. 4.6 show the average number of generated tracks, which contribute to

the number of fired pixels on the same plane (one side) within a 25 ns time frame at  $P_{beam}=1.5 \text{ GeV}/c$  and  $P_{beam}=15 \text{ GeV}/c$ , respectively. In this study, the DPM generator with a simulation of elastic and inelastic  $p\bar{p}$  interactions was used. Due to background particles, the multiplicity can go up to 10–30 tracks in one time frame. In order to prevent tracks loss in the case when hits from the same track are registered in different time frames on different planes, the track search will be done not within one, but within several time frames, e.g. 3–4 time frames. For the simplicity, in the following discussion combined time frames, used for the track reconstruction, are called *events*. By increasing the number of time frames used for the track reconstruction, number of events with higher track multiplicity is also increased. If only one time frame is considered for the track search, contribution of events with more than 1 track/events is 5.3 % at at  $P_{beam}=1.5 \text{ GeV}/c$  (Fig. 4.5) and 7.2 % at at  $P_{beam}=15 \text{ GeV}/c$  (Fig. 4.6). In case of 4 time frames, contribution of events with more than 1 track/event goes up to 11.4 % at at  $P_{beam}=1.5 \text{ GeV}/c$  and 9.1 % at at  $P_{beam}=15 \text{ GeV}/c$ . Also one should remember that the fraction of the background events strongly depends on the background model <sup>2</sup>. For an accurate background treatment, all tracks have to be reconstructed.

In case of events with high multiplicities, the track search becomes a challenge due to the small number of hits per track. To make sure that the developed track search algorithms can deal with these high track multiplicities, special tests were performed. For those tests the BOX generator was used, where tracks were generated within the  $\theta$  range of 4–8 mrad and full  $\phi$  angle coverage. The same simulated data sample was used for the track search with the Track Following and the Cellular Automaton algorithms to ensure that differences in the results are caused only by the searching methods and not by statistical fluctuations in the simulated data.

The reconstructed tracks were compared with generated information on the hit level and sorted out into following categories:

- Good Track: contains 65 % <sup>3</sup> of the hits from the same simulated track
- Missed Track: simulated track was not found
- Fake Track:
  - Split Track: simulated track was reconstructed twice
  - Ghost Track: reconstructed track contains mixture of hits from different simulated tracks

---

<sup>2</sup>A more detailed discussion about background studies is given in Chapter 6

<sup>3</sup>For tracks constructed from three hits, at least two hits should belong to the same particle. And for tracks with four hits, the requirement is at least three hits should belong to the same particle.

### Missed Tracks

The results from the study of missed tracks in dependence on the track multiplicity are presented in Fig. 4.7 (for antiproton with momentum  $1.5 \text{ GeV}/c$ ) and Fig. 4.8 (for  $15 \text{ GeV}/c$ ). At small momenta, track losses for Cellular Automaton are significantly smaller. This can be explained by the possibility of a more precise tuning of this algorithm. The internal parameters of the CA are not so tight as for the TF algorithm. The difference between the CA and the TF for high momentum tracks is not significant any more and both have similar performance.

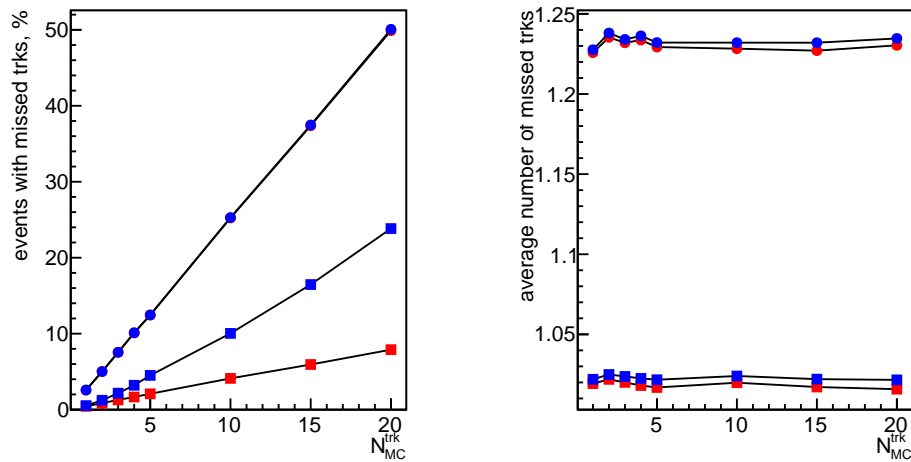


Figure 4.7: Average number of events with missed tracks (left) and average number of missed tracks per event with missed tracks (right) in dependence on track multiplicity: red – Cellular Automaton, blue – Track Following; circles – missed due to small amount of hits; squares – track search losses (momentum  $1.5 \text{ GeV}/c$ )

Sometimes tracks cannot be reconstructed due to a too small amount of reconstructed hits. For each track search algorithm there is the requirement for at least 3 hits on different layers of the detector. This means a track which leaves only 2 hits in the LMD will be lost by default. Fig. 4.9 shows the number of missed tracks versus the number of reconstructed hits (before hit merging). For both cases half to one third of the missed tracks are lost due an insufficient number of hits, independently from the simulated track multiplicity. Also this plot confirms that the CA algorithm can deal better with high multiplicity events. e.g. in case of 20 tracks/event, around a few percents of all missed tracks are tracks with maximum possible number of non-merged hits (8), but for TF this fraction is as high as 16%.

Fig. 4.10 shows the angular distribution of the missed tracks, which indicates which tracks (generated  $\theta$  and  $\phi$  values) are lost. From Fig. 4.10 left it is clear that scattered tracks going through holes between sensors cannot leave enough hits in the detector. The red area corresponds to holes between the sensors. Concerning the track search algorithm losses (Fig. 4.10 right), they mainly happen in regions close to the holes and

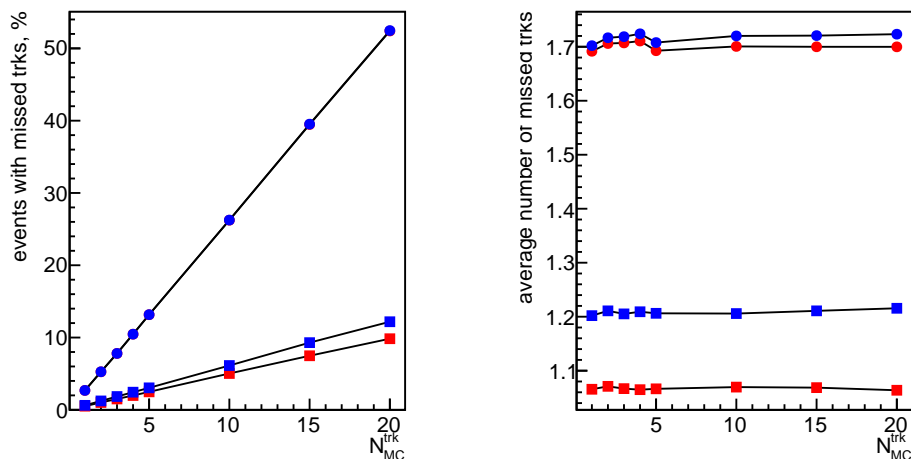


Figure 4.8: Average number of events with missed tracks (left) and average number of missed tracks per event with missed tracks (right) in dependence on track multiplicity: red – Cellular Automaton, blue – Track Following; circles – missed due to small amount of hits; squares – track search losses (momentum 15 GeV/c)

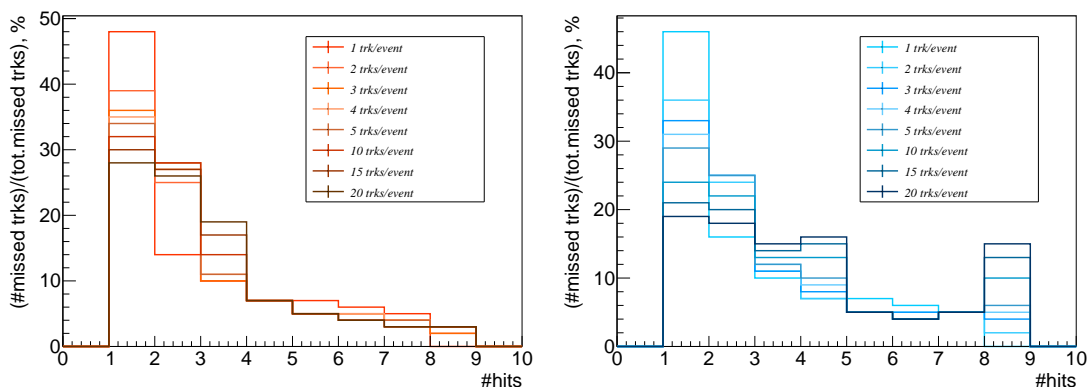


Figure 4.9: Amount of missed tracks in dependence on the number of non-merged hits for the Cellular Automaton (left) and Track Following (right) algorithm. Momentum 1.5 GeV/c

can be explained by re-scattering of the tracks at the edges of the sensors.

### Fake Tracks

The results from a study of fake tracks in dependence on the track multiplicity are presented in Fig. 4.11 (antiproton momentum 1.5 GeV/c) and Fig. 4.12 (15 GeV/c). In the following, some examples are given in order to illustrate possible reasons for fake tracks. For all examples below, tracks go through the regions of modules where sensors are glued on both sides. Although during the reconstruction hits on different sides of

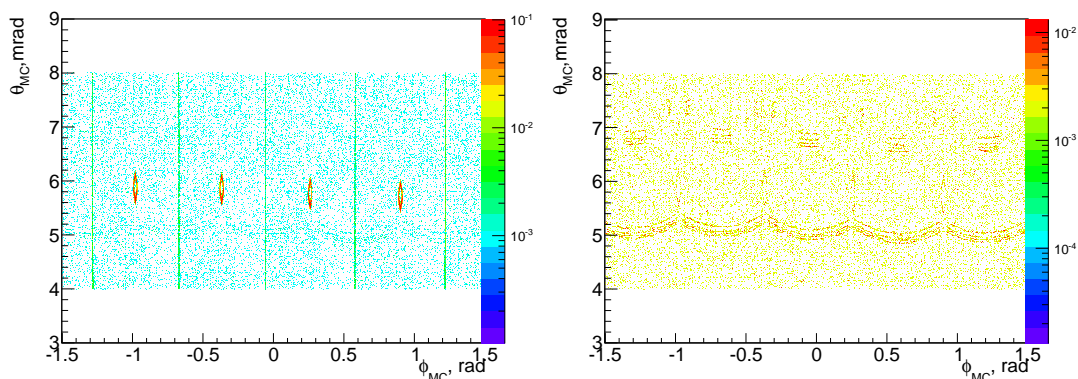


Figure 4.10: Generated  $\phi$  and  $\theta$  information of the missed tracks due to small number of hits (left) and due to track search (Cellular Automaton) losses (right): 5 trks/ev, 15 GeV/c. Both histograms are normalized to the number of events in the histogram

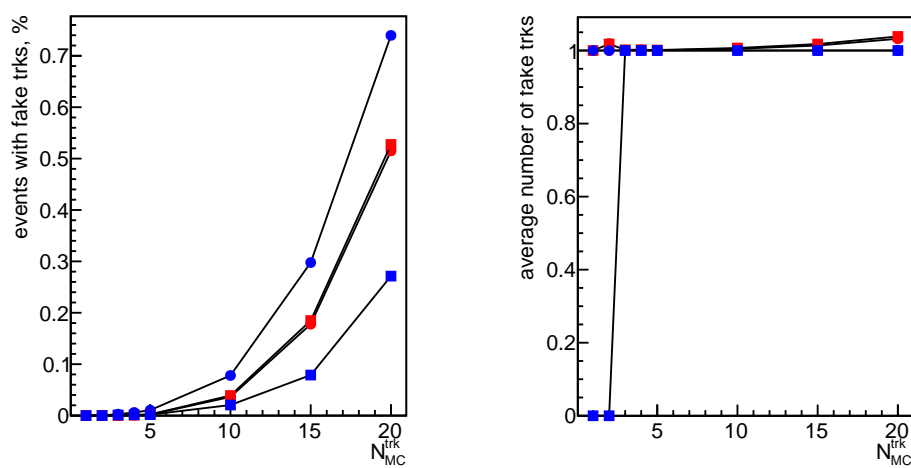


Figure 4.11: Average number of events with fake tracks (left) and average number of fake tracks per event with fake tracks (right) in dependence on the track multiplicity: red – Cellular Automaton, blue – Track Following; circles – hits mixture; squares – split tracks (momentum 1.5 GeV/c)

one module will be merged, for the track assignment if a track is reconstructed properly one has to go back to separated hits.

### Example 1: Split track

The most simple case for split tracks appearance is a double reconstruction of one track: as a 4 hit tracks and as a 3 hit track (Fig.4.13 (left)). Such a situation is prevented by the track filtering task, which compares tracks with at least 2 common hits and saves only the best of them in the list of reconstructed tracks <sup>4</sup>.

<sup>4</sup>in more detail Track Filter task is discussed in Section 4.5

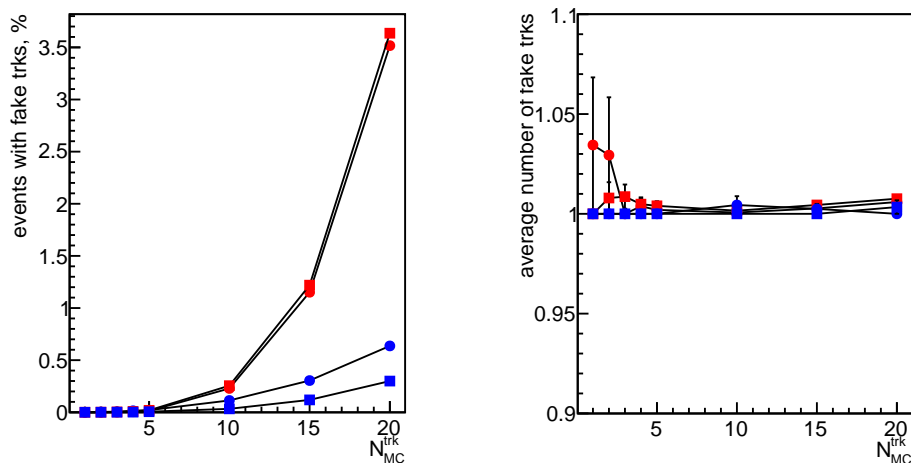


Figure 4.12: Average number of events with fake tracks (left) and average number of fake tracks per event with fake tracks (right) in dependence on the track multiplicity: red – Cellular Automaton, Blue – Track Following; circles – hits mixture; squares – split tracks (momentum 15 GeV/ $c$ )

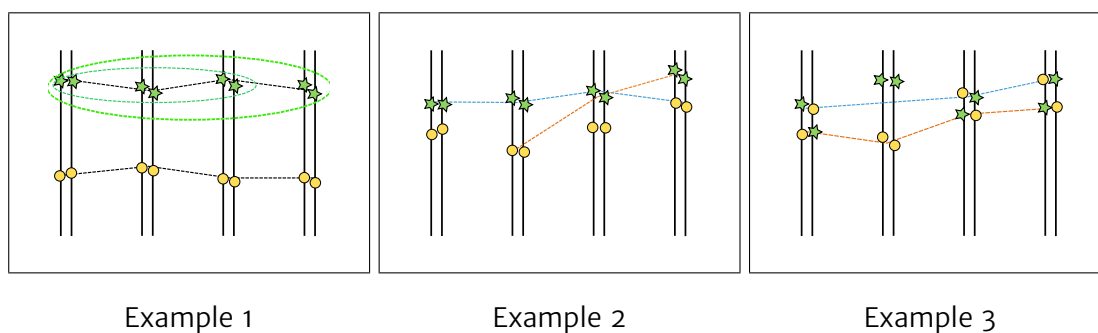


Figure 4.13: Possible reasons for split and ghost tracks

### Example 2: Split track

It also can happen that two tracks are close to each other and each of the reconstructed tracks contains points from different simulated tracks. In Fig.4.13 (center) there are two reconstructed tracks and the majority of the hits for both tracks belongs to the same simulated track. Such a situation cannot be resolved by the track filter since both reconstructed tracks contain only one commonly merged hit. Within ranking of those reconstructed tracks into the categories, one of the tracks will be marked as a good and another one as a split track.

### Example 3: Ghost tracks

Fig.4.13 (right) shows the situation when both simulated tracks were scattered during the propagation through the detector planes. After the track finding step, one track

was found as a mixture of hits on 3 layers (blue dashed line). And another one was not reconstructed perfectly, because it does not contain the required 65 % of hits from one simulated track (orange dashed line). So they both would be marked as ghost tracks and the corresponding simulated tracks would be marked as missed tracks. The track filtering step can only delete those tracks if they are not passing the cuts on track angles. But the most probably, both tracks will pass the cuts, because their directions are quite close to the expected one.

The angular distribution of fake tracks is presented in Fig. 4.14 (left) for split tracks and in Fig. 4.14 (right) for ghost tracks. Plotted values are the reconstructed values after the track fit. Split tracks are distributed rather uniformly in the region of the LMD acceptance, which is not surprising, because these tracks just duplicate real tracks. Some of the ghost tracks appear as tracks with reconstructed angles below and above the LMD acceptance. Such tracks can be suppressed for sure even by simple rectangular cuts. Track filtering (as presented in Section 4.5) suppresses the number of events with fake tracks from 0.7 % (Fig. 4.11) down to 0.03 % at 1.5 GeV/ $c$  and from 3.5 % down to 0.02 % at 15 GeV/ $c$  and increase number of events with missed tracks only by  $\sim 0.1$  %.

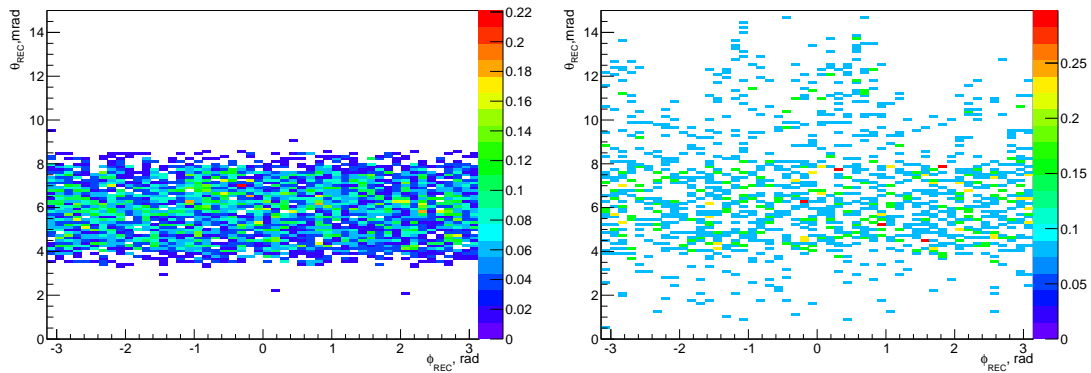


Figure 4.14: The  $\phi$  and  $\theta$  distributions of the split tracks (left) and ghost tracks (right) for track search with Cellular Automaton in simulation with 20 trks/ev. Both histograms are normalized to the number of events in the histogram.

## 4.4 Track fit

The parameters of a track-candidate after the track search are defined as a line segment between the first two points of the track. To obtain a more accurate description of the parameters, a fit based on all measured hits is performed. Since tracks in the luminosity detector are almost straight lines, the track model in the track fit procedure should be relatively simple and contain only 4 parameters<sup>5</sup>. But our task is not a pure geometrical one and trajectories cannot always be described by a simple straight line. For a particle with low momentum, energy loss and multiple scattering have to be treated rigorously. Due to the design of the luminosity detector, the energy loss is not an issue and the main task for a track fit algorithm is to take into account the multiple scattering effects. To meet this requirement, the least squares estimation with breaking lines technique [70] was developed based on the Minuit [71] minimizer from the ROOT framework.

### 4.4.1 Straight line fit with weighted hits

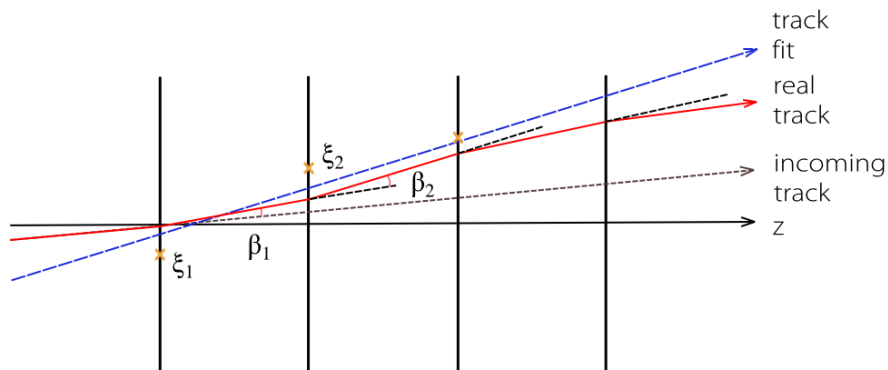


Figure 4.15: A particle scattered on measurement planes (red line is the path of the particle, dashed blue line is the track fit result), adapted from [72]

A particle with momentum  $p$  is entering nearly perpendicular to a set of parallel measuring planes (Fig. 4.15, [72]). Those planes will change the particle direction by multiple scattering in addition to measuring the crossing point of the track. The measured track position  $\xi_i$  in a plane will be given by the crossing point of the real (kinked) track altered by the measuring error  $\Delta x_i$  at each plane:

$$\xi_i = \sum_{J=i}^N \beta_J \cdot (z_i - Z_J) \cdot \Theta(z_i - Z_J) + \Delta x_i \quad (4.5)$$

In the following, lower case letters are used for measuring planes and upper case letters

<sup>5</sup>2 lines in 2D projections of 3D straight track

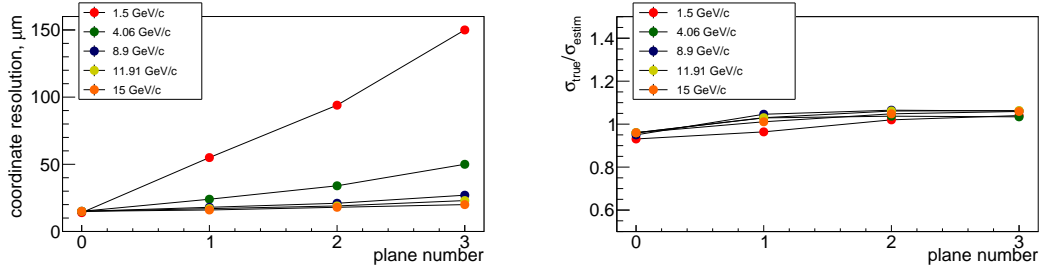


Figure 4.16: Hit resolution versus sensor plane position for tracks with different antiproton momenta (left); Ratio between estimated hit coordinate uncertainty and hit coordinate resolution (right)

for scattering planes. For this application, scattering and measuring planes are the same, but with keeping this level of generality, one can easily take into account any additional material in between.  $\beta_J$  is the kink angle in the scattering plane  $J$  placed at position  $Z_J$ . The stepping function is introduced to restrict to forward directions.

$$\Theta(z) = \begin{cases} 1 & \text{if } z \geq 0 \\ 0 & \text{if } z < 0 \end{cases} \quad (4.6)$$

The fitting function for  $n$  track crossing points  $\xi_j$  is a straight line:

$$x = a + bz \quad (4.7)$$

where  $a$  is the offset and  $b$  the slope of the track. The minimization is done by

$$\chi^2 = \chi^2(a, b) = \sum_{l=1}^n w_l (\xi_l - a - bz_l)^2 \quad (4.8)$$

with respect to the parameters  $a$  and  $b$ , where  $w_l$  is representing the weights given to the measured points (normally  $1/\sigma_x^2$ ). During hit reconstruction,  $\sigma_x$  is assumed to be equal on different planes, since it depends only on sensor parameters like the pixel size. For the treatment of multiple scattering, one can try to make the hit errors depending on the plane position by adding an expected uncertainty from multiple scattering. Then in weight  $w_l$  instead of  $\sigma_{x_{digi}}^2$  goes

$$\sigma_x^2 = \sigma_{x_{digi}}^2 + \sigma_{x_{MS}}^2 \quad (4.9)$$

where  $\sigma_{digi}$  corresponds to the uncertainty due to the digitization and  $\sigma_{MS}$  comes from the multiple scattering effect in the sensor material. Obviously, in this case  $w_l$  will be different for hits on different planes, therefore this method is called *weighted hits*. The momentum dependence of the hit resolution  $\sigma_x^j$  on plane  $j$  is taken into account by

the multiple scattering effect estimation:

$$(\sigma_{MS}^j)^2 = \sum_{i=0}^{i=j} ((i+1) \cdot d_i \cdot \theta_{MS})^2 \quad (4.10)$$

where  $d_i$  is the distance between  $i$  and  $(i-1)$  planes and  $\theta_{MS}$  is calculated according to Eq. 4.4. The coordinate resolution at different planes for tracks with different momenta is shown in Fig 4.16(left), where it is clear that multiple scattering gives a significant contribution to the hit resolution for tracks with momenta less than 8.9 GeV/c. The approximation Eq. 4.9 reproduces the actual hit resolution within 5% (right panel of Fig 4.16). But it is impossible to take into account the correlation between the measured points by corrections of weights. As it will be shown later, this has a direct influence on the results.

#### 4.4.2 Track fit with broken lines approach

A more natural approximation of a particle trajectory is a line segment with kink angles between planes:

$$x_l = a + bz + \sum_{J=1}^N \alpha_J \cdot (z_l - Z_J) \cdot \Theta(z_l - Z_J) \quad (4.11)$$

where  $a$  and  $b$  are the offset position and the slope of an incoming track,  $\alpha_J$  is the kink in the scattering plane  $J$  and  $\Theta(z_l - Z_J)$  provides a restriction to upstream kinks only. This method is called *broken lines*[72]. The  $\chi^2$  has the form:

$$\chi^2 = \chi^2(a, b, \alpha_1, \dots, \alpha_N) = \sum_{l=1}^n \frac{(\xi_l - x_l)^2}{\sigma_{x_l}^2} + \sum_{J=1}^N \frac{(\beta_J - \alpha_J)^2}{\sigma_{s_J}^2} \quad (4.12)$$

where  $\sigma_{x_l}$  is the error of the measurement at plane  $l$  and  $\sigma_{s_J}$  is the uncertainty of the scattering angle  $\beta_J$  in scattering plane  $J$  (dependent on the momentum of the particle). The number of degrees of freedom of the fit does not change by introducing the kinks in the fit since each additional parameter is compensated by the corresponding zero "measurement" of this angle. The interested reader can find the complete development of matrix equations corresponding to  $\chi^2$  and the covariance matrix calculation in [72] and papers cited there. The Minuit package requires only the function for  $\chi^2$  and corresponding matrices are calculated automatically.

The LMD planes are arranged in parallel to each other at an axis  $z'$  which is slightly displaced with respect to the global  $z$ -axis. Therefore the  $z$  coordinate depends on the  $(x, y)$  coordinates. The dependence is introduced by replacing the  $z_l$  coordinate in

Eq. 4.11 and Eq. 4.12 by  $t$ :

$$t = b(x - a) + d(y - c) + g(z - z_0) \quad (4.13)$$

The trajectory in 3 dimensions (3D line) is described by the parameters  $a, b, c, d, g$  and  $z_0$ :

$$x_l = a + bt + \sum_{J=1}^4 \alpha_J^x \cdot ((z_0 + t) - Z_J) \cdot \Theta((z_0 + t) - Z_J), \quad (4.14)$$

$$y_l = c + dt + \sum_{J=1}^4 \alpha_J^y \cdot ((z_0 + t) - Z_J) \cdot \Theta((z_0 + t) - Z_J), \quad (4.15)$$

$$z_l = z_0 + gt \quad (4.16)$$

where  $a, b, c, d, \alpha_J^x, \alpha_J^y$  are parameters from the fit,  $z_0$  is a  $z$ -coordinate of the first hit (which is fixed) and  $g$  is calculated from the normalization of the direction vector of the track to the length equal to 1:

$$g = \sqrt{1 - b^2 - d^2} \quad (4.17)$$

Finally,  $\chi^2$  has the form:

$$\chi^2 = \sum_{l=1}^4 \left( \frac{(\xi_l^x - x_l)^2}{\sigma_x^2} + \frac{(\xi_l^y - y_l)^2}{\sigma_y^2} \right) + \sum_{J=1}^4 \frac{(\alpha_J^x)^2 + (\alpha_J^y)^2}{\sigma_s^2} \quad (4.18)$$

where  $\sigma_s$  is the uncertainty of the multiple scattering angle (Eq. 4.10).

In principle, one can use the breaking angles to improve the track slopes description. But the tests have shown that this leads to only a small improvement. However, they are needed to improve the precision of the track slopes during the fit. Fig. 4.17 shows the breaking angles after the fitting procedure on the second (left) and third (right) planes for the simulation study with  $P_{beam} = 1.5 \text{ GeV}/c$ . The average value of the breaking angles is close to zero and the resolution ( $\sim 380 \mu\text{rad}$  on the second plane and  $\sim 350 \mu\text{rad}$  on the third) is close to the expected  $370 \mu\text{rad}$  from the multiple scattering, which gives evidence that the track fit procedure is working properly.

### 4.4.3 Results and comparison of track fit approaches

The implementation of the least square estimator was checked in simulation studies with the BOX generator, where one track per event in the  $\theta$  range between 4 to 8 mrad and full  $\phi$  angles coverage was generated. To make sure that the multiple scattering effect is estimated correctly, the momentum of the simulated antiprotons was chosen

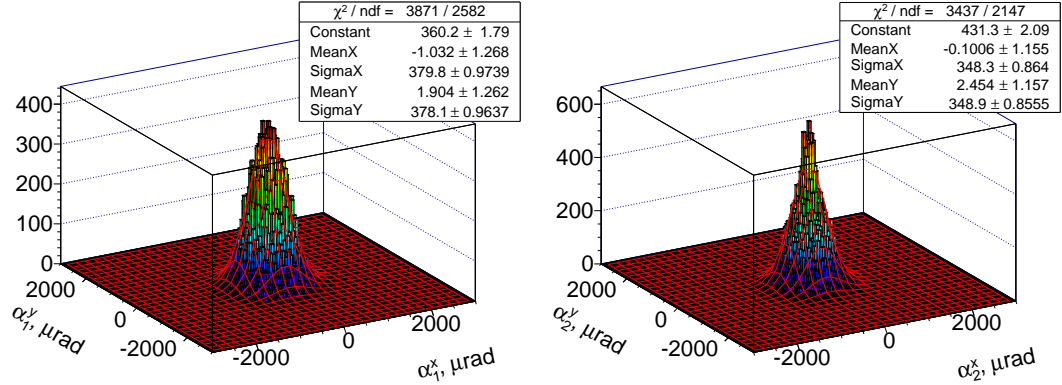


Figure 4.17: Breaking angles  $\alpha^x$  and  $\alpha^y$  on the second (left) and the third (right) plane obtained from the track fit algorithm, simulated antiprotons with 1.5 GeV/c momentum

to be 1.5, 4.06, 8.9, 11.91 and 15 GeV/c. Both methods, the straight line fit with weighted hits as well as the broken lines method, were tested.

In Table 4.2 both methods are compared in terms of resolution of the tracks starting point and the momentum vector (direction coordinates multiplied by expected momentum magnitude). As one can see from this table, the resolution for the particle direction parameters at low energies is better for tracks described by the broken lines approximation.

The difference between these two approaches is more visible in the pull distributions. The pull for a parameter  $X$  is defined as the difference between the reconstructed value of the parameter ( $X_{FIT}$ ) and the generated value ( $X_{MC}$ ) divided by the error of the reconstructed value ( $\sigma_{X_{FIT}}$ ):

$$Pull_X = (X_{FIT} - X_{MC}) / \sigma_{X_{FIT}} \quad (4.19)$$

If the parameter and its error are estimated correctly, the pull distribution can be described by a Gauss function with the mean value at 0 and the standard deviation (sigma) value equal to 1. The pull distributions of the track starting point and the momentum vector coordinates are presented in Fig. 4.18 for antiprotons with a momentum of 1.5 GeV/c. The parameter error estimation is working better for the track fit with broken lines, which has pull widths always close to 1. Therefore, it was decided to use the track fit with broken lines approach as the standard method during the track reconstruction in the LMD.

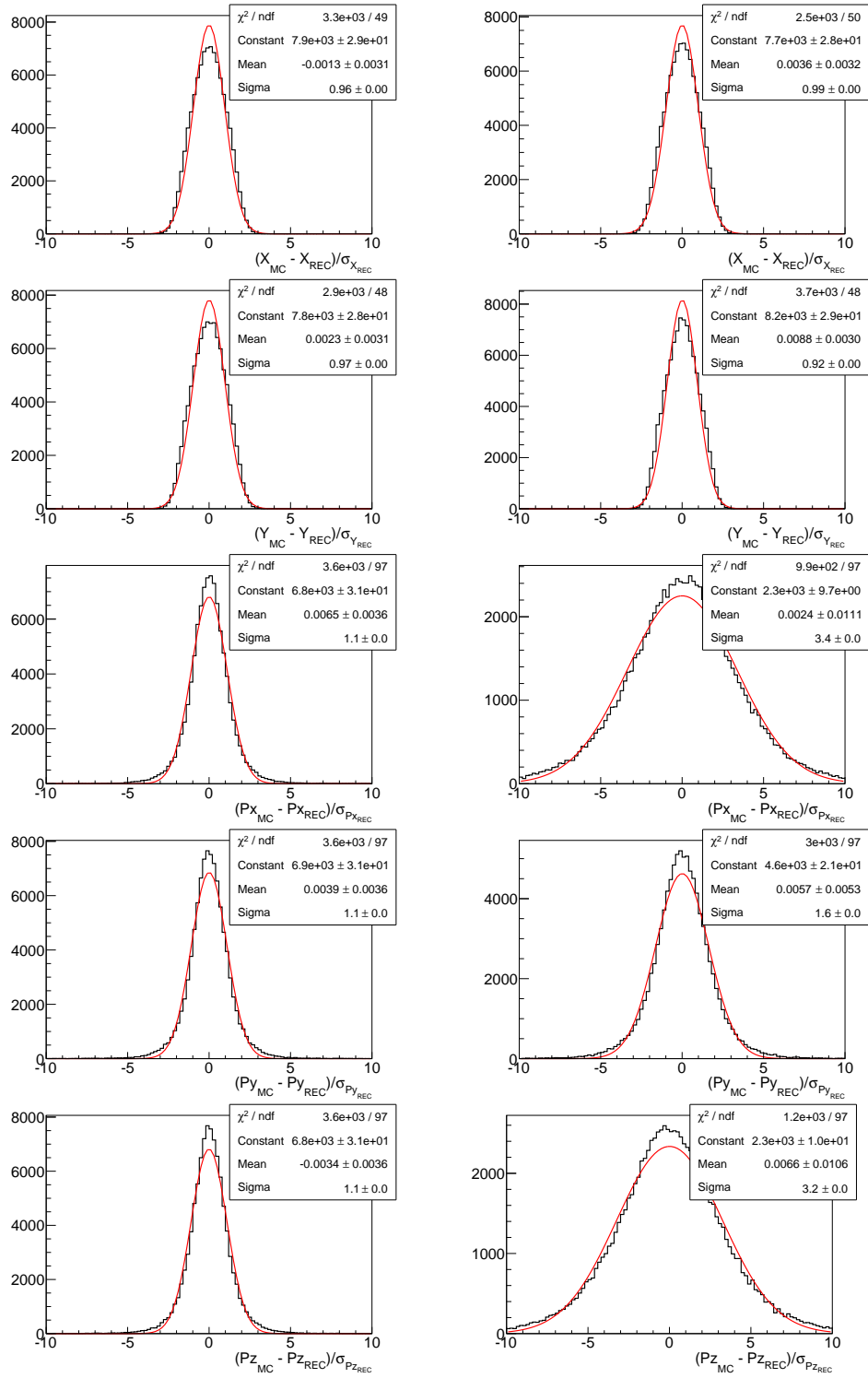


Figure 4.18: Pull distributions after fit with broken lines (left) and weighted hits (right) approaches, antiprotons with 1.5 GeV/c momentum

Beam Momentum	Track Parameter	weighted hits	broken lines
1.5 GeV/ $c$	$X_{start}$ , $\mu\text{m}$	$14.12 \pm 0.02$	$14.03 \pm 0.02$
	$Y_{start}$ , $\mu\text{m}$	$13.90 \pm 0.02$	$14.04 \pm 0.02$
	$P_x$ , keV	$515 \pm 2$	$444 \pm 2$
	$P_y$ , keV	$472 \pm 2$	$443 \pm 2$
	$P_z$ , keV	$21 \pm 0.06$	$18 \pm 0.1$
	$\theta$ , $\mu\text{rad}$	$341 \pm 1$	$293 \pm 1$
	$\phi$ , mrad	$6.63 \pm 0.04$	$6.21 \pm 0.03$
15 GeV/ $c$	$X_{start}$ , $\mu\text{m}$	$13.86 \pm 0.02$	$13.89 \pm 0.03$
	$Y_{start}$ , $\mu\text{m}$	$13.86 \pm 0.03$	$13.89 \pm 0.03$
	$P_x$ , keV	$946 \pm 2$	$945 \pm 2$
	$P_y$ , keV	$948 \pm 2$	$946 \pm 2$
	$P_z$ , keV	$38.2 \pm 0.1$	$38.1 \pm 0.1$
	$\theta$ , $\mu\text{rad}$	$63.1 \pm 0.2$	$63.1 \pm 0.2$
	$\phi$ , mrad	$1.58 \pm 0.01$	$1.58 \pm 0.01$

Table 4.2: Resolutions and their uncertainties of the track parameters for the two track fit methods

## 4.5 Track filter

### 4.5.1 Filtering of split tracks

Due to the "missing plane" track search extension, hits already connected with one track can also be used for the reconstruction of another one, e.g. in split tracks with 4 hits and with 3 hits. To overcome this issue, a special Track Filter procedure was implemented. The initial step of this procedure is to clean a sample of reconstructed tracks from split tracks. The basic logic is the following:

- Do the tracks have at least 2 common hits?
  - no: save both
  - yes: Do the tracks contain different number of hits?
    - \* yes: Save the one with the largest number of points
    - \* no: Save the one with the smallest  $\chi^2$

This step cleans the sample of reconstructed tracks without taking away good reconstructed tracks.

### 4.5.2 Filtering of background tracks

Although the luminosity detector is placed in the magnetic field free region, scattered antiprotons pass the solenoid and the dipole magnetic field before they reach the LMD. For a charged particle trajectory, this leads to certain equations of motion, which causes certain relations between the track parameters. Below, two ways are discussed of its usage for suppression of the background tracks, which have different kinematic signatures.

#### Box cut (correlation between $\hat{\phi}$ and $\hat{\theta}$ )

Since the LMD has a certain geometrical acceptance, one can use the limits of the measurement of the polar angle range as a selection criteria (cut) for the reconstructed tracks. This is done in the local coordinate system, which is determined as described below. Two hits on parallel modules have the coordinates  $(x_0, y_0, z_0)$  and  $(x_1, y_1, z_1)$ . The direction vector between these two hits has the components:

$$\vec{d} = (x_1 - x_0, y_1 - y_0, z_1 - z_0) \quad (4.20)$$

Based on the direction vector, the azimuth and polar angles are defined as:

$$\text{tg} \hat{\phi} = \frac{d_y}{d_x}, \text{tg} \hat{\theta} = \frac{\sqrt{d_x^2 + d_y^2}}{d_z} \quad (4.21)$$

Fig. 4.19 shows that  $\hat{\phi}$  and  $\hat{\theta}$ <sup>6</sup> have a certain range, defined in this space by two circles.

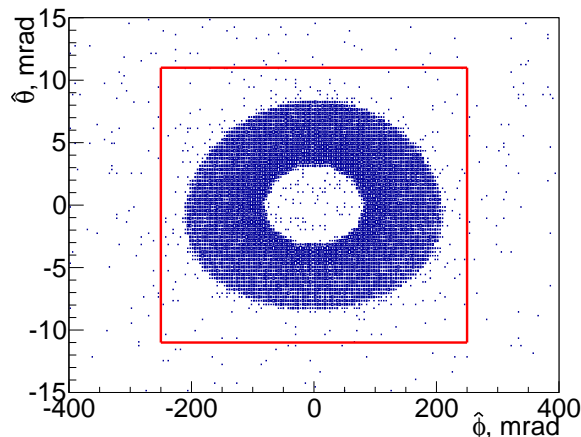


Figure 4.19:  $\hat{\theta}$  versus  $\hat{\phi}$  of the reconstructed tracks (the beam momentum 15 GeV/c), cut range shown as a red box

<sup>6</sup>From  $\hat{\theta}$  is subtracted the shift of 40 mrad, which correspond to a track bending during propagation in the

For simplicity, a rectangular area was chosen as a cut in this  $\hat{\theta}$ - $\hat{\phi}$  space:

$$|\hat{\phi}| \leq 250 \text{ mrad}; |\hat{\theta}| \leq 11 \text{ mrad} \quad (4.22)$$

	Before	After	
$P_{beam}$	$N_{rec}/N_{prim}$	$N_{rec}^{left}/N_{prim}$	$N_{second}^{left}/N_{prim}$
15	$103.04 \pm 0.07$	$100.20 \pm 0.07$	$0.62 \pm 0.03$
11.91	$102.16 \pm 0.06$	$99.97 \pm 0.06$	$0.43 \pm 0.03$
8.9	$101.46 \pm 0.05$	$99.77 \pm 0.05$	$0.25 \pm 0.02$
4.06	$100.68 \pm 0.03$	$99.37 \pm 0.04$	$0.09 \pm 0.02$
1.5	$100.77 \pm 0.03$	$99.04 \pm 0.05$	$0.08 \pm 0.02$

Table 4.3: Suppression of tracks from primary and secondary particles after applying the box cut (Eq. 4.22)  $N_{rec}$  – total number of reconstructed tracks (from secondary and primary particles),  $N_{prim}$  – number of reconstructed primary  $\bar{p}$  tracks,  $N_{second}$  – number of reconstructed secondaries,  $N_i^{left}$ : number of tracks left after the box cut

A check for the background suppression and the signal efficiency reduction introduced by this selection criteria was done in simulation studies with the BOX generator, where tracks were generated uniformly with a  $\theta$  value between 2 and 11 mrad and  $\phi$  in full coverage. Tracks which are not generated at the IP are so-called secondary particles. As it will be shown in Chapter 6, secondary particles which hit the LMD are mostly produced inside the box of the LMD. Therefore, they must have a different direction than elastically scattered  $\bar{p}$ . The results of the cut are shown in Tab. 4.3. Almost all reconstructed tracks of primary particles are kept after  $\hat{\theta}$  and  $\hat{\phi}$  cut and the amount of secondary tracks is significantly reduced, e.g. for tracks with momentum 15 GeV/c, the number of secondary particles is reduced from  $\sim 3\%$  to 0.6%.

### X&Y cut (correlation between angles and coordinates of the track)

This cut uses the relations between different track parameters, in particular between angles and coordinates of a track. The correlation between the x-coordinate  $X$  of the starting point of the track at the LMD and the polar angle  $\hat{\theta}$  is shown on the left in Fig. 4.21. And the y-coordinate  $Y$  and azimuthal angle  $\hat{\phi}$  correlation is shown on the right in Fig. 4.21. The most simple parameterization of these correlations is a linear function. A signal track should satisfy the following conditions:

$$\begin{aligned} |X_{REC} - (a + b \cdot \hat{\theta}_{REC})| &< 3 \cdot \Delta_x, \\ |Y_{REC} - (c + d \cdot \hat{\phi}_{REC})| &< 3 \cdot \Delta_y \end{aligned} \quad (4.23)$$

where  $a, b$  ( $c, d$ ) are coefficients of a linear functions, which are determined by a fit of the mean value of the signal  $X-\theta$  ( $Y-\phi$ ) distribution as shown in Fig. 4.21(4.22). The variable  $\Delta_x$  ( $\Delta_y$ ) is the width of the same distribution.

It should be stressed that in the experiment much more signal events are expected than secondary particles or particles from any other physical background. Therefore, the relation between  $X$  and  $\hat{\theta}$  (or  $Y$  and  $\hat{\phi}$ ) can be parameterized on data from the experiment, including also a non-linear behavior, which could be caused by a non-homogeneous magnetic field.

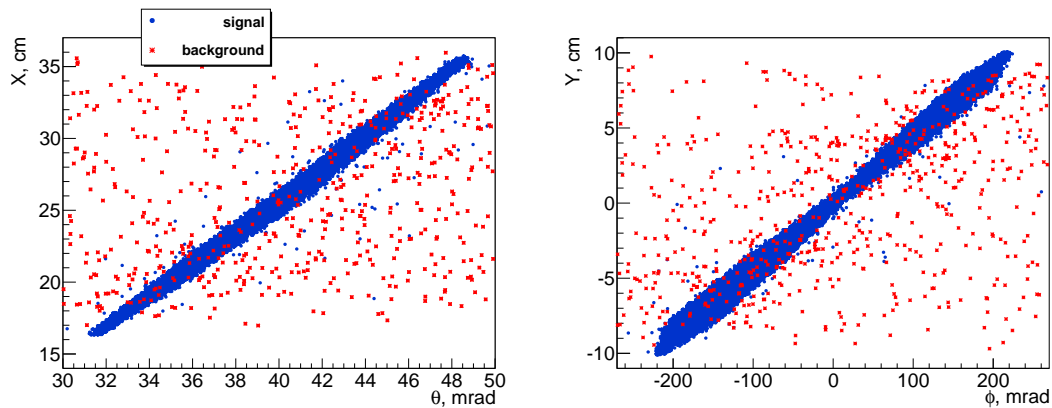


Figure 4.20: Correlations  $X(\theta)$  and  $Y(\phi)$  for signal and background tracks

A cross check of this cut was done using simulated data with tracks of different momenta produced with the BOX generator for  $\theta \in [2,12]$  mrad and  $\phi \in [0,2\pi]$  rad. In contrary to the standard simulation tools, the more realistic FTF\_BERT model in Geant4 was used. Compare to the default QGSP\_BERT\_EMV model it has a working range at low energies down to 4 GeV [73] and predicts a higher number of secondary particles in the LMD. The models are discussed in Chapter 6 in more detail.

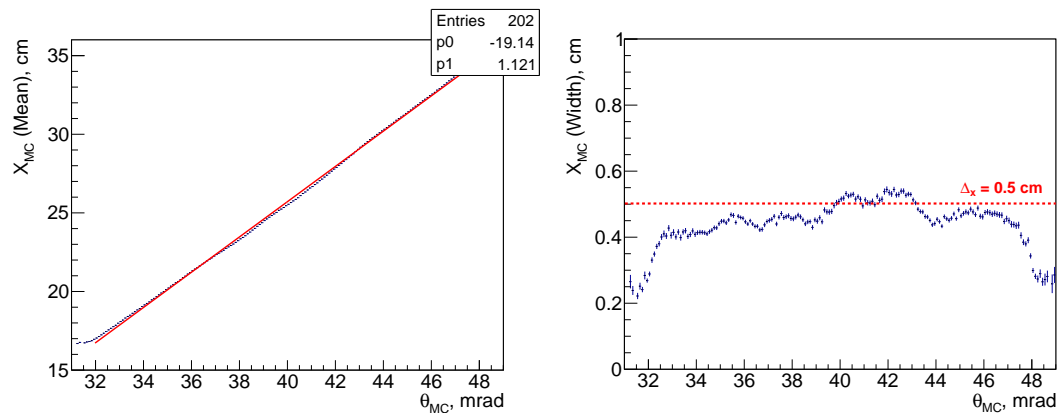


Figure 4.21: Parameterization of X cut on simulation studies with the BOX generator

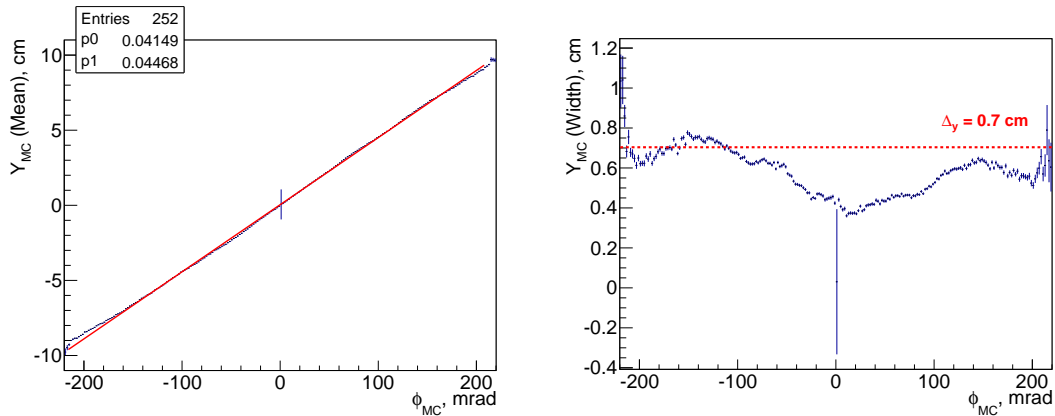


Figure 4.22: Parameterization of Y cut on simulation studies with the BOX generator

All  $\bar{\text{PANDA}}$  components were included to have all possible sources for secondary particles in order to get the number of secondary particles as realistic as possible. The ratio between the number of secondary particle tracks to the total number of simulated signal tracks before and after this cut and the comparison with the results of the box cut are shown in Fig. 4.23 in dependence on the momentum of the signal tracks. The X&Y cut suppresses the background tracks from secondary particles more efficiently and, depending on the momentum of the track, a suppression values between  $4 \times 10^{-4} \%$  to  $5 \times 10^{-3} \%$  can be achieved.

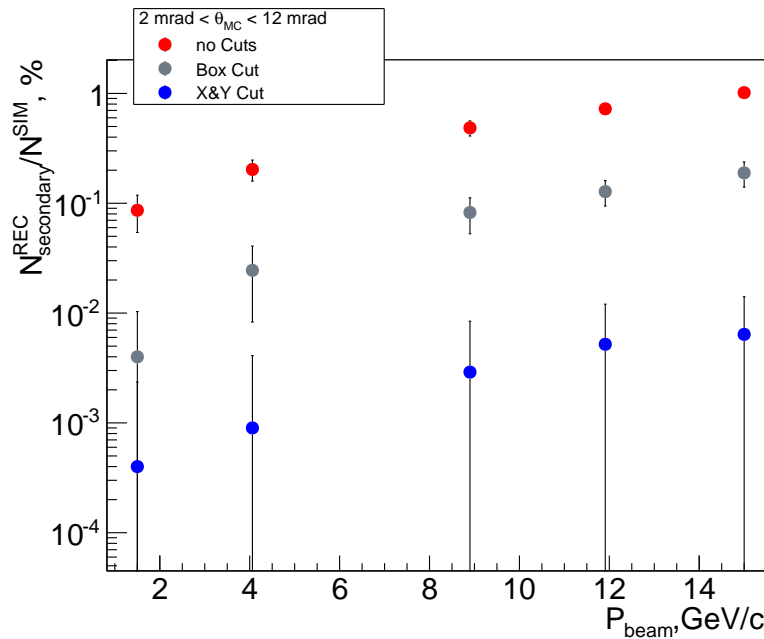


Figure 4.23: Comparison of the suppression of secondary tracks by X&Y (blue) and Box (gray) cuts obtained in simulation studies with the BOX generator

## 4.6 Back propagation to the Interaction Point

The extraction of the luminosity is done by comparing the measured angular distribution of the tracks with the theoretical model at the IP. This is necessary because the angular distribution of the elastically scattered antiprotons at the LMD is changed by the magnetic field, which the antiprotons have to pass on their way to the LMD (11 m behind the IP). Therefore, the tracks measured with the LMD have to be extrapolated back to the IP. The magnetic field in  $\bar{P}$ ANDA has quite complicated structure. The field strength for all three directions is shown in Fig. 4.24 in dependence on the distance from the IP along the beam line. The magnetic field is non-uniform, as it is visible e.g. in the solenoid region for the  $H_x$  and  $H_y$  components in Fig. 4.24. Therefore, an accurate method for particle propagation through the magnetic field is needed. Also only numerical methods can be used for this task. The GEANE package [74] and the Runge-Kutta method from the GenFit package [75] were tested with simulated data to find out the best suitable tool for this task and to allow cross checks between them.

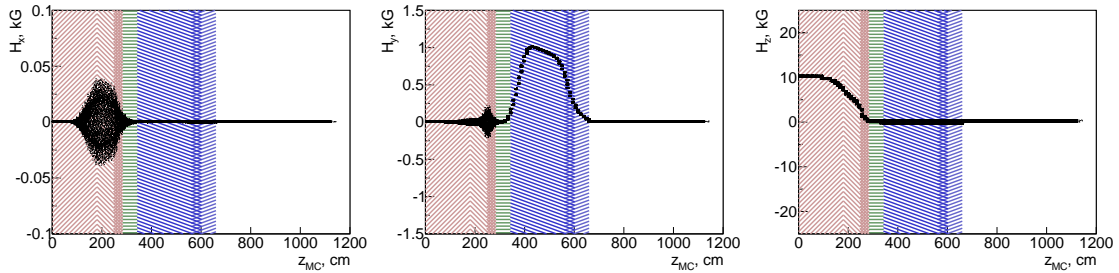


Figure 4.24: Magnetic field strength in x,y,z directions for antiprotons with momentum  $1.5 \text{ GeV}/c$ . Differently marked regions correspond to the regions of different magnetic field maps in the simulation package: red is a solenoid field, blue is a dipole field and green is a transition region

Fig. 4.25 schematically shows the trace of a propagated particle and the magnetic fields on its way. The back propagation is done in 7 steps, as it turned out that both tools cannot deal accurately enough with the instant change of the magnetic field between the different magnets. The introduced steps are shown in Fig. 4.25 by the dashed red lines.

### 4.6.1 Assumption about the momentum of the antiproton

The trajectory of a particle in the magnetic field depends on the momentum of the particle. After the track fit procedure, the starting point of a track near the LMD and the direction vector at the starting point are known. The momentum magnitude is not measured by the LMD, thus it is assumed to be equal to the momentum of the antiproton beam. However for scattered antiprotons it is not exactly true. The dependence of

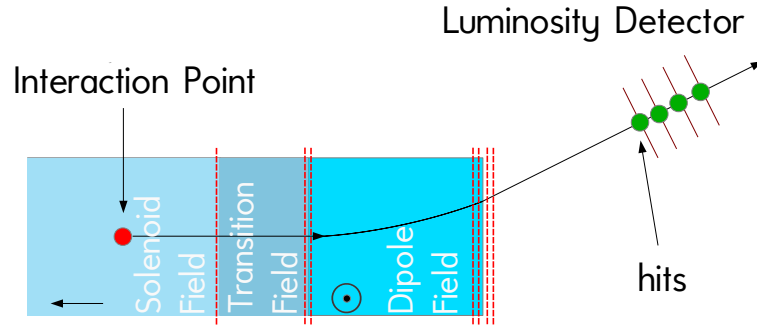


Figure 4.25: Track back propagation from the LMD to the IP through the different magnetic field regions (dashed red lines show virtual plane positions for internal propagation)

the difference between the momentum of the scattered antiproton and the beam momentum on the scattering angle  $\theta$  is shown in Fig. 4.26. As one can see the recoil momentum is very small, in the order of 100 keV/c at a beam momentum 1.5 GeV/c and 10 MeV/c at 15 GeV/c.

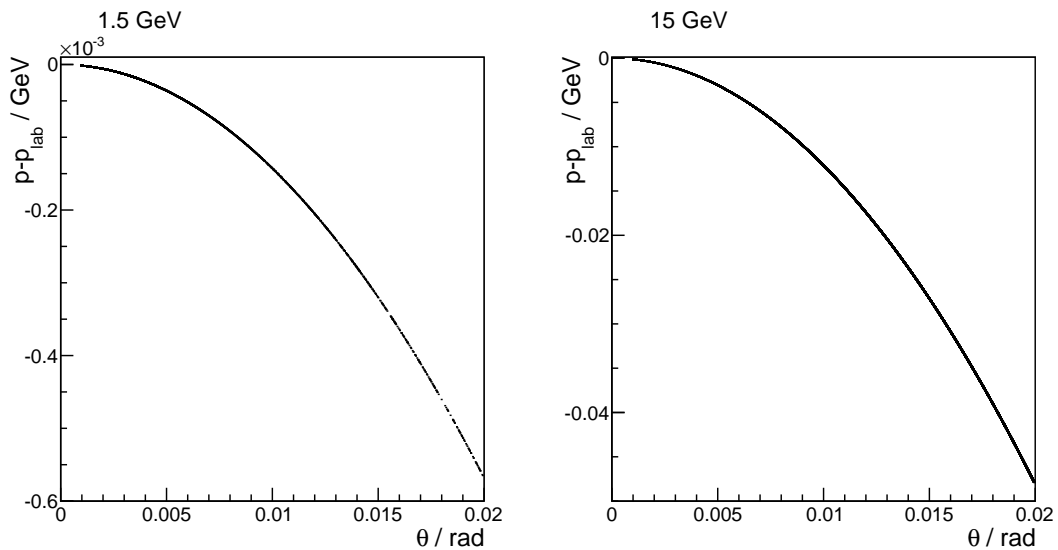


Figure 4.26: Difference between the momentum of the scattered antiproton and the beam momentum versus the scattering angle  $\theta$  ([76])

The assumption that the momentum of the scattered antiproton is equal to the beam momentum could influence the precision of final values of the propagated track parameters. In the first group of tests with simulated data, antiprotons with fixed momentum  $P_{beam}$  were generated, but for back propagation the momentum of the antiprotons was assumed to be  $P_{\bar{p}} = P_{beam} + \Delta P$ , there  $\Delta P$  was varied in a large range

between  $10^{-8}$  to  $1 \text{ GeV}/c$ . The results of this study are shown in Fig. 4.27 in terms of the deviation of the mean values of the reconstructed polar angles  $\theta$  and its resolution. It should be mentioned, that tracks in the LMD are reconstructed with some uncertainty, therefore the resolution after back propagation is getting worse. This test indicates that as soon as the assumption deviates from the real momentum by less than  $10 \text{ MeV}/c$ , no difference in both variables is visible anymore. The final precision is dominated by the reconstruction precision in the LMD.

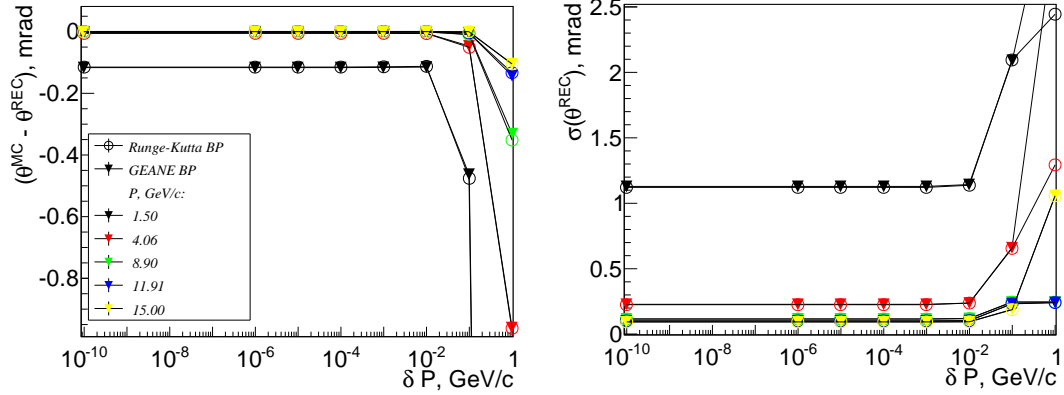


Figure 4.27: Influence of the antiproton momentum assumption on the  $\theta$  angle reconstruction: the systematic deviation (left) and the resolution (right)

In a second group of tests, which were performed with GEANE only, antiprotons were generated with  $P_{\bar{p}} = P_{beam} + \Delta P$ , but for the reconstruction (track fit and back propagation), the assumption  $P_{\bar{p}} = P_{beam}$  was used. This test emulates more precisely the real situation. Fig. 4.28 shows the ratio between the acceptance for the simulated data with the momentum deviation and the simulated data, where the momentum deviation was set to zero value. In case of the beam momentum  $1.5 \text{ GeV}/c$ , the difference is rather small and appears only on the edges of the detector, which can be explained by the limited statistic of such kind of tracks. Due to higher reconstruction resolution for tracks in simulation studies with beam momentum  $15 \text{ GeV}/c$ , the difference is also visible at the holes between sensors.

The accuracy of the reconstruction is illustrated by the relative precision of the scattering angle  $\theta$ , shown in Fig. 4.29 and Fig. 4.30. For these plots, the relative difference between the reconstructed and generated values is divided by the  $\theta$  resolution in the ideal case  $\sigma\theta_{ideal}$  was fitted by a Gaussian distribution. The mean value shows a sinusoidal shape in dependence on the  $\phi$  with a decreasing amplitude if the difference between the generated and the assumed momentum gets smaller. The maximum deviation is  $0.4\sigma\theta_{ideal}$  ( $\sim 280 \mu\text{rad}$ ) at  $1.5 \text{ GeV}/c$  for  $\Delta P = 10 \text{ MeV}/c$  and  $3.5\sigma\theta_{ideal}$  ( $\sim 320 \mu\text{rad}$ ) at  $15 \text{ GeV}/c$  for  $\Delta P = 100 \text{ MeV}/c$ . The relative difference of the  $\theta$  resolution between the generated and the assumed momentum (Fig. 4.29 and Fig. 4.30 right)

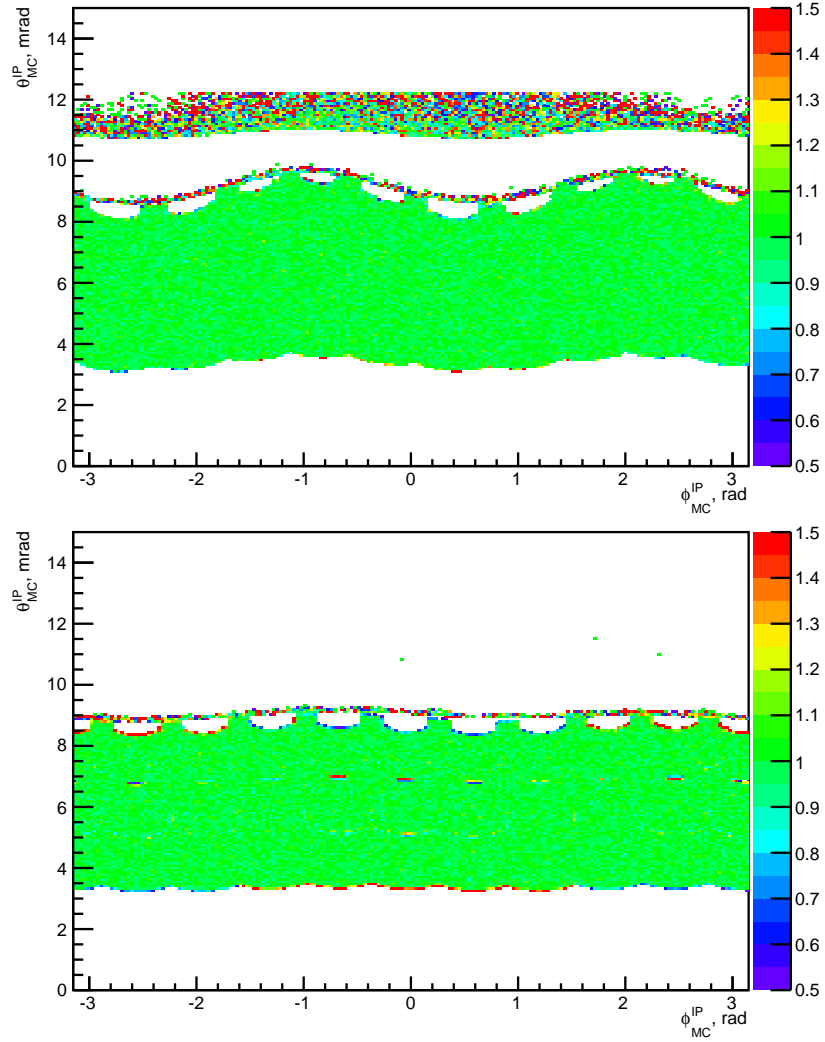


Figure 4.28: Influence of the antiproton momentum assumption on the acceptance of the LMD for maximum momentum deviation: 100 keV at  $P_{beam}=1.5\text{ GeV}/c$  (top) and 10 MeV at  $P_{beam}=15\text{ GeV}/c$  (bottom). The ratio between the simulated case and ideal acceptance is shown

does not show any significant difference between the momentum assumptions. Therefore the  $\theta$  resolution is not sensitive to any momentum deviation for both 1.5 GeV/c as well as 15 GeV/c momenta. Moreover, a difference in the momentum assumption to the real value in the order of 10 MeV/c at 1.5 GeV/c or 100 MeV/c at 15 GeV/c introduces a systematic shift during the  $\theta$  angle reconstruction only for large scattering angles ( $\theta \geq 8\text{ mrad}$ ). Sensitivity of the luminosity extraction to this shift is currently under investigation. In general, using the beam momentum as the track momentum assumption gives good results and is used for the back propagation.

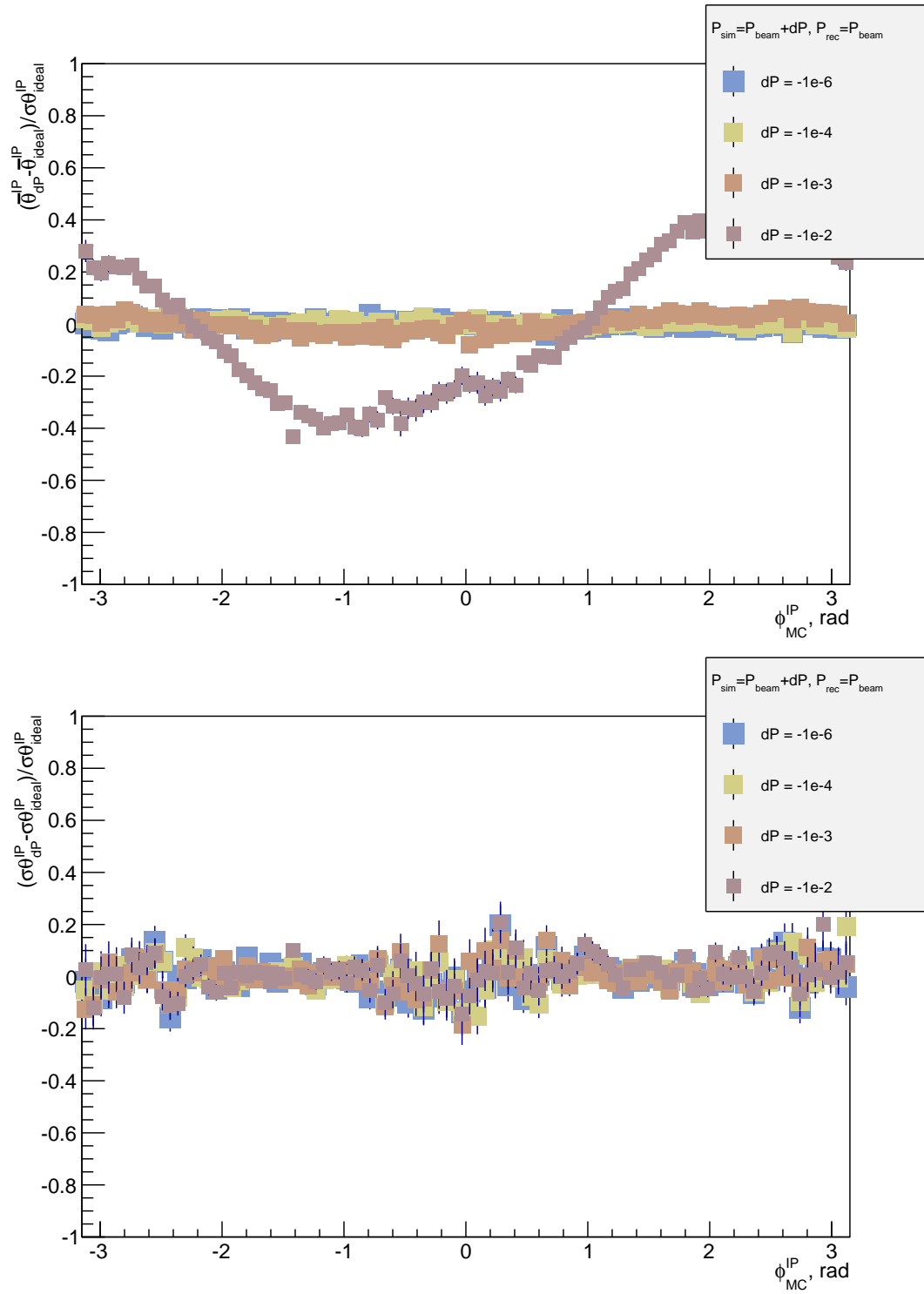


Figure 4.29: Influence of antiproton momentum assumption on reconstruction of mean value (top) and resolution (bottom) of  $\theta$  angle ( $P_{beam} 1.5 \text{ GeV}/c$ )

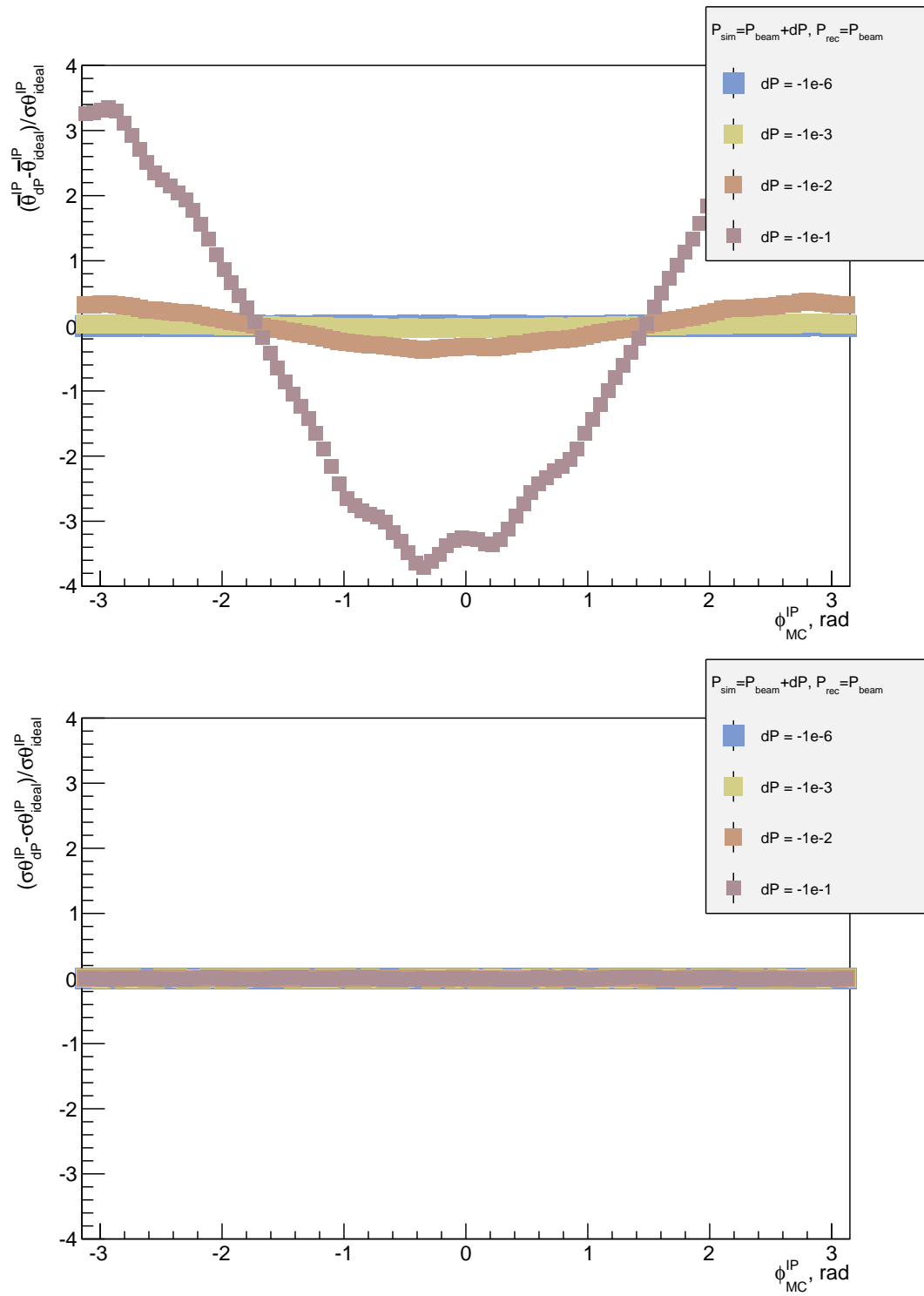


Figure 4.30: Influence of antiproton momentum assumption on reconstruction of mean value (top) and resolution (bottom) of  $\theta$  angle ( $P_{beam} 15 \text{ GeV}/c$ )

### 4.6.2 Propagation of track parameters

Charged particle tracing through a magnetic field is a typical problem in high-energy physics. The analytic formula, which expands the extrapolated track parameters in a power series of the magnetic field components, is derived in [77] and discussed in Appendix D. This formula is based on the Runge-Kutta method, which is widely used in software packages for particle propagation in a magnetic field. For example in GEANT a fourth-order <sup>7</sup> Runge-Kutta extrapolation is used to transport particles through the detector volume. Since the GEANE package is based on GEANT3, the Runge-Kutta extrapolation is used there too. Moreover, for the propagation of tracks in magnetic field in GenFit the Runge-Kutta method is also implemented.

Although, from the mathematical point of view, the GEANE and Runge-Kutta method from the GenFit are identical, they use different approximations and therefore give different results. Each back propagator was studied with simulated data. Track parameters after the reconstruction were compared with the generated values. As for the check of track fitting, the difference between the generated and the reconstructed parameters and the pull distributions are used to control the performance of the back propagation. The difference between the generated and reconstructed values is described by a Gaussian distribution, for which the mean value is expected to be close to 0 (this means the estimation of the parameters is not biased) and the standard deviation of the Gaussian distribution corresponds to the resolution of this parameter. Those are presented in Fig. 4.31. The parameter resolutions are also presented in Tab. 4.4. In terms of resolutions, both tools give equal results. Also they both introduce some systematic shifts for the reconstructed track parameters, but have a different behavior of systematic shifts for different momenta of the scattered antiproton. Therefore, it is difficult to judge which back propagation tool is better in general.

---

<sup>7</sup>Fourth-order means that the precision depends on the step size to the fifth power

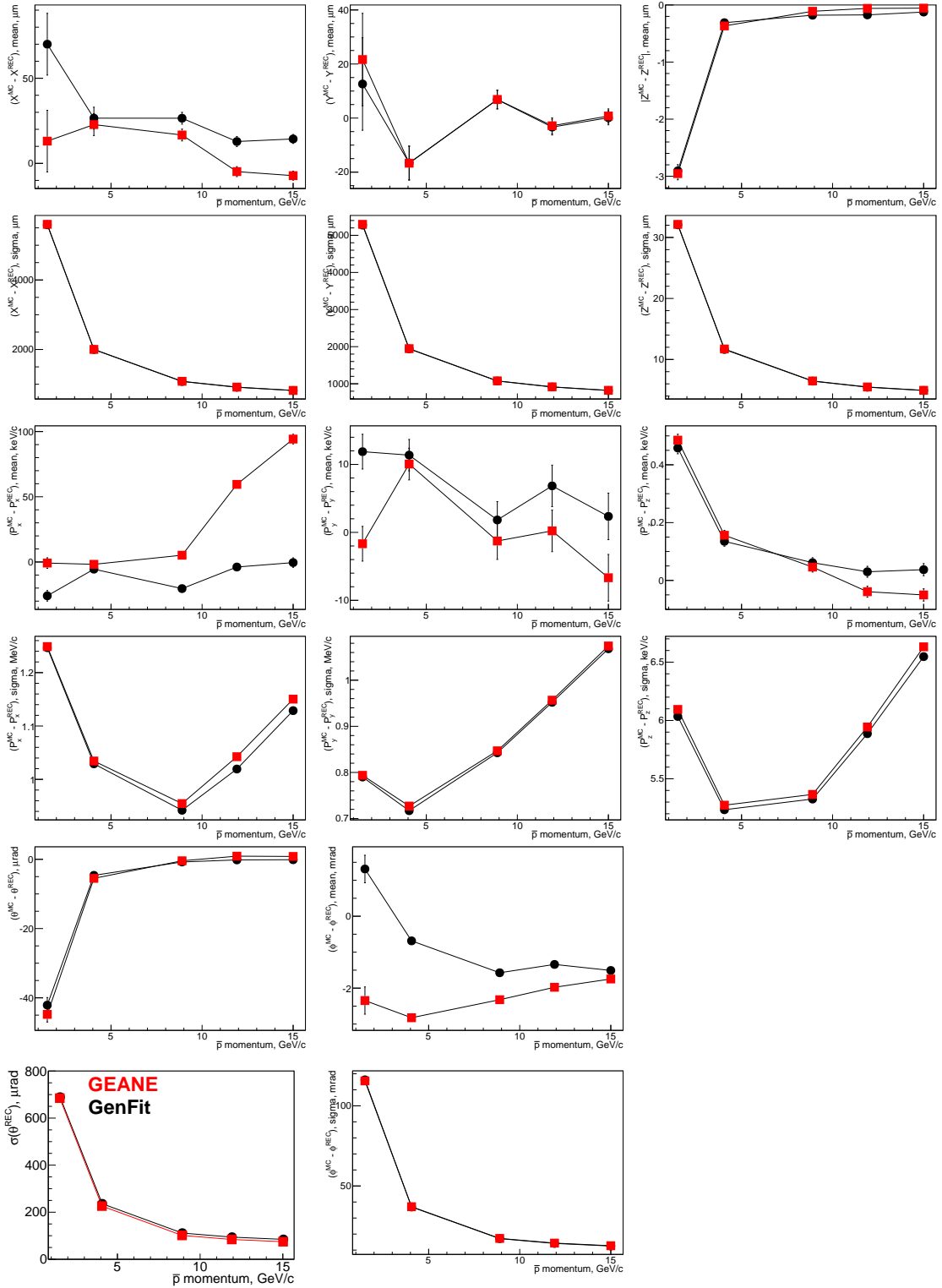


Figure 4.31: Accuracy after back propagation in terms of Gaussian fit parameters for difference between generated and reconstructed track parameters (black circles - GEANE, red squares - GenFit)

Beam Momentum	Track Parameter	GEANE	GenFit
1.5 GeV/c	$X_{start}$ , mm	$5.59 \pm 0.02$	$5.60 \pm 0.02$
	$Y_{start}$ , mm	$5.28 \pm 0.02$	$5.30 \pm 0.02$
	$P_x$ , MeV/c	$1.247 \pm 0.003$	$1.249 \pm 0.003$
	$P_y$ , MeV/c	$0.790 \pm 0.002$	$0.794 \pm 0.002$
	$P_z$ , keV/c	$6.03 \pm 0.02$	$6.09 \pm 0.02$
	$\theta$ , $\mu$ rad	$678.46 \pm 1.92$	$684.39 \pm 1.92$
	$\phi$ , mrad	$116.22 \pm 0.35$	$115.55 \pm 0.35$
15 GeV/c	$X_{start}$ , mm	$0.819 \pm 0.002$	$0.822 \pm 0.002$
	$Y_{start}$ , mm	$0.818 \pm 0.002$	$0.822 \pm 0.002$
	$P_x$ , MeV/c	$1.129 \pm 0.003$	$1.150 \pm 0.003$
	$P_y$ , MeV/c	$1.068 \pm 0.003$	$1.074 \pm 0.003$
	$P_z$ , keV/c	$6.55 \pm 0.02$	$6.63 \pm 0.02$
	$\theta$ , $\mu$ rad	$73.36 \pm 0.19$	$74.25 \pm 0.19$
	$\phi$ , mrad	$12.54 \pm 0.04$	$12.72 \pm 0.04$

Table 4.4: Parameters resolutions after back propagation

The accuracy of the estimation of the errors of the track parameters was checked on the pull distributions (i.e the difference between the generated and reconstructed values divided by the error of reconstructed parameter). Here one expects the standard deviation of the pull distribution to be close to 1 as an indication that the error was estimated correctly. None of the back propagators (Fig. 4.32) provides a correct error estimation in the whole antiproton momentum range, since the sigma of the pull distributions is never constantly equal one. Also one can note a different behavior of the sigma of the pull distributions for the x,y and z coordinates of the Point of Closest Approach (PCA) of the track in the IP in comparison to the estimation of the errors, and thus for the sigma of the pull distributions, for the momentum components. For the PCA, GEANE is slightly overestimating errors, but GenFit is significantly underestimating them. For the momentum components, a difference between GEANE and GenFit appears only for the z-component, where GEANE is significantly overestimating the errors.

At the time when this thesis is written, there is no documentation available about the GenFit errors estimation algorithm. In the Appendix E, only formulas for error estimation used in GEANE are discussed.

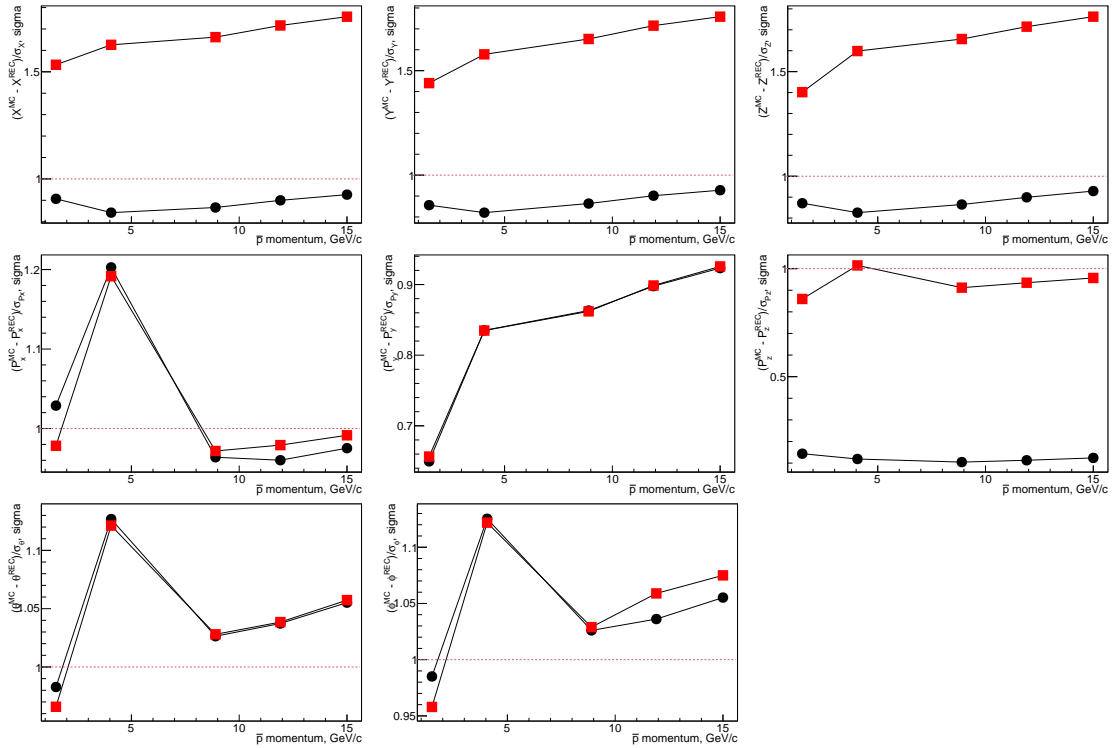


Figure 4.32: Accuracy of error estimation after back propagation in terms of the standard deviation ( $\sigma$ ) of pull distributions (black circles – GEANE, red squares – GenFit)

### 4.6.3 Tests of forward and backward propagation with GEANE

After back propagation, the resolution of the track parameters significantly decreases, especially for low momentum tracks (Tab. 4.2 versus Tab. 4.4). E.g the resolution of the  $\theta$  angle becomes  $\sim 700 \mu\text{rad}$  near the IP, although after the track fit in the LMD it is  $\sim 350 \mu\text{rad}$ . Also some systematic shift of the  $\theta$  angle is observed (see Fig. 4.31). Therefore, the behavior of the extrapolation of parameters as well as their errors was studied more carefully in a dedicated simulation studies. This was done for antiprotons with a momentum of  $1.5 \text{ GeV}/c$  uniformly generated in  $\theta \in [4, 8] \text{ mrad}$  and  $\phi \in [0, 2\pi]$  with the BOX generator. In contrast to the default simulation conditions, here in the beam pipe an ideal vacuum<sup>8</sup> was assumed.

In addition to the standard back propagation procedure, where the distance between the IP and the first LMD plane is divided into 7 steps, each step was subdivided into 10 steps in between. Each track reconstructed in the LMD was propagated backward with GEANE to the IP in 70 steps and the results of each internal propagation step (track parameters as well as their errors) were saved (REC). At the same time each generated track from the IP was propagated forward with GEANE to the LMD through the same 70

<sup>8</sup>no material inside the beam pipe

steps (MC). Moreover, due to the simulation procedure, one already has the generated information about the forward propagated tracks by GEANT4. The hit information at the LMD was back propagated with GEANE to the IP, again with 70 steps (MCLMD). These 3 samples (Fig. 4.33) are compared to each other as described in the following.

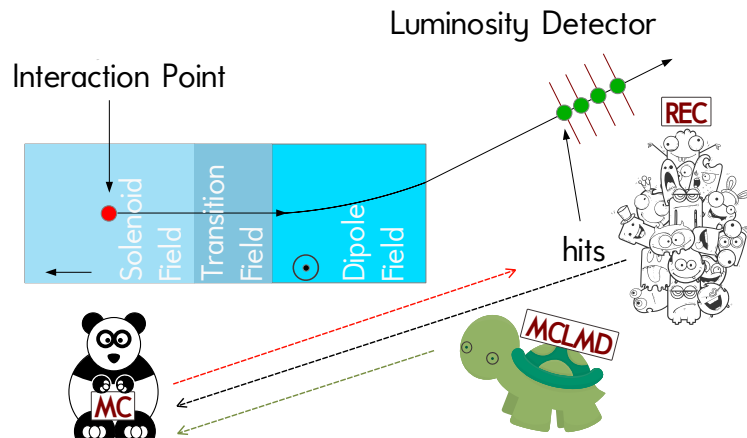


Figure 4.33: Schematic view of propagation tests

It turned out that forward propagated generated MC tracks are different from backward propagated generated hits MCLMD (Fig. 4.34, red). Most probably, the reason for it is the different approach for the particle parameters transportation in both cases: during propagation the particle trajectory is simply recalculated according to the bending of the particle track in the magnetic field, while during transportation with GEANT4 there are also some physical processes applied like bremsstrahlung or secondary particle production. The precision of each approach is currently not known and should be a topic for the further investigation. In the current study, the results between each other are compared and the relative accuracy is investigated. Because GEANE is using internal variables for the track description (see Appendix E), the behavior of the parameters  $v'$  and  $w'$ , which describe the direction of a track, are chosen for the discussion.

The change of the track variables during propagation along the  $z$ -axis was traced. As one can see in Fig. 4.34 (left), the mean values of the difference between the MC and the REC samples (black) differs from zero value, but never exceeds the resolution (Fig. 4.34, right) of this difference. So the relative shifts occurring during the propagation are on level of the relative precision or below. Also one should note here that the relative difference between REC and MCLMD (green) is usually smaller than the corresponding difference between REC and MC (black). This can be a hint that the transportation of the simulated tracks with GEANT4 is not precise enough and should be tuned.

Another important topic is the back propagation of the covariance matrix. As was shown in Fig. 4.32, GEANE has a tendency to overestimate the errors especially for low beam momenta. Eq. E.19 tell us that errors for different variables are correlated, but

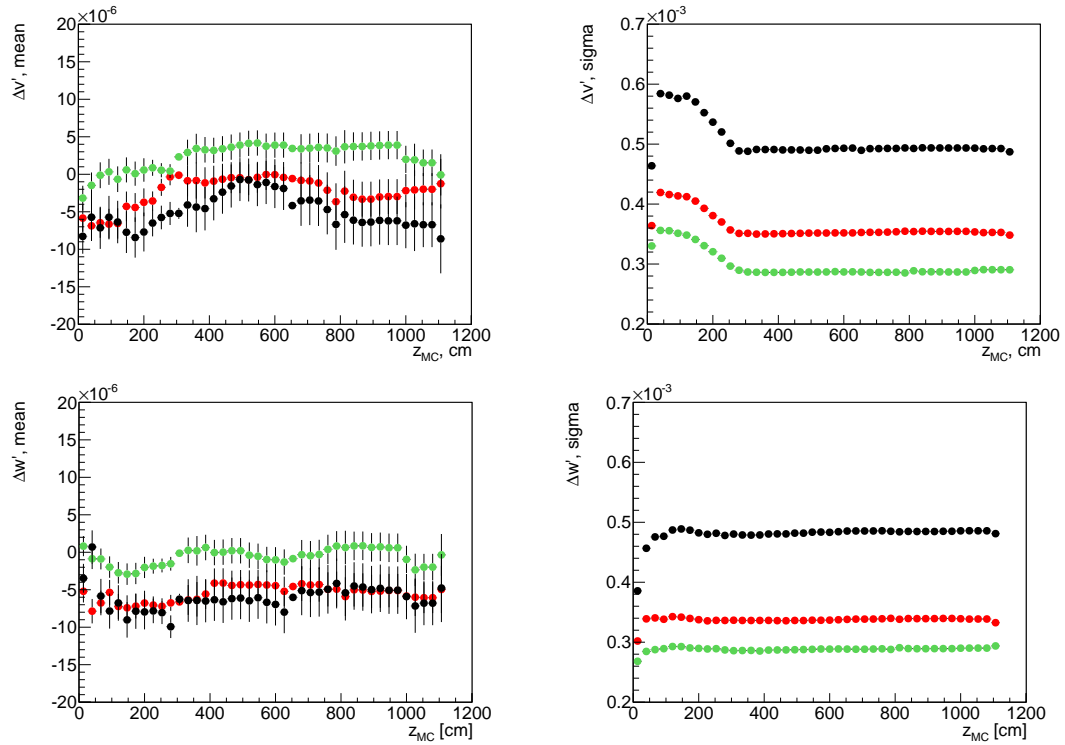
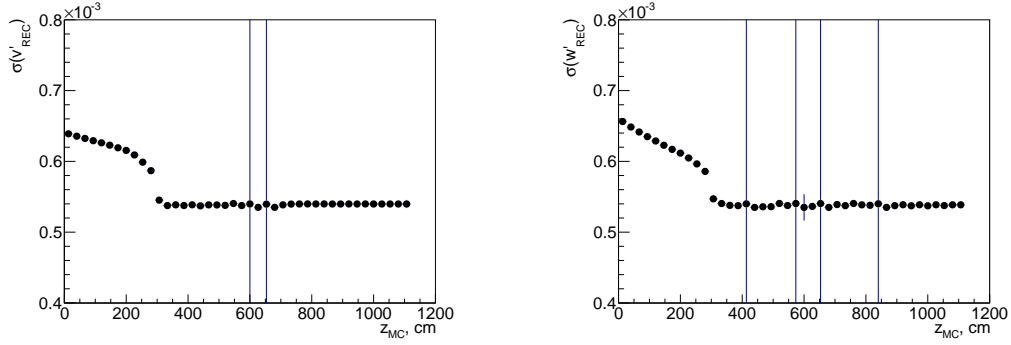
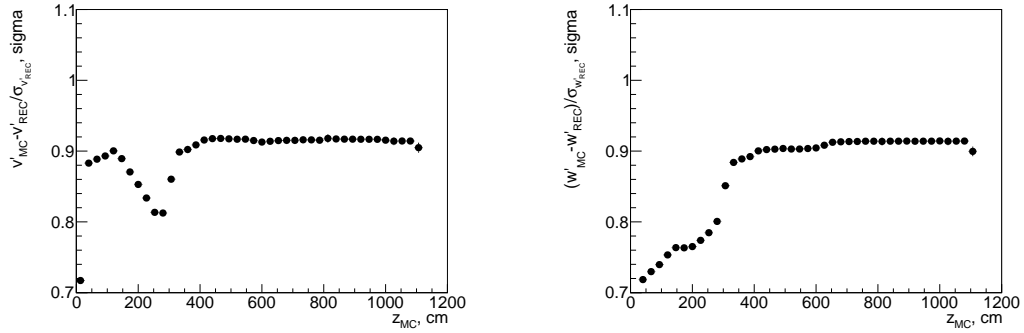


Figure 4.34: Mean (left) and standard deviation (right) of the differences of  $v'$ ,  $w'$  variables versus  $z$  coordinate. Black: MC and REC; Red: MC and MCLMD; Green: MCLMD and REC

without a magnetic field, errors for  $v'$  and  $w'$  are constants, while the errors of the coordinates of the track,  $v$  and  $w$ , are not. Indeed, as shown on Fig. 4.35, errors of  $v'$  and  $w'$  are constant in the region where no magnetic field is present and, moreover, if there is only a  $B_y$  component present, those errors are staying constants too. Also, as expected, the behavior of  $v$  and  $w$  errors is different and they are increasing during the back propagation from 11 m to 0 m (not shown).

Unfortunately, it is not possible to study the error propagation of the tracks during the simulation and the transport through the detector, because the initial errors are exactly 0. But one can trace the ratio between the parameters resolution (standard deviation of difference between MC and REC tracks parameters) and the error estimation for these parameters (Fig. 4.36). Here the trend of the errors overestimation close to the IP is clearly visible. Moreover, a significant error overestimation begins when the particle enters the transition field region and continues in the solenoid field. Therefore, one can conclude that GEANE has some issues for the covariance matrix estimation in the regions where the particle trajectory is almost parallel to the magnetic field.

The behavior of the scattering angle  $\theta$ , the systematic shift and the resolution are shown in Fig. 4.37, and follow the behavior of the  $v'$  and  $w'$  parameters discussed above.

Figure 4.35: Error propagation for  $v'$  and  $w'$  parametersFigure 4.36: Standard deviation of the ratio between the resolution and the errors for  $v'$  and  $w'$  parameters during back propagation

Only a part of the systematic shifts is introduced by the precision of reconstructed tracks. Another part already appears during the propagation of generated tracks to the LMD by the simulation and particle transportation procedure with GEANT4. Near the IP, it leads to the following values:

$$\begin{aligned}\Delta_{\theta}(MCLMD - REC) &\sim -15 \mu\text{rad} \\ \Delta_{\theta}(MCLMD - MC) &\sim 20 \mu\text{rad}\end{aligned}\quad (4.24)$$

The difference between the generated tracks and the reconstructed and back propagated tracks  $\Delta_{\theta}(MC - REC)$  can be calculated as the difference of differences:

$$\Delta_{\theta}(MC - REC) \approx \Delta_{\theta}(MCLMD - REC) - \Delta_{\theta}(MCLMD - MC) = -35 \mu\text{rad} \quad (4.25)$$

which is close to the obtained value  $-40 \mu\text{rad}$  (Fig. 4.31).

The  $\theta$  resolution obtained at the IP can be calculated from the two separated reso-

lutions:

$$\begin{aligned} |\sigma_{\theta}(MCLMD - REC)| &\sim 400 \mu\text{rad} \\ |\sigma_{\theta}(MCLMD - MC)| &\sim 460 \mu\text{rad} \end{aligned} \quad (4.26)$$

to:

$$\sigma_{\theta}(MC - REC) \approx \sqrt{\sigma_{\theta}^2(MCLMD - REC) + \sigma_{\theta}^2(MCLMD - MC)} = 610 \mu\text{rad} \quad (4.27)$$

which is again close to the obtained value of  $680 \mu\text{rad}$  (Tab. 4.4) and proves the hypothesis about the distortions of the tracks during the forward propagation by GEANT4.

This study shows the importance of a very good knowledge of the  $\bar{\text{PANDA}}$  magnetic field and its inhomogeneity. Because the calculation of a particle trajectory through the magnetic field strongly relies on this information. Since magnets are already designed, but not constructed yet, their real performance is not known. Their field maps should be measured as precise as possible to ensure a good accuracy not only for the LMD track reconstruction, but also for the  $\bar{\text{PANDA}}$  tracking systems.

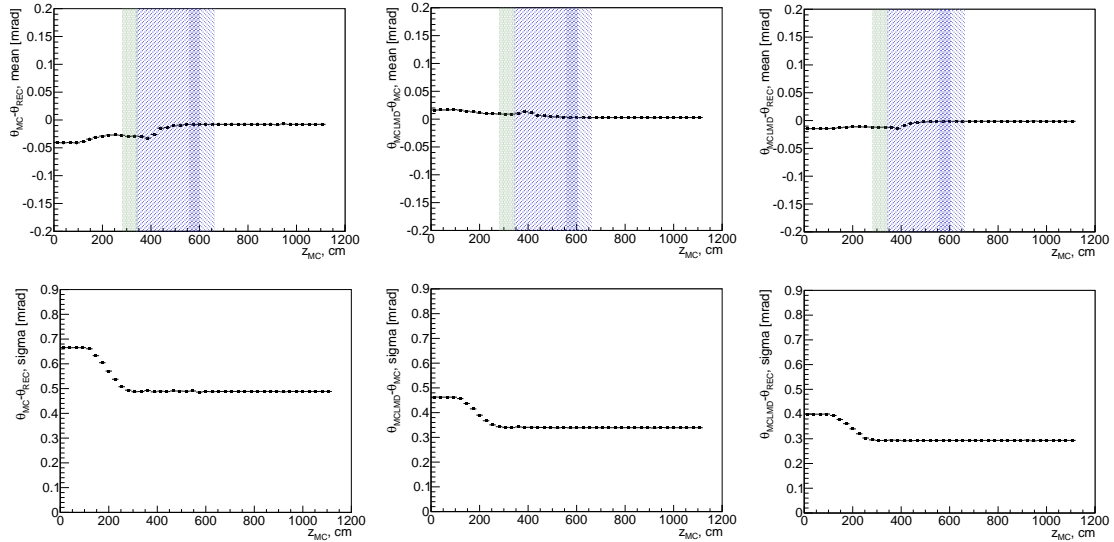


Figure 4.37: Difference of the  $\theta$  angles during the propagation versus  $z$ -coordinate between: MC and REC (left), MCLMD and MC (center) and MCLMD and REC (right). The first row shows the mean, the second row the standard deviation of the distributions

## 4.7 Reconstruction of the Interaction Point

A precise track reconstruction in the LMD relies on a precise knowledge of the IP, which is used as the destination point for the back propagation. In simulation studies, the IP is known with infinite precision, which will not be the case later in the experiment. One should consider the following effects:

1. Beam spatial distribution
2. Target spatial distribution
3. Beam shift and tilt
4. Target shift and tilt
5. Rest gas

The rest gas can be considered as an extreme limit of target and the beam shifts, where the IP is significantly shifted to large values along the  $x$ ,  $y$  and  $z$  axis. The expected amount of the rest gas is rather high and  $\sim 10\%$  of the target material can be expected in the narrow beam pipe around the IP [78].

With the current track reconstruction, we can determine only a systematic shift of the IP. One can use the flexibility of the back propagation procedure during which the track is recalculated to the PCA of the IP. In case of a systematic shift of the IP, this is visible by the mean values of the PCA distribution for a bunch of reconstructed tracks.

To study the accuracy of reconstruction of the shifted IP,  $10^6$  tracks with a momentum of  $1.5 \text{ GeV}/c$  were simulated with the BOX generator, where  $\theta_{MC}$  was distributed within 2 and 12 mrad and  $\phi_{MC}$  from 0 to  $2\pi$ . For the beam a Gaussian shape with 0.08 cm widths in  $x$  and  $y$  was assumed. In the first part of this study the mean of the beam distribution in the  $(x,y)$  plane was fixed at  $(0,0)$ . Along the  $z$  axis, the IP was simulated uniformly within  $-50$  to  $50$  cm. This gives some indication how precise the  $x$  and  $y$  coordinate of the IP could be determined if only the  $z$ -position of the IP is shifted. In the second part of the study, the mean distribution of the IP in  $(x,y)$  plane was generated uniformly in  $x$  and  $y$  from  $-0.9$  to  $0.9$  cm (size of the beam pipe) still with a Gaussian shape with 0.08 cm widths. And again the  $z$  coordinate of the IP was simulated uniformly within  $-50$  to  $50$  cm. This emulates situation when interaction happens with the rest gas in the beam pipe near the IP.

### **(x,y) distribution at the IP: Gaussian shape around (0,0)**

Fig. 4.38 shows the accuracy of reconstruction of the  $x$  coordinate of the IP in dependence on the  $z$  coordinate shift. The mean of the Gaussian distribution of the  $x$  coordinate is reconstructed with a systematic shift below  $50 \mu\text{m}$  and a resolution 0.6 cm. The spatial resolution of the reconstruction in this case is worse than for a point-like

beam (Tab. 4.4) and can be explained by the 0.08 cm size of the spatial distribution of the beam. However a determination of the  $z$  coordinate shift is not possible in this case (Fig. 4.39), since the  $z$  coordinate of the PCA is always close to 0, independently from the initial shift of the IP. The reason for this is clear. During the back propagation, the extrapolation of the track parameters is done along the  $z$  axis to the  $z$  coordinate value set by the user. Therefore, it is not surprising that the final  $z$  coordinate of the track is close to the set value.

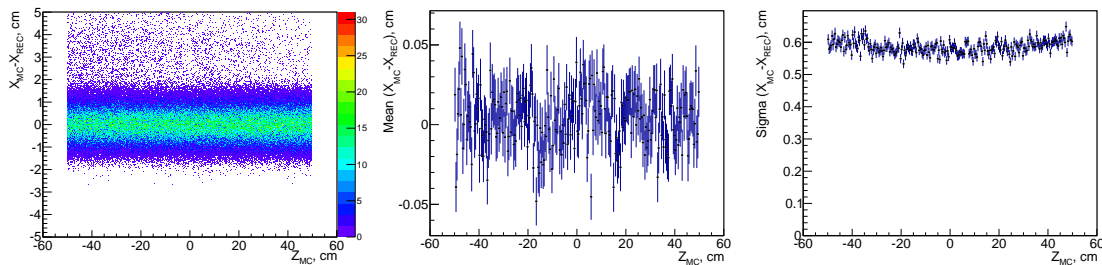


Figure 4.38: Accuracy of the  $x$  coordinate of the IP reconstruction versus the  $z$  coordinate of the IP in case of Gaussian shape of the beam profile around (0,0) and shifted  $z$  coordinate of the IP

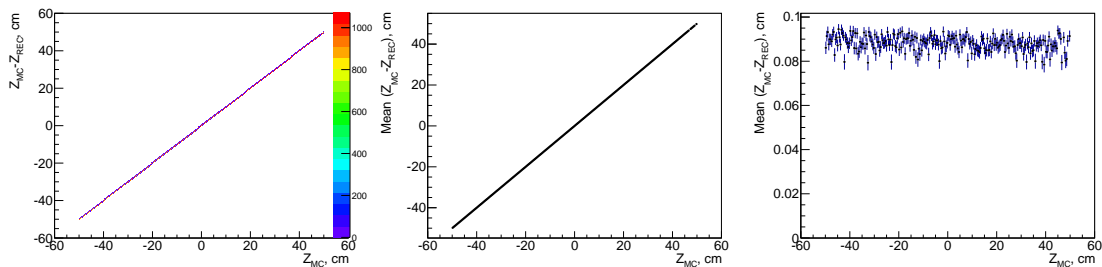


Figure 4.39: Accuracy of the  $z$  coordinate of the IP reconstruction versus the  $z$  coordinate of the IP in case of Gaussian shape of the beam profile around (0,0) and shifted  $z$  coordinate of the IP

### Uniform distribution of (x,y) coordinates of the IP between -0.9 and 0.9 cm

As in the previous case, the  $z$  coordinate of the PCA is always close to 0, independently from the initial  $z$  coordinate. Fig. 4.40 shows that the shift of the  $x$  and  $y$  coordinates can only be determined with some systematic shift, which is stronger if the shift of  $x$  or  $y$  coordinate is large. The systematic shift in the  $x$  and  $y$  coordinates appears, if the  $z$  coordinate is shifted by more than 10 cm and more predominate for negative shifts of the  $z$  coordinate. This is demonstrated in Fig. 4.41, where the systematic shift of the  $x$  coordinate is shown for a constant shifts of the  $z$  coordinate. It should be mentioned here that no influence was observed of the initial  $y$  coordinate on the  $x$  coordinate reconstruction (and vice versa).

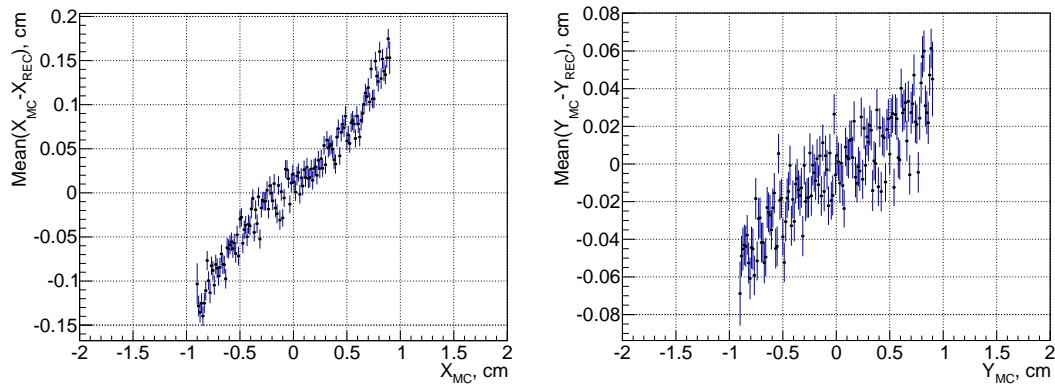


Figure 4.40: Accuracy of the  $x$  and  $y$  coordinate of the IP reconstruction versus the  $x$  or  $y$  coordinate of the IP in case of uniformly distributed  $(x,y)$  interaction coordinates. The  $z$  position of the IP is uniformly distributed between  $-50$  and  $50$  cm

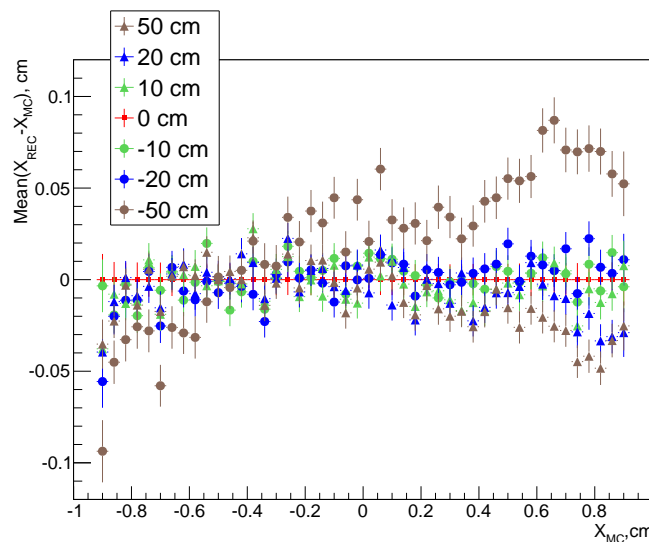


Figure 4.41: Accuracy of the  $x$  coordinate of the IP reconstruction versus the  $x$  coordinate of the IP in case of uniformly distributed  $(x,y)$  interaction coordinates and shifted  $z$  position of the IP as indicated by different colors

The rest gas is expected to be uniformly distributed within some volume. The result of this study is that a determination of the interaction point with the rest gas on a track by track basis is not feasible due to the finite spatial resolution of the track reconstruction. Moreover, the  $z$  coordinate of the IP between the beam and the target can be determined only by external measurements. However it should not have a significant influence on the precision of luminosity extraction, because the scattering angle  $\theta$  can still be accurately determined even for significant shifts of the  $z$  coordinate of the IP, if the  $x$  and  $y$  coordinates of the IP are accurately known.

## 4.8 Computing time for the track reconstruction

The CPU time of the reconstruction steps was estimated with simulation studies on a modern PC <sup>9</sup>, where  $10^4$  events with different track multiplicities were generated with the BOX generator. The results are presented in terms of time <sup>10</sup> needed for the reconstruction of 1 event (Fig. 4.42 for track search with CA and Fig. 4.43 for track search with TF). The slowest part of the reconstruction chain is the back propagation and currently no improvement is expected. Also the hit reconstruction is relatively slow, but this part should be re-implemented in the nearest future to take into account read-out scheme of the HV-MAPS. The track search and track fit steps were already tuned for the best speed performance and further improvement can be expected only in case of a new implementation of these steps. Track filtering or the application of cuts is a very simple and fast procedure.

At least  $2 \times 10^5$  events are required for an accurate luminosity fit at  $P_{beam} = 1.5 \text{ GeV}/c$  [76]. This number of elastically scattered antiprotons can be accumulated within just 1 s of data taking. With the current reconstruction speed, the complete reconstruction of these events takes  $\sim 12$  min. For the online monitoring of the luminosity, a faster and simplified online reconstruction tools are currently investigated [32].

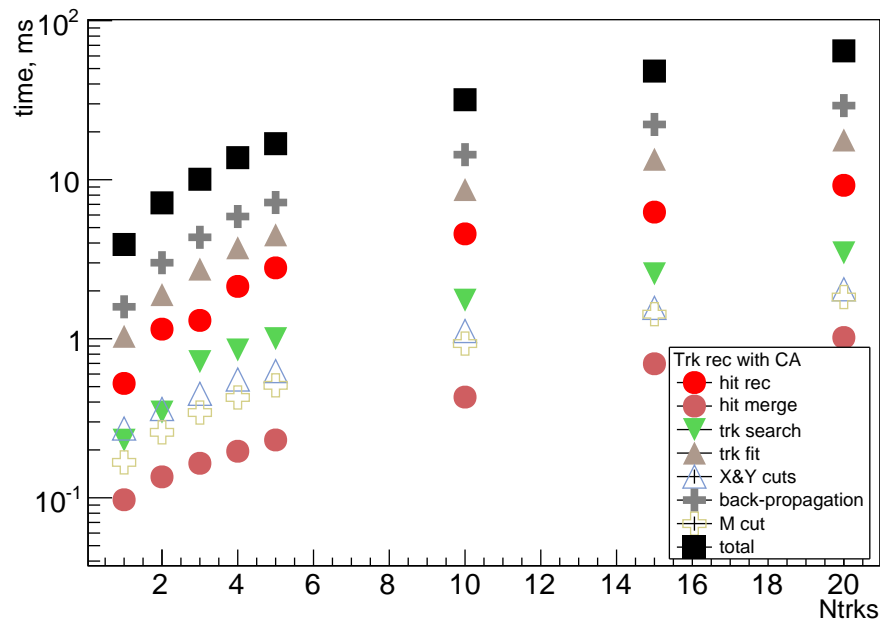


Figure 4.42: CPU time necessary for each single step of the track reconstruction (track search with CA)

<sup>9</sup>Intel Xeon E5-1603 @2.8 GHz

<sup>10</sup>including handling the data with the PANDARoot framework (reading/writing I/O)

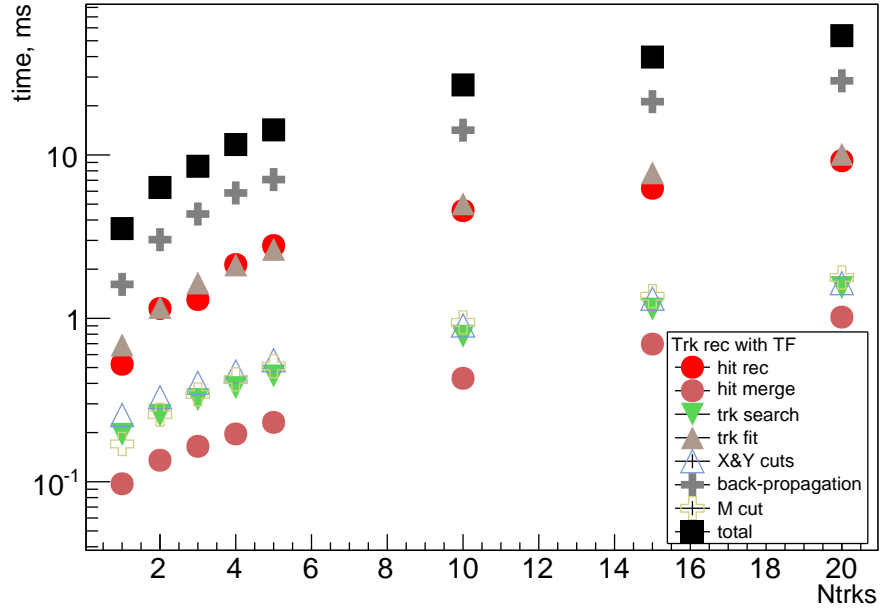


Figure 4.43: CPU time necessary for each single step of the track reconstruction (track search with Track-Following)

## 4.9 Luminosity extraction

For the extraction of the luminosity from data, the acceptance of the detector and the resolution of the LMD have to be taken into account [76]:

$$N(\theta_{\text{rec}}) = L \cdot \int \sigma(\theta_{\text{MC}}) \cdot \varepsilon(\theta_{\text{MC}}) \cdot R(\theta_{\text{rec}}, \theta_{\text{MC}}) d\theta_{\text{MC}} \quad (4.28)$$

$N(\theta_{\text{rec}})$  describes the distribution of elastically scattered antiprotons, measured by the LMD and back propagated to the IP.  $\sigma(\theta_{\text{MC}})$  gives the probability of an incoming antiproton being scattered into an angular element  $d\theta_{\text{MC}}$  at an angle of  $\theta_{\text{MC}}$ . The registration probability at this solid angle is taken into account by  $\varepsilon(\theta_{\text{MC}})$ . Due to a certain precision of the LMD reconstruction, the tracks generated at an angle of  $\theta_{\text{MC}}$  can be reconstructed at an angle of  $\theta_{\text{rec}}$ . The probability for this transition is denoted by  $R(\theta_{\text{rec}}, \theta_{\text{MC}})$ . To obtain the total probability of elastically scattered antiprotons at the angle  $\theta_{\text{rec}}$ , an integral over all possible generated angles  $\theta_{\text{MC}}$  has to be performed. Finally, for the comparison with data, this probability has to be multiplied with the luminosity  $L$ .

Fig. 4.44 from [76] presents the reconstructed angular distributions for beam momenta 1.5 GeV/ $c$  (left) and 15 GeV/ $c$  (right), respectively. Also it shows the result of the luminosity fit with the model from Eq. 4.28. In these fits, the luminosity was the

only fit parameter and exactly the same theoretical model (and its parameters) was applied as the one used in the data generation. Thus, this result demonstrates only the influence of the LMD track reconstruction accuracy on the luminosity extraction, and that it is rather small, in the order of  $\sim 0.05\%$ .

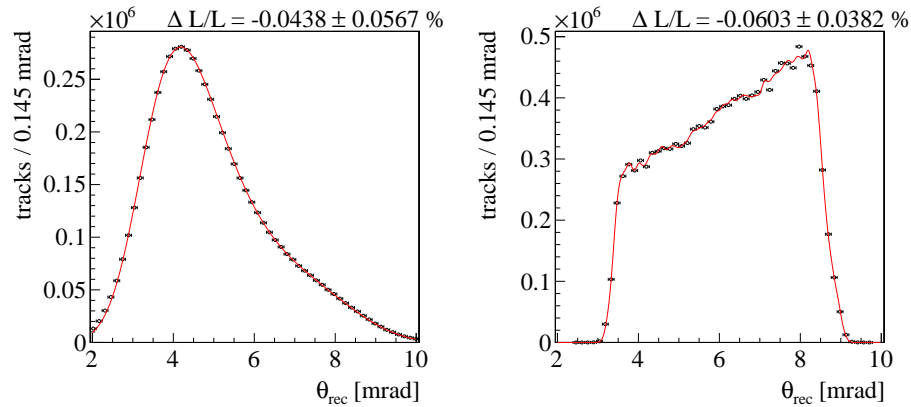


Figure 4.44: Luminosity fit results for 1.5 GeV/c (left) and 15 GeV/c (right) beam momentum [76]

The final luminosity accuracy can be influenced by many circumstances or complications, like:

- model uncertainties
- background
- misalignment
- beam & target imperfections

Currently the model uncertainty limit the accuracy (see Sec. 3.3.2.5). As was shown above, the  $x$  and  $y$  coordinates of the IP can be extracted from the experimental data. In more detail, the beam and target imperfections and their influence on the luminosity measurement is studied in [76]. In the following, the alignment of the LMD components (Chapter 5) and the background (Chapter 6) studies are discussed.

## Modules alignment

During the track reconstruction and the luminosity determination procedure, it is assumed that the geometry of the detector is perfectly known. This also includes the assumption that the position of each part of the detector is known very accurately. However, the accuracy of positioning of each element of the detector is limited because of the construction process. Due to the design of the detector there are four groups of elements where a misalignment may occur and could influence the accuracy of the track reconstruction:

- sensors glued to sensor modules
- sensor modules inserted to the support structure
- two movable halves of the detector plane
- position of the LMD box with respect to the global frame of  $\bar{P}$ ANDA

The determination of a sensor misalignment on the sensor module should be done only once. Due to the gluing no movement during the time of the detector operation is expected. How stable the modules are attached to the support structure will be checked with the LMD prototype. For safety reasons each half of the LMD will be moved away from the antiproton beam during the beam injection in the HESR. Thus one can expect a misalignment of the modules due to this mechanical movement, which ideally should be constantly monitored.

This chapter describes a fast track-based software alignment procedure to align sensors modules of the LMD among themselves. Due to the fact that signal tracks usually go through the sensor modules in a row parallel to each other (see Fig. 5.1), the alignment procedure is done for each row separately. One row of four sensor modules is called a *sector*. A similar alignment approach can be easily applied to the alignment of sectors among each other or the alignment of the detector halves, following a method

given in [79]. Since tracks are going mainly through one sector, the alignment of the sectors or the detector halves requires a large data set and the software realization of these procedures is subject of future studies.

For the software alignment of the sensor modules a method is chosen, which is based on a non-iterative least squares fitting with utilization of a C++ implementation of the "matrix-crushing" algorithm Millepede [80, 81]. This method is described in detail after a discussion of the the difference between the iterative and the non-iterative algorithms.

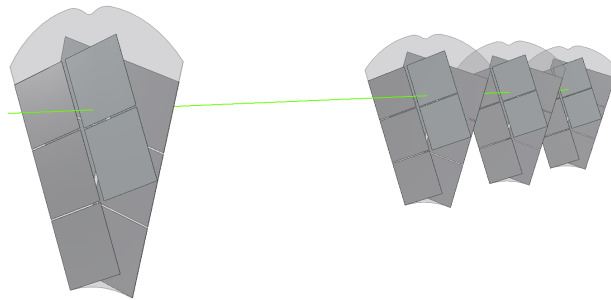


Figure 5.1: Illustration of a track (green line) hitting the modules of one LMD sector

## 5.1 Influence of misaligned modules on the track reconstruction accuracy

Each module has six degrees of freedom for the positioning in respect to an external frame and hence six alignment constants (denoted as  $\Delta_i$ ) relative to the ideal position of the module:  $\Delta_x, \Delta_y, \Delta_z$  for translation along and  $\Delta_\alpha, \Delta_\beta, \Delta_\gamma$  for rotation around the  $x, y$  and  $z$  axes, respectively. From the construction procedure a shift of the modules  $\Delta_i$  in  $x, y$  or  $z$  direction is expected to be  $\sim 200 \mu\text{m}$ . Then it should be taken into account that the height of each module  $h$  is 76 mm and the width varies from  $d_1 = 22 \text{ mm}$  (bottom) to  $d_2 = 63 \text{ mm}$  (top). Therefore the expected rotation misalignment:

$$\begin{aligned}\Delta_\alpha &= \frac{\Delta_z}{h} = 2.63 \text{ mrad}; \\ \Delta_\beta &= \frac{\Delta_z}{d_2} = 3.17 \text{ mrad}; \\ \Delta_\gamma &= \frac{\Delta_z}{h} = 2.63 \text{ mrad}\end{aligned}\tag{5.1}$$

The influence of the misaligned modules was checked in dedicated simulation studies. Each module was shifted and rotated by sampling from a Gaussian distribution centered at 0 with a width  $\Delta_i$  for translation and  $\Delta_i$  for rotation. With the misaligned

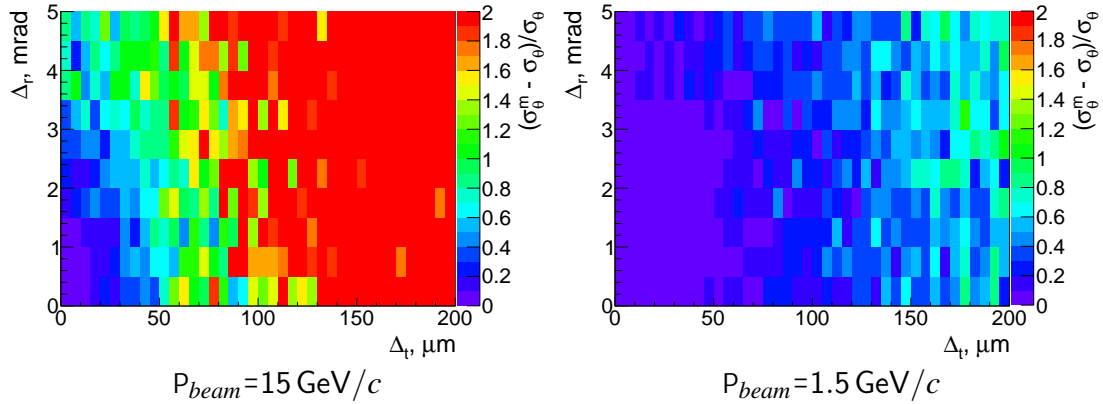


Figure 5.2: Influence of the misalignment of the modules on  $\theta$  resolution as a function of variation of the translation ( $\Delta_t$ ) and rotation ( $\Delta_r$ ) misalignment

geometry the standard track reconstruction was performed and the results in terms of the resolution of the track parameters were compared with the perfectly aligned case. Fig. 5.2 shows the relative difference of the  $\theta$  resolution  $\sigma_\theta^m$  in comparison to the resolution  $\sigma_\theta$  in the perfectly aligned case in dependence on the translation and rotation misalignment. The resolution becomes worse by more than 10% for particles with a momentum of 15 GeV/c if the translation and rotation misalignment exceeds:

$$\Delta_t > 15 \mu\text{m}, \Delta_r > 1 \text{ mrad} \quad (5.2)$$

and for particles with momentum 1.5 GeV/c when:

$$\Delta_t > 40 \mu\text{m}, \Delta_r > 3.5 \text{ mrad} \quad (5.3)$$

For the misalignment expected from the construction ( $\Delta_t \sim 200 \mu\text{m}$  and  $\Delta_r \sim 3 \text{ mrad}$ ) the resolution is two times worse for 15 GeV/c and by at least 50% worse for 1.5 GeV/c. Therefore an alignment procedure is absolutely necessary to allow an accurate track reconstruction and thus an accurate luminosity extraction.

An effect of the misalignment is also visible on the residuals between reconstructed tracks and hits assigned to them. Fig. 5.3 illustrates the influence of the misalignment on the residuals. The larger the misalignment is, the larger are the residuals. This relation is used in the so-called *software alignment* methods, which are based on reconstructed tracks and aim to minimize the residuals between tracks and their hits.

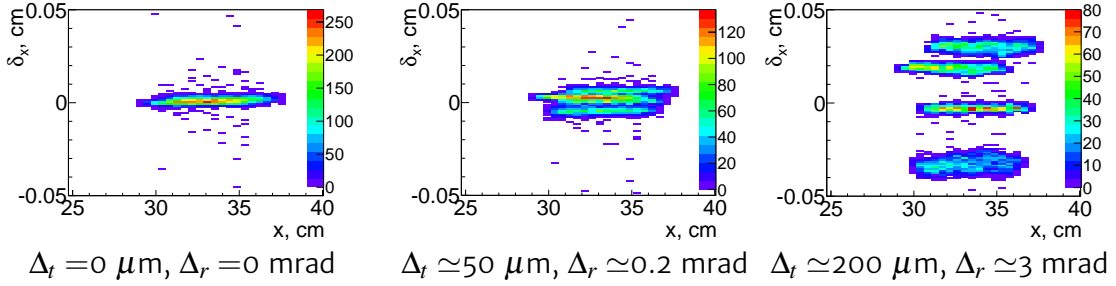


Figure 5.3: Residuals  $\delta_x$  between reconstructed tracks and hits in dependence on the  $x$  coordinate for the ideal (left) and two misaligned (center, right) cases

## 5.2 Iterative and Non-Iterative Methods

A comprehensive discussion of the difference between the iterative and the non-iterative methods is provided in the LHCb note [79]. The main steps of this discussion are presented below with some small changes (misprinting corrections) in the equations.

The standard way to obtain the alignment constants by using tracks is to minimize the residuals between tracks and hits in the detector. In a perfect detector, without any resolution error, the residuals will only depend on the misalignment. Hence, minimizing the residuals will allow us to retrieve the misalignment constants. More quantitatively, the most general track equation is related to the track measurements (e.g. hits) by the following relation:

$$\mathbf{Y} = f(\mathbf{X}) + \boldsymbol{\varepsilon} \quad (5.4)$$

where a track state  $\mathbf{Y}$  is the vector of the measurements on the track,  $\mathbf{X}$  is a vector of the input parameters of the function  $f$ , which defines the track, and  $\boldsymbol{\varepsilon}$  is the vector of residuals. The most common way to minimize the residuals is by using the least squares method by minimizing the following  $\chi^2$ -function:

$$\chi^2 = \sum_i (\mathbf{Y}_i - f(\mathbf{X}_i))^T V_i^{-1} (\mathbf{Y}_i - f(\mathbf{X}_i)) = \sum_i \boldsymbol{\varepsilon}_i^T V_i^{-1} \boldsymbol{\varepsilon}_i \quad (5.5)$$

where the sum is taking over all track measurements and  $V$  is the covariance matrix of tracks state  $\mathbf{Y}$ . If  $\mathbf{Y}$  has  $n$  coordinates, the problem is reduced to the solution of a system of  $n$  equations:

$$\left( \frac{\partial \chi^2}{\partial Y_k} \right)_{k \in [1, n]} = 0 \quad (5.6)$$

This system could be solved only if the problem is linearizable i.e. if one could express

the track equation as follows:

$$f(\mathbf{X}) = \mathbf{X} \cdot \boldsymbol{\alpha} \quad (5.7)$$

where  $\mathbf{X}$  is now a matrix containing the local derivatives of the tracks and  $\boldsymbol{\alpha}$  is a vector containing the local parameters of the tracks. In this case, and if we consider in addition that the different coordinates of  $\mathbf{Y}$  are not correlated ( $V_i$  is then a diagonal matrix containing the errors on the coordinates), the solution to the problem is:

$$\boldsymbol{\alpha} = \left( \sum_i \mathbf{X}_i^T V_i^{-1} \mathbf{X}_i \right)^{-1} \left( \sum_i \mathbf{X}_i^T V_i^{-1} \mathbf{Y}_i \right) \quad (5.8)$$

Getting the residuals is now straight-forward.

The LMD track is defined as a straight line:

$$\begin{cases} x_m = x_{trk} + \varepsilon_x = a \cdot z + b + \varepsilon_x \\ y_m = y_{trk} + \varepsilon_y = c \cdot z + d + \varepsilon_y \end{cases} \quad (5.9)$$

where  $x_{trk}(y_{trk})$  is the reconstructed track coordinate,  $x_m(y_m)$  the measured  $x(y)$  coordinate of the track (i.e. hit) and then  $\mathbf{Y} = (x_m, y_m)$ ,  $\boldsymbol{\varepsilon} = (\varepsilon_x, \varepsilon_y)$ ,  $V = \begin{pmatrix} \sigma_x^2 & \sigma_{xy} \\ \sigma_{xy} & \sigma_y^2 \end{pmatrix}$ ,  $\boldsymbol{\alpha} = (a, b, c, d)$  and  $\mathbf{X} = \begin{pmatrix} z & 1 & 0 & 0 \\ 0 & 0 & z & 1 \end{pmatrix}$ .

Changing the measured points of the track will modify the residuals. This is the basic principle exploited by an iterative minimization method. Changing the measurement is equivalent to displacing the sensitive area. The idea is to move the module, recalculate the measured points and then fit the tracks with the new measurements and analyze the new residuals. Then the method is iterated until the solution with (hopefully) the minimal set of residuals is reached. This method is simple and in fact has already proven its efficiency in the detector alignment in many occasions. However, it has a few disadvantages which are potentially important for the LMD. The first disadvantage is that it may be too time consuming, and consequently ineffective for a fast alignment. The other significant disadvantage of basic iterative methods is that they are blind in the sense that they ignore the relationship between the residuals and the misalignment. The track is biased by its measured points, but this information is not used in the procedure. The effect of this loss of information is that outliers (incorrect points) might be more easily propagated through the iterations and then lead to biases in the final result. Sophisticated techniques more or less manage to dispose a hit like that. However the problem can be overcome by simply taking into account directly the relationship between the residuals and the misalignment.

In non-iterative methods the track and residuals are fitted simultaneously. To do so, one first needs to find a linear relationship between the residual and the alignment

constants. The track equation is now given by:

$$\mathbf{Y} = \mathbf{X} \cdot \boldsymbol{\alpha} + \mathbf{C} \cdot \Delta \quad (5.10)$$

where  $\Delta$  contains the global parameters, i.e. the alignment constants and  $\mathbf{C}$  is a matrix containing the global derivatives, i.e. derivatives with respect to the global parameters. The problem is then solved exactly as before. The difference is that the solution now contains not only the local track parameters but also the global alignment parameters. It is not necessary to deal with the residuals directly and one gets the track parameters and the alignment constants in one step.

The price which one has to pay is that all tracks become correlated. By definition, the global parameters are common to all tracks. So, by including them into the fit, the tracks are no longer independent. This means that it is necessary to fit all the tracks simultaneously. For the iterative case to fit a track only a system of  $n_{loc}$  equations has to be solved, where  $n_{loc}$  is the number of local track parameters needed to describe one track. In non-iterative method the final size of the system of equations is given by:

$$n_{tot} = n_{loc} \cdot n_{trks} + n_{gl} \quad (5.11)$$

where  $n_{trks}$  is number of tracks and  $n_{gl}$  number of alignment constants.

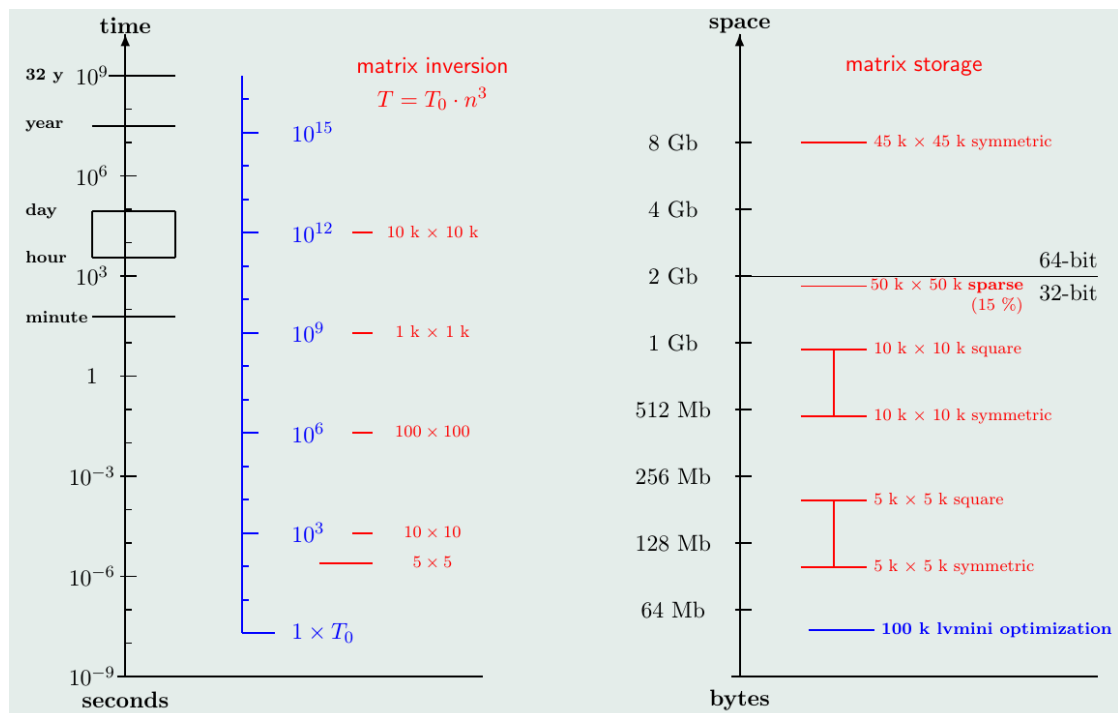


Figure 5.4: Running time and memory space needed for standard matrix inversion [80]

In order to get a good accuracy on the global alignment parameters, a significant number of tracks is needed. For the LMD, it turned out to be  $\sim 10^4$  tracks. Therefore the inversion of a  $4 \cdot 10^4 \times 4 \cdot 10^4$  matrix is required. The time needed for the inversion of the matrices of different sizes by the standard computing methods is shown in the left of Fig. 5.4. So without the Millepede algorithm, this task would take around one day and would be possible only on the most powerful modern computers due to the significant space required to store this matrix ( $\sim 8$  Gb, as shown on the right of Fig. 5.4). The same inversion by using the Millepede algorithm and running it on a PC with a processor i7-4500U (1.8 GHz) takes  $\sim 5$  s CPU time and requires just  $\sim 40$  Mb memory space.

### 5.3 Introduction to Millepede

Millepede was developed by Volker Blobel for the alignment of the H1 detector [80]. In the case of the LMD, only straight tracks are considered for Eq. 5.10:

$$y = \sum_j x_j \cdot \alpha_j + \sum_k c_k \cdot \Delta_k \quad (5.12)$$

where  $j$  is the index for dimensions in space and  $k$  the index for the number of global parameters. The  $\chi^2$  to be minimized for one track is given by the relation:

$$\chi^2 = \sum_i w_i (y^i - \sum_j x_j^i \cdot \alpha_j - \sum_k c_k^i \cdot \Delta_k)^2, \quad (5.13)$$

with the weight for each measured hit coordinate  $w_i = 1/\sigma_i^2$  and the uncertainty of the measurement  $\sigma_i$ . It is also assumed that the measurements are uncorrelated. All tracks are fitted simultaneously, then the single  $\chi^2$  sum up to:

$$\chi^2 = \sum_{trk,i} w_{trk,i} (y^{trk,i} - \sum_j x_j^{trk,i} \cdot \alpha_j^{trk} - \sum_k c_k^{trk,i} \cdot \Delta_k)^2, \quad (5.14)$$

where  $\sum_{trk,i}$  stands for sum over all tracks and their coordinates as  $\sum_{trk} \sum_i$ . Differentiating with respect to the tracks parameters allows to derive the required system of equations

and produces the following result:

$$\begin{pmatrix} \Delta_1 \\ \dots \\ \Delta_{n_{gl}} \\ \dots \\ \alpha_1^1 \\ \dots \\ \alpha_{n_{loc}}^{n_{trk}} \end{pmatrix} = \begin{pmatrix} V_{11} & \vdots & V_{12} \\ \dots & \dots & \dots \\ V_{21} & \vdots & V_{22} \end{pmatrix}^{-1} \cdot \begin{pmatrix} \sum_{trk,i} w_{trk,i} \cdot c_1^i \cdot y^{trk,i} \\ \dots \\ \sum_{trk,i} w_{trk,i} \cdot c_{n_{gl}}^i \cdot y^{trk,i} \\ \dots \\ \sum_i w_{1,i} \cdot x_1^{1,i} \cdot y^{1,i} \\ \dots \\ \sum_i w_{n_{trk},i} \cdot x_{n_{loc}}^{n_{trk},i} \cdot y^{n_{trk},i} \end{pmatrix} \quad (5.15)$$

The largest part of the matrix  $V$  is  $V_{22}$  and it is only filled with symmetric sub-matrices of dimensions  $n_{loc} \times n_{loc}$ . In addition, those blocks are on the diagonal so that  $V_{22}$  is nearly empty and relatively simple to invert, this is the key to solve the problem. The full solution requires to invert  $V$ , i.e. to find the four sub-matrices  $A$ ,  $B$ ,  $C$ , and  $D$  such that:

$$\begin{pmatrix} V_{11} & \vdots & V_{12} \\ \dots & \dots & \dots \\ V_{21} & \vdots & V_{22} \end{pmatrix} \cdot \begin{pmatrix} A & \vdots & B \\ \dots & \dots & \dots \\ C & \vdots & D \end{pmatrix} = 1 \quad (5.16)$$

In fact one needs only  $A$  and  $B$  as these are the only parts required to find the alignment constants ( $\Delta_1 \dots \Delta_{n_{gl}}$ ):

$$\begin{pmatrix} \Delta_1 \\ \dots \\ \Delta_{n_{gl}} \end{pmatrix} = A \cdot \begin{pmatrix} \sum_{trk,i} w_{trk,i} \cdot c_1^i \cdot y^{trk,i} \\ \dots \\ \sum_{trk,i} w_{trk,i} \cdot c_{n_{gl}}^i \cdot y^{trk,i} \end{pmatrix} + B \cdot \begin{pmatrix} \sum_i w_{1,i} \cdot x_1^{1,i} \cdot y^{1,i} \\ \dots \\ \sum_i w_{n_{trk},i} \cdot x_{n_{loc}}^{n_{trk},i} \cdot y^{n_{trk},i} \end{pmatrix} \quad (5.17)$$

Inverting by blocks produces:

$$\begin{cases} A = (V_{11} - V_{12} \cdot V_{22}^{-1} \cdot V_{12}^T)^{-1} \\ B = -A \cdot V_{12} \cdot V_{22}^{-1} \end{cases} \quad (5.18)$$

Thus to obtain the final results one needs to invert the matrix  $V_{22}$ , which is straight-

forward. The matrix  $A$  is also relatively easy to derive by inverting the matrix of only  $n_{gl} \times n_{gl}$  dimensions. Since the matrix  $B$  has a linear dependence on the matrix  $A$ , the final result is given by multiplying matrix  $A$  by a vector.

The central work of the Millepede algorithm is solving of Eq.5.17. Millepede solves the problem based on the track parameters as well as the global and local derivatives, which have to be provided by the user. The program then performs the local fit of each track ( $V_{22}$  sub-part), and then updates the matrix  $A$  and the final vector, taking into account contributions of the global derivatives, which appear in  $V_{11}$  and  $V_{12}$ . When the loop over all tracks is finished, Millepede performs the inversion to obtain the matrix  $A$ , using the enhanced Gauss pivot method and then deduces the alignment constants.<sup>1</sup> A second loop is then performed in order to remove the outlier tracks. In the alignment studies for the LMD modules the program always converged after this second loop.

## 5.4 Residuals and Global Parameters

In order to use the method discussed above, a linear relationship between the residuals and the misalignment constants has to be determined.

### 5.4.1 Position of hits in the frame of one LMD sector

In one LMD sector (Fig. 5.1) a hit is defined by the coordinates  $r_{hit}^s = (x_{hit}^s, y_{hit}^s, z_{hit}^s)$ . The sector frame is the reference frame for the LMD internal alignment. The same hit is expressed as  $r_{hit} = (x_{hit}, y_{hit}, z_{hit})$  in the local module frame, with  $r_{hit}$  defined as:

$$r_{hit} = R \cdot (r_{hit}^s - r_0^s) \quad (5.19)$$

where  $R$  is the rotation and  $r_0^s$  is the translation to make the transition from the global (sector) to the local (module) frame. If a module is perfectly aligned (it is in ideal position) in the sector:

$$r_{hit} = r_{hit}^s - \begin{pmatrix} 0 \\ 0 \\ z_0^s \end{pmatrix} \quad (5.20)$$

where  $z_0^b$  is the module position on the  $z$ -axis. If the module is misaligned, the same hit will have a different expression in the local frame  $r_{hit}^{new}$ . The contribution to the residual

<sup>1</sup>For inversion of matrices with very large size alternative inversion techniques are implemented in Millepede II [80]

due to misalignment is given by:

$$\varepsilon = r_{hit}^{new} - r_{hit} \quad (5.21)$$

In the most general case, one has 6 degrees of freedom: 3 translations along the  $x$ ,  $y$ , and  $z$  axes (called  $\Delta_x$ ,  $\Delta_y$ ,  $\Delta_z$  respectively), and 3 rotations around the  $x$ ,  $y$ , and  $z$  axes (called  $\Delta_\alpha$ ,  $\Delta_\beta$ ,  $\Delta_\gamma$  respectively). Then  $r_{hit}^{new}$  hit is given by the relation:

$$r_{hit}^{new} = R_{\Delta_\gamma} R_{\Delta_\beta} R_{\Delta_\alpha} \cdot (r_{hit}^{s,new} - (r_0^s + \begin{pmatrix} 0 \\ 0 \\ z_0^s \end{pmatrix})) \equiv \Delta_R \cdot (r_{hit}^{s,new} - (r_0^s + \Delta_r)) \quad (5.22)$$

Here  $r_{hit}^{s,new}$  and not  $r_{hit}^s$  is used because the module was transferred to the global frame and the hit in the global frame has also moved. Hence, we need to derive the new interception point between the track and the displaced module.  $r_{hit}^{s,new}$  and  $r_{hit}^s$  belong to the same LMD track, which could be defined by two straight lines in the ( $x$ ;  $z$ ) and ( $y$ ;  $z$ ) planes. Thus one has:

$$r_{hit}^{s,new} = r_{hit}^s + h \cdot \begin{pmatrix} a \\ c \\ 1 \end{pmatrix} \quad (5.23)$$

where  $h$  is the parameter to be determined. By definition  $r_{hit}^{s,new}$  belongs to the displaced module, which means that its value in the displaced sensor frame,  $r_{hit}^{new}$ , is orthogonal to the  $z$ -axis in that frame:

$$r_{hit}^{new} \cdot \begin{pmatrix} 0 \\ 0 \\ 1 \end{pmatrix} = 0 \quad (5.24)$$

the full form of the Eq. 5.24 by using Eq. 5.22 is:

$$\Delta_R \cdot (r_{hit}^{s,new} - (r_0^s + \Delta_r)) \cdot \begin{pmatrix} 0 \\ 0 \\ 1 \end{pmatrix} = 0 \quad (5.25)$$

Assuming that rotations are small, a simplified expression for  $\Delta_R$  can be used:

$$\Delta_R = \begin{pmatrix} 1 & \Delta\gamma & \Delta\beta \\ -\Delta\gamma & 1 & \Delta\alpha \\ -\Delta\beta & -\Delta\alpha & 1 \end{pmatrix} \quad (5.26)$$

In first order one finds:

$$\Delta_R \cdot \Delta_r \approx \begin{pmatrix} \Delta_x \\ \Delta_y \\ \Delta_z \end{pmatrix} \quad (5.27)$$

Thus:

$$h = \frac{\Delta_z + x_{hit}^s \cdot \Delta\beta + y_{hit}^s \cdot \Delta\alpha}{1 - a \cdot \Delta\beta - b \cdot \Delta\alpha} \approx \Delta_z + x_{hit}^s \cdot \Delta\beta + y_{hit}^s \cdot \Delta\alpha \quad (5.28)$$

Now the expression of  $r_{hit}^{new}$  can be derived as:

$$r_{hit}^{new} = \Delta_R \cdot (r_{hit} + h \cdot \begin{pmatrix} a \\ c \\ 1 \end{pmatrix}) - \Delta_R \cdot \Delta_r \quad (5.29)$$

$$= \Delta_R \cdot \begin{pmatrix} x_{hit} \\ y_{hit} \\ 0 \end{pmatrix} + h \cdot \Delta_R \cdot \begin{pmatrix} a \\ c \\ 1 \end{pmatrix} - \Delta_R \cdot \Delta_r \quad (5.30)$$

which gives:

$$\begin{aligned} x_{hit}^{new} &= x_{hit} - \Delta_x + y_{hit} \cdot \Delta\gamma + a \cdot (\Delta_z + x_{hit} \cdot \Delta\beta + y_{hit} \cdot \Delta\alpha) \\ y_{hit}^{new} &= y_{hit} - \Delta_y - x_{hit} \cdot \Delta\gamma + c \cdot (\Delta_z + x_{hit} \cdot \Delta\beta + y_{hit} \cdot \Delta\alpha) \end{aligned} \quad (5.31)$$

$r_{hit}^{new}$  is the measured value and  $r_{hit}$  is the value corrected for the misalignment. The expression for the residuals as a function of the measured values is given by:

$$\begin{aligned} \epsilon_x &= x_{hit}^{new} - x_{hit} = -\Delta_x + y_{hit} \cdot \Delta\gamma + a \cdot (\Delta_z + x_{hit} \cdot \Delta\beta + y_{hit} \cdot \Delta\alpha) \\ \epsilon_y &= y_{hit}^{new} - y_{hit} = -\Delta_y - x_{hit} \cdot \Delta\gamma + c \cdot (\Delta_z + x_{hit} \cdot \Delta\beta + y_{hit} \cdot \Delta\alpha) \end{aligned} \quad (5.32)$$

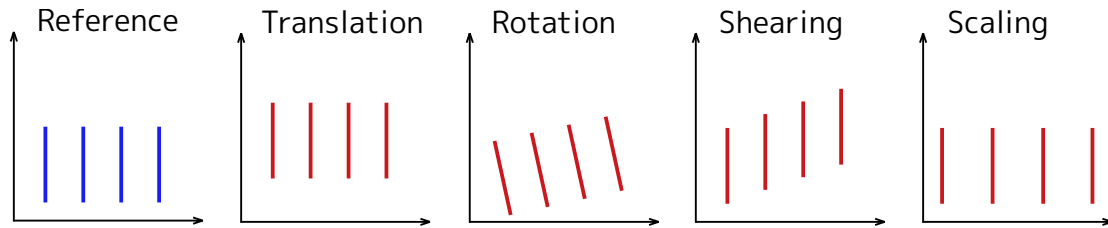


Figure 5.5: Illustration of the four basic types of linear transformations

Note the sensitivity to  $\Delta_z$ ,  $\Delta_\alpha$  and  $\Delta_\beta$  is proportional to the track slope, which is small in the case of the LMD. Hence these degrees of freedom are less important.

### 5.4.2 Constraining the internal alignment within Millepede

By definition, the internal alignment is insensitive to shifts of the complete sector. Thus it is necessary to introduce a set of constraints into the alignment procedure to prevent these correlated movements of the modules. The most simple solution is to control the variation of the alignment constants. The expectation is that maximum of the shift is in the order of the mechanical accuracy can be easily added as a constraining term to the  $\chi^2$ :

$$\chi_{const}^2 = \chi^2 + \frac{\Delta_i^2}{\sigma_i^2}, \quad (5.33)$$

where  $\Delta_i$  is the alignment parameter to be controlled, and  $\sigma_i$  is the maximum variation expected for the parameter. Currently these are taken from estimates of the mechanical accuracy of the system. This constraint is straightforward to be implemented, as only  $1/\sigma_i^2$  has to be added to the matrix element  $A_{i,i}$ .

However, one could also fix more powerful constraints with Millepede, using relationships between the alignment constants. Constraint equations are the best way to prevent global deformations of the system during the alignment procedure. The only possible deformations, in the case of the LMD, are linear transformations. The most simple example is a translation. There are four sorts of linear deformations, which are summarized in Fig.5.5. In three dimensions, this leads to 12 possible global deformations. Three of them can be neglected at first order: shearing in the XY plane, and scaling of the X and Y axis. In addition, due to the LMD geometry, it will be difficult to distinguish XZ and YZ shearing from Y and X rotations. Thus, following [79], only the XZ and YZ shearing are constrained.

Hence 7 possible deformations have to be constrained: a Z axis rotation, X, Y, Z translations, XZ and YZ shearing, and Z axis scaling. The way to introduce these constraints in Millepede is explained in detail in [80]. For the explanation of the basic

principle the X translation is taken as an example. Before the alignment:

$$\langle \Delta_x \rangle = \Delta_X \quad (5.34)$$

where  $\Delta_X$  is a global offset, which cannot be determined by an internal alignment. To avoid global translations along the  $x$  axis during the alignment procedure, a constraint equation is needed to be fixed. It can be performed by introducing the new parameter  $\Delta'_x$  related to  $\Delta_x$ :

$$\Delta'_x = \Delta_x - \Delta_X \quad (5.35)$$

By construction:

$$\langle \Delta'_x \rangle = 0 \quad (5.36)$$

Using this new formalism, known as *the canonical convention*, one is able to set 7 constraint equations. It should be mentioned here that the alignment constants from the internal alignment process are the  $\Delta'_i$ , i.e. the "offset-free" constants. As a further step the general offset of the modules in a sector can be extracted during alignment of the sectors. Therefore it is not subject of the studies presented below. For the comparison between the resulting  $\Delta'_i$  and the input parameters of the simulation studies, the general offset was subtracted from the input parameters.

## 5.5 Simulation test

Both track search algorithms (Chapter 4) have certain internal parameters, e.g. the size of the corridor during the track search with the Track Following algorithm or the breaking angle limit by using the Cellular Automaton algorithm. For the alignment tests discussed below the Cellular Automaton algorithm was used. A tuning of the breaking angle parameter was checked in dedicated simulation studies, where the modules were misaligned in all translation and rotation degrees of freedom. A generation of the tracks was done with the BOX generator, where one track per event was simulated within 3 and 8 mrad of the  $\theta$  angle and the full  $\phi$  angle. Afterwards, the simulated tracks were reconstructed with different values of the breaking angle limit. Fig. 5.6 shows the values of this parameter required to reach 90% of the track reconstruction efficiency with modules misaligned by translation  $\Delta_t$  and rotation  $\Delta_\alpha$  misalignment. For all following alignment studies the value of this parameter was set to 0.001.

The simulation studies were performed to proof that the alignment method discussed above can reach the desired alignment accuracy stated in Eq. 5.2 and Eq. 5.3. For the generation, the BOX generator was used in the  $\theta$  range from 2 to 12 mrad.

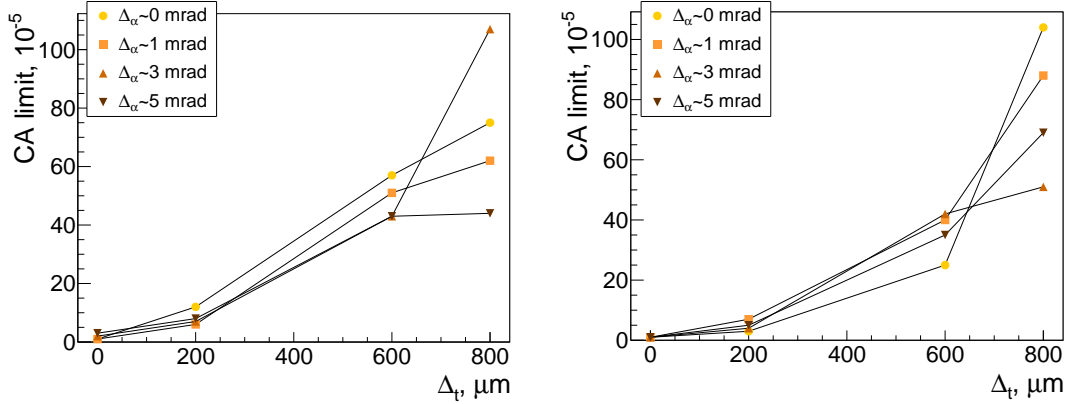


Figure 5.6: Required breaking angle limit for Cellular Automaton algorithm in case of translation  $\Delta_r$  and rotation  $\Delta_\alpha$  modules misalignment; tracks with momentum 1.5 GeV/c (left) and 15 GeV/c (right)

Statistical and systematic effects were studied in parallel.

For the statistical study several data samples<sup>2</sup> were generated for the same set of misalignment parameters as shown on the left panel of Fig. 5.7. The misalignment parameters for each module were sampled from a Gaussian distribution centered at 0 with a width  $\Delta_r$  for the translation and  $\Delta_r$  for the rotation degrees of freedom. Afterwards the parameters were applied at the hit reconstruction stage during the calculation of hit coordinates in the global frame. In such a way hits reconstructed with the misaligned geometry were obtained, which then are used in the standard track reconstruction procedure.

Then number of different sums of data samples was processed through the alignment algorithm as shown on the right side of Fig. 5.7. For the alignment task a self-written package is used, which is based on the toy tool Knossos [79] where the implementation of the Millepede algorithm is provided<sup>3</sup>. The alignment algorithm extracts the misalignment parameters, which are compared to the input parameters. By tracing the accuracy of the improvement of the parameters by matching them to the input values it is possible to figure out how many tracks are needed to perform the alignment accurately. To figure out the maximum limits for translation and rotation misalignment, which still can be corrected, a wide range of  $\Delta_r$  and  $\Delta_r$  values, from 0 to 800 μm and from 0 to 5 mrad, respectively, were used.

For the systematic studies different sets<sup>4</sup> of misalignment constants were generated and the procedure described above was repeated for each of these sets. The results shown below are the average of all misalignment parameter sets with a particular size of  $\Delta_r$  and  $\Delta_r$  and over all modules.

<sup>2</sup>100 samples, each with  $5 \times 10^4$  events with multiplicity 1 track/event

<sup>3</sup>Finally Millepede II will be used, but for these preliminary tests Knossos was sufficient

<sup>4</sup>5 samples of each  $\Delta_r$  and  $\Delta_r$  combination

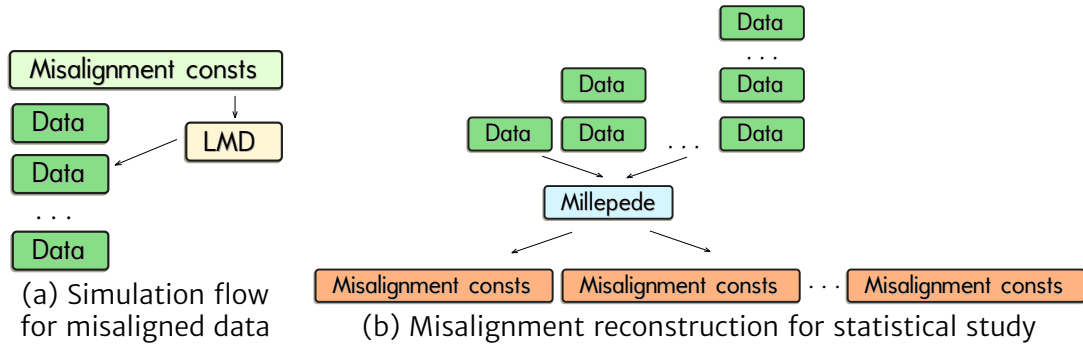


Figure 5.7: Schematic flow of misalignment studies

## 5.6 Limits for translation and rotation misalignment for high energy tracks

The most simple case for the misalignment determination is the usage of high energy tracks. In this case the uncertainty due to multiple scattering is negligible. Currently the multiple scattering is not included into the track model Eq. 5.9 is used in the simultaneous fit of the tracks and alignment parameters. Therefore the first tests were performed for antiproton tracks with a momentum of  $15 \text{ GeV}/c$ .

The results of the systematic study<sup>5</sup> of the determination of the alignment parameters is shown in Fig. 5.8 for the most sensitive parameters  $\Delta_x$  and  $\Delta_y$ . The conclusion of this study is that the desired accuracy, i.e.  $\Delta_t < 15 \mu\text{m}$ ,  $\Delta_r < 1 \text{ mrad}$ , can be achieved if the translation misalignment is below  $500 \mu\text{m}$  and the rotation misalignment is below  $5 \text{ mrad}$ . It should be mentioned that these limits can be extended by tuning of the internal parameters of Millepede, but since the limits are above the expected mechanical accuracy Millepede tuning was postponed.

The number of minimum required events for the alignment procedure is shown in Fig. 5.9 again for the  $\Delta_x$  and  $\Delta_y$  parameters. This test was done with the initial misalignment of  $\Delta_t \sim 200 \mu\text{m}$  and  $\Delta_r \sim 3 \text{ mrad}$ . As one can see starting from  $\sim 5 \times 10^4$  trks/sector there is no significant improvement. Thus it is possible to achieve  $\Delta_t \sim 2 \mu\text{m}$  and  $\Delta_r \sim 0.1 \text{ mrad}$  accuracy with just  $5 \times 10^4$  trks/sector. The minimum number of required tracks was also checked for different combinations of initial misalignment parameters  $\Delta_t$  and  $\Delta_r$  and the results are shown in Fig. 5.10. The number of tracks needed for an accurate alignment varies in dependence on the initial misalignment parameters. For a large misalignment more tracks are required for the alignment procedure than for a small misalignment. But with  $10^5$  trks/sector always good results can be achieved. Such number of tracks can be obtained within seconds of data taking. For Millepede it takes  $\sim 70 \text{ s}$  to process this number of tracks. As shown in Sec. 4.8 the track reconstruct-

<sup>5</sup>all available reconstructed data, i.e.  $2.5 \cdot 10^5$  tracks/sector, was used

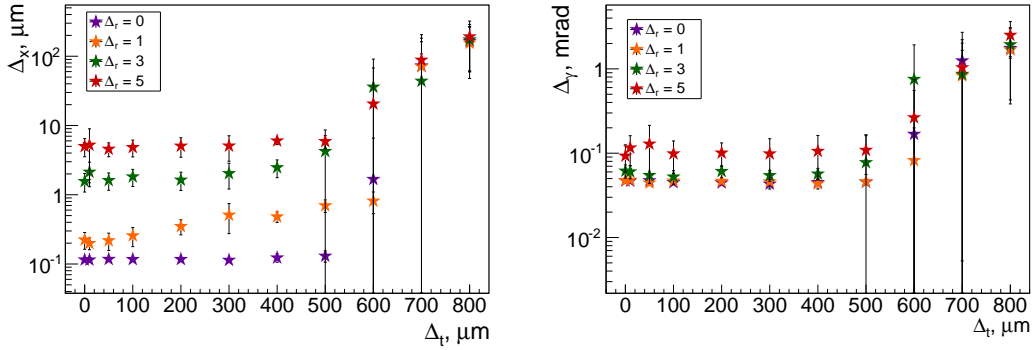


Figure 5.8: Remaining misalignment  $\Delta_x$  (left) and  $\Delta_\gamma$  (right) after the alignment procedure in dependence on the initial misalignment values of  $\Delta_t$  in translation and  $\Delta_r$  in rotation, for tracks with the momentum  $15 \text{ GeV}/c$

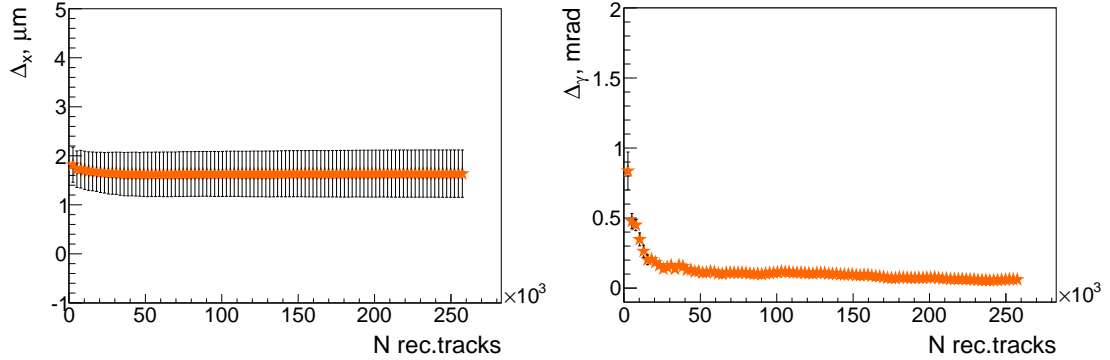


Figure 5.9: Remaining misalignment for  $\Delta_x$  (left) and  $\Delta_\gamma$  (right) parameters dependence on the number of tracks used for the alignment procedure with initial misalignment  $\Delta_t \sim 200 \mu\text{m}$  and  $\Delta_r \sim 3 \text{ mrad}$ , for tracks with the momentum  $15 \text{ GeV}/c$

tion takes  $\sim 1 \text{ ms}$  for one track, thus for  $10^5$  trks  $\sim 100 \text{ s}$  will be needed. Summing up all numbers it can be concluded that  $\sim 3 \text{ min}$  are required for the alignment procedure. Moreover, since this procedure is based simply on tracks and no dedicated data taking run is needed, the software alignment can be done as often as it is desired (e.g. after each movement of the LMD planes).

## 5.7 Limits for translation and rotation misalignment for low energy tracks

Currently multiple scattering is not included in the track model used during the alignment procedure. Fig. 5.11 illustrates the behavior of  $\Delta_x$  and  $\Delta_\gamma$  parameters in dependence on the number of tracks with momentum  $1.5 \text{ GeV}/c$  used for the alignment procedure for  $\Delta_t \sim 200 \mu\text{m}$  and  $\Delta_r \sim 3 \text{ mrad}$  initial misalignment. As one can see the

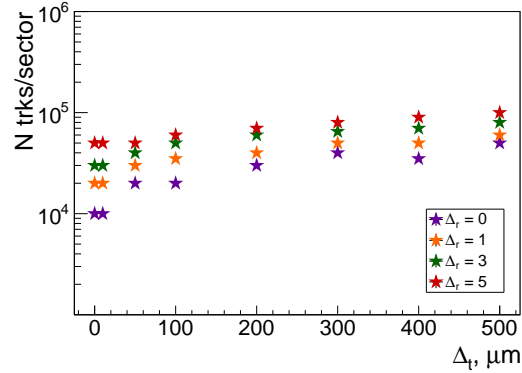


Figure 5.10: Required minimum number of tracks to achieve good alignment accuracy, for tracks with the momentum  $15 \text{ GeV}/c$

alignment procedure cannot treat multiple scattering, thus the resulting alignment parameters become worse by using a large number of tracks.

There are two possible ways to resolve this problem. The first one is to fix non-sensitive alignment parameters of the LMD (e.g.  $\Delta_z, \Delta_\alpha, \Delta_\beta$ ). The second solution would be to introduce multiple scattering and its parameters in the track model as it was done in the track fit procedure, described in Sec. 4.4. The last solution seems to be more accurate and this is a subject for future studies. For the reference here the results of the first solution are presented.

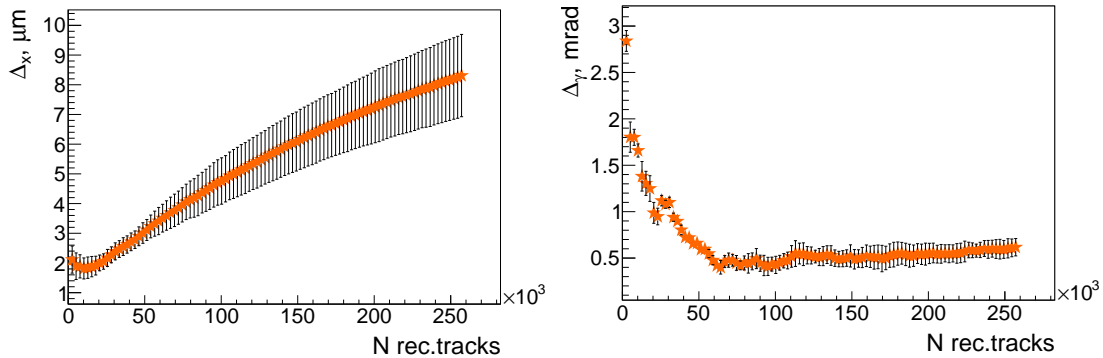


Figure 5.11: Remaining misalignment of  $\Delta_x$  (left) and  $\Delta_y$  (right) parameters in dependence on the number of tracks used for the alignment procedure with  $\Delta_t \sim 200 \mu\text{m}$  and  $\Delta_r \sim 3 \text{ mrad}$  initial misalignment, for tracks with the momentum  $1.5 \text{ GeV}/c$

Fig. 5.12 shows the  $\Delta_x$  and  $\Delta_y$  parameters improvement in dependence on the number of tracks used for the alignment procedure with fixed  $\Delta_z, \Delta_\alpha, \Delta_\beta$  values for  $\Delta_t \sim 200 \mu\text{m}$  and  $\Delta_r \sim 3 \text{ mrad}$  initial misalignment. Compared to the results with the non-fixed values (Fig. 5.11) the resulting misalignment is getting smaller with a higher number of tracks. The improvement down to  $\Delta_t \sim 2 \mu\text{m}$  and  $\Delta_r \sim 0.1 \text{ mrad}$  can be achieved with  $10^5$  trks/sector. And again the modules can be aligned to the desired accuracy, i.e. re-

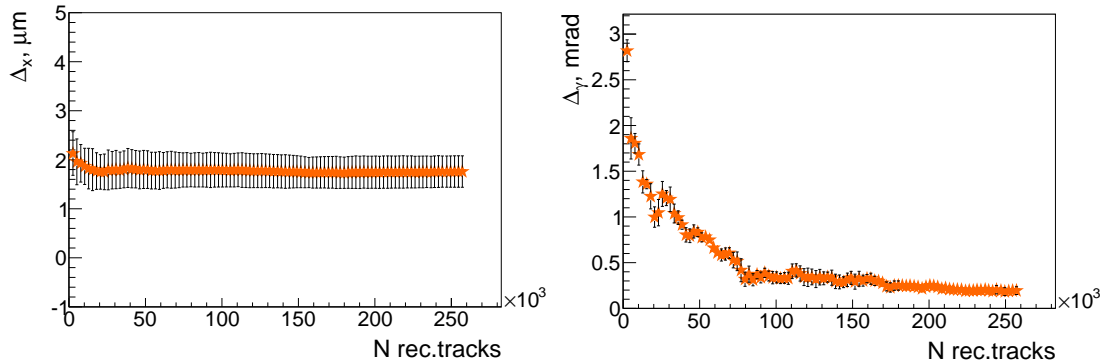


Figure 5.12: Remaining misalignment of  $\Delta_x$  (left) and  $\Delta_\gamma$  (right) parameters in dependence on number of tracks used for the alignment procedure with fixed  $\Delta_z$ ,  $\Delta_\alpha$ ,  $\Delta_\beta$ , initial misalignment  $\Delta_t \sim 200 \mu\text{m}$  and  $\Delta_r \sim 3 \text{mrad}$ , for tracks with the momentum  $1.5 \text{GeV}/c$

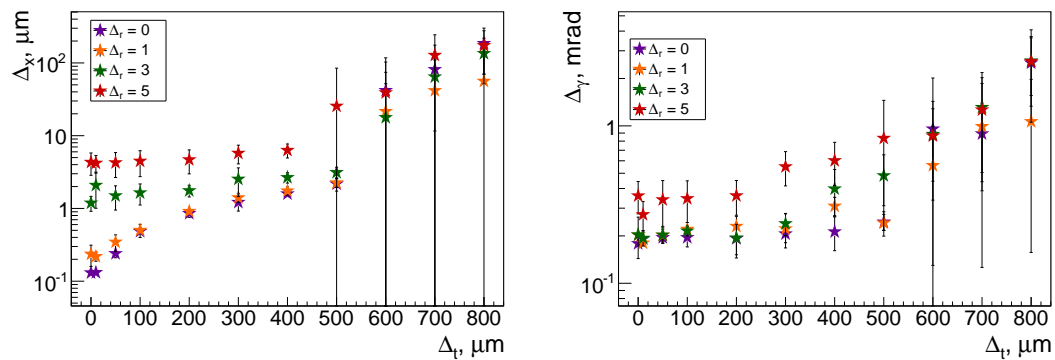


Figure 5.13: Remaining misalignment  $\Delta_x$  (left) and  $\Delta_\gamma$  (right) after the alignment procedure with fixed d.o.f in dependence on the initial misalignment values of  $\Delta_t$  in translation and  $\Delta_r$  in rotation, for tracks with the momentum  $1.5 \text{GeV}/c$

maintaining misalignment  $\Delta_t < 40 \mu\text{m}$  and  $\Delta_r < 3.5 \text{mrad}$ , if an initial misalignment below  $\Delta_t \leq 500 \mu\text{m}$  in translation and  $\Delta_r \leq 5 \text{mrad}$  in rotation as shown on Fig. 5.13.

# Background studies for the luminosity measurement

One of the main difficulties of the luminosity measurement at  $\bar{P}$ ANDA will be the presence of background. Currently there are no theoretical predictions of any differential cross section at small polar angles for the  $p\bar{p}$  inelastic interaction. And unfortunately in the nearest future no improvement of this situation is expected on the theory side. At the same time the LMD is supposed to be a relatively simple tracking system. It provides an accurate measurement of the track direction, but no measurement of the momentum magnitude or the particle species of the tracks. The latter information could be useful for the signal separation from background tracks, since from the inelastic interactions one can expect various particle species with different momenta.

The absence of any reliable quantitative assumptions about the background sources (channels, cross sections, particle species, their momenta, angular distributions and others) make an accurate simulation study challenging. This also means that one has to be prepared for any scenario. However, thanks to the magnetic field and the limited acceptance of the LMD, by far not all particles created in proton-antiproton inelastic reactions reach the LMD and produce enough hits for a track. By studying the behavior of the tracks of the inelastic background channels in comparison to the signal tracks, general properties for the reliable suppression of these channels are extracted.

First of all the kinematic signature was identified for the particles, which can reach the LMD. This was done in simplified simulation studies by the usage of the Runge-Kutta method, based on Eq. D.13 and [82], for the propagation of the tracks in a magnetic field. In the first part of this chapter the assumptions used for a simplification of the problem, the accuracy tests and results are discussed. The second part is dedicated to the studies with the DPM generator. DPM provides the description for various  $p\bar{p}$  inelastic channels with an estimate of their cross section [64]. Moreover in the DPM

generator the  $p\bar{p}$  elastic interaction [49] is also implemented. Therefore with the DPM generation of signal and background events, it is possible to examine their difference after the reconstruction.

## 6.1 Simplified simulation studies

In Section 4.6.2 the calculation of charged particle trajectories in the magnetic field was discussed. As it was already pointed out by Eq. D.1 the momentum of a particle has to be known. Moreover, for antiprotons coming from the elastic scattering the assumption to use the beam momentum is precise enough. Because this value is close to the real momentum of the particle. A small deviations between the assumed and the real momentum does not introduce a significant influences on the result of reconstruction. In general background particles can have any momentum. Thus the back propagation cannot be performed correctly if the deviation from the real momentum of the particle is too large. e.g. if a background particle originally comes from the IP, the resulting PCA after back propagation could be significantly shifted from the IP. If this is a systematic effect, it could be used for separation the background from the signal tracks.

In this study the Runge–Kutta method is used for a simplified estimate of the trajectories of particles with different momentum vectors (magnitudes and polar and azimuthal angles). By calculating of the trajectories to the detector starting from the IP (forward direction) the properties of the particles reaching the LMD are determined. Then the trajectory of each particle is calculated back to the IP, but the beam momentum magnitude is used instead of its real momentum. Using this method, general features of the reconstructed background tracks are determined.

### 6.1.1 Parameterization of the magnetic field

The  $\bar{P}$ ANDA magnetic field has a complicated structure. However the main influence on the tracks registered by the LMD is given by the dipole field which has negligible  $B_x$  and  $B_z$  components, thus the main influence comes from  $B_y$  component. For simplicity only this component was taken into account in this study. It was parameterized by a polynomial of 6th order. Fig. 6.1 shows the  $B_y$  component as it is provided in the PANDARoot software package, which is fitted by the polynomial distribution. Although this fit function does not describe the magnetic field perfectly, it gives a reasonable behavior in the  $z$  range between 325 cm and 620 cm. Before and after this range,  $B_y$

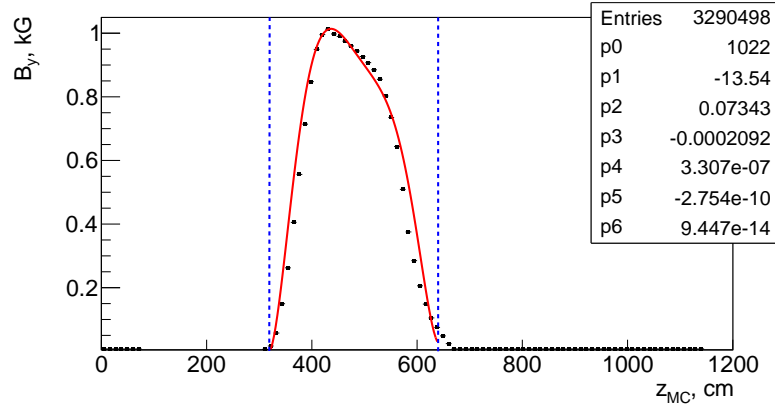


Figure 6.1:  $B_y$  component of  $\bar{\text{PANDA}}$  dipole field in dependence of the  $z$  coordinate ( $P_{beam}=1.5 \text{ GeV}/c$ )

is set to be 0:

$$B_y = \begin{cases} 0, & \text{if } z < 325 \text{ cm;} \\ \sum_{i=0}^6 p_i \cdot z^i, & \text{if } 325 \text{ cm} \leq z \leq 620 \text{ cm;} \\ 0, & \text{if } z > 620 \text{ cm.} \end{cases} \quad (6.1)$$

Such a parameterization was extracted twice: at the beam momentum of  $1.5 \text{ GeV}/c$  and  $15 \text{ GeV}/c$ .

### 6.1.2 Forward extrapolation

Obviously the main advantage of a complete simulation with GEANT4 is the accurate treatment of non-homogeneous magnetic fields. The comparison of the results between the simplified calculation and the simulation with GEANT4 gives an estimate about the systematic deviations introduced by the non-homogeneous magnetic field, which is not taken into account in this simplified simulation study. In both cases tracks were generated under the following conditions:

- starting point  $(x, y, z) = (0, 0, 0)$
- uniform in  $\theta \in [3, 8]$  mrad and  $\phi \in [-\pi, \pi)$  rad
- momentum  $p = P_{beam}=1.5 \text{ GeV}/c$
- charge  $q_{[e]} = -1$

Then results of the forward extrapolation were compared at a distance of  $z \approx 11 \text{ m}$ . For the simulation with GEANT4 the hit information on the first plane was used to obtain

the  $(x, y)$  coordinates of the hits and the direction of a track  $(\hat{\theta}, \hat{\phi})$  in the coordinate system of the LMD. For the simplified study a virtual plane at  $z=1124$  cm was considered. In this case the coordinates  $(x, y)$  and the direction  $(\hat{\theta}, \hat{\phi})$  of the tracks are the results of the track extrapolation to this  $z$  position. As shown in Fig. 6.2(top) the hit distributions in the  $(x, y)$  coordinates are qualitatively in agreement with each other. For the GEANT4 simulation distribution of  $(\hat{\theta}, \hat{\phi})$  (Fig. 6.2) the center position is higher than for the simplified simulation by  $\sim 2$  mrad. This can be explained by a slightly different shape of the magnetic field used in the simplified parameterization. In the following the results of the simplified simulation studies at different momenta will be always compared among each other. Therefore the absolute systematic shift of the polar angle  $\hat{\theta}$  does not have any influence.

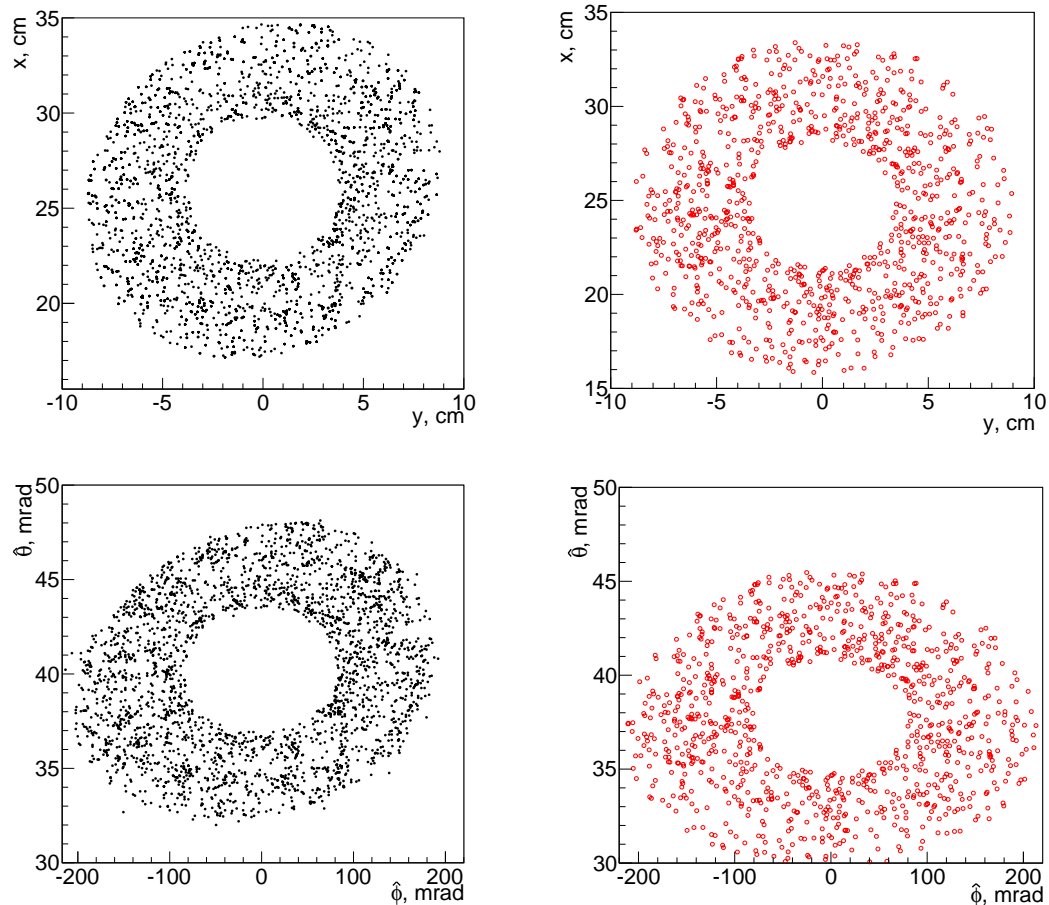


Figure 6.2:  $(x, y)$  (top) and  $(\hat{\theta}, \hat{\phi})$  (bottom) distributions of tracks at  $z=1124$  cm behind the IP after propagating particles through the magnetic field using GEANT4 (left) or the simplified extrapolation with the Runge-Kutta method (right)

### 6.1.3 Simulated data

$2 \times 9$  samples<sup>1</sup> with  $2 \times 10^6$  tracks each were generated under the following conditions:

- starting point  $(x, y, z) = (0, 0, 0)$  cm
- uniform in  $\cos\theta$  for  $\theta \in [0, \pi/8]$ , uniform in  $\phi \in [-\pi, \pi]$
- $p = P_{beam} + r \cdot P_{beam}$ , where  $r \in [-0.8, 0.8]$
- charge  $q[e] = -1, 1$

In each of the 9 samples for each charge value a different track momentum (parameter  $r$ ) was used. The aim is to cover tracks flying in forward direction with positive and negative charge, with a momentum different from the beam momentum  $P_{beam}$  within  $\pm 80\%$ . The data was generated with two magnetic field cases, which are planned to be used at the lowest  $1.5 \text{ GeV}/c$  and the highest  $15 \text{ GeV}/c$  beam momentum.

### 6.1.4 Check for consistency: forward - backward extrapolation

The accuracy check of the track extrapolation with the simplified Runge-Kutta method is done by back extrapolation to the starting point  $(x, y, z) = (0, 0, 0)$  with the momentum magnitude exactly the same as used in the generation. Therefore after the back extrapolation, the  $(x, y)$  coordinates of the tracks should be close to the initial values  $(0, 0)$ . A deviation from zero value gives an estimate of the systematic shift introduced by the uncertainty of the calculation. After the forward-backward propagation the  $y$  coordinate is 0 with  $\sim 1 \mu\text{m}$  precision independently of the track momentum and used magnetic field. This is not the case for the  $x$  coordinate, which deviates from the expected value. Fig. 6.3 shows the results for antiprotons propagated in the magnetic field at  $P_{beam} = 1.5 \text{ GeV}/c$  (left) and at  $P_{beam} = 15 \text{ GeV}/c$  (right). As one can see the deviation is as large as  $\sim 100 \mu\text{m}$  at  $P_{beam} = 1.5 \text{ GeV}/c$  and up to  $\sim 300 \mu\text{m}$  at  $P_{beam} = 15 \text{ GeV}/c$ .

The systematic shifts for the  $x$  coordinate after the back propagation with GEANT4 (Fig. 4.31) are  $\sim 70 \mu\text{m}$  and  $\sim 20 \mu\text{m}$  at  $P_{beam} = 1.5 \text{ GeV}/c$  and  $15 \text{ GeV}/c$ , respectively. The deviations in the simplified simulation studies are large, but still small compared to the resolution obtained in the GEANT4 simulation. For  $1.5 \text{ GeV}/c$  beam momentum, the spatial resolution near the IP is  $\sim 5 \text{ mm}$  and for  $15 \text{ GeV}/c$  it is  $\sim 1 \text{ mm}$ . For a reliable separation the deviation in the reconstructed parameters of the background and signal tracks should be large than the resolution of the corresponding parameter. In this sense systematic shifts introduced by the simplified method on the level of  $\sim 100 \mu\text{m}$  and  $\sim 300 \mu\text{m}$  (respectively for  $1.5$  and  $15 \text{ GeV}/c$ ) are acceptable.

---

<sup>1</sup>9 samples for each charge

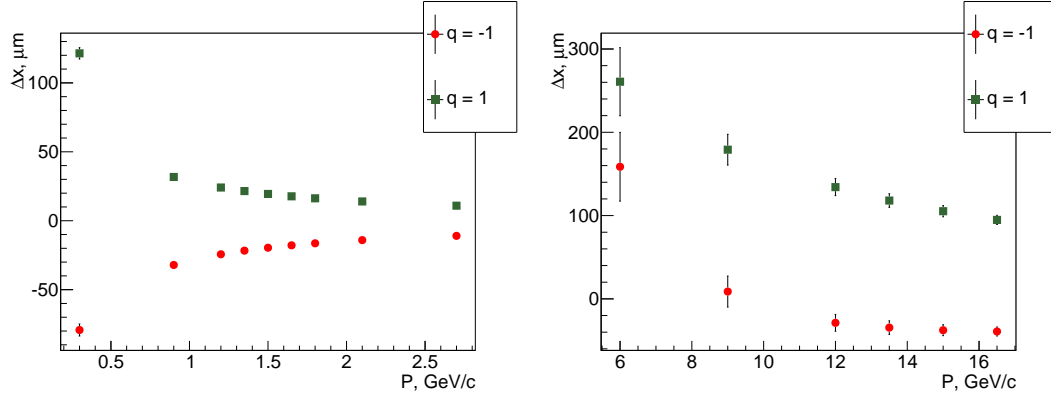


Figure 6.3: Shift of the x coordinate after forward-backward propagation for antiproton tracks with different momenta with the magnetic field for  $P_{beam}$  1.5 GeV/c (left) and  $P_{beam}$  15 GeV/c (right)

### 6.1.5 Tracks selection and suppression by cuts

In the case of the standard track reconstruction the suppression of the background is done before the back propagation (see Section 4.5.2). In this simplified simulation study, this procedure is emulated to study the suppression power on the background tracks with different track momenta. After extrapolation of each generated track to the LMD position  $z_e=1124\text{cm}$ , the following selection criteria are applied:

- Sensor area cut or  $(x,y)$  cut:  
 $3\text{ cm} < r < 9\text{ cm}$ ,  
 where  $r = \sqrt{(x - x_0)^2 + (y - y_0)^2}$ ,  $x_0 = 25\text{ cm}$ ,  $y_0 = 0$
- Angle cut or  $(\hat{\theta}, \hat{\phi})$  cut:  
 $|\hat{\theta} - \hat{\theta}_0| < 11\text{ mrad}$ ,  $|\hat{\phi} - \hat{\phi}_0| < 250\text{ mrad}$   
 where  $\hat{\theta}_0 = 38\text{ mrad}$  and  $\hat{\phi}_0 = 0$

The  $(x,y)$  cut selects only tracks which are passing the area of the LMD measurement sensors. And the  $(\hat{\theta}, \hat{\phi})$  cut emulates the background suppression by narrowing the range of the track angles to a range, which can be reached by elastic scattering events. The amount of tracks surviving the cuts is shown in Fig. 6.4 for the simulation studies at  $P_{beam} = 1.5\text{ GeV}/c$ . For the normalization the number of signal events  $N_{sig}$  is used, i.e number of tracks generated with  $q_e = -1$  (the charge of  $\bar{p}$ ) and the momentum equal to the beam momentum, which survived after both cuts<sup>2</sup>. All tracks with a charge different from the  $q_e = -1$  are completely suppressed after the cuts. Of course tracks with  $q_e = -1$  and a momentum close to the beam momentum  $1.5\text{ GeV}/c$  are able to pass all cuts with high probability. The bands in Fig. 6.5 show the  $\theta$  (left) and  $\phi$  (right)

<sup>2</sup>Not all tracks simulated with the momentum equal beam momentum and the charge equal  $\bar{p}$  charge pass the cuts, because simulation was done in wide  $\theta$  range compare to the acceptance of the LMD. The ratio between reconstructed signal tracks  $N_{sig}$  and the simulated  $N_{sim}$  is  $N_{sig}/N_{sim} = 0.12\%$

generated values for tracks with  $q_e=1$ , which were able to reach the LMD. Such particles could increase the counting rates in the LMD, but most probably will not disturb the luminosity extraction procedure because they will be suppressed by the cuts before the back propagation. Fig. 6.6 shows similar distributions for  $q_e=-1$ . Particles which passed all cuts had  $\theta$  angles below 20 mrad and a momentum above 0.9 GeV/c.

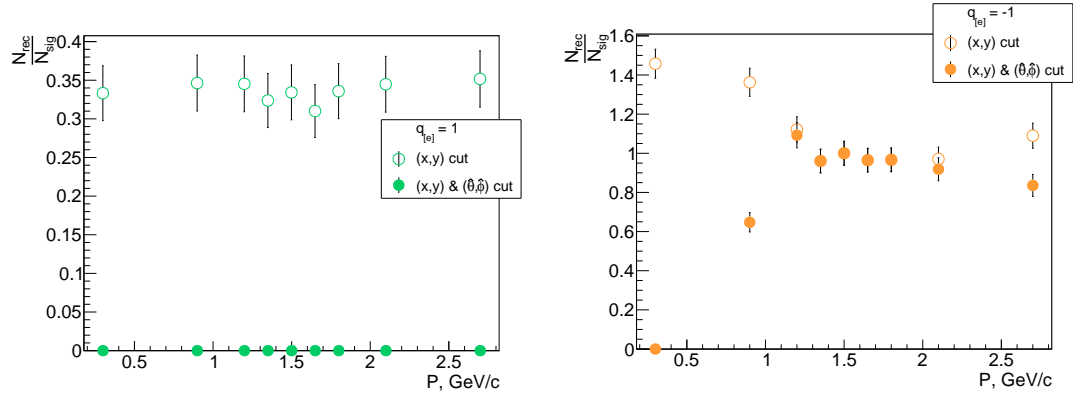


Figure 6.4: Number of tracks passing cuts in dependence of the track momentum. For  $q[e] = 1$  (left) and  $q[e] = -1$  (right). Error bars show statistical uncertainty ( $3\sigma_{N_{rec}/N_{sig}}$ ), beam momentum 1.5 GeV/c

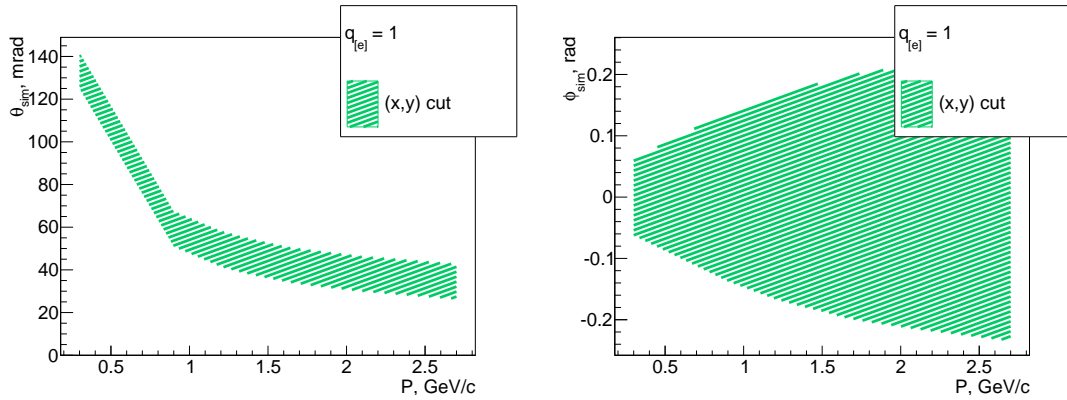


Figure 6.5:  $\theta$  and  $\phi$  values of the generated tracks with  $q[e]=1$ , which could reach the LMD, beam momentum 1.5 GeV/c

### 6.1.6 Backward extrapolation with «wrong» momentum

Background tracks which passed all the cuts are back propagated with a momentum assumption of  $p = P_{beam}$ , which is in fact deviating up to 70 % from the real momentum, as can be seen in Fig. 6.4. Thus it is interesting how this assumption affects the final reconstructed track parameters. Fig. 6.7 presents the distributions for reconstructed  $\theta$

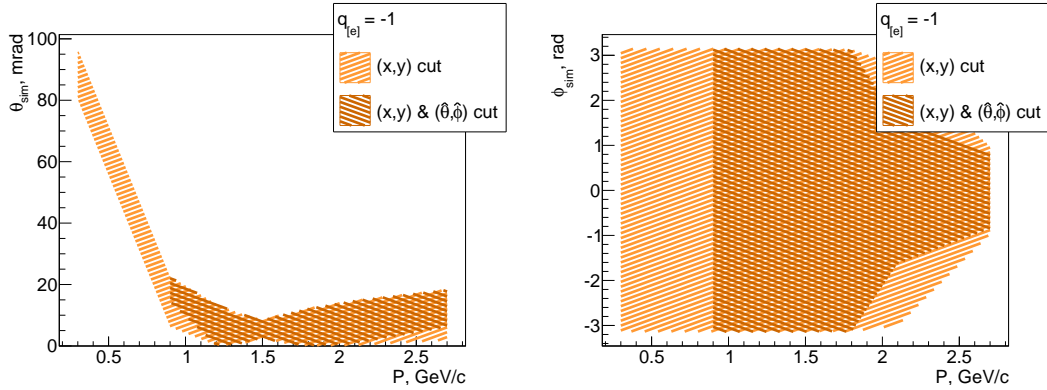


Figure 6.6:  $\theta$  and  $\phi$  values of the generated tracks with  $q[e]=-1$  which passed the cuts, beam momentum  $1.5 \text{ GeV}/c$

angle and x-coordinates of PCA. Unfortunately the background tracks, which pass both cuts, have reconstructed  $\theta$  angle in the expected region from 3–8 mrad as shown in Fig. 6.7(left) by the dark orange region. But the x coordinate of the PCA is systematically deviating from the expected zero value and the larger the difference between the real momentum of the particle and  $P_{beam}$ , the larger this deviation as shown in the right plot of Fig. 6.7. This deviation can reach a level of up to several cm, which is larger than the spatial resolution. Therefore this variable is a good candidate for the background suppression.

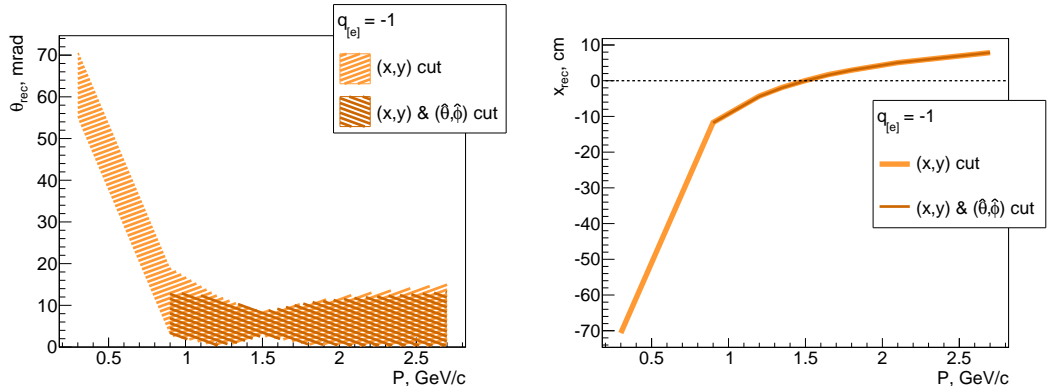


Figure 6.7:  $\theta$  and  $X_{PCA}$  reconstructed values for tracks with  $q[e]=-1$  which passed the cuts, beam momentum  $1.5 \text{ GeV}/c$

A study was also performed for a magnetic field as it will be used for the beam momentum of  $15 \text{ GeV}/c$ . As in the  $1.5 \text{ GeV}/c$  case, tracks of particles with  $q[e]=1$  are suppressed completely after the cuts (Fig. 6.8 normalization done in the same way as for  $1.5 \text{ GeV}/c$ , here  $N_{sig}/N_{sim}=0.05 \%$ ). The background particles which reach the LMD and pass all cuts have small values of  $\theta$  (Fig. 6.9), which are close to the LMD range if the momentum of a particle is close to the beam momentum. And as for the low

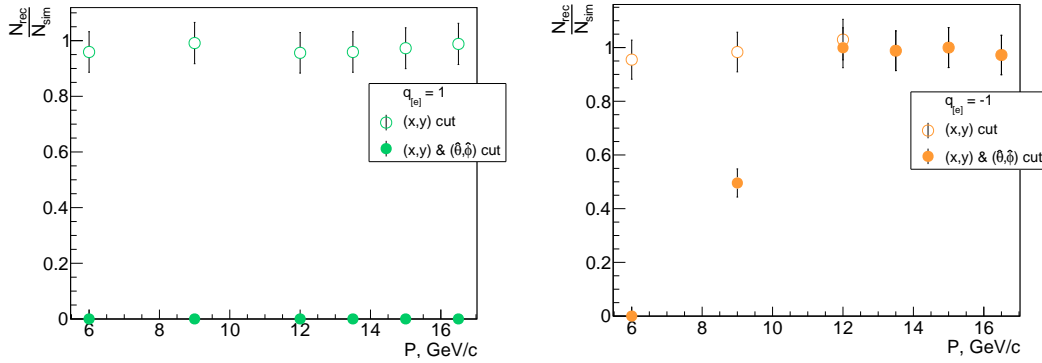


Figure 6.8: Number of tracks passing cuts in dependence of the track momentum. For  $q[e] = 1$  (left) and  $q[e] = -1$  (right). Error bars show statistical uncertainty ( $3\sigma_{N_{rec}/N_{sig}}$ ), beam momentum  $15 \text{ GeV}/c$

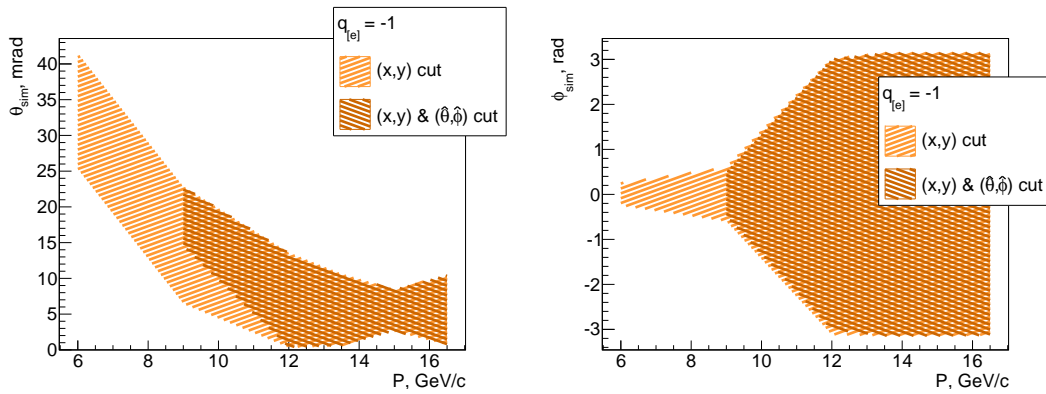


Figure 6.9:  $\theta$  and  $\phi$  values of the generated racks with  $q[e] = -1$ , which passed the cuts. Beam momentum  $15 \text{ GeV}/c$

$P_{beam}$  case, the x coordinate of the PCA is shifted after the back propagation (Fig. 6.10). However the shift for the surviving background tracks is close to the systematic shift introduced by the accuracy of calculation (Fig. 6.3).

This study shows that background tracks should have certain kinematics ( $\theta$  and  $\phi$  angles and momentum) properties to reach the LMD and pass cuts which are used to select the elastic scattered antiprotons. These values are different for particles, which feature a momenta significantly different from the beam momentum  $P_{beam}$ . The closer the background particle momentum is to  $P_{beam}$ , the closer are its kinematic variables to that from signal events, which can be fully reconstructed and pass all the cuts. Even though particles with a charge opposite to the antiproton charge can reach the LMD, they are fully suppressed by the angular cut. For tracks with a charge equal to the antiproton charge this suppression works only if the particle momentum is less than  $P_{beam}$  by at least 40%.

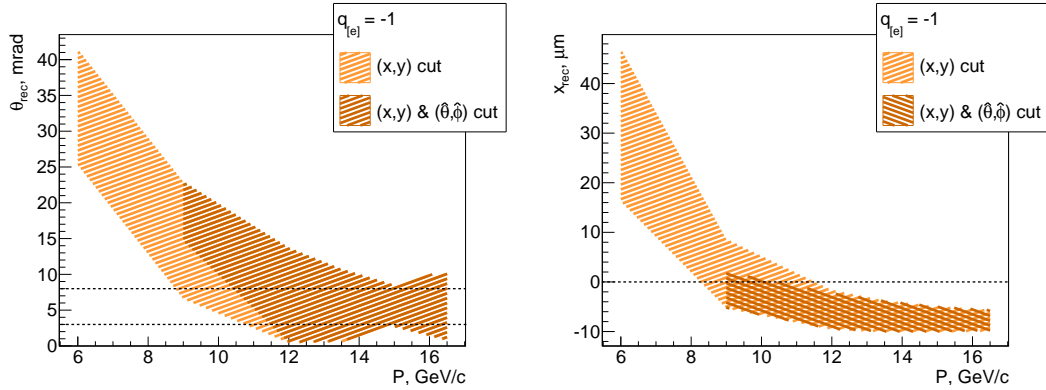


Figure 6.10:  $\theta$  and  $X_{PCA}$  reconstructed values for tracks with  $q[e]=-1$ , which passed the cuts. Beam momentum  $15 \text{ GeV}/c$

## 6.2 Background studies with the DPM generator

Only a qualitative description of the properties of the remaining background tracks can be provided in the simplified simulation study. For the quantitative estimation a description of the  $p\bar{p}$  inelastic interactions is needed. This is a purpose of the DPM generator, which is a basic background generator used for  $\bar{\text{PANDA}}$  simulation studies.

Usually the internal structure of hadrons is described in terms of quarks and gluons. Experimentally quarks and gluons were not observed as stand-alone particles and moreover the spatial configuration of quarks and gluons inside hadrons is still under investigation. This phenomenon lies in the non-perturbative domain of QCD, where calculations from basic principles are difficult. Therefore many different phenomenological approaches are induced. Among others the dual models found great popularity as a basic model used in modern simulation programs (e.g GEANT4), where this approach is generally used to simulate processes with light hadrons, i.e. color-neutral objects with u,d and s quarks.

The Dual Parton Model is a synthesis of the Regge phenomenology, quark ideas and  $1/N_f$  expansion of QCD [83]. The energy dependence of the cross sections of the  $p\bar{p}$ -processes is given by the Regge phenomenology. The cross sections are in correspondence with diagrams of the  $1/N_f$  expansion of QCD. The diagrams describe the creation of unstable intermediate states – quark-gluon strings. The string fragmentation is considered at quark level. The main problem is the description of the low mass string fragmentation and the fragmentation of massive constituent quarks. It is solved by choosing various phenomenological dependencies. As a result a good description of various inelastic reactions was reached and this approach is used in the Monte Carlo generator, called DPM, for the simulation of background events at  $\bar{\text{PANDA}}$ . The DPM model is described in Appendix F in more detail.

The advantage of Dual Models is a direct physical picture, which together with quan-

tum field theory leads to many reasonable results. A disadvantage is the large number of parameters which have to be tuned by experimental data. The model also lacks of an accurate description of any particular finale state, e.g its differential cross sections, angular distributions of particles in finale state, etc. Nevertheless it provides estimation of the total cross section for each channel.

### 6.2.1 DPM validation on available data

The DPM generator provides a generation of all inelastic  $p\bar{p}$  channels with light hadrons at once. For the estimation of the DPM accuracy, it is reasonable to compare DPM generator results with the dominating inelastic channels of the  $p\bar{p}$  interaction. Unfortunately only very little data on  $\bar{p}p$  interactions is available for the PANDA energy range. An overview of the previous experiments is presented in Appendix B.

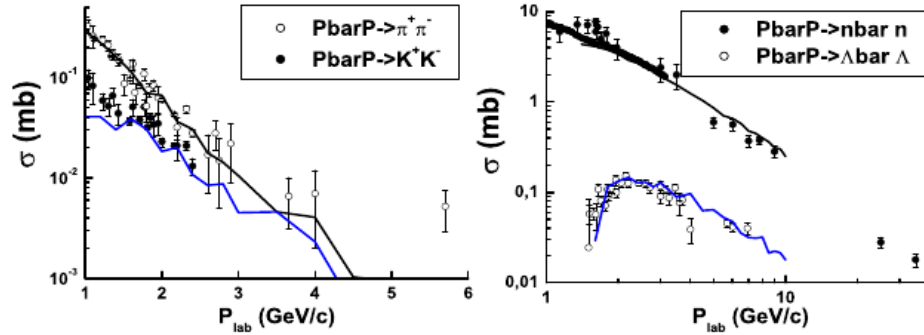


Figure 6.11: Cross sections for 2-particle final state reactions, solid line shows the DPM prediction ([83])

Fig. 6.11 shows the comparison between data [84] and the DPM model for 2-particle final states and Fig. 6.12 for 3-particle and 4-particle final states [83]. There is an agreement between DPM and the data for 2-particle final states channels visible. In general DPM matches data within the experimental errors. As can be seen in Fig. 6.11 only for  $p\bar{p} \rightarrow \pi^+\pi^-$  and beam momenta above 5 GeV/c the measured cross section is around  $5 \cdot 10^{-3}$  mb, but DPM predicts this value to be much lower. However at such energies, channels with more pions are dominating and the total inelastic cross section is  $\sim 30$  mb [1]. Thus the discrepancy for such small contributions to the total cross section can be ignored. For channels with 3- and 4-particles in the final state, DPM is in good agreement with  $p\bar{p} \rightarrow \pi^+\pi^-\pi^0$ ,  $p\bar{p} \rightarrow \Lambda\bar{\Lambda}\pi^0$  and  $p\bar{p} \rightarrow \Lambda\bar{\Lambda}\pi^+\pi^-$  in the whole energy range. At low energies (below  $P_{beam}=4$  GeV/c) DPM overestimates the cross section for the channels  $p\bar{p} \rightarrow p\bar{p}\pi^0$ ,  $p\bar{p} \rightarrow p\bar{p}\pi^+\pi^-$  and underestimates it for  $p\bar{p} \rightarrow 2(\pi^+\pi^-)$ .

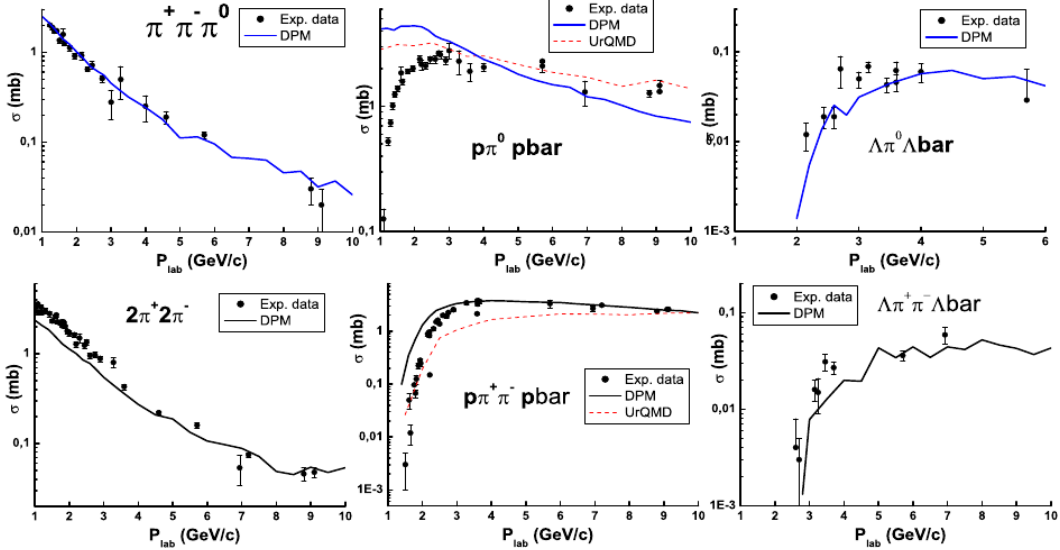


Figure 6.12: Cross sections of 3-particle (upper figure) and 4-particle (bottom figure) final state reactions, solid line shows the DPM prediction ([83])

No comparison for other interesting channels, e.g. the 5-pion final state, which dominates among the multi-pions channels at  $P_{beam}$  below 8 GeV/c (Fig. 6.13), is provided in the DPM publications. The  $p\bar{p}$  reactions with a cross sections on the level of mb are discussed in [85]. The data and the fit from [85], generously provided by Alaa Dbeyssi, were used for a DPM comparison at lowest and highest  $P_{beam}$  (1.5 and 15 GeV/c) respectively. The results are presented in Fig. 6.13 for channels with multiple pions final states (left) and for channels with antiprotons in the final state (right). The cross section for the multiple pion channels is decreasing with beam momentum. And depending on the number of pions in the final state, it varies between 2–20 mb at low beam momenta to  $10\ \mu\text{b}$ –1 mb at high beam momenta. The DPM results lie in that cross section ranges for both beam momentum values. However its absolute estimate is not very accurate. Moreover, for the channel  $p\bar{p} \rightarrow \pi^+\pi^-\pi^0$  there is a significant discrepancy at the lowest  $P_{beam}$  (Fig. 6.13, left), which was not observed in the results of [83]. The reason for this is not clear, some assumptions are discussed in Appendix F.

For channels with antiprotons (Fig. 6.13, right), particularly  $p\bar{p} \rightarrow p\bar{p}\pi^0$  and  $p\bar{p} \rightarrow p\bar{p}\pi^+\pi^-$ , DPM gives a similar overestimation of the cross section at low beam momenta as in [83]. The channel  $p\bar{p} \rightarrow \bar{p}\pi^+n$  follows this trend. These processes are described by the same diagram in DPM, therefore a similar systematic discrepancy behaviour can be explained by the accuracy of the estimation of this particular DPM contribution.

At the highest planned energy point at  $\bar{\text{P}}\text{ANDA}$ , there is no data available for any of these channels. However [85] provided extrapolations between lower and higher beam momenta. One can note (Fig. 6.13) that DPM does not match these extrapolations.

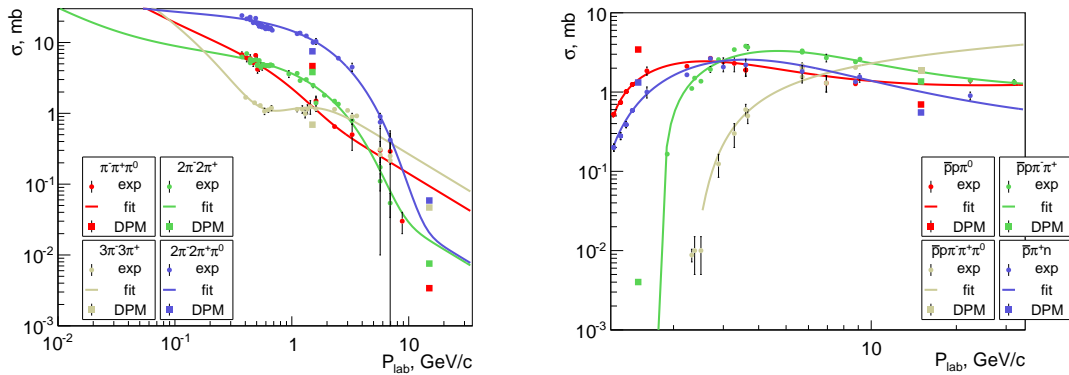


Figure 6.13: Comparison between DPM results and experimental data ([84]) in the PANDA energy range, fit results from [85]

The DPM generator was not intended to provide the correct behavior of the differential cross sections, e.g. in dependence on polar angle, of inelastic interactions. A comparison of angular distributions between DPM and the dedicated  $p\bar{p} \rightarrow \pi^+\pi^-$  generator [86] is shown in Fig. 6.14 and illustrates this fact. Most essential for the simulation of the background channels is that at small polar angles the DPM generator always predicts a smaller number of events than the dedicated  $p\bar{p} \rightarrow \pi^+\pi^-$  generator. Thus for simulations with the DPM generator, the background contributions from inelastic events registered in the LMD for this particular channel are underestimated. Unfortunately it is not possible to validate the angular distributions of each individual inelastic channel contributing to the background in the LMD, due to the enormous number of them. But from the comparison given above one can conclude that quantitative results of the simulation studies with DPM should be used with caution.

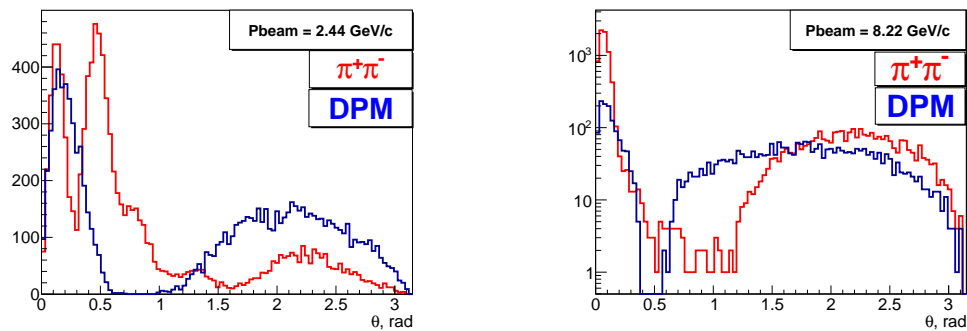


Figure 6.14: Angular distributions obtained with a dedicated  $p\bar{p} \rightarrow \pi^+\pi^-$  (red) and the DPM (blue) generators

Thus in the following not only the total amount of background contribution, but also some intermediate information is provided, e.g. a list of inelastic channels contributing

to the background. Hopefully in the nearest future, these channels will be measured more precisely with  $\bar{\text{PANDA}}$  and the accuracy of the estimation will be improved. To conclude, the study presented here should be considered as a first step towards a more accurate background estimation for the luminosity measurement.

## 6.2.2 Simulation description

All background sources can be subdivided into three groups. To the first group belong particles which are produced at the IP through proton-antiproton inelastic interactions. In the following this group is called *primary inelastic* particles. The second group consists of particles which are produced through the interaction of primary particles with material of the  $\bar{\text{PANDA}}$  detector. This group is referred as *secondary* particles. As it is shown in the next section, elastically scattered antiprotons at  $\theta$  angles above the LMD acceptance range cannot be reconstructed correctly and thus should be considered as a third background source. Besides inelastic channels, the DPM generator also allows to simulate  $p\bar{p}$  elastically scattered events in the full  $\theta$  range. Therefore DPM is taking care of all sources of background produced at the IP.

The secondary particles production is a task of the simulation package GEANT4. The modelling of secondary hadronic interactions in a wide range of energies is one of the most challenging tasks. For this reason, the set of hadronic physics models is one of the key components of GEANT4. Since there is no a single hadronic model to cover the entire energy domain from zero to the TeV scale for all known processes and all known particles, models have to be combined to cover the large energy range. This concept is known as a physics list, where every two adjacent models may have an overlap in their validity range. There are two models for this task in the  $\bar{\text{PANDA}}$  energy range: The Quark-Gluon String Precompound (QGSP) model [87] and the quark-gluon string model – FRITIOF (FTF) [88]. None of them was explicitly validated in this energy range on real data. Although the developers of GEANT4 claim that the FTF model should be in general more accurate [89]. The energy range of the FTF model starts from  $\sim 3$  GeV, while the QGSP should be valid for energies above 12 GeV (Fig.6.15, left). At low energies the Bertini approximation is used. This is proven to be valid below 5 GeV [89] and it should work with a certain accuracy between 5 and 10 GeV [88]. Therefore from the validation ranges provided by the GEANT4 team the most suitable physics list for  $\bar{\text{PANDA}}$  should be FTF\_BERT, which combines the FTF and the Bertini models.

For the comparison between the QGSP and the FTF models, a simulation study was performed, in which the antiprotons were generated uniformly within  $\theta \in [2,12]$  mrad and  $\phi \in [0,2\pi]$ . Fig.6.15 (right) shows the number of completely reconstructed tracks from secondary particles in dependence on the antiproton momentum for the simulation performed with the QGSP\_BERT\_EMV and the FTF\_BERT physics lists. The QGSP model predicts the number of secondary particles between 0.05% and 0.5%. From the

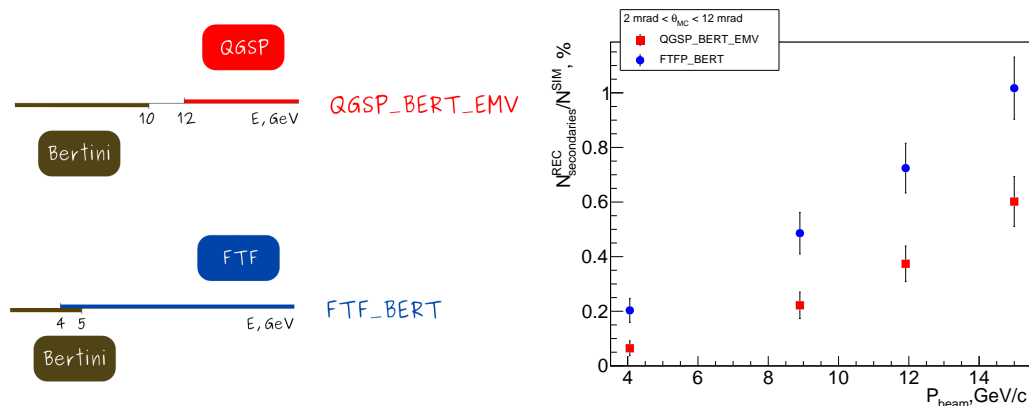


Figure 6.15: QGSP\_BERT\_EMV versus FTF\_BERT models of GEANT4: (left) the energy coverage range; (right) number of secondary tracks reconstructed in the LMD for each model (no cuts applied)

FTF model a more significant fraction of secondary particles can be expected (up to 1%). Therefore the FTF\_BERT physics list is used in simulations for the background studies.

For the estimation of the secondary particle production with GEANT4, one has to provide the information about all possible material in the way of the particles to the LMD. For signal antiprotons (coming from elastic scattering at small angles), the description of the beam pipe vacuum and the LMD would be enough. However the possibility of secondary particle production within other sub-systems of the  $\bar{\text{P}}\text{ANDA}$  cannot be excluded. Therefore all sub-systems available in the detector geometry description of PANDARoot were included in the simulation. The state of art<sup>3</sup> geometry model is shown in Fig. 6.16. The detector cave is surrounded by air. Also the realistic vacuum in the beam pipe<sup>4</sup> was used in the simulation.

<sup>3</sup>end of 2013, svn version r23744

<sup>4</sup>201309 version

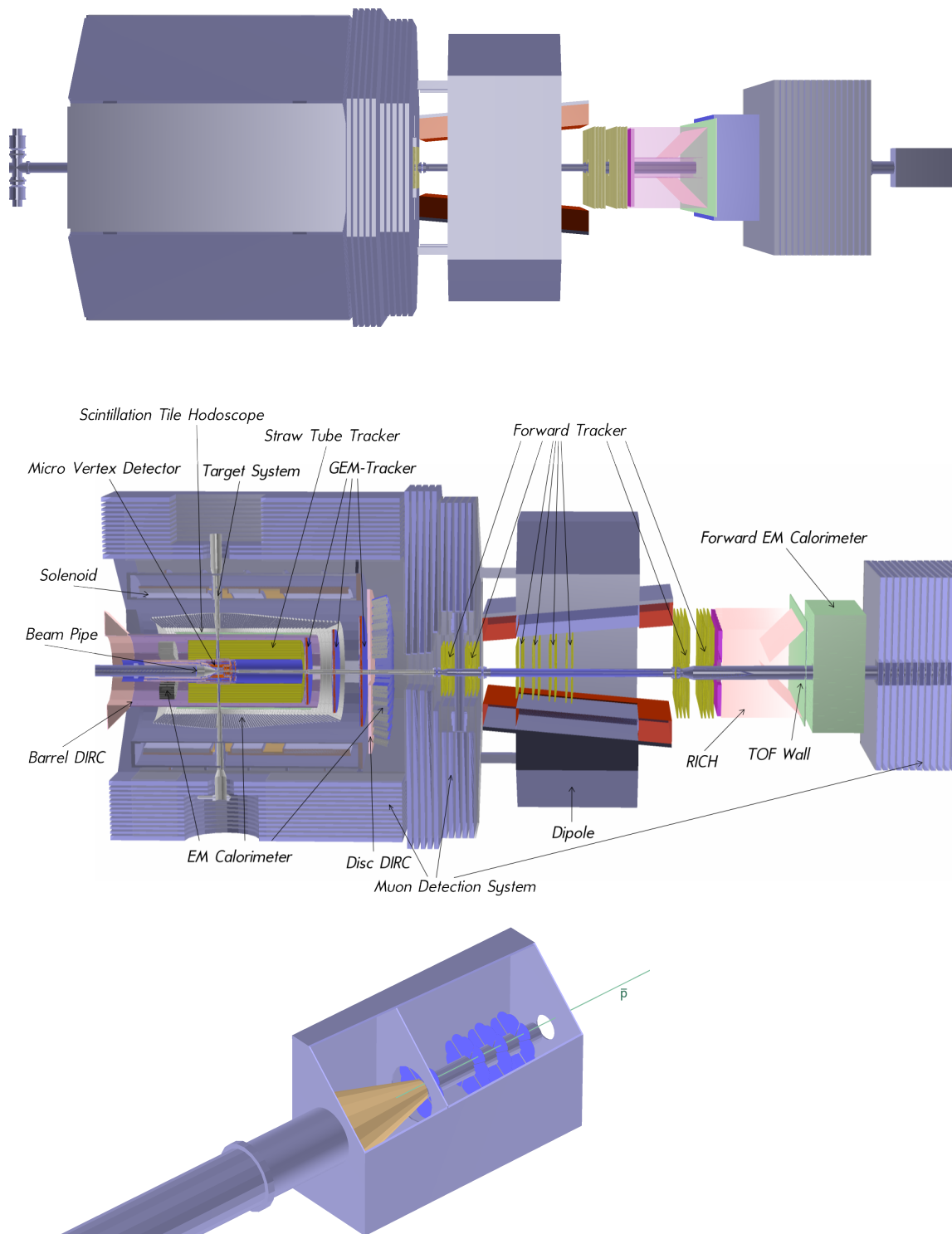


Figure 6.16: PANDArOOT geometry model: general overview (top), the LMD (bottom) and all other Panda subsystems (middle) components used in simulation

### 6.2.3 Antiprotons from elastic scattering as a background source

Besides primary particles from inelastic interactions at the IP and secondary particle production in the detector material, it turned out there is a third source of background: elastic scattered antiprotons with relatively large scattering angles. These particles are re-scattered on their way to the LMD, thus their original polar angle at the IP cannot be reconstructed accurately. Fig. 6.17 illustrates this background source, where the reconstructed polar angles  $\theta_{REC}$  are shown versus the generated values  $\theta_{MC}$ . Tracks with a generated polar angle  $\theta_{MC}$  below 8 mrad show a strong correlation to the reconstructed angles (visible as a band with higher density of tracks in Fig. 6.17). For tracks with  $\theta_{MC}$  above 8 mrad, the reconstructed angles are randomly distributed within all possible values. It should be mentioned that the detector is designed to have  $\sim 100\%$  acceptance for  $\theta \in [3, 8]$  mrad. Thus tracks with  $\theta_{MC}$  above 8 mrad should not be reconstructed at all. They can only be seen because of re-scattering of these tracks on the way to the LMD, which most probably happens on the walls of the beam pipe.

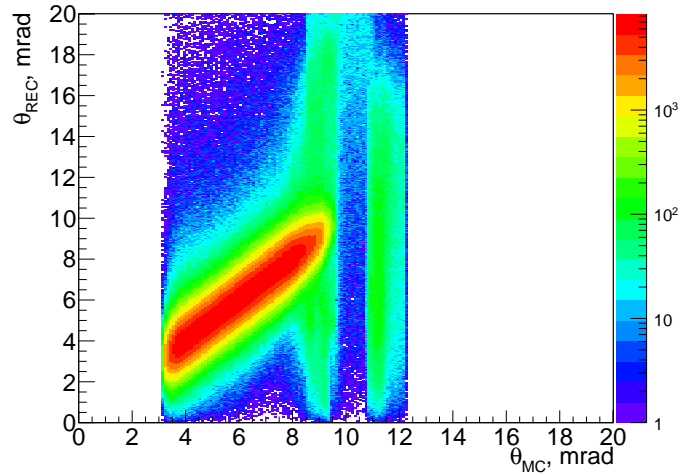


Figure 6.17: Reconstructed versus generated polar angle  $\theta$  for elastic scattered antiprotons at  $P_{beam}=1.5 \text{ GeV}/c$

The information about the re-scattering process is not stored during the simulation steps. Thus the simulation data does not contain enough information to identify these kind of events. The polar angle is the most important variable of the reconstructed tracks. So one can define the border between good and bad reconstructed tracks by looking at a difference between the generated  $\theta_{MC}$  and the reconstructed  $\theta_{REC}$  polar angle:

$$|\theta_{MC} - \theta_{REC}| < \Delta\theta \quad (6.2)$$

There is still the question how large the difference  $\Delta\theta$  can be before the usage of too

many background tracks within this corridor will affect the precision of the luminosity extraction. Therefore a simulation study with luminosity extraction was performed for  $P_{beam}=1.5\text{ GeV}/c$ . During the reconstruction no cuts were used. But for the luminosity extraction procedure only tracks were used which satisfied the condition (6.2), where  $\Delta\theta$  was varied between 0.7 mrad and 70 mrad. The difference between generated and the reconstructed luminosity  $\Delta L$  as a function of  $\Delta\theta$  is shown in Fig. 6.18. If  $\Delta\theta$  is too large the data sample had a significant contribution from background tracks and therefore the luminosity value is overestimated and  $\Delta L$  is negative. If  $\Delta\theta$  is too small then too many correctly reconstructed tracks are cut and one can observe an underestimation of the luminosity value. Also it should be mentioned that for small values of  $\Delta\theta$ , it is difficult to determine the correct behavior of the detector resolution, which is required for the accurate luminosity fit, leading to an increase of the systematic error. The balance in terms of almost no systematic shift for the luminosity determination is achieved with tracks within a  $\Delta\theta=2.1$  mrad corridor. This value corresponds to  $3\sigma_\theta$  of the  $\theta$  resolution at this energy. This study was repeated for  $P_{beam}=15\text{ GeV}/c$ , where the optimal  $\Delta\theta$  is also found to be  $3\sigma_\theta$ . Therefore tracks within the  $3\sigma_\theta$  corridor are considered as *signal* tracks. Tracks coming from elastic scattering, but with a large difference between the generated and the reconstructed values are regarded as the *elastic* background contribution.

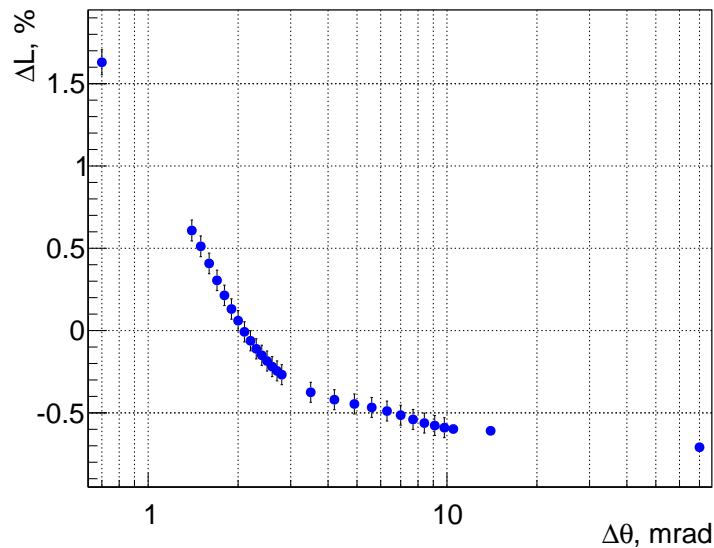


Figure 6.18: Influence of the  $\Delta\theta=|\theta_{MC}-\theta_{REC}|$  corridor on the luminosity extraction at  $P_{beam}=1.5\text{ GeV}/c$

## 6.2.4 Background distribution

The complete simulation with the DPM generator was done at five different beam momenta. At each energy  $2 \times 10^7$  events in the "elastic and inelastic" mode of DPM were generated, for which the elastic scattering  $\theta_{min}$  was set to  $0.12^\circ$ . Each simulation was repeated 3 times to make sure that the results are reproducible and in the following the average results are presented.

Fig. 6.19 shows the contribution of each background source and the sum as a ratio between the number of reconstructed background tracks to the number of reconstructed signal tracks. The inelastic background contribution is increasing with an increase of the antiproton beam momentum. This is expected since the ratio between the inelastic and the elastic cross section is rising with increasing energy. The total amount of reconstructed background tracks varies between  $\sim 4\%$  at low beam momentum to  $\sim 20\%$  at the highest momentum. The number of completely reconstructed tracks per event is also different for low and high energy cases as shown in Fig. 6.20. At  $P_{beam}=15\text{ GeV}/c$  it can be as high as 8 track per event. It should be stressed that without the dipole magnet in front of the LMD the amount of the background events would be much higher and could reach the 15% level at  $P_{beam}=1.5\text{ GeV}/c$  and 50% at  $P_{beam}=15\text{ GeV}/c$ .

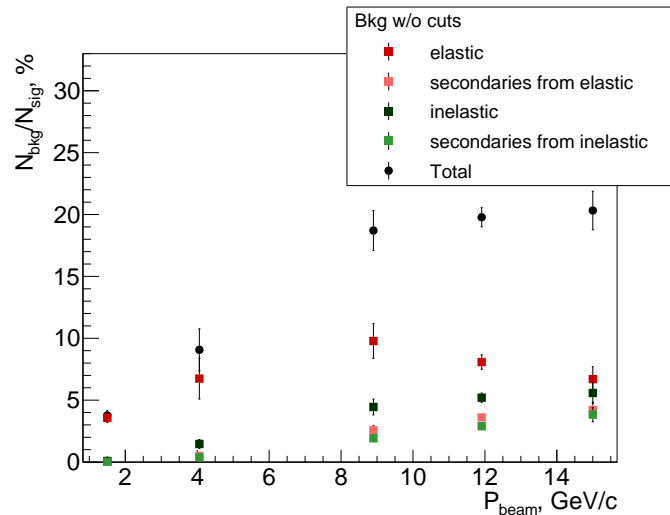


Figure 6.19: Relative background contributions (no cuts) in dependence on the beam momentum

The pie charts in Fig. 6.21 show the contribution of different particle species from primary and secondary inelastic interactions which hit the LMD at  $15\text{ GeV}/c$ . To complete this information in Tab. 6.1 a list of inelastic channels is given, which contribute to the background by primary particles tracks. Channels with a high total cross section have a higher chance to produce background particles. At  $15\text{ GeV}/c$  beam momentum,

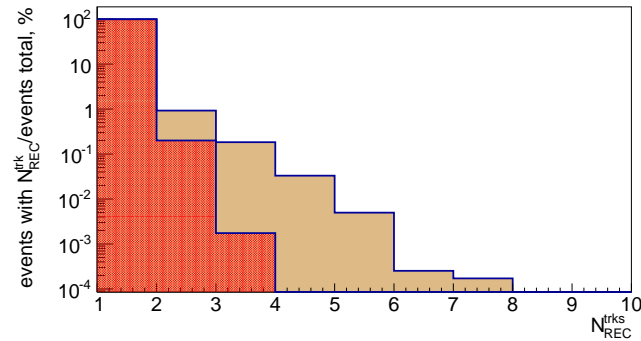


Figure 6.20: Number of reconstructed in the LMD tracks per event before cuts for 1.5 GeV/c (red) and 15 GeV/c (beige) obtained in simulations with DPM (elastic and inelastic  $p\bar{p}$ )

inelastic channels with antiprotons in the final state dominate and the same tendency is observed in the background contribution in the LMD. For secondary particles pions dominate, however, the antiproton fraction is still the largest (see Fig. 6.22 right). At low beam momentum final states with pions dominate, thus the main background particles for the LMD at low energies are pions (Fig.6.22 left). Therefore a system for particle identification would be very useful only at low beam momenta, where a relative contribution from pions is as large as 80%.

The kinematic distributions of the background tracks (Fig. 6.23), are in agreement with the results of the previous simplified simulation studies (Section 6.1). The main contribution are tracks with small polar angles  $\theta$ . The momentum spectrum of the background particles is rather broad. The distance between the IP and the LMD is not that far and time of flight for the background particles is different from the time of flight for the signal only by 3 ns.

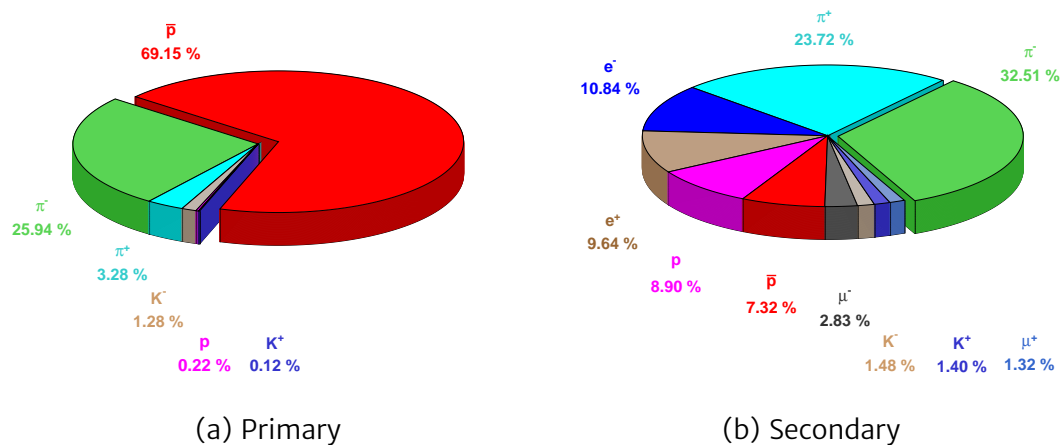


Figure 6.21: Relative contribution to the primary and secondary background sources at 15 GeV/c without cuts (elastic contribution is excluded)

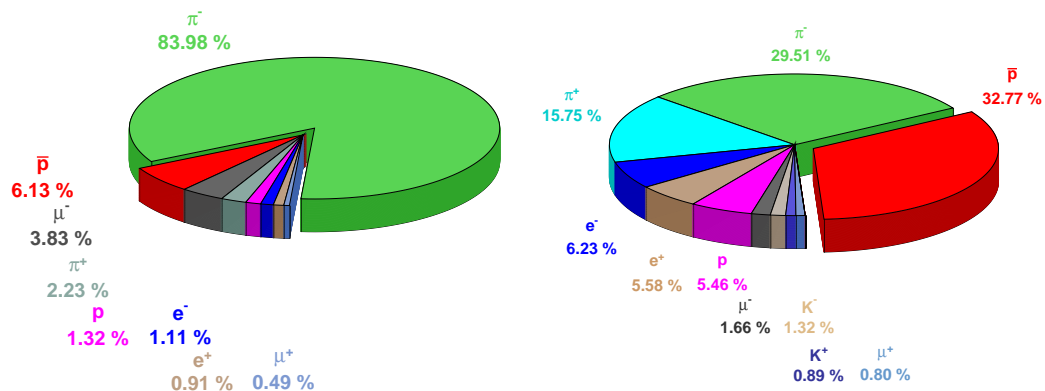


Figure 6.22: Relative contribution to the sum of primary and secondary background at 1.5 GeV/c (left) and at 15 GeV/c (right) without cuts (elastic contribution is excluded)

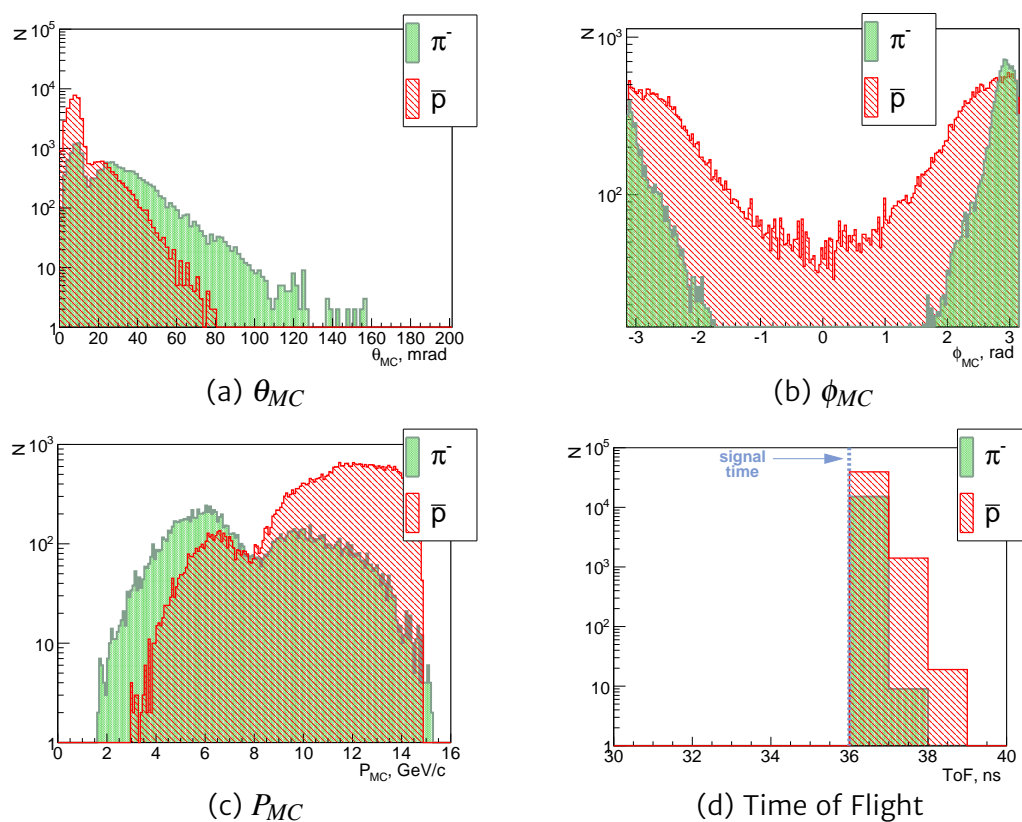


Figure 6.23: Distributions of generated variables for background contributions at  $P_{beam} = 15 \text{ GeV}/c$  without cuts

Particle	$N_i^{REC}/N_{tot.bkg}^{REC}, \%$	Final state	$\hat{\sigma}^{REC}, \text{nb}$	$\sigma_{tot}^{DPM}, \text{mb}$
$\bar{p}$	9.64	$\bar{p}\pi^-\pi^+p$	7766.85	$1.3671 \pm 0.0075$
	8.44	$\bar{p}\pi^-\pi^0\pi^+p$	6803.53	$1.8896 \pm 0.0088$
	8.03	$\bar{p}\pi^0p$	6475.16	$0.6878 \pm 0.0053$
	6.29	$\bar{p}\pi^+n$	5067.88	$0.5507 \pm 0.0047$
	4.72	$\bar{p}\pi^0\pi^+n$	3806.36	$0.018 \pm 0.005$
	3.20	$\bar{p}\pi^-2\pi^0\pi^+p$	2580.01	$1.276 \pm 0.004$
	2.31	$\bar{p}\pi^-\pi^02\pi^+n$	1861.3	$0.853 \pm 0.003$
	2.24	$\bar{p}\pi^-2\pi^+n$	1809.36	$0.5100 \pm 0.0046$
	2.22	$\bar{p}2\pi^0p$	1790.93	$0.333 \pm 0.004$
	1.70	$\bar{p}2\pi^-\pi^02\pi^+p$	1368.75	$0.9903 \pm 0.0064$
	1.68	$\bar{p}2\pi^0\pi^+n$	1346.97	$0.393 \pm 0.004$
	1.40	$\bar{p}2\pi^-2\pi^+p$	1130.85	$0.6762 \pm 0.0053$
	0.93	$\bar{p}\pi^-3\pi^0\pi^+p$	752.23	$0.547 \pm 0.008$
	...			
<b>total</b>	69.15	438 channels		
$\pi^-$	1.55	$3\pi^-2\pi^03\pi^+$	1248.12	$0.5846 \pm 0.0049$
	1.38	$3\pi^-3\pi^03\pi^+$	1112.42	$0.6983 \pm 0.0053$
	1.27	$3\pi^-\pi^03\pi^+$	1023.63	$0.2683 \pm 0.0033$
	1.25	$2\pi^-2\pi^02\pi^+$	1008.55	$0.2013 \pm 0.0029$
	1.24	$2\pi^-3\pi^02\pi^+$	998.5	$0.3543 \pm 0.0038$
	0.78	$2\pi^-4\pi^02\pi^+$	631.60	$0.3834 \pm 0.0040$
	0.75	$3\pi^-4\pi^03\pi^+$	603.12	$0.579 \pm 0.007$
	0.70	$\bar{p}\pi^-\pi^+p$	561.24	$1.3671 \pm 0.0075$
	0.66	$2\pi^-\pi^02\pi^+$	532.76	$0.0590 \pm 0.0016$
	...			
<b>total</b>	25.94	693 channels		

Table 6.1: Origin of primary background particles at  $P_{beam}=15 \text{ GeV}/c$  (no cuts).  $N_i^{REC}$  – number of reconstructed tracks for the inelastic channel;  $\sigma_{tot}^{DPM}$  – total cross section for the channel estimated by the DPM;  $\hat{\sigma}^{REC}=N_i^{REC} \cdot L$  – effective cross section for the channel in the LMD

## 6.2.5 Background reduction

With the current DPM model the main background contribution is caused by re-scattered elastic antiprotons (Fig. 6.19). Therefore cuts applied before and after back propagation were optimized to suppress mainly this particular contribution. For this purpose large samples of  $2 \times 10^7$  with elastic events were generated with DPM at 5 beam momentum values as in the previous study. For the secondary particles production the FTF\_BERT physics list was used in GEANT4. For saving the computing time in the detector geometry only the LMD and the beam pipe were included. After optimisations the cuts were tested on samples with elastic and inelastic events, obtained by the DPM generator and the complete simulation as discussed in Section 6.2.2. The results of these tests are shown in Fig. 6.25 and Fig. 6.36.

### Cut before back propagation (X&Y cut)

The parameters for the X&Y cut (Sec. 4.5.2) are corridors with widths  $\Delta_x$  and  $\Delta_y$ . Increasing those would lead to a 100% signal efficiency, but such loose cuts do not help to reduce background (Fig.6.24). To keep the signal efficiency at the level of  $\sim 99\%$ , the corridor widths of  $\Delta_x=3\text{ cm}$  and  $\Delta_y=4\text{ cm}$  were chosen. This cut suppresses the secondary particle contribution and helps significantly decrease the amount of inelastic primary tracks. As show in Fig.6.25, the total amount of background goes down to the level 2-3% in the whole momentum range.

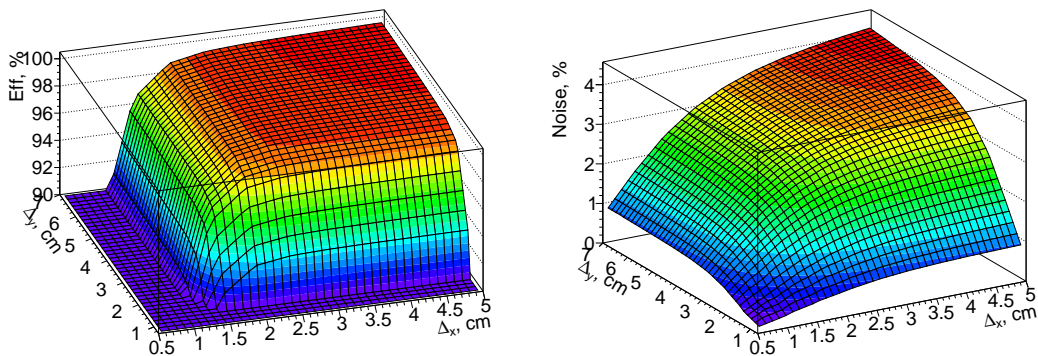


Figure 6.24: Efficiency for signal (left) and background (right) tracks in dependence on the corridors widths  $\Delta_x$  and  $\Delta_y$  for  $P_{beam}=1.5\text{ GeV}/c$

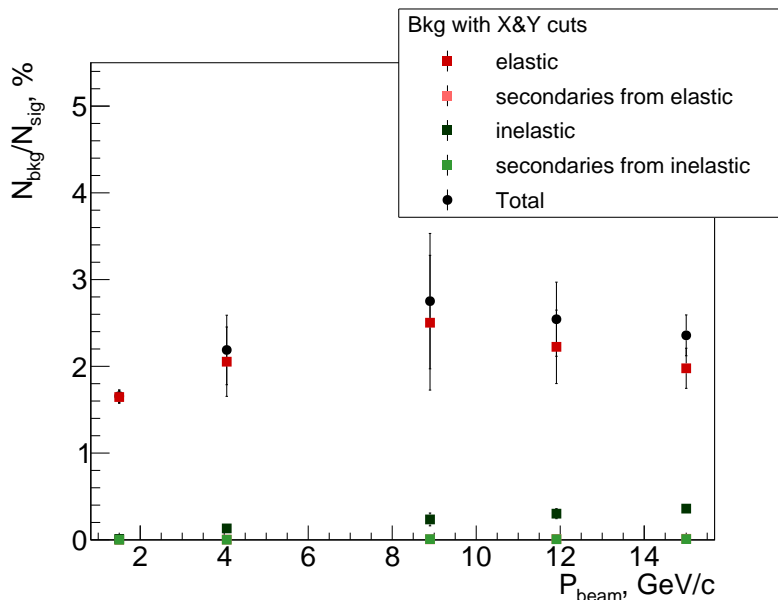


Figure 6.25: Relative background contributions (after X&Y cut) in dependence on the beam momentum

### Cut after back propagation (M cut)

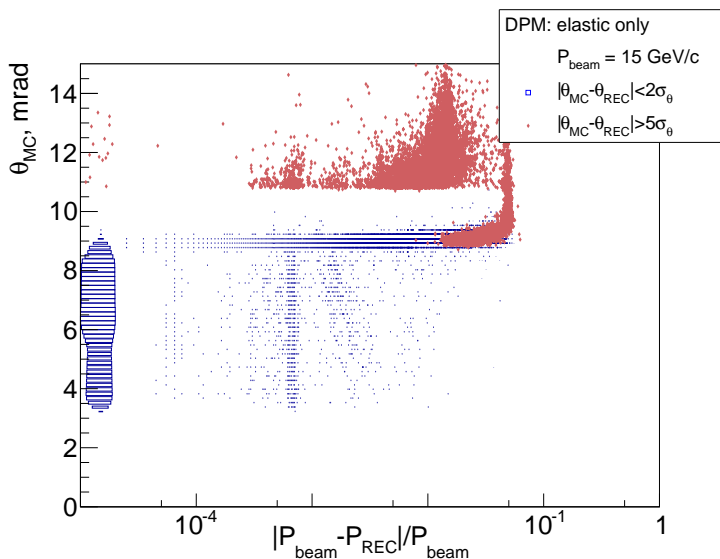


Figure 6.26: Difference between assumed and reconstructed momenta in simulations with  $P_{\text{beam}} 15 \text{ GeV/c}$  (blue – signal; red – background tracks)

After back propagation, the reconstructed track parameters should lie in certain regions, due to the limited acceptance of the LMD. e.g. the polar angle  $\theta$  is expected to be between 3 and 8 mrad, the PCA to the IP should be near the IP within the spatial resolution, etc. Another parameter is the momentum magnitude. Because elastically

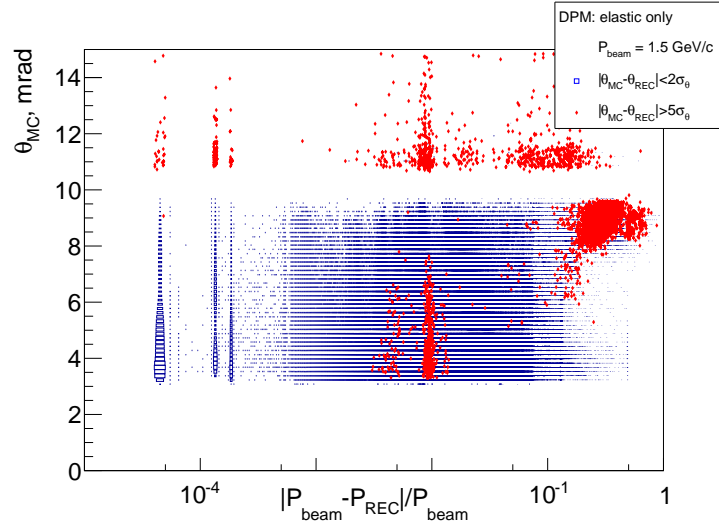


Figure 6.27: Difference between assumed and reconstructed momenta in simulations with  $P_{beam}$  1.5 GeV/c (blue – signal; red – background tracks)

scattered antiprotons fly within the beam pipe in high vacuum, the material budget seen by the antiprotons on its way to the LMD is very low. The momentum magnitude change by the remaining air molecules and the transition foil is only several hundreds of keV, which is very small compared to the GeV scale of the particle momentum values. If an antiproton track is back propagated through almost the same trajectory as it had during its passage from the IP to the LMD, the increase of its momentum magnitude should be also on the level of several hundreds of keV. The latter statement is not true for background particles, because for them an exact true value of the momentum magnitude is not known. Assuming the same momentum as elastically scattered antiprotons, they are propagated through a trajectory, which is different to the original one, and their momentum magnitude could be significantly changed during back-propagation, if the particle passes material in between. In Fig.6.26 the difference between the assumed and back propagated momenta is shown for different groups of tracks. For the simulation study at 15 GeV/c the picture is very clear: the relative difference of the signal tracks ( $\Delta\theta < 2\sigma_\theta$ ) is peaking at  $\sim 10^{-5}$  and tracks from the elastic background ( $\Delta\theta > 5\sigma_\theta$ ) are shifted to higher values of up to  $\sim 10^{-1}$ . Therefore this variable can be used for the separation between signal and background tracks at high energies. Unfortunately for tracks with low momentum, particularly at 1.5 GeV/c, this variable cannot be used due to the bad resolution of the reconstruction (see Fig. 6.27).

Low momentum tracks require a special and more complicated treatment. Here a multivariate analysis is required, taking into account multidimensional correlations. 6 parameters of the track after back-propagation are used for signal/background classi-

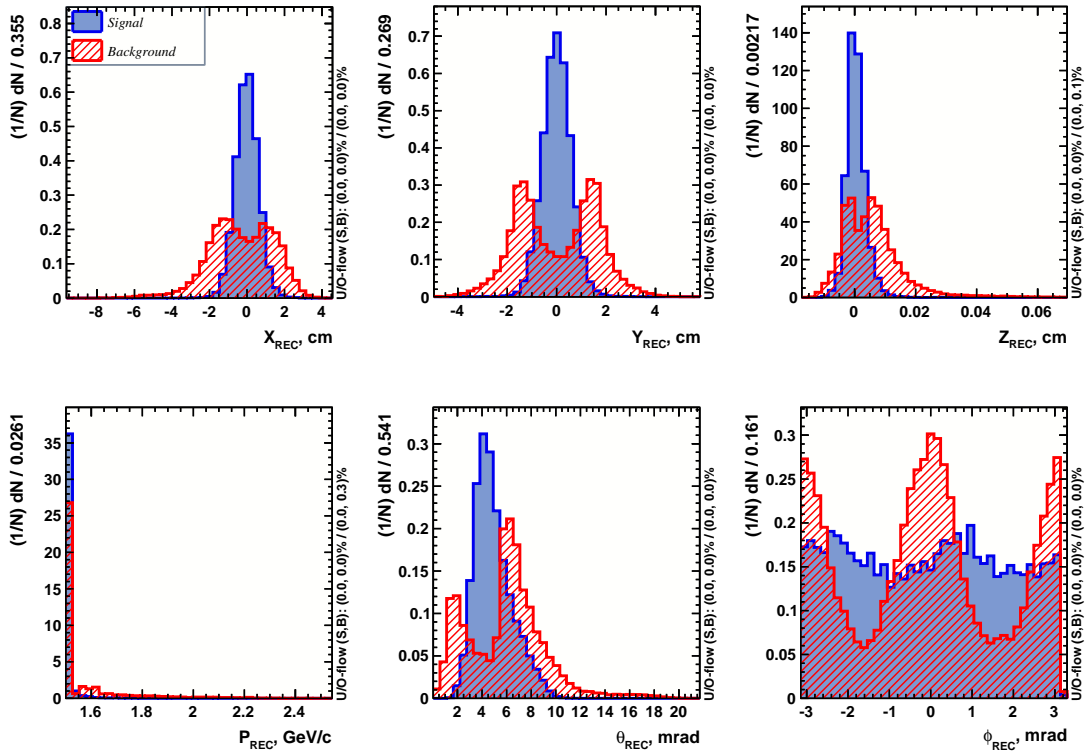


Figure 6.28: Reconstructed variables of signal (blue) and elastic background (red) tracks,  $P_{beam}=1.5 \text{ GeV}/c$

fication:  $X_{REC}$ ,  $Y_{REC}$  and  $Z_{REC}$  of the PCA to IP,  $P_{REC}$  the momentum magnitude and  $\phi_{REC}$ ,  $\theta_{REC}$  the angles of the momentum vector. Fig. 6.28 shows the distributions of reconstructed variables for signal and elastic background tracks. Unfortunately most of the variables have a similar range for both signal as well as background tracks, thus a classical separation by rectangular cuts on values of one or several variables would not be efficient. However the shapes of the distributions are different. e.g. the coordinates of the PCA have a Gaussian shape for the signal and a clearly non-Gaussian shape for the background tracks. Moreover as shown in Fig. 6.29 there are different correlations between the variables of reconstructed tracks for signal and background. e.g. the correlation between the  $X_{REC}$  and  $Y_{REC}$  coordinates of reconstructed tracks is peaking around the IP for signal tracks and spreading a bit more around the IP for background tracks. Also background tracks have  $\theta_{REC}$  above 8 mrad more often with larger values of the x coordinate than for signal tracks. Although none of the reconstructed variables looks reliable for a clear separation into signal and background tracks, their shapes and correlations have some systematic behavior and can be used for this task.

In the high energy community the Toolkit for Multivariate Data Analysis (TMVA) [90] is often used for multivariate analysis. This package provides a large number of ma-

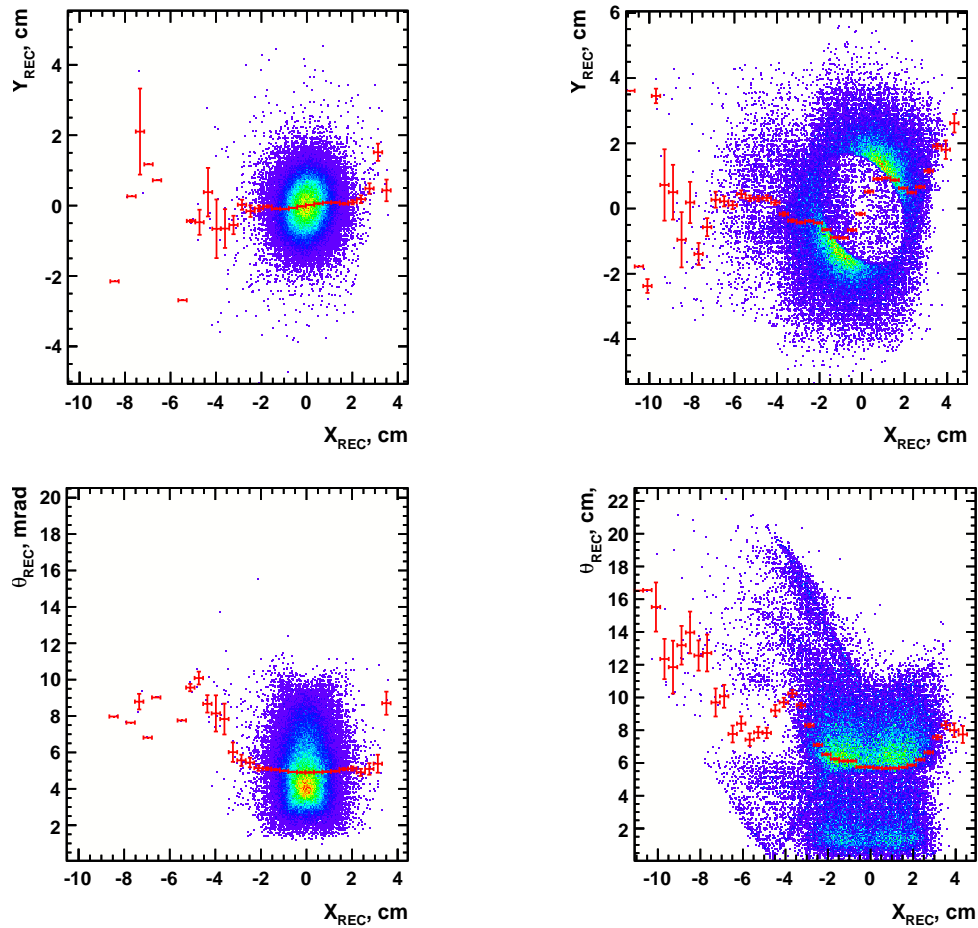


Figure 6.29: Correlations between reconstructed variables of a signal (left) and a background (right) tracks

chine learning algorithms for classification and regression tasks. A typical classification analysis consists of two independent phases: the training phase, in which signal and background samples are provided by the user and the parameters of the multivariate methods are found, tested and evaluated; and an application phase, where the chosen methods are applied to the concrete classification problem they have been trained for.

The variables behavior and the requirement to use the correlation between the reconstructed variables restrict number of methods, which can be used. Below different methods from the TMVA are discussed and their performance, i.e. background rejection versus signal efficiency curve (Fig. 6.30), is evaluated and explained.

### Rectangular cuts optimization (CutsGA)

The simplest and most common classifier for selecting signal events from a mixed sample of signal and background events is the application of an ensemble of rectan-

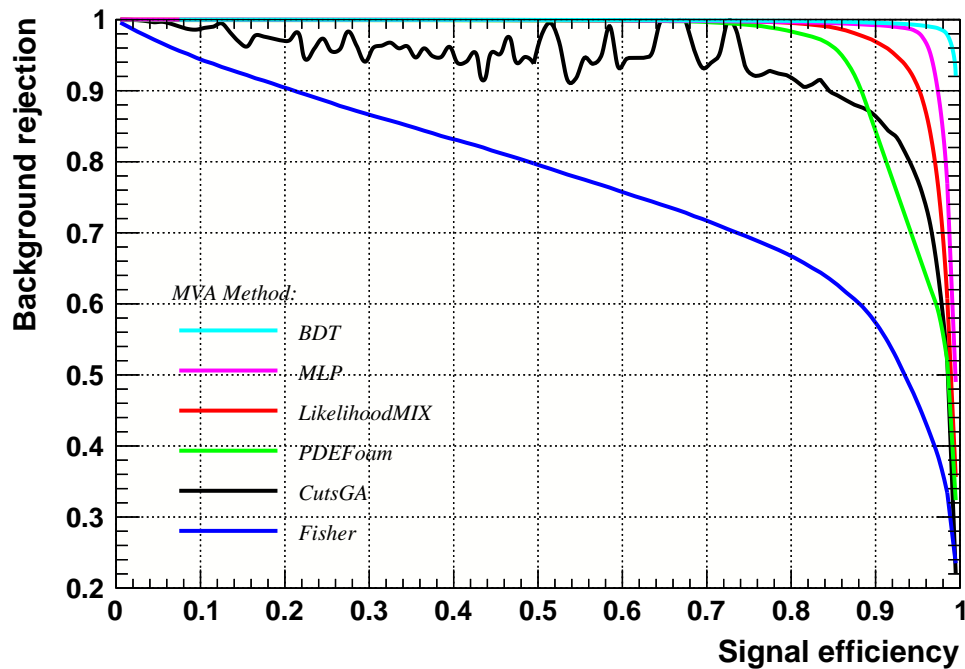


Figure 6.30: Background rejection versus signal efficiency for different TMVA methods

gular cuts on discriminating variables. The optimization of cuts performed by TMVA maximizes the background rejection at a given signal efficiency, and scans over the full range of the latter quantity. The TMVA cut optimization can be performed with the use of different fitter options: Minuit, Genetic Algorithm and Simulated Annealing [90]. Among them, the Genetic Algorithm (GA) currently provides the best cut optimization convergence, therefore it was used in our case. As can be seen from Fig. 6.30, where background rejection versus signal efficiency is shown by the black curve for CutsGA, the behavior of this method is rather unstable. Probably it can be stabilized by increasing the number of events used for the training phase. However, one cannot hope for a better background rejection with high signal efficiency, since our variables for signal and background are not well distinguishable by a simple rectangular separation (Fig. 6.28, black curve).

### Projective likelihood estimator (LikelihoodMIX)

The method of maximum likelihood builds a model out of probability density functions (PDF) that reproduces the input variables for signal and background events. For a given event, the likelihood for being of signal type is obtained by multiplying the signal probability densities of all input variables, which are assumed to be independent, and normalizing this by the sum of the signal and background likelihoods. Because

correlations among the variables are ignored, this approach is also called "naive Bayes estimator". Since the parametric form of the PDFs is generally unknown, the PDF shapes are empirically approximated by the training data with non-parametric functions. They can be chosen individually for each variable and are either polynomial splines of various degrees fitted to histograms or unbinned kernel density estimators (KDE). In our case both non-parametric approaches are used by choosing the LikelihoodMIX option. The choice of one particular approach is done automatically by TMVA for each variable and is based on the variables behavior. Polynomial splines are used for the coordinates of the PCA and the  $\theta$  and  $\phi$  angles of the reconstructed tracks and KDE for the momentum magnitude. This method has a good performance, but as mentioned before, ignores correlations among the variables. Therefore the performance of this method (Fig. 6.30, red curve) is worse than methods taking into account correlations among the variables.

### **Multidimensional likelihood estimator (PDEFoam)**

This is a generalization of the projective likelihood classifier. If the multidimensional PDF for signal and background events were known, this classifier would exploit the full information contained in the input variables, and would hence be optimal. In practice however, huge training samples are necessary to sufficiently populate the multidimensional phase space. Kernel estimation methods may be used to approximate the shape of the PDF for finite training statistics. The probability density estimator (PDE) Foam method divides the multi-dimensional phase space in a finite number of hyper-rectangles (cells) of constant event density. This "foam" of cells is filled with the averaged probability density information sampled from the training data. For a given number of cells, the binning algorithm adjusts the size and position of the cells inside the multi-dimensional phase space based on a binary split algorithm, that minimizes the variance of the event density in the cell.

The test statistics was not sufficient for the training of this method<sup>5</sup>. Therefore the results of its application are rather bad and even worse than for the projective likelihood estimator (Fig. 6.30, green curve).

### **Fisher discriminants (Fisher)**

In the method of Fisher discriminants, the event selection is performed in a transformed variable space with zero linear correlations, by distinguishing the mean values of the signal and background distributions. The linear discriminant analysis determines an axis in the (correlated) hyperspace of the input variables such that, when projecting the output classes (signal and background) events upon this axis, they are pushed as far as possible away from each other, while events of a same class are confined in a close vicinity. By construction of the method, no discrimination is achieved at all, when

<sup>5</sup>From simulation there are  $5 \cdot 10^6$  signal and  $1.7 \cdot 10^5$  background events available. However only  $2 \cdot 10^5$  signal and  $5 \cdot 10^4$  background events were used for comparison test between the methods, since for some methods training on full statistic would take several days.

a variable has the same sample mean for signal and background, even if the shapes of the distributions are very different. Therefore this method does not work very well in this case and has the worst performance of background rejection at the same signal efficiency, in comparison to other methods (Fig. 6.30, dark blue curve).

### Artificial neural networks (MLN)

An Artificial Neural Network (ANN) is generally presented as a system of interconnected "neurons", which can compute values from inputs. Mathematically, a neuron's network function  $f(x_{input})$  from input variables  $x_{input}$  is defined as a composition of other functions  $g_i(x_{input})$ , which can further be defined as a composition of other functions. This can be conveniently represented in a network structure, with arrows depicting the dependencies between the variables. This is shown in Fig. 6.31, where a set of composition functions are indicated as a "hidden" layer of the network. Therefore one can view the neural network as a mapping from a space of input variables  $x_{input}$  into a one-dimensional <sup>6</sup> space of output variables. TMVA provides access to several implementations of ANNs. Among them, the multi-layer network (MLN) is the recommended one, due to its high speed and flexibility [90] and therefore it is used in this study (Fig. 6.30, purple curve).

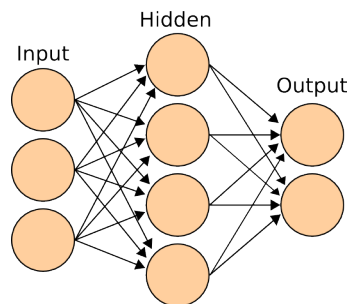


Figure 6.31: An artificial neural network is an interconnected group of nodes [16]

### Boosted Decision Trees (BDT)

A decision tree is a binary tree-structured classifier like the one sketched in Fig. 6.32. Repeated left/right (yes/no) decisions are taken for one single variable at a time, until a stop criterion is fulfilled. This way the phase space is split into many regions, that are eventually classified as signal or background, depending on the majority of training events that end up in the final leaf node. The boosting of the decision tree extends this concept from one tree to several trees, which form a forest. The trees are derived from the same training ensemble by re-weighting events, and are finally combined into a single classifier, which is given by a weighted average of the individual decision trees. Boosting stabilizes the response of the decision trees with respect to statistical fluctuations in the training sample, and is able to considerably enhance the performance

<sup>6</sup>in case of a signal-versus-background discrimination problem

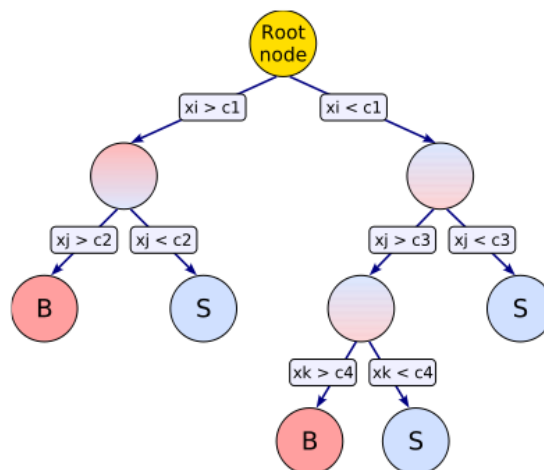


Figure 6.32: Boosted Decision Trees [90]

with respect to a single tree [91]. In this study the Gradient-Boost method [90] was used.

Decision trees are insensitive to the inclusion of poorly discriminating input variables. While for ANNs it is typically more difficult to deal with such additional variables, the decision tree training algorithm will basically ignore non-discriminating variables since only the best discriminating variable is used for each node splitting.

### Method choice

After the classification, a decision about the signal or background nature of a track is combined into a one-dimensional variable called *response*. During the application of the classification method, the cut is applied on the response calculated for each reconstructed track for the background rejection. In the ideal case, the response distributions of the signal and the background are located around different values and are well separated from each other. In reality the signal and background distributions can in general overlap, due to mis-classification, which indicates that it is impossible to suppress the background without, at least, a slight signal rejection. Therefore the best algorithm can be chosen by the smallest overlap between the signal and background response. Alternatively the method with the largest integral of the background rejection versus signal efficiency curve can be used (Fig. 6.30). Both select the method where it is possible to have maximum background rejection with maximum signal efficiency. The response distributions for the tested methods are shown in Fig. 6.33 and Fig. 6.34. As can be seen from these plots, a good separation for signal and background tracks by the response variable is achieved only for the BDT method. This method also has the largest integral of the background rejection versus the signal efficiency curve, as can be seen in Fig. 6.30. Here methods in the legend are ranked according to their integral values.

Therefore the BDT method was chosen and trained with a large data sample.

The response of the BDT method ranges from  $-1$  to  $1$ . For the signal this variable is peaking at  $1$  and for the background at  $-1$ . The optimum cut value can be chosen by a significance calculation at different values of the classifier response [90]:

$$\frac{S}{\sqrt{S+B}} \quad (6.3)$$

where  $S$  is number of signal and  $B$  is number of background events. The best significance is achieved if the cut on the response variable is set to  $-0.5$ . The corresponding signal and background efficiencies for the test sample with only elastic signal and background events are  $99.6\%$  and  $9.95\%$  (Fig. 6.35), respectively.

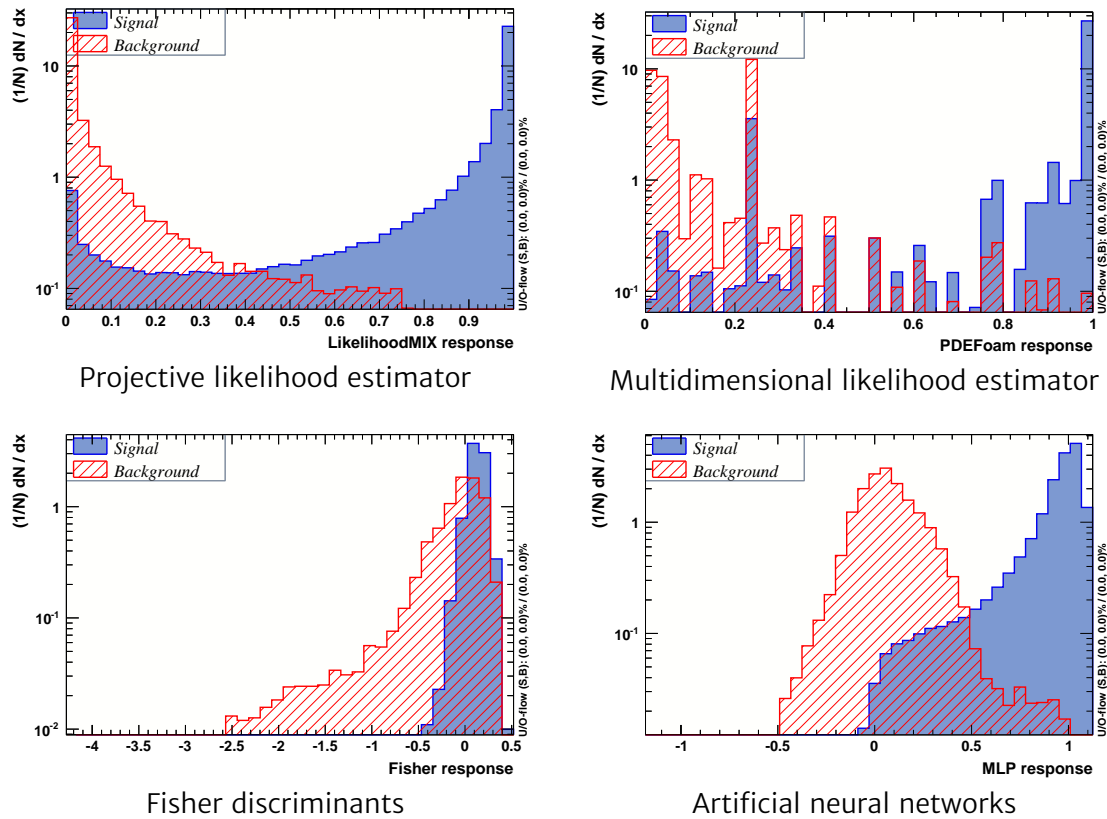


Figure 6.33: Response distributions for different TMVA methods

The separation of signal from background tracks based on a multivariate analysis is only used for the lowest beam momentum case ( $1.5 \text{ GeV}/c$ ). For higher beam momenta the cut based on the momentum check is used. This background rejection is done after the back propagation step and called the M cut <sup>7</sup>. The M cut was tested with DPM

<sup>7</sup>Multivariate for  $1.5 \text{ GeV}/c$  and Momentum for higher energy

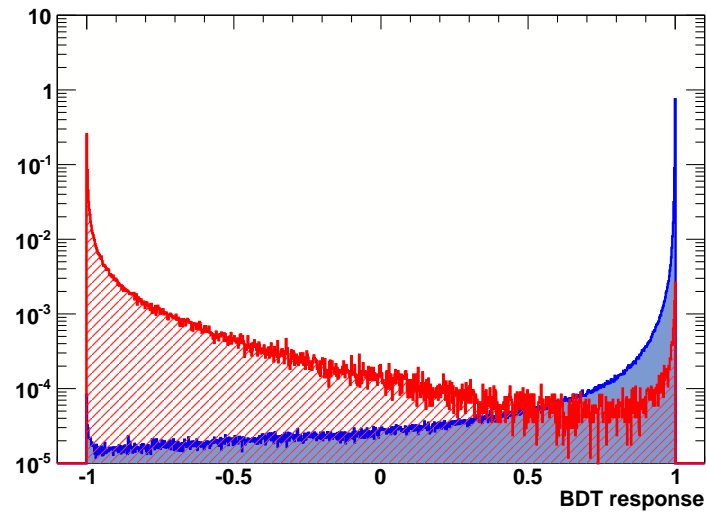


Figure 6.34: Response distributions for signal (blue) and background (red) with Boosted Decision Trees method

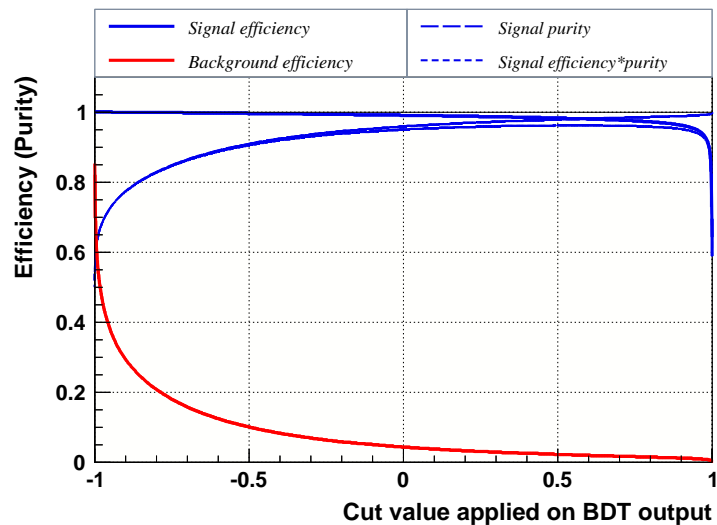


Figure 6.35: Signal and background efficiency in dependence on the cut on the BDT response

simulation of elastic and inelastic events at the 5 beam momenta. As can be seen in Fig. 6.36, the total background amount is around or below 1% and comes mainly from the elastic background part.

The contribution of inelastic background events is significantly suppressed after the cuts. For the simulation at  $P_{beam}=15 \text{ GeV}/c$ , only two particle species survived after the cuts:  $\bar{p}$  (with a relative to inelastic background contribution of  $\sim 94\%$ ) and  $\pi^-$

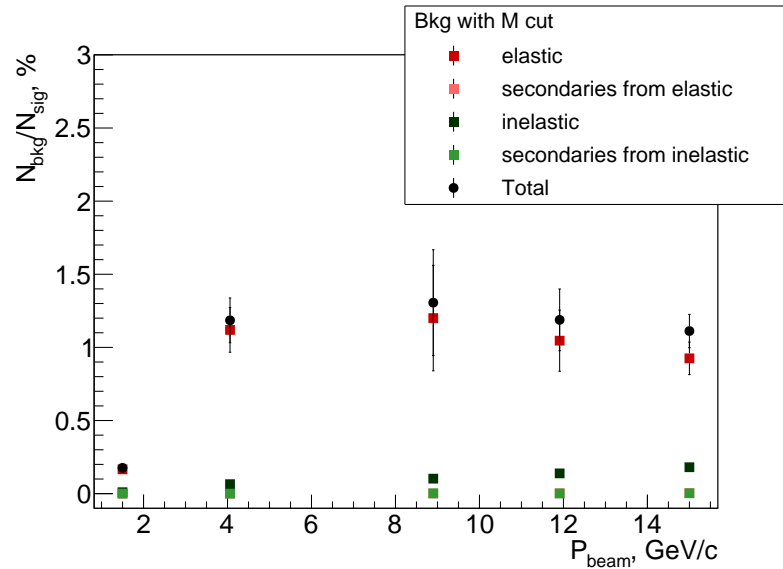


Figure 6.36: Relative background contributions (after X&Y cuts and M cut)

( $\sim 6\%$ ). Fig. 6.37 shows the distributions for each of them. This result is in agreement with the result for the simplified simulation studies: polar angles  $\theta$  of below 20 mrad and momenta close to the beam momentum within  $\pm 1 \text{ GeV}/c$ . This would mean that for the separation of signal and background tracks, a precision in the momentum measurement on the level of 1% would be needed.

During the time of writing this thesis, the FTF model from Geant4 became available as a stand-alone background generator within PANDARoot. It was not possible to repeat the extensive background study with this generator once more. However, a preliminary comparison between the FTF and DPM models on the generator level (see Appendix F) shows that FTF predicts more particles at small  $\theta$  angles and 5 times more reconstructed inelastic background tracks after all applied cuts at the beam momentum  $15 \text{ GeV}/c$ . Therefore complete simulation studies with the FTF generator with higher statistic at different beam momenta are subject of future investigations.

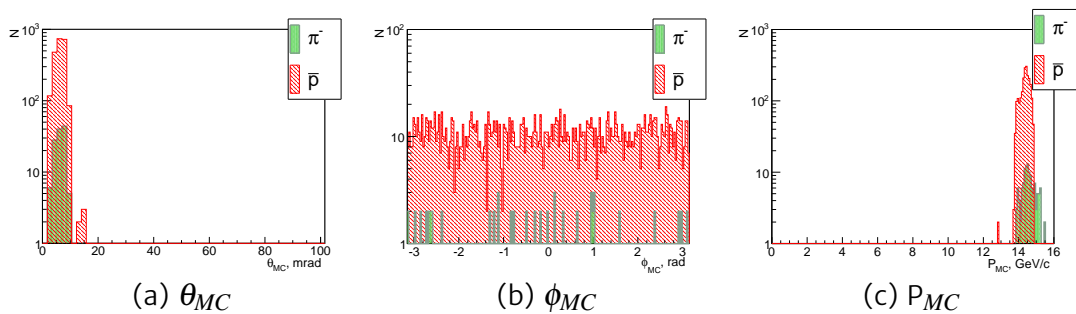


Figure 6.37: Distributions for the contributions of inelastic background after the application of all cuts ( $P_{beam} = 15 \text{ GeV}/c$ )

### The luminosity extraction precision

The influence of the remaining elastic background on the luminosity extraction was checked for the lowest (Tab. 6.2) and the highest (Tab. 6.3) beam momenta. Since the largest contribution is elastic background, the data samples generated for the cut optimisation containing only elastic DPM events were used for this study too. In Tab. 6.2 and Tab. 6.3 the  $R$  value is defined as the ratio between the number of tracks from each contribution and the number of reconstructed signal tracks without applied cuts.  $\Delta L/L$  specifies the relative difference between the generated and reconstructed luminosity. Tab. 6.2 and Tab. 6.3 show that the background below 1% has no influence on the precision of the luminosity extraction at both beam momenta.

Cut	$R$ sig, %	$R$ el. bkg, %	$R$ second. bkg, %	$\Delta L/L$ , %
No	100	3.56	0.1	$-0.93 \pm 0.07$
X&Y	99.7	1.67	$4 \cdot 10^{-5}$	$-0.49 \pm 0.07$
X&Y and M	99.1	0.17	$3 \cdot 10^{-5}$	$-0.04 \pm 0.07$

Table 6.2: Influence of the cuts on the luminosity extraction precision ( $P_{beam}=1.5$  GeV/c)

Cut	$R$ sig, %	$R$ el. bkg, %	$R$ second. bkg, %	$\Delta L/L$ , %
No	100	6.7	4.2	$2.41 \pm 0.07$
X&Y	99.8	2.36	0.01	$1.27 \pm 0.07$
X&Y and M	99.6	0.93	$3 \cdot 10^{-3}$	$-0.008 \pm 0.07$

Table 6.3: Influence of the cuts on the luminosity extraction precision ( $P_{beam}=15$  GeV/c)

# Simulation studies $p\bar{p} \rightarrow h_c \rightarrow 5\pi$

## 7.1 Charmonium as a framework for QCD tests

Quarkonium is a general name for a bound state of a quark and its corresponding antiquark, and refers usually to *charmonium* ( $c\bar{c}$ ) and *bottomonium* ( $b\bar{b}$ ) states. The lighter quarks (up, down, and strange) are much less massive than the heavier quarks thus the physical states actually seen in experiments are quantum mechanical mixtures of the pure  $q\bar{q}$  states. The top quark decays through the electroweak interaction before forming a bound state and hence toponium does not exist.

In proton-antiproton interactions the production of bottomonium is much less probable than that for charmonium. e.g. the cross section at the peak of the charmonium state  $\chi_{c1}$  ( $\sqrt{s}=3.51$  GeV) is  $\sim 100$  nb and the cross section at the peak of the corresponding bottomonium state  $\chi_{b1}$  ( $\sqrt{s}=9.89$  GeV) is estimated to be not larger than 1 nb [92]. Therefore it is not surprising that at  $\bar{P}$ ANDA the planned studies are concentrated around the charm physics, which also requires lower energy of the beam. Below the discussion is restricted to charmonium only, although most of the arguments are valid for bottomonium too.

Charmonium is an excellent system to test the concept of QCD. Unlike the case of light-quark hadrons, for charmonium the value of  $\alpha_s$  is sufficiently small  $\sim 0.3$  to make perturbative calculations possible. Furthermore, the relatively small binding energy, compared to the rest mass of its constituents, allows  $c\bar{c}$  states to be described non-relativistic (with  $v^2/c^2 \approx 0.25$ ) and makes it easier to unfold the complicated effects of QCD dynamics. In addition, charmonium states provide a unique laboratory for understanding the interplay between perturbative and non-perturbative effects in QCD, because the mass of the charm quark provides a natural boundary between the perturbative and non-perturbative regimes. The fact that the charmonium resonances are eigenstates of  $J^{PC}$  produces symmetry conserving simplifications. From the exper-

imental point of view the bound  $c\bar{c}$  states are well separated in energy and narrow in width, as opposed to the light-quark resonances which have large and often overlapping widths.

By making precise measurements of the masses, widths, and branching ratios of the charmonium states, important information about the dynamics of the strong interaction may be extracted. For instance, by comparing the hadronic and electromagnetic branching ratios of charmonium states, an estimate of the strong coupling constant  $\alpha_s$  can be derived. Unknown quantities, such as the squared absolute value of the wave function at the origin  $|\psi(0)|^2$ , or poorly measured quantities, such as branching ratios between the resonance and the initial state, may often cancel in the ratio, thus leaving  $\alpha_s$  as the only unknown quantity [93]. e.g. in the case of  $\eta_c$ ,  $\eta'_c$ ,  $\chi_{c0}$ , and  $\chi_{c2}$  such cancellation occur when one compares the branching ratio into two photons and the branching ratio into two gluons. Different theoretical models provide different predictions for the radiative partial widths of charmonium states, which can be compared to the experimental results. Examples include the electric dipole transitions of the three  $\chi_{cJ}$  states to  $J/\psi$ , and the magnetic dipole transition of  $J/\psi$  to  $\eta_c$ , and  $\psi'$  to  $\eta'_c$  [93].

The interest to charmonium spectroscopy is recently growing again due to the observation of X, Y, Z states, which do not fit into the picture of the expected charmonium spectrum as predicted by potential models. It is suggested that those states may not be ordinary  $c\bar{c}$  states, but might consist of four quarks. The precise determination of the excitation curves of these states is still missing in order to distinguish between the different theoretical interpretations [94]. This is due to the fact that those states have a very narrow width, which is at least difficult or even impossible to measure with existing facilities. It should be mentioned here that with  $\bar{P}$ ANDA this difficulty will be overcome and widths up to  $\sim 100$  keV can be measured [95]. Another powerful method for the determination of the nature of the X, Y, Z states is the measurement of the radiative partial widths, e.g. in [96] different model predictions are compared for  $X(3872) \rightarrow \gamma J/\psi$  and  $X(3872) \rightarrow \gamma \psi'$ .

## 7.2 Potential models

One technique used in calculations of hadronic resonances is the replacement of the non-Abelian gauge field theory of QCD by a non-relativistic potential model. Non-relativistic models for charmonium are possible because of the relatively large mass of the charm quark, which have  $v^2/c^2 \sim 0.25$  in their bound states, as opposed to  $v^2/c^2 \sim 0.8$  for the light quark mesons. Using corrections for relativistic, channel coupling and radiative effects, the success of potential models for theoretical predictions even extends to various decays of charmonium states as well as their masses and widths.

In 1975 Appelquist and Politzer recognized that the single gluon exchange between a charm quark and antiquark should give rise to a Coulombic potential proportional to  $1/r$  at small distances [97]. They coined the name "orthocharmonium" for the  $J/\psi$  in analogy with the  $^3S_1$  orthopositronium, and went on to extend the analogy to predict the existence of  $^1S_0$  "paracharmionium". Appelquist and Politzer were able to predict the complete spectrum of bound charmonium states based on a charmonium potential which was expected to be an intermediate between a Coulombic and a harmonic oscillator potential. Due to similar behavior of the potentials the charmonium spectrum looks similar to that of the positronium (bound states of  $e^+$  and  $e^-$ ) as can be seen in Fig.7.1 where both spectra are shown.

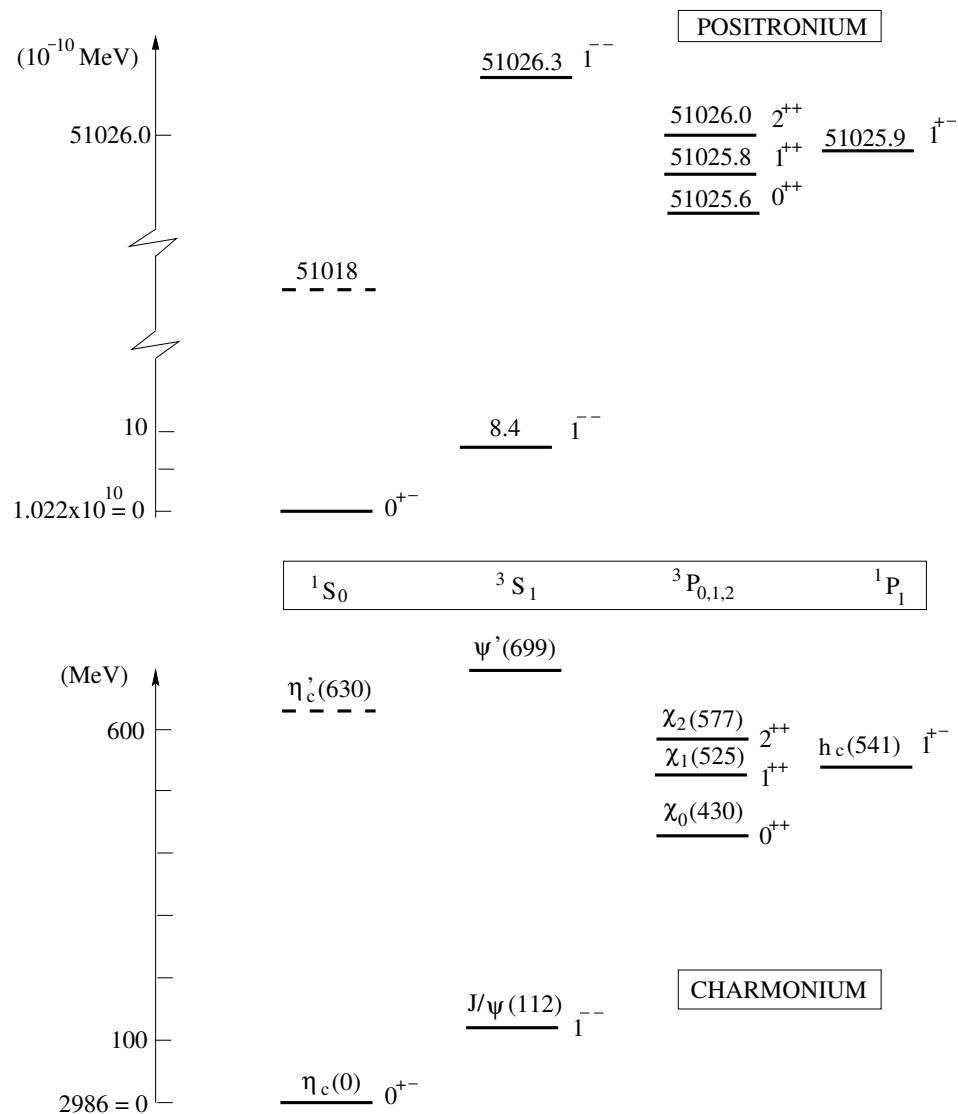


Figure 7.1: Positronium (top) and charmonium (bottom) spectra [98]

Nowadays the static quark-antiquark potential in strong interaction is often expressed as a Cornell-type potential [99]:

$$\begin{aligned}
 V(r) = & -\frac{4}{3} \frac{\alpha_s}{r} + kr + \frac{32\pi\alpha_s}{9m_c^2} \delta(r) \vec{S}_c \vec{S}_{\bar{c}} \\
 & + \frac{1}{m_c^2} \left( \frac{2\alpha_s}{r^3} - \frac{k}{2r} \right) \vec{L} \vec{S} + \frac{1}{m_c^2} \frac{4\alpha_s}{r^3} \left( \frac{3\vec{S}_c \vec{r} \cdot \vec{S}_{\bar{c}} \vec{r}}{r^2} - \vec{S}_c \vec{S}_{\bar{c}} \right) \quad (7.1)
 \end{aligned}$$

The first term is a Coulomb-like term describing one-gluon exchange, which is very similar to the Coulomb term in QED potentials for positronium or the hydrogen atom, except that here the coupling constant is given by the strong coupling constant  $\alpha_s$  instead of the fine-structure constant  $\alpha_{em}$ . The second term is a linear term, which phenomenologically describes the QCD confinement, and which is completely absent in QED. The linear shape is supported by Lattice QCD calculations. The parameter  $k$  is the string constant of the QCD string between the quark and the anti-quark. The last terms represent the spin-orbit, spin-spin and tensor potentials, leading to the mass splittings in the spectrum. QCD-motivated potential models successfully described the  $J/\psi$  and  $\psi'$  as  $\bar{c}c$  states soon after they were discovered. Later other low-lying  $\bar{c}c$  states were discovered and found to have properties that agree reasonably well with the model predictions.

Charmonium states are labeled using the spectroscopic notation  $n^{2S+1}L_J$ , where  $n$  is the number of nodes in the radial excitation plus one,  $S$  is the combined spin of the two quarks (0 spin-singlet, or 1 spin-triplet states),  $L$  is the relative orbital angular momentum (S, P, D correspondingly for 0, 1, 2), and  $J$  is the total angular momentum. Parity and charge conjugation, as in any quark-antiquark state, are given by  $P = (-1)^{L+1}$  and  $C = (-1)^{L+S}$  respectively. A more abbreviated notation is to characterize the states just by their  $J^{PC}$ . The states predicted by potential model are called *conventional charmonium states*. The recently found X, Y, Z states do not fit into the Cornell-type potential model prediction and are usually referred as *charmonium-like states*.

Precise measurements of the different resonance masses, or more particularly the differences between them, are a very effective way to test the spin-dependence of the different potential models. For instance, the tensor and spin-orbit interaction split up the masses of the  $\chi_{cJ}(1^3P_J), J = 0, 1, 2$  states (fine splitting). The spin-spin force splits the vector and pseudoscalar states, and this is responsible for the mass difference between  $J/\psi$  and  $\eta_c$ , and between  $\psi'$  and  $\eta'_c$  (hyperfine splitting). A measurement of the deviation of the  $h_c(1^1P_1)$  mass from the center of gravity of the  $\chi_{cJ}$  states would indicate a departure from first order perturbation theory, since the spin-spin potential is a contact potential, which survives only with the finite wave function at the origin. Thus, this potential gives rise to hyperfine splitting between the triplet ( $S = 1$ ) and

singlet ( $S = 0$ ) states only for S-wave states, and not for P-wave or any other higher L-states. This behavior is the direct consequence of the long-range confinement potential having been assumed to be a pure Lorentz scalar. A non-zero hyperfine splitting may give an indication of a non-vanishing spin-spin interaction in charmonium potential models [100].

The spin-averaged centroid mass of the triplet states:

$$\langle m(1^3P_J) \rangle \equiv [m(\chi_{c0}) + 3m(\chi_{c1}) + 5m(\chi_{c2})]/9 \quad (7.2)$$

is expected to be near the  $h_c$  mass, therefore making the hyperfine mass splitting:

$$\Delta m_{hf}[h_c(1P)] \equiv \langle m(1^3P_J) \rangle - m[h_c] \quad (7.3)$$

Current values [101]:

$$\begin{aligned} \langle m(1^3P_J) \rangle &= 3525.30 \pm 0.07 \text{ MeV} \\ m[h_c] &= 3525.45 \pm 0.15 \text{ MeV} \end{aligned} \quad (7.4)$$

give

$$\Delta m_{hf} = -0.15 \pm 0.17 \quad (7.5)$$

which is close to zero as expected from the lowest-order perturbative QCD. A more precise measurement of  $m[h_c]$  is needed to draw more accurate conclusion regarding  $\Delta m_{hf}$ .

Most of the studies of charmonium(-like) states are performed in  $e^+e^-$  annihilation, in which only the  $c\bar{c}$  vector states ( $J^{PC} = 1^{--}$ ) can be directly formed via the intermediate photon (Fig. 7.2). All other states are only reached by decays, mostly radiative, from these vector states. A different technique was invented by the R704 experiment at the ISR accelerator at CERN [102], which demonstrated that high resolution charmonium spectroscopy could be done by using proton-antiproton annihilation.

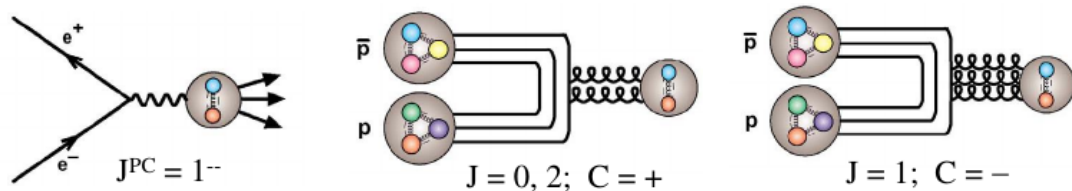


Figure 7.2: Schematic diagrams for the formation process in  $e^+e^-$  (left) and  $p\bar{p}$  experiments mediated by two (center) and three (right) gluons

The usage of antiproton-proton annihilation reactions enables two ways to investigate resonances. In the *formation* mode a single resonance is formed directly in the

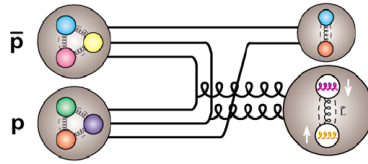


Figure 7.3: Schematic diagram for the production process in  $p\bar{p}$  experiments

annihilation process, which correspondingly must have the  $J^{PC}$  quantum numbers accessible by a fermion–antifermion pair. In this case  $c\bar{c}$  mesons are populated via two and three gluon annihilations leading to  $C = +1$  (with even  $J$ ) and  $C = -1$  (with odd  $J$ ) states respectively (Fig. 7.2). In the *production* mode at least one additional particle is produced together with the resonance of interest, therefore the last one does not have the restriction on  $J^{PC}$ . By comparison of both methods it is possible to classify the resonances and identify those with exotic quantum numbers, i.e. quantum numbers forbidden for ordinary quark–antiquark mesons. However the formation mode is preferable for accurate measurement of widths and excitation curves of resonances via the resonance scan technique, because the resolution here is limited only by the beam resolution (see Section 3.1.2).

### 7.3 Current status of $h_c(1^1P_1)$ meson

Although the charmonium family has been studied for many years, our knowledge is sparse on the singlet state  $h_c(1^1P_1)$ . At the  $e^+e^-$  colliders this state can be obtained only in the decay  $1^{--} \rightarrow 1^{+-}\pi^0$ , which is isospin-violating and therefore its branching ratio is only  $\leq 10^{-3}$ . This is a serious limitation even for studies at current  $e^+e^-$  colliders with high luminosity. e.g. at BESIII in  $1.06 \times 10^8$   $\psi'$  events used for the measurement of  $h_c(1^1P_1)$ , only  $N=3679 \pm 319$  events were extracted in the exclusive channel, i.e. in the  $\psi'$  decay  $\psi' \rightarrow h_c\pi^0 \rightarrow \gamma\eta_c$  and in the inclusive  $\pi^0$  recoil-mass spectrum the yield of  $h_c$  was estimated to be  $N=10353 \pm 1097$  events [103]. The resonance scan technique was used by the Fermilab  $p\bar{p}$  experiments E760 and E835 [45], where this resonance was measured in the direct formation mode  $p\bar{p} \rightarrow h_c$ . Unfortunately these experiments were harmed by the limited beam time available to them and therefore were limited by statistics. Below a short overview is presented starting from the first observations and the following studies of  $h_c$ .

#### 7.3.1 Mass

The discovery of  $h_c$  were reported by two experiments in 2005. CLEO [104],[105] reported an observation in the isospin-forbidden decay chain  $e^+e^- \rightarrow \psi' \rightarrow \pi^0 h_c, h_c \rightarrow \gamma\eta_c$ . And E835 [106] found an evidence in  $p\bar{p} \rightarrow h_c, h_c \rightarrow \gamma\eta_c, \eta_c \rightarrow \gamma\gamma$ . CLEO [107]

later updated its measurements with a larger data set, refining its mass measurement to a precision of  $0.2 \text{ MeV}/c^2$ ; E835 obtained an uncertainty of  $\sim 0.3 \text{ MeV}/c^2$ .

CLEO utilized two detection methods. The first one was a semi-inclusive selection that required detection of both the transition  $\pi^0$  and the radiative photon, but only inferred the presence of the  $\eta_c$  through kinematics (the inclusive reaction). The second one, with the exclusive reactions, exploited the full reconstruction in fifteen different  $\eta_c$  decay modes, five of them previously unseen. These two methods had some statistical and fully systematic correlation for the mass measurement because both rely on the  $\pi^0$  momentum determination. However because the parent,  $\psi'$  state, has a precisely known mass and is produced nearly at rest by the incoming  $e^+e^-$  pair, the mass of the  $h_c$  is accurately determined by fitting the distribution of the recoil mass against the  $\pi^0$ . CLEO's two methods comprise comparable precision and gave consistent masses within their uncorrelated uncertainties. The statistical uncertainties from the numbers of signal and background events in the exclusive (inclusive) analysis are larger than the systematic errors caused by the calorimeter energy resolution.

The E835 measurement of  $p\bar{p} \rightarrow h_c \rightarrow \gamma\eta_c \rightarrow \gamma\gamma\gamma$  relies on the knowledge of the initial center-of-mass energy of the  $p\bar{p}$  reaction for each event during a scan of the  $h_c$  mass region as well as upon the reconstruction of all three photons with kinematics consistent with the production and decay hypothesis. Unlike the CLEO result, background reactions are negligible. The accuracy of the mass measurement was limited equally by statistics (13 signal events with a standard deviation in center-of-mass energy of 0.07 MeV) and the systematic uncertainty due to the  $\bar{p}$  beam energy stability.

Using a sample of  $1.06 \times 10^6 \psi'$ , in 2010 BESIII [108] reported a mass result using the  $\pi^0\gamma$  exclusive method, matching CLEO's precision. The new analysis published by the BESIII collaboration in 2012 [109] is currently the most accurate measurement of the  $h_c$  mass:  $M(h_c) = 3525.31 \pm 0.11 \text{ (stat)} \pm 0.14 \text{ (syst)} \text{ MeV}/c^2$ .

### 7.3.2 Width

The predictions for the total width of the  $h_c$  lie in the range of 0.4–1 MeV. The current value  $\Gamma(h_c) = 0.7 \pm 0.28 \text{ (stat)} \pm 0.22 \text{ (syst)} \text{ MeV}$  [109] is in agreement with the predictions. Predictions for the partial widths of various  $h_c$  decays are shown in Tab. 7.1. The most prominent decay of the  $h_c$  is expected to be the radiative transition to  $\eta_c$  with the predicted partial width in the range of several hundred keV and a branching ratio of  $\sim 50\%$ . The current value of the branching ratio  $B(h_c \rightarrow \gamma\eta_c) = 51 \pm 6\%$  [1] is also in agreement with the prediction.

The decay channels can be classified in few basic categories.

#### Radiative transitions

An electromagnetic transition between quarkonium states, which occurs via the emission of a photon. Example:  $h_c \rightarrow \gamma\eta_c$

Authors	$\Gamma(\eta_c\gamma)$ (keV)	$\Gamma(J/\psi\pi^0)$ (keV)	$\Gamma(J/\psi\pi^0\pi^0)$ (keV)	$\Gamma(hadrons)$ (keV)	$\Gamma(total)$ (keV)
Renard [110]	240			370	500-1000
Novikov [111]	975			60-350	
McClary [112]	485				
Kuang [113]		2	4-8	54	395-400
Galkin [114]	560				
Chemtob [115]		0.006	53		
Bodwin [116]	450			530	980
Chen [117]		0.3-1.2	4-14	19-51	360-390
Chao [118]	385				
Casalbuoni [119]	450				
Ko [120]	400	>1.6			
Gupta [121]	341.8				

Table 7.1: A summary of predictions for the partial widths of  $h_c$  decays [98]

### Hadronic transitions

The general form for a hadronic transition is:  $\Phi_i \rightarrow \Phi_f + h$ , where  $\Phi_i$  ( $\Phi_f$ ) and  $h$  stand for the initial-state (finale-state) quarkonia and the emitted light hadron(s). The mass difference  $m_{\Phi_i} - m_{\Phi_f}$  varies from a few hundred MeV to slightly over a GeV, hence the kinematically allowed  $h$  are dominated by a single particle ( $\pi^0$ ,  $\eta$ ,  $\omega$ , ...) or two-particle ( $2\pi$  or  $2K$ ) states. It should be mentioned that such decay modes were not seen for  $h_c$  so far [1]. Example:  $h_c \rightarrow J/\psi\pi\pi$

### Decay to light hadrons

Light hadrons are states created from light quarks (u,d and s). In this decay mode there are no charmonium states involved in the final state. Basically it is the group of decays to non-charmonium states. Example:  $h_c \rightarrow \pi^+\pi^-\pi^0$

The radiative transitions to light hadrons are also included in this group of processes. Example:  $h_c \rightarrow \gamma\eta'$

As already mentioned, the radiative decay  $h_c \rightarrow \eta_c\gamma$  is the dominating decay. However it is also predicted that the inclusive width of the decay to light hadrons should have a similar size, mainly due to the contributions from the radiative transitions to light hadrons. e.g. in [110] the width of  $h_c \rightarrow \gamma\eta'$  is estimated to be  $\sim 210$  keV which is close to the estimation of the width of  $h_c \rightarrow \eta_c\gamma$  width  $\sim 240$  keV in this work. So far the search for radiative transitions to light hadrons was not performed. At  $\bar{P}$ ANDA this

measurement can be done by looking at the recoil-mass spectrum of the  $\gamma$ .

The situation with other non-radiative exclusive decays to light hadrons is also not clear. So far only multi-pions decay channels were investigated. Because the  $h_c$  should have negative G-parity, multi-pion decays are likely to involve an odd number of pions. Searches for channels with 3, 5 and 7 pions in the final state had been performed by CLEO [122]. The statistics were limited due to non-direct production of the  $h_c$  in  $e^+e^-$  experiments. For the channels with 3 and 7 pions in the final state it was possible to give an estimation for an upper limit only (Tab. 7.2).

Mode	Fraction ( $\Gamma_i/\Gamma$ )
$\pi^+\pi^-\pi^0$	$< 0.22\%$
$2\pi^+2\pi^-\pi^0$	$2.2^{+0.8}_{-0.7}\%$
$3\pi^+3\pi^-\pi^0$	$< 2.9\%$

Table 7.2:  $h_c$  hadronic decay modes [1]

The direct  $h_c$  production is the advantage of a  $p\bar{p}$  experiment. But hadronic channels are difficult to measure in  $p\bar{p}$  interactions due to the high cross section of the hadronic background, i.e. the non-resonance production of such final states. The expected production cross section for  $h_c$  is 10–100 nb. At energies close to  $h_c$  mass  $p\bar{p} \rightarrow 2(\pi^-\pi^+)\pi^0$  is the dominating inelastic channel with a cross section  $\sim 1$  mb. From this perspective the decay  $h_c \rightarrow 2(\pi^-\pi^+)\pi^0$  will be the most challenging channel due to a signal to background ratio of  $\sim 10^{-4}$ . The attractive side of this measurement is that a high statistic data sample should be available after only a few days of data taking with  $\bar{P}$ ANDA. Also one should not forget that so far only this hadronic decay channel was measured for  $h_c$  (Tab. 7.2). Remaining questions are:

- If we assume some particular model for the decay description, would it be possible to extract this channel at  $\bar{P}$ ANDA ?
- How much statistics this measurement would require to get a clear separation between signal and background?
- Which  $\bar{P}$ ANDA sub-systems are essential for this measurement?

These questions are important to make a decision whatever this measurement is feasible and can or cannot be done at the beginning of data taking. In the following, answers to the questions will be given by a simulation study using the Fast Simulation approach.

## 7.4 Construction of the analysis model

The hadronic transitions, e.g.  $h_c \rightarrow J/\psi \pi \pi$ , are characterized by the clean signature of the decay  $J/\psi \rightarrow e^+ e^-$ . In contrast to this, the hadronic decay channels can only be extracted if an decay model is introduced, thus the analysis for this measurement is model dependent. With the known description of the decay mechanism, non-resonant background can be suppressed up to certain level. The most simple mechanism is a charmonium decay via a meson pair. Such an approach is discussed in [123], where pseudoscalar (P) and vector (V) mesons are considered. The angular momentum and parity conservation are crucial here:

$$(-1)^{J_c} P_c = (-1)^{J_1+J_2} P_1 P_2 \quad (7.6)$$

where  $J_i$  and  $P_i$  are spin and parity of the meson  $i$ . It leads to the following predictions:

- $h_c \rightarrow PP$  (forbidden by angular momentum and parity conservation)
- $h_c \rightarrow PV$  (allowed)

This approach can be extended to combinations with scalar (S) and pseudovector ( $V_p$ ) mesons. Tab. 7.3 gives an overview of all combinations.

Table 7.3: Allowed (+) and forbidden(-) decay modes of  $h_c$

PP	PV	VV	PS	SS	SV	$V_p S$	$V_p V$	$V_p P$	$V_p V_p$
-	+	-	+	-	-	+	+	-	-

For the decay modes with a pseudovector meson (e.g.  $V_p S$ ), the following decay chain can be assumed:  $h_c \rightarrow h_1 f_0 \rightarrow (\rho \pi^0)(\pi^+ \pi^-) \rightarrow 2(\pi^+ \pi^-) \pi^0$ . Compared to the decay modes with pseudoscalars discussed below, where the direct reconstruction of the daughters of the  $h_c$  decay from the final state is used, decays with a pseudovector meson require an additional step in the reconstruction. For example the reconstruction of a  $\rho$  candidate from the  $\pi^+ \pi^-$  pair and only then the reconstruction of  $h_1$  from the  $\rho$  and  $\pi^0$  candidates. It complicates the analysis. Also poorly determined the mass and width of known pseudovector mesons, i.e.  $h_1$  [1], could become additional sources of systematic uncertainties, which have to be carefully studied. For simplicity, decay modes with pseudovector mesons are excluded in this study.

Using the PV or PS model of the  $h_c$  decay to  $2(\pi^+ \pi^-) \pi^0$ , the final state can be accessed by the following intermediate resonances:

- $h_c \rightarrow \eta \omega$  [PV]
- $h_c \rightarrow \eta \rho$  [PV]

•  $h_c \rightarrow \eta f_0$  [PS]

where  $\eta$  decays subsequently to  $\pi^+\pi^-\pi^0$  and the  $f_0$ ,  $\omega$  and  $\rho$  states to a  $\pi^+\pi^-$  pair.

One should note that  $h_c \rightarrow \eta\omega$  is not forbidden by any conservation law. But the following decay  $\omega \rightarrow \pi\pi$  violates the isospin conservation and has branching fraction of only  $1.53^{+0.11}_{-0.13}\%$ . The decay  $h_c \rightarrow \eta\rho$  is already isospin violating, although the following decays are not isospin violating and have significant branching fractions ( $28.1 \pm 0.34\%$  for  $\eta \rightarrow \pi^+\pi^-\pi^0$  and  $\sim 100\%$  for  $\rho \rightarrow \pi^+\pi^-$ ). The decay  $h_c \rightarrow \eta f_0$  violates G-parity, but again following decays have large branching fractions (e.g  $f_0 \rightarrow \pi\pi$  is dominant for  $f_0(600,980)$  and  $34.9 \pm 2.3\%$  for  $f_0(1500)$ ). Isospin or G-parity violating decays are not strictly forbidden because they can proceed through electromagnetic  $c\bar{c}$  annihilation and may receive contributions from the isospin-violating part of QCD. The latter contributions, being related to the u-d quark mass difference, seem to be small [123].

Branching fractions for each contribution can be estimated as:

$$\mathcal{B}(h_c \rightarrow 2(\pi^+\pi^-\pi^0)) = \mathcal{B}(h_c \rightarrow 1+2) \times \mathcal{B}(1 \rightarrow \pi^+\pi^-\pi^0) \times \mathcal{B}(2 \rightarrow \pi^+\pi^-) \quad (7.7)$$

The branching fractions  $\mathcal{B}(h_c \rightarrow 1+2)$  for each intermediate state are not known. The following estimations are done with the assumption  $\mathcal{B}(h_c \rightarrow \eta\omega)=1$ . The isospin violating decay  $h_c \rightarrow \eta\rho$  most probably goes via  $c\bar{c} \rightarrow \gamma gg$  annihilation [110] therefore  $\mathcal{B}(h_c \rightarrow \eta\rho) \sim \alpha^2 = 5.3 \times 10^{-5}$ . The G-violating decay is possible only via electromagnetic decay, thus  $\mathcal{B}(h_c \rightarrow \eta f_0) \sim \alpha^2$ . This leads to the following relations:

$$\mathcal{B}(h_c \rightarrow \eta\omega \rightarrow 2(\pi^+\pi^-\pi^0)) \sim 4 \cdot 10^{-3} \quad (7.8)$$

$$\mathcal{B}(h_c \rightarrow \eta\rho \rightarrow 2(\pi^+\pi^-\pi^0)) \sim 1.5 \cdot 10^{-5} \quad (7.9)$$

$$\mathcal{B}(h_c \rightarrow \eta f_0(600,980) \rightarrow 2(\pi^+\pi^-\pi^0)) \sim 1.5 \cdot 10^{-5} \quad (7.10)$$

$$\mathcal{B}(h_c \rightarrow \eta f_0(1500) \rightarrow 2(\pi^+\pi^-\pi^0)) \sim 5.2 \cdot 10^{-6} \quad (7.11)$$

The same intermediate states could also lead to the  $\pi^+\pi^-3\pi^0$  final state, if  $\eta$  decays to  $3\pi^0$ . The branching fractions in this case are slightly higher due to the higher branching fraction of  $\eta \rightarrow 3\pi^0$  ( $32.57 \pm 0.23\%$ ) in comparison to the  $\pi^+\pi^-\pi^0$  final state. E.g.

$$\mathcal{B}(h_c \rightarrow \eta\omega \rightarrow \pi^+\pi^-3\pi^0) \sim 5 \cdot 10^{-3} \quad (7.12)$$

The detection of both hadronic decay modes offers possibility to measure the ratio between the corresponding branching fractions  $\frac{\mathcal{B}(h_c \rightarrow \pi^+\pi^-3\pi^0)}{\mathcal{B}(h_c \rightarrow 2(\pi^+\pi^-\pi^0))}$ . Also a cross-check of the analysis can be done by comparing this ratio with the ratio between  $\mathcal{B}(\eta \rightarrow \pi^+\pi^-\pi^0)$  and  $\mathcal{B}(\eta \rightarrow 3\pi^0)$  which is well known.

From the background point of view the non-resonant contribution of the inelastic

channel  $p\bar{p} \rightarrow \pi^- \pi^+ 3\pi^0$  has a cross section  $\sim 0.1$  mb [64]. Therefore the expected signal to background ratio should be  $\sim 10$  times higher than for  $h_c \rightarrow 2(\pi^+ \pi^-) \pi^0$ . Both final states,  $h_c \rightarrow 2(\pi^+ \pi^-) \pi^0$  and  $h_c \rightarrow \pi^+ \pi^- 3\pi^0$ , are considered in the simulation study with different intermediate states.

## 7.5 Generation of datasets

Simulation engines like GEANT are universal tools, which provide the general and accurate description for interactions of all known particles with a detector material. The price for this universality is the computing time. Usually the propagation of particles through the material of a detector is the most time consuming part of a simulation study. Sometimes the accurate description of the detector response might be not needed, e.g for the rough estimation of an efficiency for a particular channel. A possible solution is a parameterization of the detector response. This simplified approach is called Fast Simulation (FastSim). Parameters in the FastSim approach are detection efficiencies, spatial acceptance, kinematic acceptance and resolutions of the single detector components. The detector response is modeled as accepting/rejecting of a particle and varying the particle parameters according to the resolutions. It also adds PID probabilities<sup>1</sup> for it. Thus in FastSim particle propagation through the volume of material and the reconstruction of the corresponding object are combined together. To make FastSim more realistic many additional effects were included, such as covariance matrices for the tracks (to enable kinematic fitting), electron bremsstrahlung losses, merging of close-by neutral particles, etc [124].

For the generation of the complete decay chain, the event generator EvtGen [63] was used. This flexible tool provides several descriptions of the decay, so called decay models. These models differ mainly in the angular distribution of the two particle decay. Models used in this study are shown in Tab. 7.4. Events with pure phase-space distribution of final state particles are generated for the channels  $h_c \rightarrow \pi^+ \pi^- 3\pi^0$  and  $h_c \rightarrow 2(\pi^+ \pi^-) \pi^0$  to compare results with models, which use an angular distribution for the final state particles.

For the background estimation the DPM generator is used in the inelastic mode (Ch. 6). For the production of both, signal and the background events, the beam momentum  $P_{beam} = 5.61$  GeV/ $c$  ( $E_{CM} = 3.526$  GeV) was chosen, which is very close to the mass of the  $h_c$ .

---

<sup>1</sup>some raw PID information like  $dE/dX$  is modeled too

Table 7.4: Models used for generation of datasets with EvtGen: phase-space model without intermediate resonances (PHSP), helicity amplitudes (HELAMP), vector decay to 2 scalar mesons (VSS), pseudoscalar decay to 3 pseudoscalar mesons (PTO3P)

reaction	subsequent decay	model
$p\bar{p} \rightarrow 2(\pi^+\pi^-)\pi^0$		PHSP
$p\bar{p} \rightarrow \eta\omega$	$\eta \rightarrow \pi^+\pi^-\pi^0$ $\omega \rightarrow \pi^+\pi^-$	HELAMP PTO3P VSS
$p\bar{p} \rightarrow \eta\rho$	$\eta \rightarrow \pi^+\pi^-\pi^0$ $\rho \rightarrow \pi^+\pi^-$	HELAMP PTO3P VSS
$p\bar{p} \rightarrow \eta f_0$	$\eta \rightarrow \pi^+\pi^-\pi^0$ $f_0 \rightarrow \pi^+\pi^-$	HELAMP PTO3P HELAMP
$p\bar{p} \rightarrow \pi^+\pi^-\pi^0$		PHSP
$p\bar{p} \rightarrow \eta\omega$	$\eta \rightarrow 3\pi^0$ $\omega \rightarrow \pi^+\pi^-$	HELAMP PTO3P VSS

## 7.6 Analysis

The analysis is performed in the following steps:

1. Selection of all charged pions
2. Reconstruction of  $\pi^0$  candidates from  $2\gamma$  within a  $\pi^0$  mass window ( $m(\pi^0) \pm 0.05$  MeV)
3. Selection of events with 2 positive, 2 negative and 1 neutral pion for  $h_c \rightarrow 2(\pi^+\pi^-)\pi^0$  or 1 positive, 1 negative and 3 neutral pions for  $h_c \rightarrow \pi^+\pi^-3\pi^0$
4. Reconstruction of  $h_c$  candidates
5. Application of a kinematic fit with constrains (momentum and energy conservation) and selection of events with  $\chi^2 < 20$ . In case of several candidates per event, one with the smallest  $\chi^2$  is chosen

This approach does not use assumption about intermediate decay and this analysis method is referred as *PHSP-analysis* in the following. As it will be shown the background suppression with the PHSP method is very low. A more sophisticated model-

dependent suppression is needed in order to overcome this. The event selection based on a particular model is introduced between steps 3. and 4. of the analysis chain.

By using simulated data, it is exactly known which model is used during the generation of the events. Therefore the optimal selection criteria can be adjusted and extracted. For the decay models PV, PS, the kinematic signature of the decay products in the rest frame of the  $h_c$  is used. The decay  $h_c \rightarrow \eta \omega$  is taken as an example. But the similar approach is also used for all the other combinations of intermediate resonances. Both  $\eta$  and  $\omega$  have a certain and correlated distributions in the phase-space, which is visible for example in the Peyrou diagram, where the transverse momentum  $p_\perp$  distribution is plotted as a function of the longitudinal  $p_z$ . The Peyrou diagram has parabola band shape as can be seen in Fig. 7.4(left), where this distribution is shown for  $\eta$  meson candidates. The two-dimensional distribution can be described by polynomials for the mean value of the band (Fig. 7.4 center) and its width (Fig. 7.4 right). After applying this band as a cut only  $\eta$  and  $\omega$  candidates lying within the bands selected. Those cuts help to significantly suppress the combinatorial background (Fig. 7.5) as well as the physical non-resonant background. For further background suppression mass cuts on the invariant mass of two and three pions for  $\omega$  and  $\eta$  candidates are applied. Distributions of the invariant mass of the  $\omega$  and  $\eta$  mesons, after applying the kinematic cuts, and corresponding mass cuts are shown in Fig. 7.6.

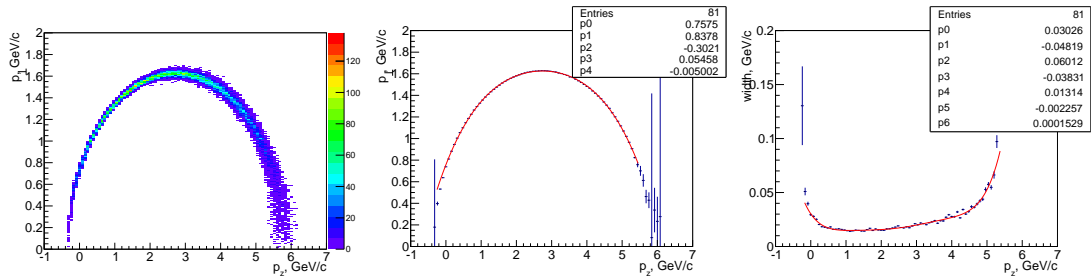


Figure 7.4: Transverse momentum  $p_\perp$  versus longitudinal momentum  $p_z$  distribution for  $\eta$  (left), its mean value (center) and width (right) fit by polynomial functions

By using the cut combination, the signal efficiency can be kept on the level of  $\sim 45\%$  and the background reduction is  $\sim 10^{-6}$ . Taking into account not only  $\eta\omega$ , but also  $\eta\rho$ ,  $\eta f_0$ , etc contributions can be done in two ways.

The first, exclusive way, is adding each contribution separately with accurate cuts from the corresponding Peyrou diagram (Fig. 7.7) and the additional mass windows. Because the Peyrou distribution of  $\eta$  is strongly dependent on the second meson produced, the selection of candidates by cuts on this distribution does not give any advantage due to necessity to increase the band width for the cut (Fig. 7.8).

The second, inclusive way, is the selection only by the mass cut on the  $\eta$  candidates. The invariant mass distributions for  $\eta$  candidates for signal and background events are shown in Fig. 7.9, where it is visible that by a mass cut, e.g.  $0.25 < M_{3\pi}^2 < 0.35$ ,

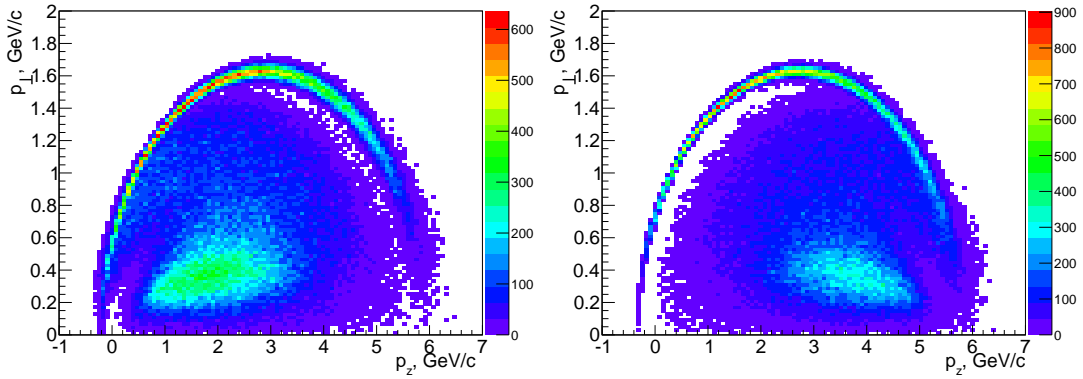


Figure 7.5: Signal events and combinatorical background for  $\omega$  (left) and  $\eta$  (right) in the Peyrou diagram

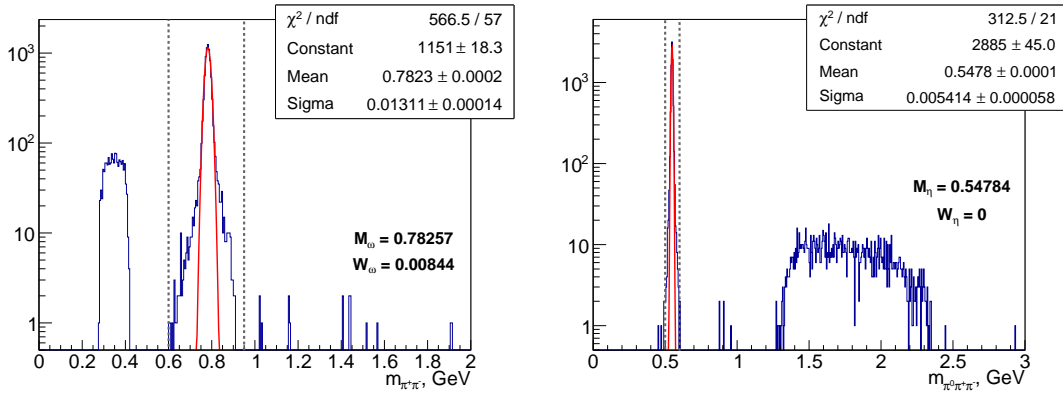


Figure 7.6: Distribution of the invariant mass of the  $\omega$  (left) and  $\eta$  (right) mesons: the parameters used in the generation are shown in bold; red line shows fit by Gaussian function; the mass window set around the mean value of the fit to the 3 standard deviations is shown by grey dashed line

combinatorial as well as non-resonant background can be suppressed. For the rough estimations of the signal efficiency and the background suppression the analysis is done in an inclusive way, which is referred as  $\eta$ -analysis in the plots below.

## 7.7 Results and Discussion

The reconstruction efficiency can be determined by the ratio between reconstructed and generated  $h_c$  events. For both signal channels,  $h_c \rightarrow 2(\pi^+\pi^-)\pi^0$  and  $h_c \rightarrow \pi^+\pi^-3\pi^0$ , the reconstruction efficiency on the level of  $\sim 40\%$  can be achieved for the full PANDA detector set-up. However the signal efficiency for the channel  $h_c \rightarrow 2(\pi^+\pi^-)\pi^0$  are very close for the cases when the signal was simulated with uniform phase-space model

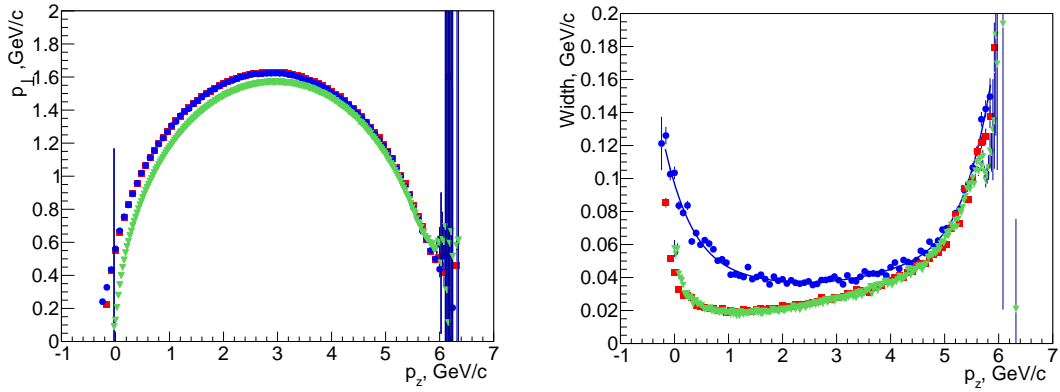


Figure 7.7: Mean (left) and width (right) of Peyrou diagrams for  $\omega$ (red) and  $\rho$ (blue) and  $f_0(980)$ (green)

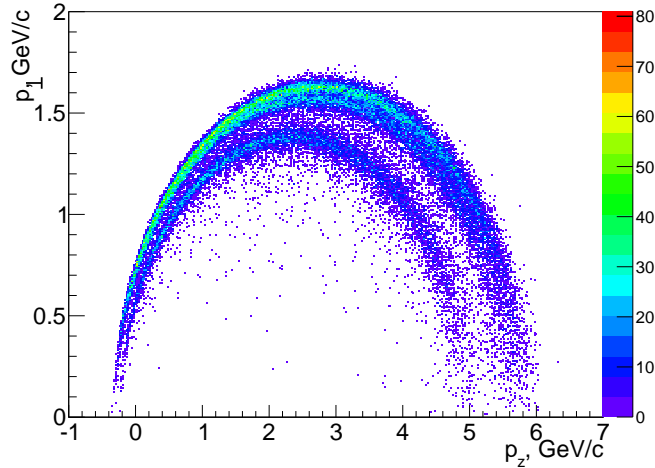


Figure 7.8: Peyrou diagram for  $\eta$  with contributions from  $\eta\omega$ ,  $\eta\rho$ ,  $\eta f_0$  of  $h_c$  decay

(42 %) and with some intermediate decay model (e.g. for  $\eta\omega$  it is 44 %). In opposite to this the signal efficiency for  $h_c \rightarrow \pi^+\pi^-3\pi^0$  are different for the phase-space (56 %) and model with intermediate resonances (e.g. for  $\eta\omega$  it is 40 %). This is due to different angular distribution of the neutral pions (Fig. 7.10). For the case with intermediate resonances in the decay, there are more neutral pions flying in backward direction in respect to the beam. The efficiency for their detection is smaller than for pions going into the forward direction. Significant background rejection can be achieved only if the assumption about the intermediate decay is used. Then the background reconstruction efficiency is  $\sim 2 \times 10^{-5}$  for the  $2(\pi^+\pi^-)\pi^0$  and  $\sim 5 \times 10^{-6}$  for the  $\pi^+\pi^-3\pi^0$  final state.

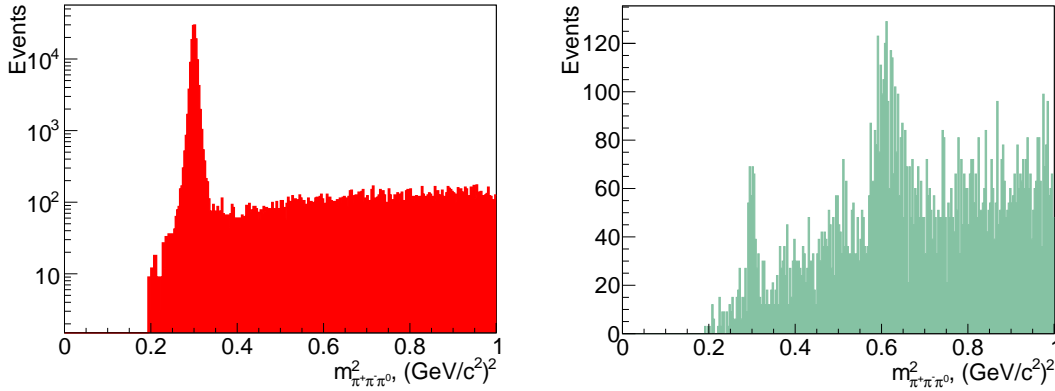


Figure 7.9: Signal (red) with  $\eta$  contribution ( $\eta\omega$ ,  $\eta\rho$ ,  $\eta f_0$ ) and DPM background (green) distributions of  $m^2(\pi^+\pi^-\pi^0)$

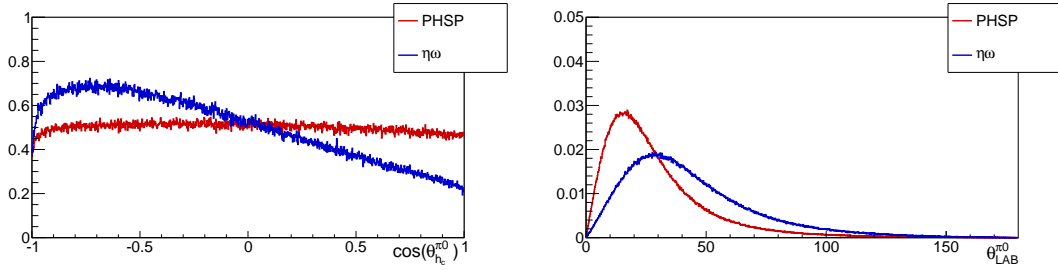


Figure 7.10: Angular distributions (normalized to 1) of reconstructed neutral pions for different models of decay  $h_c \rightarrow \pi^+\pi^-\pi^0$  in the rest frame of  $h_c$  (left) and in the LAB frame (right)

As a future experiment,  $\bar{P}$ ANDA collaboration discusses different options, e.g. measurements which could be done with not fully equipped detector. Therefore the reconstruction efficiency of this process was studied with different detector set-ups:

- Full set-up = all sub-systems included
- without EmcBar = barrel part of the EMC calorimeter excluded
- without FwdSpec = only the complete barrel part of the  $\bar{P}$ ANDA included
- without Disc DIRC = Disc DIRC in PID detectors is excluded
- STT only = STT used as a stand-alone tracking system in barrel part (without MVD and GEM)

The results for the efficiencies are shown on Fig. 7.11, 7.12 and summarized in Tables 7.5, 7.6 for decay channels  $h_c \rightarrow 2(\pi^+\pi^-)\pi^0$  and  $h_c \rightarrow \pi^+\pi^-\pi^0$  respectively.

Concerning the importance of different detector sub-systems for this measurement, it is not surprising that the exclusion of the Disc DIRC does not change the signal

efficiency. This sub-system is required for a clear separation between pions and kaons. In the studied channels there are only pions in the final state. Also the background distributions from channels with kaons in the final state is expected to be small due to the small cross section of these final states [64]. The Forward Spectrometer also does not play an important role for this measurement due to the multi-particle final state and the requirement of a complete event reconstruction. Within the proposed model, final state particles prefer to fly within angles, which are not covered by the Forward Spectrometer, but by the Barrel part of the  $\bar{P}$ ANDA detector. For this reason the barrel part of the EMC and MVD+GEM are important.

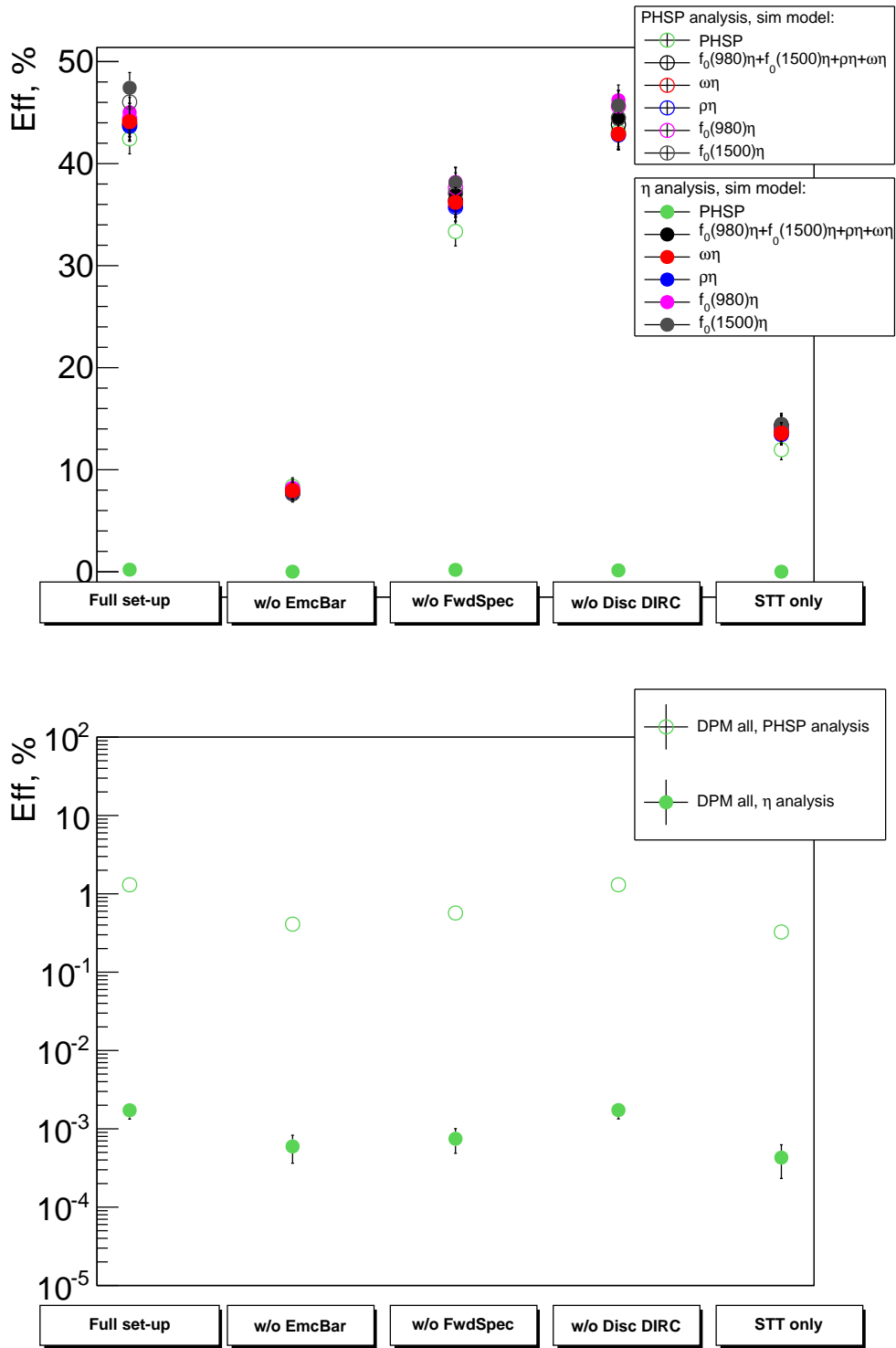


Figure 7.11: Efficiency of the signal (top) and the background (bottom) events of the decay channel  $h_c \rightarrow 2(\pi^+\pi^-)\pi^0$  with only  $\eta$  mass window cut

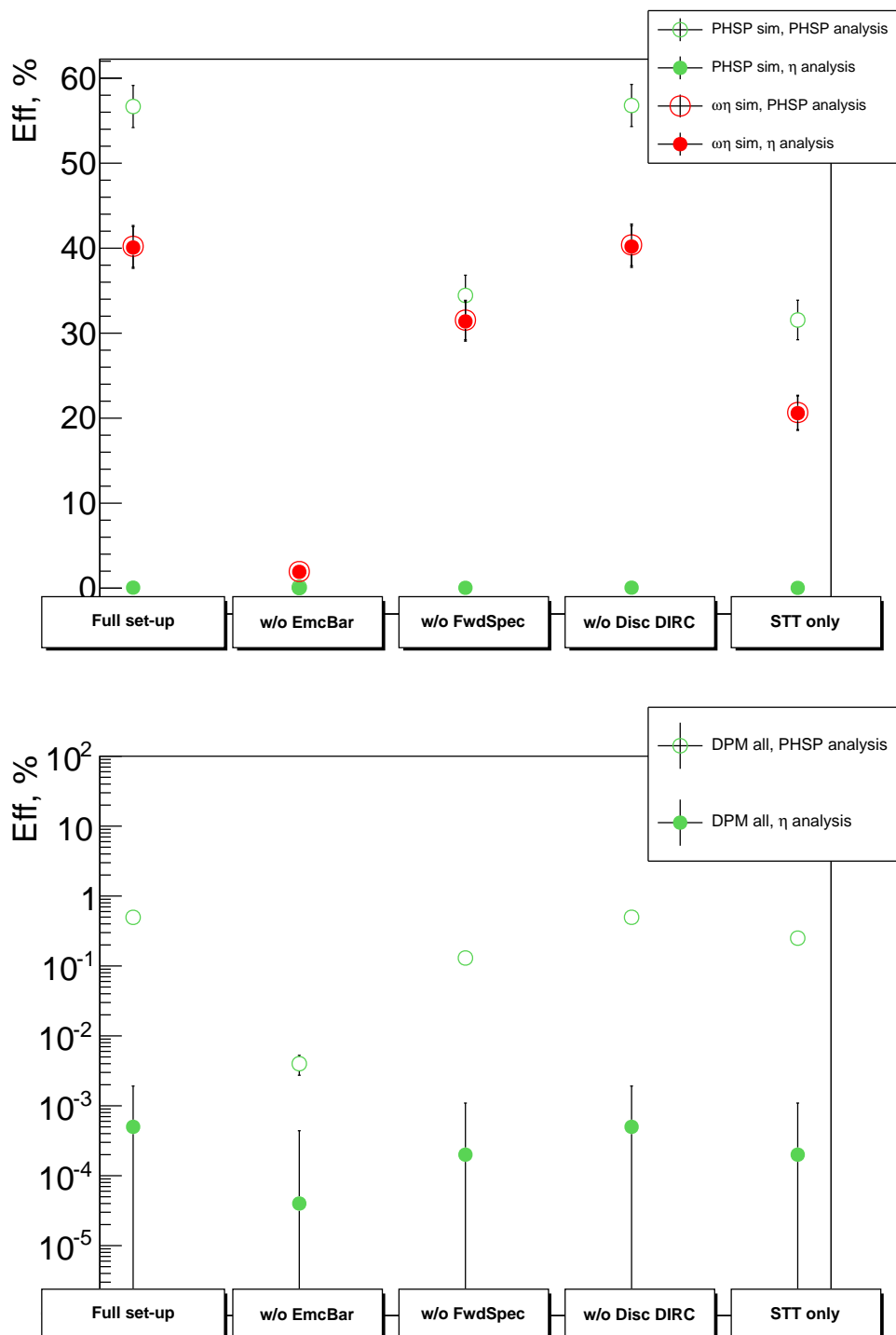


Figure 7.12: Efficiency of the signal (top) and the background (bottom) events of the decay channel  $h_c \rightarrow \pi^+ \pi^- 3\pi^0$  with only  $\eta$  mass window cut

Table 7.5: Reconstruction efficiency (,%) for  $h_c \rightarrow 2(\pi^+\pi^-)\pi^0$  signal events and the background events (bottom row) extracted for different detector set-ups and different generations and analysis models

Channel	Analysis	Full	w/o EmcBar	w/o FwdSpec	w/o Disc DIRC	STT only
PHSP	PHSP	42.44	8.38	33.35	43.14	11.96
	$\eta$ -cut	0.21	0.01	0.19	0.14	0.01
$\eta f_0(1500)$ , $\eta f_0(980)$ $\eta\rho, \eta\omega$	PHSP	43.83	7.69	36.38	43.83	14.32
	$\eta$ -cut	44.18	7.79	36.95	44.39	14.48
$\eta\omega$	PHSP	44.11	7.94	36.21	42.9	13.58
	$\eta$ -cut	44.11	7.96	36.2	42.89	13.59
$\eta\rho$	PHSP	43.67	7.85	35.73	42.81	13.45
	$\eta$ -cut	43.74	7.86	35.82	42.91	13.51
$\eta f_0(980)$	PHSP	44.4	8.13	37.64	45.63	13.97
	$\eta$ -cut	45.01	8.21	38.2	46.21	14.24
$\eta f_0(1500)$	PHSP	46.04	7.64	37.11	44.47	13.91
	$\eta$ -cut	47.43	7.85	38.14	45.71	14.45
DPM	PHSP	1.30	0.41	0.57	1.31	0.33
	$\eta$ -cut	$2 \cdot 10^{-3}$	$6 \cdot 10^{-4}$	$7 \cdot 10^{-4}$	$2 \cdot 10^{-3}$	$4 \cdot 10^{-4}$

Table 7.6: Reconstruction efficiency (,%) for  $h_c \rightarrow \pi^+\pi^-3\pi^0$  signal events and the background events (bottom row) extracted for different detector set-ups and different generations and analysis models

Channel	Analysis	Full	w/o EmcBar	w/o FwdSpec	w/o Disc DIRC	STT only
PHSP	PHSP	55.96	0.09	34.05	56.08	31.07
	$\eta$ -cut	0.06	0.002	0.04	0.06	0.03
$\eta\omega$	PHSP	39.92	1.93	31.17	39.87	20.52
	$\eta$ -cut	39.86	1.93	31.11	39.79	20.48
DPM	PHSP	0.496	0.004	0.13	0.497	0.25
	$\eta$ -cut	$5 \cdot 10^{-4}$	$4 \cdot 10^{-5}$	$2 \cdot 10^{-4}$	$5 \cdot 10^{-4}$	$2 \cdot 10^{-4}$

For the estimation of the beam time required for this measurement the time-dependent significance is calculated. The following definition of the significance is used:

$$\text{Significance}(t) = \sqrt{L \cdot t} \frac{\sigma_s \cdot \varepsilon_s \cdot f_{BR}}{\sqrt{\sigma_s \cdot \varepsilon_s \cdot f_{BR} + \sigma_b \cdot \varepsilon_b}} \quad (7.13)$$

where the parameters:

$\sigma_s$  – signal cross section

$\sigma_b$  – background cross section

$f_{BR}$  – branching fraction for given decay

$L$  – average luminosity

are known before and the parameters obtained in the simulation study are:

$\varepsilon_s$  – reconstruction efficiency for signal events

$\varepsilon_b$  – reconstruction efficiency for background events

The production cross section  $\sigma_s$  of  $p\bar{p} \rightarrow h_c$  is expected to be in the order of 10–100 nb [125]. For the background all inelastic channels were simulated with DPM, corresponding to the cross section  $\sigma_b = \sigma_{tot.inel} = 50$  mb. The branching ratios are estimated according to Eq. 7.11 and Eq. 7.12:  $f_{BR}(h_c \rightarrow 2(\pi^+\pi^-)\pi^0) = 4 \times 10^{-3}$  and  $f_{BR}(h_c \rightarrow \pi^+\pi^-3\pi^0) = 5 \times 10^{-3}$ . For the luminosity the average value of  $10^{32} \text{cm}^{-2} \text{s}^{-1}$  is assumed.

The dependence of the significance on the measurement time is shown in Fig. 7.13. For the highest assumed signal cross section 100 nb, due to the high level of the background rejection the channel  $h_c \rightarrow \pi^+\pi^-3\pi^0$  could require just 2 weeks for measurement to achieve a 5 sigma significance. In contrast, for the channel  $h_c \rightarrow 2(\pi^+\pi^-)\pi^0$ , data has to be taken at least for 10 weeks to reach the same level of the significance. One should mention, if reconstruction efficiency for signal events is large enough, the time needed for collecting the amount of data necessary for an significant observation will be not too long. For example it would require just around one week for both of the channels to collect  $10^4$  events, if the production cross section  $\sigma_s$  turned out to be 100 nb.

The preliminary results of the Fast Simulation look promising and a measurement of the channel  $h_c \rightarrow 2(\pi^+\pi^-)\pi^0$  and  $h_c \rightarrow \pi^+\pi^-3\pi^0$  is feasible at  $\bar{P}$ ANDA. As it was demonstrated, to suppress background to some reasonably small fraction, an appropriate model assumption is needed. For simplicity, decay modes with pseudovector mesons were excluded in this study. However compared to the modes included in the analysis, modes with pseudovector mesons do not have a suppression due to isospin violation in the subsequent decay. Therefore it may give a significant contribution and

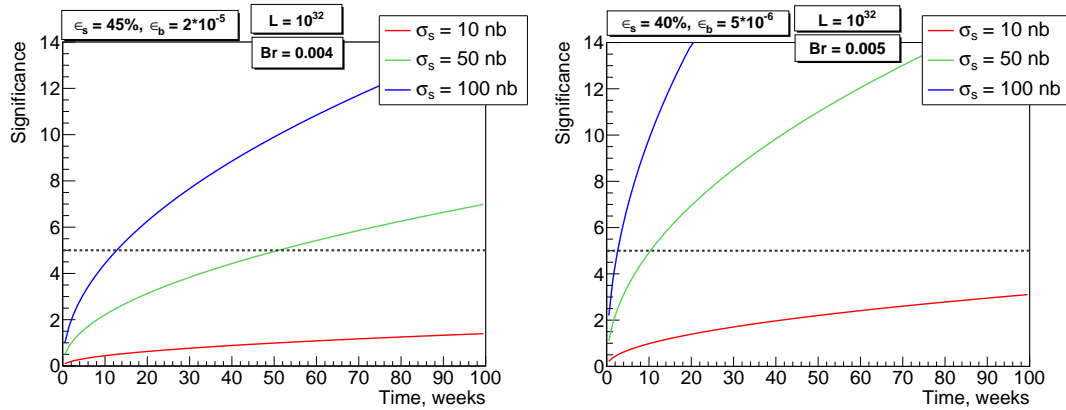


Figure 7.13: Time needed to collect the amount of data necessary to observe a signal of a certain significance for  $h_c \rightarrow 2(\pi^+\pi^-)\pi^0$  (left) and  $h_c \rightarrow \pi^+\pi^-3\pi^0$  (right)

should be considered for the next iteration of the study with the complete simulation. One should also note that no model was used for the production of the  $h_c$ . Different production mechanism of  $h_c$  could significantly increase the importance of Forward Spectrometer of  $\bar{P}$ ANDA. It can also change the result in terms of efficiency and time needed to achieve the required significance. Since very general the DPM model was used for background simulation, a systematic uncertainty according to the background description has to be taken into account. Therefore it could be interesting here to use the FTF model, which is currently an alternative to the DPM (Ch. 6).

## Summary

The future fixed target experiment  $\bar{P}$ ANDA has an ambitious physics program. In this experiment an antiproton beam will be exploited to study different topics in Hadron Physics, such as Hadron Spectroscopy, Nucleon Structure, Hadrons in Matter and Hypernuclear Physics. It will perform precise spectroscopy measurements of hadronic systems, which appear in  $p\bar{p}$  annihilation in the charmonium mass range, corresponding to an antiproton beam momentum range of 1.5 to 15 GeV/ $c$ . The High Energy Storage Ring (HESR), where the  $\bar{P}$ ANDA experiment will be hosted, will be able to provide a beam with high momentum resolution (up to  $\Delta p/p \sim 4 \times 10^{-5}$ ) or with high intensity (with a peak luminosity up to  $2 \times 10^{32} \text{cm}^{-2} \text{s}^{-1}$ ). This paves the way for determinations of masses and widths recently found resonances with unprecedented precision as well as a more extensive search of missing states, e.g. glueballs.

A precise luminosity information is crucial for absolute cross section measurements and scanning experiments. This experimental characteristic will be monitored by the Luminosity Detector (LMD), a dedicated subsystem of the  $\bar{P}$ ANDA detector. For the luminosity determination the differential cross section of the  $\bar{p}p$  elastic scattering in dependence on the scattering angle is going to be used. The measurement will be performed at very small momentum transfer  $t$  (and thus very small scattering angle), where the Coulomb part of the elastic cross section dominates. This part can be calculated very precisely. However, for high  $\bar{P}$ ANDA beam energies the hadronic contribution at small  $t$  cannot be ignored. To make use of the complete  $p\bar{p}$  elastic scattering description, the LMD will perform a differential counting of the scattered antiprotons versus the scattering angle  $\theta$ . Currently the main limitation on the accuracy of the luminosity measurement at  $\bar{P}$ ANDA is the systematic uncertainty of the model for elastic scattering. As shown in this work, the systematic uncertainty of the model varies between 1% and 10%, depending on the beam momentum and the data used for the comparison. An improvement of the model accuracy is expected from an independent measurement

of the  $\bar{p}p$  elastic scattering in the  $\bar{P}$ ANDA energy range by the future KOALA experiment.

As a detector, the LMD is a small tracking system, which will be inserted 11 m downstream from the IP. It is designed to measure the forward scattered antiprotons with angles between 3 and 8 mrad in polar angle and the full azimuth angle. The LMD consists of 4 planes, each plane contains 10 modules with pixel sensors (HV-MAPS), sensitive to the position of the track. For the determination of the luminosity, the cross section in dependence on the scattering angle has to be extracted from the data. The data reconstruction includes several crucial steps: finding and fitting of the tracks of the elastically scattered antiprotons and backtracking them to the interaction point in order to get rid of the influence of the magnetic field, which the particles pass before reaching the LMD.

Fig. 8.1 demonstrates how the luminosity will be extracted from raw data<sup>1</sup>. The data treatment starts with the determination of alignment parameters and variables needed to tune the simulation (e.g exact position of the IP). As a second step, the two-dimensional functions for the acceptance and the detector resolution are extracted from the Monte Carlo simulation with a realistic model of the detector. Then the data for the luminosity fit are reconstructed taking the misalignment of the detector components into account and cleaned from background contributions.

Although the material budget of the LMD is very low, the remaining material affects the resolution of low momentum tracks by multiple scattering. To overcome this problem, the Cellular Automaton (CA) algorithm was implemented in addition to the more simple Track Following (TF) algorithm for the track search. It was shown that CA deals better with high multiplicity events at low energies. For the Track Fit, multiple scattering is taken into account by the "breaking-lines" approach. Another feature of the reconstruction chain is the back propagation of the tracks to the IP. The back propagation of the track parameters works fine, however it was shown that the extrapolation of the co-variance matrix is not accurate enough and should be studied more carefully. The track reconstruction chain was checked in different simulation tests and extensively used in different steps needed for the accurate luminosity determination.

In order to achieve the best resolution for the scattering angle measurement, even a misalignment of  $50\ \mu\text{m}$  between modules has to be avoided. This potential problem was attacked with a software alignment method based on reconstructed tracks. The Millipede algorithm is a widely used solution for this task, because it allows the determination of all alignment parameters in a simultaneous linear least squares fit with an arbitrary number of tracks. Due to the fact that the LMD prototype does not exist yet and the real misalignment scale is not known, extensive tests were made to prove that the Millipede algorithm is applicable for the LMD.

Another open question is how many tracks of background reactions, mainly of inelastic antiproton proton reactions, will reach the LMD. Different background sources

---

<sup>1</sup> The yellow boxes show parts covered in this thesis

and methods for the suppression of the background were investigated in this work. The quantitative results of this study are model-dependent because a proper description of the background is difficult from the theory side, especially in the LMD angular range. Due to the lack of data in the  $\bar{\text{PANDA}}$  momentum range on the one hand and a significant number of inelastic channels on the other hand, currently it is impossible to validate the background event generators. Nevertheless, an attempt was done to use the DPM generator for the description of the inelastic background. By comparing the behavior of the distributions of the reconstructed variables for signal and background tracks different cuts are proposed, including cuts based on a multivariate analysis.

During the background studies it turned out, that antiprotons from elastic scattering at  $\theta$  angles larger than 9 mrad can also contribute as an additional background source. It was demonstrated that this background component, as well as tracks from inelastic interactions and secondary particles, can be rejected by a two-steps track filtering procedure. The first step is based on correlations between the starting point of the track and its direction, which are caused by the dipole magnetic field in front of the LMD. The second part of the background rejection procedure uses the expected value of the beam momentum of the tracks at high energies and relations between different variables at low energies. It was shown that even for low momentum tracks, which have the worst resolution of track parameters, it is possible to perform an accurate background rejection with the help of multivariate analysis.

$\bar{\text{PANDA}}$  already has a powerful software framework for simulation studies with the complete detector response or just using approximations of the response in order to save computing time. The advantage of the simplified simulation was used to investigate the measurement of hadronic decays of the  $h_c$  meson with the  $\bar{\text{PANDA}}$  detector. The direct  $h_c$  production can only be performed in a  $p\bar{p}$  experiment. But hadronic channels could be very difficult to measure, due to the high cross sections of non-resonance production of these final states in  $\bar{p}p$  interactions.

The channels  $h_c \rightarrow 2(\pi^+\pi^-)\pi^0$  and  $h_c \rightarrow \pi^+\pi^-3\pi^0$  were chosen due to the high cross sections of these final states in  $\bar{p}p$  interactions. To suppress the background contribution to some reasonably small fraction an appropriate model assumption is needed. In this study a very naive model is introduced and the high suppression of background is demonstrated with the resulting background efficiency of  $\varepsilon_b \sim 10^{-5}$  for  $h_c \rightarrow 2(\pi^+\pi^-)\pi^0$  channel. For the  $h_c \rightarrow \pi^+\pi^-3\pi^0$  channel the background contribution is much smaller due to the smaller cross section of  $p\bar{p} \rightarrow \pi^+\pi^-3\pi^0$  at the same center of mass energy. Therefore a background efficiency  $\varepsilon_b \sim 10^{-6}$  seems easily achievable. The measurement of  $h_c \rightarrow \pi^+\pi^-3\pi^0$  at  $\bar{\text{PANDA}}$  could be the first measurement of this decay mode. The detection of two hadronic decay modes opens the possibility to measure the ratio between the corresponding branching fractions  $\frac{\mathcal{B}(h_c \rightarrow \pi^+\pi^-3\pi^0)}{\mathcal{B}(h_c \rightarrow 2(\pi^+\pi^-)\pi^0)}$ . And a cross check of the analysis can be done by comparing this ra-

tio with the ratio between  $\mathcal{B}(\eta \rightarrow \pi^+ \pi^- \pi^0)$  and  $\mathcal{B}(\eta \rightarrow 3\pi^0)$ , which are well known. The preliminary results of the simulation study look promising. However, more reliable theoretical models have to be tested in the future.

Nowadays computer simulations have taken an essential role in the preparation of physics experiments. It is possible to simulate the whole experimental setup, including as many details as possible from the particle reactions, the geometry description, the detection performance, the reconstruction and the physical analysis steps before the start of data taking. The simulation of detector components assists the designing process and the development of the reconstruction strategy. Also different theoretical approaches can be compared coherently in advance to judge if this particular experiment has the potential to find out which approach describes the data best. During the preparation of this thesis, the simulation approach was extensively used at all stages. Many details of the detector design as well as the reconstruction software were specified with simulation results. Unfortunately real experimental data are not available for the ultimate tests yet. Nevertheless the LMD reconstruction software is complete and ready to be tested on real data. Finally, it was also shown that the  $\bar{\text{P}}\text{ANDA}$  detector is well suited for measurements of specific channels with a high hadronic background contribution.

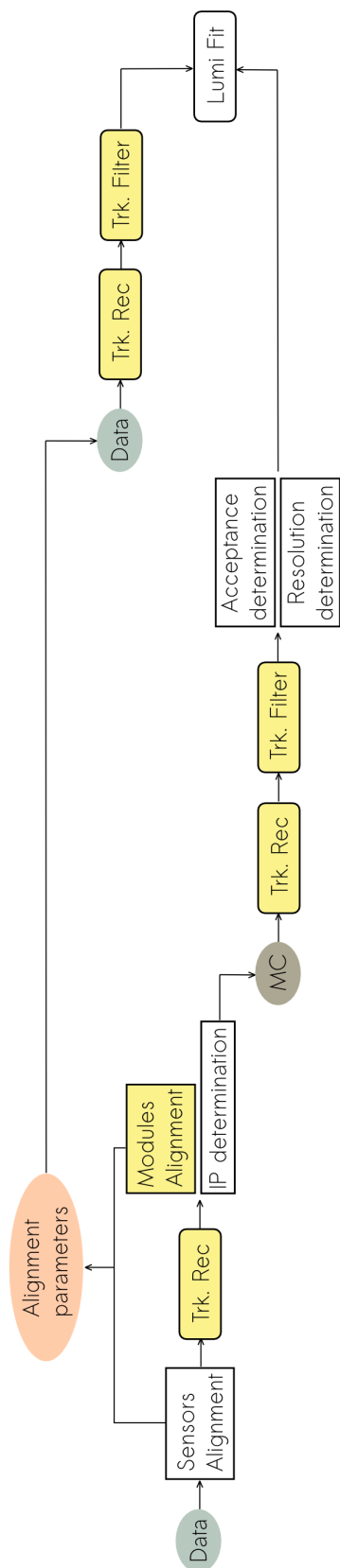


Figure 8.1: Flow of the luminosity detector software

# Access to elementary particles in experiments

Experiments in different fields contain some conceptual similarities. In elementary particle physics an experimentalist aims to make a research of interesting phenomena in appropriate and the clearest possible experimental conditions. As it is also done in chemistry, biology, medicine, social psychology, etc. And as in every of the mentioned fields, there are typical features for all experiments in this particular field, which are specific and unique. This is reflected in specific terms, which are usually used to report results. This thesis is not an exception and many of the terms are used in following chapters. Below some of the most useful terms are introduced to make sure the author and the reader have a common understanding of them.

Our knowledge of the laws of physics in the sub-nuclear domain (at distance scales of about  $10^{-13}$  cm and smaller) is for the most part derived from analyzing the outcomes of high-energy collisions of elementary particles. While the size and sophistication of each component of high-energy experiments have steadily grown, the basic experimental setup has remained unchanged since the late 1960s.

The unit of energy used in particle physics is the electron-volt (eV) which is the amount of energy picked up by an electron passing between the poles of a 1 V battery. Energies of a few eV are sufficient to pull electrons from atoms. Energies a million times higher (MeV), are involved when dealing with nuclear phenomena such as fission in reactors. To study the constituent particles of the nucleus, energies at least a thousand times higher (GeV), are needed. The main component of any experiment is the source of the particles with these energies. Usually the particles are accelerated in dedicated facilities (accelerators) to gain the energy needed for the experiment. Depending on the experiment the energy can vary from several keV ( $10^3$  eV) up to tens TeV ( $10^{12}$  eV). A particle accelerator uses a carefully designed combination of electric and magnetic

fields to produce and accelerate narrowly focused beams of energetic particles (typically electrons, protons, and their antiparticles).

The region where collisions occur (the *interaction point*) is surrounded by a set of particle detectors, which attempt to identify the particles coming out of the collision, and measure their energies and momenta. Simplified scheme of experiment is shown on Fig. A.1. Due to interaction particles of a beam with particles of a target, different particles coming from the target to a detector, where they are registered. If only momenta of particles are changed due to interaction, such process is called *elastic scattering*. If not only momenta are changed, but also new particles are arises, such process is called *inelastic*. The same interacting particles (*initial state*) can result in different particles (*final state*). A reaction under study is called *signal channel*. Final states which are different from one expected from the signal channel are called *background (channels)*. Usually distinction a signal from a background is challenging task. Therefore modern detectors are sophisticated systems which aims to registrate all particles in a final state and measure as much parameters of the particles as possible.

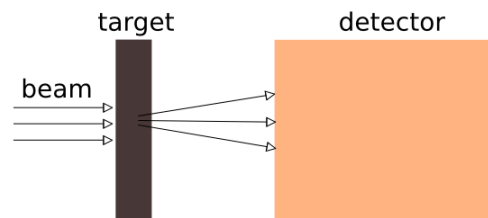


Figure A.1: Scheme of classical experiment in Elementary Particle Physics

One particular example of transition between initial state to final state is called *event*. Since physics at subatomic distance scales is governed by laws of quantum mechanics, the outcome of each collision cannot be known ahead of time. The best that any theory can do is to predict the probabilities of various possible outcomes. The experiments collect and analyze outcomes of huge number of collisions. The number of events with specified properties within the collected data set is proportional to the probability of an event. It is convenient to express the probability of a particular event by a *cross section*. The cross section is defined as the transition rate per unit incident flux per target particle. For a colliding experiments where another beam of particles is used instead of a target, also the concept of a cross section is used to express the likelihood of interaction between particles.

During the analysis of experiment results obtained for a signal channel are compared with theoretical predictions. Physical quantities used to analyze events include cross sections and/or angular distributions of final state particles. Agreement between theory and experiment generally considered as confirmation of the theory. Disagreement, if experiment was proved to be correct, means that theory needs improvement

or complete change. The discussion of all known or answered questions in elementary particle physics is a subject of an enormous number of monographs and textbooks. In a short form current progress is presented in "The Review of Particle Physics" [1]. The current thickness of this review goes over 1500 page (Fig. A.2) and shows that the field is rather broad. It also should be note that since the first "The Review of Particle Physics" was published 40 years ago, number of its pages increased 10 times and it reflects the speed of the progress in the Elementary Particle Physics. Nevertheless there are still many unanswered questions and puzzles. In this context the strong interaction is the one of the most mysterious topics. This thesis is related to studies of the strong interaction via investigation of hadrons.

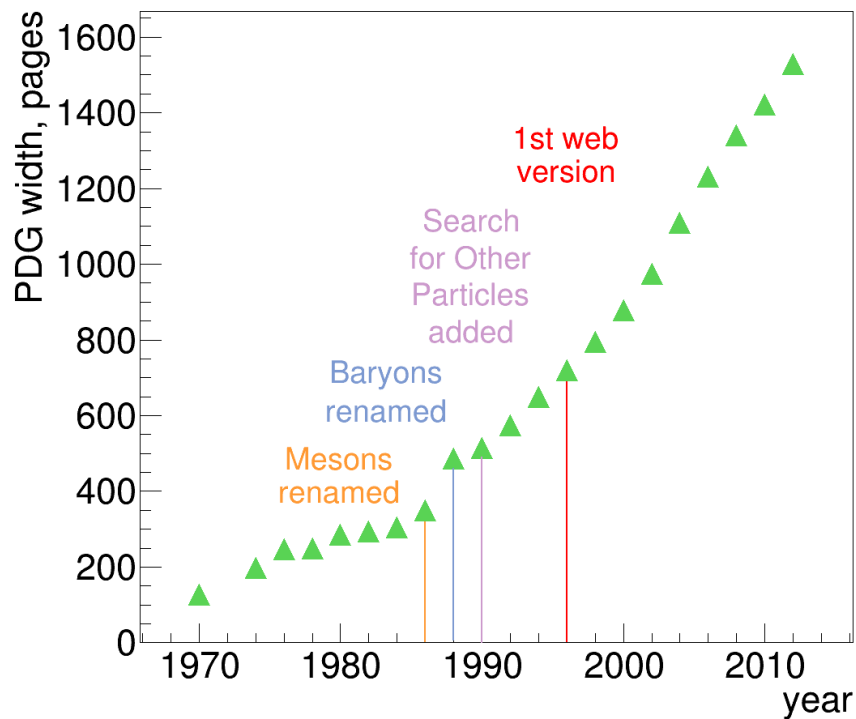


Figure A.2: Number of pages of the "The Review of Particle Physics" in dependence of publishing year

# Overview of antiproton–proton experiments in the past

The study of  $\bar{p}p$  interactions began in 1960s with bubble chambers at LBL, CERN and BNL. Later it was pursued at these laboratories together with Serpukov and KEK. The most precise currently available data about antiproton proton collisions at low and medium energies (in the PANDA energy range) came from the high intensity and small momentum uncertainty machines LEAR [126] and ISR [127] at CERN and the antiproton accumulator at Fermilab [47]. The overview of the experiments is presented in Tab. B.1 and Tab. B.2. Below after a short introduction into the bubble chamber detection technique, the history of studies of  $\bar{p}p$  interactions is shortly discussed.

## B.1 Bubble chamber

A bubble chamber is a vessel filled with a super-heated high density and transparent liquid used to detect electrically charged particles moving through it. It is normally made by filling a large cylinder with a liquid heated to just below its boiling point. As particles enter the chamber, a piston suddenly decreases its pressure, and the liquid enters into a super-heated, meta-stable phase. Charged particles create an ionization track, around which the liquid vaporizes, forming microscopic bubbles. Bubbles grow in size until they are large enough to be seen or photographed. Several cameras are mounted around it, allowing a three-dimensional image of an event to be captured. A spatial resolution in the order of  $100\ \mu\text{m}$  was achieved for this device [128]. A bubble chamber can be operated at magnetic field, which allows to measure particles momenta. However this detector has many drawbacks, such as the need for a photographic readout rather than three-dimensional electronic data. The time during which

bubble chamber is sensitive is only few milliseconds and photographing of the formed tracks must take place during this short time [129]. The key feature of bubble chamber operation that affected the design of beams is the fact that the chambers cannot be triggered. As a result it was important that only desired particles entering the chamber during its sensitive time. This led to the development of separated beams, containing only the wanted particles. The importance of each individual particle was further raised by the need to keep the total number of particles entering the chamber per sensitive time (i.e. per picture) below some maximum permitted by obscuration of one track by another. In practical situations this corresponded to a flux limit in the order of 20 tracks per picture [130].

In modern research bubble chambers are used again in searches for Dark Matter [131]. But in the begging of 80s it was difficult to cope with increasing energies and intensities of beams by this detection technique.

## B.2 CERN

Between 60s and 80s years of XX century, the data with antiproton beams were obtained at secondary beam line of CERN Proton Synchrotron (PS), which was running at energy 28 GeV. Pictures of  $\bar{p}p$  interactions in medium energies were taken by 81 cm/200 cm Hydrogen Bubble Chambers (HBC81, HBC-2M), Gargamelle Heavy Liquid Bubble Chamber (GGM) and the Big European Bubble Chamber (BEBC)[132]. The energy range of the antiproton beam momentum was varied between 1.2–12 GeV/ $c$  with beam spread  $\pm 1.5\%$ . It should be mentioned here that some channels with charged particles in final state in this energy range have been measured so far only in experiments with the bubble chambers at CERN [51].

To obtain antiproton beams with high intensity in CERN was constructed antiproton accumulator complex (AAC) [133]. From the early 1980s AAC was supplying antiprotons to experiments at the intersecting storage rings (ISR), the low energy antiproton ring (LEAR) and super proton synchrotron (SPS) when is was running as  $S\bar{p}pS$  collider. The ISR and the  $S\bar{p}pS$  both were mainly operated as antiproton-proton colliders at high energies (up to  $\sqrt{s}=62$  GeV/ $c$  and  $\sqrt{s}=630$  GeV/ $c$  respectively). However at ISR fixed target experiment R-704 [127] with antiproton beam and hydrogen target was performed in charmonium range. A beam momentum was operated in the range from 3.5 to 6.5 GeV/ $c$  with momentum spread  $\Delta p/p \approx \pm 4 \times 10^{-4}$ . The maximum beam current reached was 5.5 mA corresponding to  $1.1 \times 10^{11}$  circulating antiprotons. The target ( $H_2$  gas jet) had a density of  $10^{14}$  atoms/cm<sup>3</sup> and a diameter at the intersection with the beam of  $\sim 0.9$  cm. Therefore peak luminosity  $3 \times 10^{30}$  cm<sup>-2</sup>s<sup>-1</sup> was achieved. The detector was a two-arm non-magnetic spectrometer. It was complemented by a large-acceptance guard counter system. And a silicon solid-state telescope monitored

the luminosity by measuring the yield of large-angle protons at  $90^\circ$  from  $p\bar{p}$  elastic scattering [134]. Uncertainty of the luminosity measurement was estimated  $\pm 5\%$ . Charmonium  $c\bar{c}$  states were the first time studied with  $p\bar{p}$  interactions [135], e.g. the resonant formation of  $J/\Psi$  in antiproton-proton annihilations was for the first time observed there [127]. Although the experiment was dedicated to the detection of electromagnetic decays of charmonium, a few runs with a trigger accepting hadrons were performed too [134].

In the LEAR measurements were performed with antiproton beams with low momentum (60–1940 MeV/ $c$ ). The beam intensity was up to  $2 \times 10^6 \bar{p}/s$  with a resolution  $\Delta p/p \sim 10^{-3}$ . The ASTERIX spectrometer was used to study the formation and the ground state of the  $\bar{p}p$  atom and exclusive final states of  $\bar{p}p$  annihilation at rest in a  $H_2$  gas target [136]. The physics program of the ASTERIX was continuing and extending by followed experiments with better detectors: Crystal Barrel with particular emphasis on neutral final states [137] and the OBELIX designed to collect high-statistics data in kaonic final states [138]. Later the JETSET experiment searched for hadronic resonances by using of proton-antiproton annihilations into the gluon-rich OZI-suppressed channel  $\bar{p}p \rightarrow \phi\phi$ . In order to obtain high luminosity and a good final-state mass resolution, a molecular hydrogen-cluster jet target and a compact detector system surrounding the beam-jet interaction region were employed [139].

### B.3 Brookhaven National Laboratory

In the United States, in particularly at the Brookhaven Alternating Gradient Synchrotron (AGS) and the Argonne National Laboratory Zero Gradient Synchrotron (ZGS),  $\bar{p}p$  interactions were also initially studied with separated antiproton beams and bubble chambers filled with hydrogen, which played both roles a target as well as a detector material [130]. At Brookhaven at that time 3 bubble chambers were operated: 30", 31" and 80". All of them were exposed by beams of different particles including antiproton beams. Although energy of the beam could be varied in wide range, the data were published only for a few beam momenta as it is reflected in Tab. B.2. Later the Multiparticle Spectrometer came to operation, which was served with antiproton beam too [140].

### B.4 Fermilab

In the beginning of 1990s The Fermilab Antiproton Accumulator (AA) came to operation. The AA is a storage ring designed to accumulate and cool antiprotons for the Tevatron colliding beam program. However it also contributed to studies of charmonium states in  $\bar{p}p$  interactions by experiments E760 [141] and E835 [47]. The constrains from the

available space led to the cylindrical, nonmagnetic detector. Its limited number of physical topics which could be studied there. Experiment E760 was designed to study charmonium states formed exclusively in anti-proton proton collisions, and their decays to electromagnetic final states. An internal hydrogen jet target intersected the antiproton beam (up to  $4 \times 10^{11} \bar{p}$ ) stored in the accumulator ring, providing a point-like source with instantaneous luminosity in the range of  $(3-9) \cdot 10^{30} \text{ cm}^{-2} \text{ s}^{-1}$ . A high performance stochastic cooling system compensated for the effects of scattering and energy loss in multiple traversals of the target by the beam, keeping its momentum spread at  $\Delta p/p < 2.5 \cdot 10^{-4}$  [141]. Typically, the data for an integrated luminosity  $\sim 1 \text{ pb}^{-1}$  were collected with one beam fill. It should be mentioned that energy-scan technique was extensively applied here for determination properties of resonances [44].

Later the detector was upgraded to perform experiment E835, which also studied charmonium states and their decays to electromagnetic final states. There the typical instantaneous luminosity during the data taking was  $2 \times 10^{31} \text{ cm}^{-2} \text{ s}^{-1}$ . The capability for operation at high rates was achieved by segmenting the detectors and by equipping all channels with time-to-digital converters (TDC), which allowed rejection of out-of-time signal [47]. As soon as the antiproton source at Fermilab was fully dedicated to provide luminosity for the Tevatron Collider, medium-energy antiproton fixed-target experiments were closed.

Available data for  $p\bar{p}$  collisions is compiled in [84], which was issued in 1984. Information about experiments, which data was used in [84], is given in Tab. B.1 and Tab. B.2. Experiments done or published after 1984, such as R-704(CERN) and E760/E835(FNAL), are also included to Tab. B.1 and Tab. B.2 to complete a picture about sources for the currently available data.

Name	Place	$P_{beam}$ , GeV/c	beam intensity	Detector set-up	Statistic ( $\mathcal{L}$ or number of events)	Date
HBC 81	PS	1.2-5.7	?	bubble chamber	$\sim 3 \cdot 10^5$ pictures	between 1963 and 1967 [132]
HBC-2M	PS	1.2-12	10 $\bar{p}$ /picture	bubble chamber	$\sim 4 \cdot 10^8$ pictures 50 events/ $\mu\text{b}$	between 1963 and 1975 [132],[142]
GGM	PS	1.6-12	?	bubble chamber	$\sim 7 \cdot 10^5$ pictures	between 1971 and 1976 [132]
BEBC	PS	12	$\sim 10$ $\bar{p}$ /picture	bubble chamber in magnetic field	$\sim 3 \cdot 10^5$ pictures (10 events/ $\mu\text{b}$ )	between 1973 and 1985 [143], [144]
R-704	ISR	3.5-6.5	$10^{10}$	two-arm non-magnetic spectrometer a large-acceptance guard counter charged-particle tracking, $\gamma$ s silicon detector ( $\mathcal{L}$ monitor)	$309 \text{ nb}^{-1}$	?-1984 [127]
PS-185	LEAR	<2 GeV/c	$1.5 \cdot 10^5$	forward decay spectrometer charged particle tracks	$4 \cdot 10^{10} \bar{p}$	1984-1996 [145],[146]
Crystal Barrel	LEAR	0.06-1.94	$10^4-10^6$ $\bar{p}$ /s	magnetic spectrometer K/ $\pi$ separation coverage of charged particles and $\gamma$ s in full $4\pi$	$10^8$ events at rest, $\sim 2 \cdot 10^7$ events at flight	1989-1996 [126], [137]
JETSET	LEAR	1.1-2.0	$5 \cdot 10^{10}$ $\bar{p}$ /s	charged-particle tracking, $\gamma$ s, PID "forward" coverage $\theta_{lab}$ in $7^\circ-45^\circ$ "barrel" in $45^\circ-135^\circ$	$5 \cdot 10^8$ events	1991-1994 [139]

Table B.1: The past CERN experiments with antiproton-proton collisions in medium energies (for the bubble chambers total statistic is given of all energy points in range from lowest till highest available beam momentum)

Name	Place	$P_{beam}$ , GeV/c	beam intensity	Detector set-up	Statistic ( $\mathcal{L}$ or number of events)	Date
BNL-E-0789	AGS (BNL)	1.29-1.55	0.15% of $10^7$ particles/s	$\pi/K$ separation, coverage 14% of the azimuth	$2.5 \cdot 10^5$ events	1984-1985 [147]
BNL 30in HBC	AGS (BNL)	up to 4.0	?	bubble chamber	$\sim 1 \cdot 10^6$ pictures	1968-1970 [148], [149]
BNL 31in HBC	AGS (BNL)	up to 4.0	?	bubble chamber	$\sim 1 \cdot 10^6$ pictures	1968-1970 [148], [149]
BNL 80in HBC	AGS (BNL)	6.94, 8, 14.75	?	bubble chamber in magnetic field	$\sim 2 \cdot 10^6$ pictures	1968-1973 [150],[148]
Multiparticle spectrometer	BNL	3.0-6.0	$2.5 \cdot 10^4$ $\bar{p}$ /pulse	magnetic spectrometer $K/\pi/\bar{p}$ separation	?	1974-? [140], [151]
ANL-MURA	ZGS	1.6-2.2	?	bubble chamber (30in HBC)	?	1974-1978 ?
BC-064	SLAC	8.8 GeV	1-2 $\bar{p}$ /pulse	hybrid chamber charged tracks, PID hadron calorimeter	$4 \cdot 10^4$ pictures	1976-1978 [152], [153]
E-129 (LASS)	SLAC	8.3, 13	?	magnetic spectrometer $4\pi$ acceptance $K/\pi/p$ separation	?	1977-1978 [154], [155]
E-760	AA(FNAL)	4-7	$3.5 \cdot 10^{11}$ $\bar{p}$	nonmagnetic detector $2\pi$ (azimuth) and $2^\circ - 70^\circ$ (polar) coverage, tracking system, PID calorimeter	?	1990-1992 [141], [156]
E-835	AA(FNAL)	3.5-7.5	$6 \cdot 10^{11}$ $\bar{p}$	upgrade of E760 components	$254.6 \text{ pb}^{-1}$	1996-1997 1999-2000 [47]

Table B.2: The past experiments in the United States of America with antiproton-proton collisions in medium energies (for the bubble chambers total statistic is given of all energy points in range from lowest till highest available beam momentum)

## B.5 Proton antiproton elastic scattering

$P_{lab}$ , GeV/c	$ t $ range, (GeV/c) <sup>2</sup>	Comment	Reference
1.5	0.05 - 1.5 (*)	not included syst.err 4%	[52]
1.6	0.06 - 1.7 (*)	not included syst.err 4%	[52]
1.71	0.07 - 1.85 (*)	not included syst.err 4%	[52]
1.78	0.001 - 0.1 (*)	not included syst.err 4%	[52]
1.81	0.07 - 2.05 (*)	not included syst.err 4%	[52]
1.86	0.08 - 2.1 (*)	not included syst.err 4%	[52]
1.91	0.07 - 2.2 (*)	not included syst.err 4%	[52]
2.01	0.08 - 2.3 (*)	not included syst.err 4%	[52]
2.12	0.1 - 2.5 (*)	not included syst.err 4%	[52]
2.23	0.1 - 2.5 (*)	not included syst.err 4%	[52]
2.33	0.1 - 2.6 (*)	not included syst.err 4%	[52]
2.33 (**)	0.04 - 2.9	not included syst.err 2.7%	[157]
2.43	0.11 - 2.6 (*)	not included syst.err 4%	[52]
2.607	0.001 - 0.1	not included syst.err 2%	[54]
2.85 (**)	0.04 - 3.7	not included syst.err 2.2%	[158]
3.0	0.02 - 1.3		[159]
3.55 (**)	0.16 - 3.9	not included syst.err 20%	[160]
3.65	0.003 - 1.4	not included syst.err 4%	[159]
3.7 (***)	0.001 - 0.016	not included syst.err 2%	[50]
4.07 (***)	0.001 - 0.016	not included syst.err 2%	[50]
4.2	0.001 - 0.019	not included syst.err 1%	[55]

Table B.3: Overview of previous experiments for  $p\bar{p}$  elastic scattering: (\*) – data is given for  $\cos(\theta_{CM})$ ; (\*\*) – data was used for DPM model; (\*\*\*) – data was used for E760 model

$P_{lab}$ , GeV/c	$ t $ range, (GeV/c) <sup>2</sup>	Comment	Reference
5.0	0.03 - 1.2	not included syst.err 4%	[159]
5.0	0.16 - 7.6	not included syst.err 15%	[161]
5.6 (***)	0.001 - 0.02	not included syst.err 2%	[50]
5.7 (**)	0.03 - 2.5		[162]
5.72 (***)	0.0008 - 0.02	not included syst.err 2%	[50]
5.94 (***)	0.0008 - 0.02	not included syst.err 2%	[50]
6.0	0.0015 - 0.035	not included syst.err 1%	[55]
6.2	0.31 - 1	not included syst.err 20%	[163]
6.23 (***)	0.001 - 0.02	not included syst.err 2%	[50]
7.976-8.024	0.05 - 0.86	not included syst.err 10%	[53]
8.0	0.0018 - 0.08	not included syst.err 1%	[55]
8.0	0.02 - 0.85	not included syst.err 5%	[164]
10.0	0.0018 - 0.1	not included syst.err 1%	[55]
10.1	0.2 - 3	not included syst.err 5%	[165]
10.4 (**)	0.02 - 0.2	not included syst.err 2%	[166]
15.952-16.048 (**),(!)	0.11 - 1.3	not included syst.err 10%	[53]
16.0	0.085 - 1.2	not included syst.err 5%	[164]

Table B.4: Overview of previous experiments for  $p\bar{p}$  elastic scattering: (\*\*) – data was used for DPM model; (!) – data was used for DPM model with  $P_{lab}$  15.95 GeV/c; (\*\*\*) – data was used for E760 model

# Extraction of the model parameters for $\bar{p}p$ differential elastic cross section by the LMD

Due to not very accurate knowledge about parameters of the model for the elastic scattering, it would be useful to extract the parameters from the data obtained with the LMD. Below is demonstrated how accurate the parameters of the models can be extracted in the simultaneous fit of the model and the luminosity and influence of such procedure on the luminosity extraction accuracy.

For this studies  $3 \times 10^7$  events of  $p\bar{p}$  elastic scattering in the full  $\theta$ <sup>1</sup> and  $\phi$  range were generated with DPM generator. Two extreme beam momenta cases are studied: 1.5 GeV/c, with the realistic shape of the IP<sup>2</sup>, and 15 GeV/c with the point-like beam. At both momenta for the acceptance and resolution distributions  $3 \times 10^7$  events were simulated with BOX generator, where  $\theta_{MC}$  was generated uniformly within 2 and 12 mrad and in  $\phi$  between 0 and  $2\pi$ . The beam shape for the simulations with BOX generator was used the same as one for the corresponding DPM data. Then the complete reconstruction chain was performed. In contrast to default procedure of the luminosity fit, besides the luminosity the model parameters were released too.

---

<sup>1</sup> $\theta_{min} = 0.12^\circ$

<sup>2</sup>square shape in (x,y) with position at (0,0) and 0.08 cm width in x and y, target at z=0 with thickness 0.05 cm and Gaussian shape

## C.1 Results for $P_{beam} = 1.5 \text{ GeV}/c$

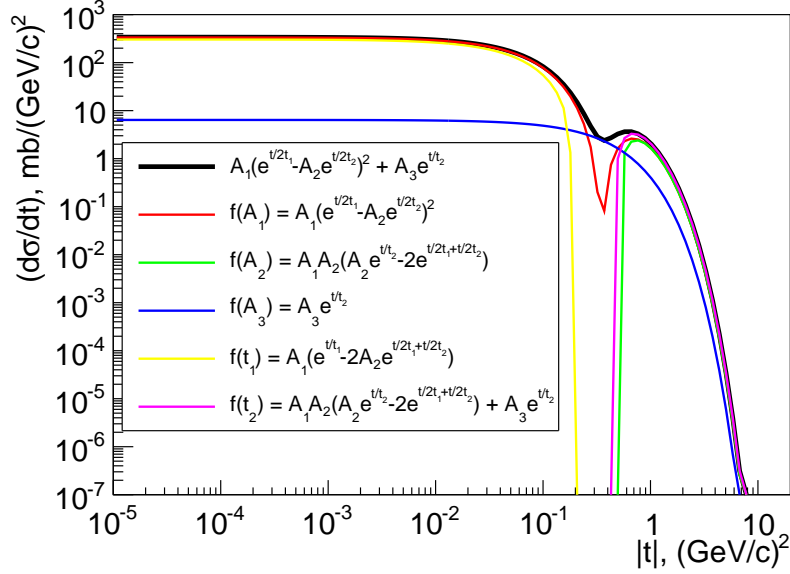


Figure C.1: The DPM model behavior at  $P_{beam} = 1.5 \text{ GeV}/c$

Fig. C.1 shows the prediction of the DPM model for the hadronic part of the differential cross section of the elastic scattering at the beam momentum  $1.5 \text{ GeV}/c$ . Also contributions of terms related to each parameter are presented. At this energy the acceptance of the LMD corresponds to the  $|t|$ -range between  $\sim 10^{-5}$  and  $\sim 10^{-4} (\text{GeV}/c)^2$ , where the contributions of terms related to  $A_2$  and  $t_2$  parameters are negligible. Therefore these parameters were fixed to the values from the generator and were not used in the simultaneous fit of the model and the luminosity.

The tests were performed for the data with and without cuts to check the results dependency on the amount of the background. The results are presented in the Tab. C.1. The true parameters values, used in the DPM generator, are show in the first row of the table (in the brackets). At this beam momentum, the accuracy of the luminosity extraction does not change significantly when the model parameters are used in the fit. This is due to high contribution of the Coulomb term of the differential cross section of the elastic scattering, which is the model independent. However the result of the fit for the parameters of the model deviates significantly from the values used in the DPM. Especially in the case with the highest background level without any cuts applied for the reconstructed data, when the parameters errors from the fit are rather small and do not reflect the actual deviation from the true values.

Cut	Bkg, %	Fit parameters	$\Delta L/L$ , %	$A_1$ (565.035)	$A_3$ (6.40097)	$t_1$ (0.0899)
X&Y and M	0.17	$L$ $L, A_1, A_3, t_1$	$0.047 \pm 0.062$ $0.075 \pm 0.001$	$546.28 \pm 1.99$	$-4.57 \pm 1.99$	$0.11 \pm 2.00$
X&Y	1.67	$L$ $L, A_1, A_3, t_1$	$0.47 \pm 0.22$ $1.08 \pm 0.44$	$763.93 \pm 228.07$	$123.52 \pm 133.98$	$0.136 \pm 170.5$
no cuts	3.66	$L$ $L, A_1, A_3, t_1$	$3.09 \pm 0.34$ $3.12 \pm 0.02$	$715.007 \pm 1.99$	$95.37 \pm 1.99$	$0.14 \pm 2.00$

Table C.1: Results of the fit ( $P_{beam}=1.5$  GeV/c)

## C.2 Results for $P_{beam}$ 15 GeV/c

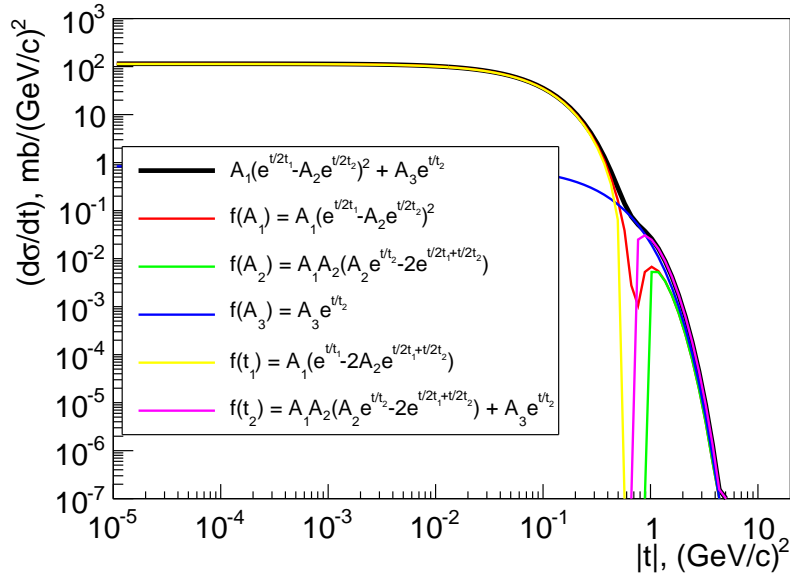
Figure C.2: DPM model function behavior at  $P_{beam}$  15 GeV/c

Fig. C.2 shows the DPM prediction for the hadronic part of the differential cross section of elastic scattering at the beam momentum 15 GeV/c. Also contributions of terms related to each parameter are presented in the figure. At this energy the LMD acceptance corresponds to the  $|t|$ -range between  $10^{-3}$  and  $10^{-2}$  (GeV/c)<sup>2</sup>. Again the contributions of the terms related to  $A_2$  and  $t_2$  parameters are negligible in the LMD  $|t|$ -range.

The results of the fit are shown in Tab. C.2. At this beam momentum value the

hadronic contribution of the elastic scattering dominates in the LMD measurement range. Therefore the luminosity strongly correlates with the model parameters and its extraction accuracy becomes significantly worse in the simulations fit with the model parameters. e.g. in the case when there is no cuts applied on the reconstructed data, the relative accuracy of the luminosity extraction is  $\sim 3\%$  if only the luminosity is used as free parameter in the fit, but it becomes  $\sim 15\%$  if the model parameters are used in the fit too. The result for the fit of the parameters of the model is close to the true values used in the generation with the DPM only in case if all cuts are applied on the data and the amount of the background is below  $1\%$ . It should be stressed here that the cuts tuning was done on the simulated data with the background model, which correctness should be proven in the experiment.

Cut	Bkg, %	Fit parameters	$\Delta L/L,$ %	$A_1$ (131.453)	$A_3$ (0.837)	$t_1$ (0.0899)
X&Y and M	0.93	$L$ $L, A_1, A_3, t_1$	$-0.042 \pm 0.067$ $-0.04 \pm 0.86$	$131.45 \pm 0.93$	$0.84 \pm 0.71$	$0.0890 \pm 0.002$
X&Y	2.37	$L$ $L, A_1, A_3, t_1$	$1.84 \pm 0.07$ $-21.2 \pm 0.67$	$156.65 \pm 1.21$	$16.04 \pm 0.88$	$0.0669 \pm 0.0008$
no cuts	10.9	$L$ $L, A_1, A_3, t_1$	$2.92 \pm 0.07$ $14.5 \pm 0.96$	$117.60 \pm 0.75$	$-9.14 \pm 0.58$	$0.112 \pm 0.002$

Table C.2: Results of the fit ( $P_{beam}=15 \text{ GeV}/c$ )

### C.3 Conclusion

As shown in this study, the simultaneous fit of the luminosity and the model parameters gives good results only at high beam momentum ( $15 \text{ GeV}/c$ ) and for relatively clean data sample with the background contribution below  $1\%$ . Therefore this procedure can be done only after the data obtained in the experiment is well understood. Nevertheless the range of the beam momenta, where such procedure for the parameters can be applied, is limited due to the LMD acceptance. Thus for the determination of the model parameters in the full beam momenta range of the  $\bar{\text{P}}\text{ANDA}$  a dedicated KOALA experiment will be performed. And determination of the parameters by the LMD data can be used for the cross check of the KOALA results at high beam momenta.

# Track extrapolation in a non-homogeneous magnetic field

Extrapolated track parameters at point  $z_e$  can be calculated from equations of motion in magnetic field [77]:

$$\begin{aligned}
 x' &= t_x, \\
 y' &= t_y, \\
 t_x' &= h(t_x t_y B_x - (1 + t_x^2) B_y + t_y B_z), \\
 t_y' &= h((1 + t_y^2) B_x - t_x t_y B_y - t_x B_z), \\
 \frac{q}{p'} &= 0.
 \end{aligned} \tag{D.1}$$

where  $(x_0, y_0)$  are initial track coordinates at point  $z_0$  and  $(t_x, t_y)$  is track direction at this point,  $h = \kappa \frac{q}{p} \sqrt{1 + t_x^2 + t_y^2}$ ,  $\kappa [(GeV/c)kG^{-1}cm^{-1}] = 2.99792458 \cdot 10^{-4}$ ,  $p [GeV/c]$  – momentum,  $q [e]$  – signed charge and  $B [kG]$  – magnetic field (the primes denote derivatives with respect to  $z$ ).

The extrapolated coordinates  $x(z_e)$ ,  $y(z_e)$  are obtained by integration of the track directions:

$$x = x(z_0) + \int_{z_0}^{z_e} t_x(z) dz,$$

$$y = y(z_0) + \int_{z_0}^{z_e} t_y(z) dz \quad (D.2)$$

Therefore we will focus only on the extrapolation of the directions  $t_x, t_y$ . First of all let's rewrite the Eq.(D.1):

$$\begin{aligned} t_x &= \sum_{i_1=x,y,z} a_{i_1}(z) \cdot B_{i_1}(z) \\ t_y &= \sum_{i_1=x,y,z} b_{i_1}(z) \cdot B_{i_1}(z) \end{aligned} \quad (D.3)$$

Here the functions  $a_{i_1}(z)$  and  $b_{i_1}(z)$  are:

$$\begin{aligned} a(z) &\equiv h \cdot (t_x t_y, -1 - t_x^2, t_y) \\ b(z) &\equiv h \cdot (1 + t_y^2, -t_x t_y, -t_x) \end{aligned} \quad (D.4)$$

And the magnetic field  $B(z)$  is taken at the particle trajectory as a function of  $z$ :

$$B(z) = B(x_{track}(z), y_{track}(z), z) = (B_x(z), B_y(z), B_z(z)) \quad (D.5)$$

The Eq.(D.3) is linear on the magnetic field and only the multipliers  $a$  and  $b$  depend on the track directions  $t_x, t_y$ . One can calculate the  $a$  and  $b$  derivatives using the Eq.(D.3). The analytic formula will be based on this property of the equation of motion. General formula of extrapolation is given for function  $T(z) \equiv T(t_x(z), t_y(z))$ , by substitution  $T \equiv t_x, T \equiv t_y$ .

The  $T$  derivative is:

$$T'(z) = \frac{\partial T}{\partial t_x} t'_x(z) + \frac{\partial T}{\partial t_y} t'_y(z) = \sum_{i_1=x,y,z} \left( \frac{\partial T}{\partial t_x} a_{i_1} + \frac{\partial T}{\partial t_y} b_{i_1} \right) \cdot B_{i_1}(z) \quad (D.6)$$

For the  $T'$  derivative new functions  $T_{i_1}(z)$  are introduced:

$$T_{i_1}(z) \equiv \left( \frac{\partial T}{\partial t_x} a_{i_1} + \frac{\partial T}{\partial t_y} b_{i_1} \right) \quad (D.7)$$

So we can rewrite Eq.(D.6):

$$T'(z) = \sum_{i_1=x,y,z} T_{i_1} \cdot B_{i_1}(z) \quad (D.8)$$

The derivatives of the new functions  $T_{i_1}(z)$  can be expanded in the same way:

$$T'_{i_1}(z) = \sum_{i_2=x,y,z} \left( \frac{\partial T_{i_1}}{\partial t_x} a_{i_2} + \frac{\partial T_{i_1}}{\partial t_y} b_{i_2} \right) \cdot B_{i_2}(z) = \sum_{i_2=x,y,z} T_{i_1 i_2}(z) \cdot B_{i_2}(z) \quad (D.9)$$

So the trick is rewrite derivative  $T_{i_1 \dots i_{k-1}}$  as:

$$T'_{i_1 \dots i_{k-1}}(z) = \sum_{i_k=x,y,z} T_{i_1 \dots i_k}(z) \cdot B_{i_k}(z) \quad (D.10)$$

where functions  $T_{i_1 \dots i_k}(z)$  are defined recursively:

$$T_{i_1 \dots i_k}(z) \equiv \frac{\partial T_{i_1 \dots i_{k-1}}}{\partial t_x} a_{i_k} + \frac{\partial T_{i_1 \dots i_{k-1}}}{\partial t_y} b_{i_k} \quad (D.11)$$

Then the function  $T(z_e)$  can be represented as:

$$\begin{aligned} T(z_e) &= T(z_0) + \int_{z_0}^{z_e} T'(z_1) dz_1 \\ &= T(z_0) + \sum_{i_1} \int_{z_0}^{z_e} T_{i_1}(z_1) B_{i_1}(z_1) dz_1 \\ &= T(z_0) + \sum_{i_1} \int_{z_0}^{z_e} (T_{i_1}(z_0) + \int_{z_0}^{z_e} T'_{i_1}(z_2) dz_2) B_{i_1}(z_1) dz_1 \\ &= T(z_0) + \sum_{i_1} T_{i_1}(z_0) \int_{z_0}^{z_e} B_{i_1}(z_1) dz_1 + \sum_{i_1} \int_{z_0}^{z_e} B_{i_1}(z_1) \int_{z_0}^{z_e} \sum_{i_2} B_{i_2} T_{i_1 i_2}(z_2) dz_2 dz_1 = \dots \end{aligned} \quad (D.12)$$

This equation can be written in compact form:

$$T(z_e) = T(z_0) + \sum_{k=1}^n \sum_{i_1, \dots, i_k} T_{i_1 \dots i_k}(z_0) \cdot \left( \int_{z_0}^{z_e} B_{i_1}(z_1) \dots \int_{z_0}^{z_{k-1}} B_{i_k}(z_k) dz_k dz_1 \right) + O\left(\frac{\kappa B(q/p)(z_e - z_0)^{n+1}}{(n+1)!}\right) \quad (D.13)$$

Substituting  $T \equiv t_x$  and  $T \equiv t_y$  in formula (D.13) one can obtain the extrapolated track parameters with the error of the order of  $(n+1)$ . Note in (D.13) the magnetic field components are separated from the track parameters. The track directions entering the formula are taken at initial position  $z_0$ , while the magnetic field is integrated along

the particle trajectory.

The method given above is called Runge–Kutta extrapolation. This method is widely used in software packages for particle propagation in a magnetic field. For example in GEANT a fourth–order Runge–Kutta extrapolation is used to transport particles through the detector volume. Since the GEANE package is based on GEANT3 also the Runge–Kutta extrapolation is used there too.

# Appendix E

## Propagation of the covariance matrix of track parameters in a magnetic field

For track with parameters errors  $(\delta\mathbf{x})_l$  at track length  $l$ , errors at point  $l + dl$  can be calculated as:

$$(\delta\mathbf{x})_{l+dl} = \delta(\mathbf{x})_l + dl \cdot A_{l+dl} \cdot (\delta\mathbf{x})_l + dl \cdot B_{l+dl} \cdot (\delta\mathbf{x})_l + (\delta\mathbf{x}^M)_{l+dl} \quad (\text{E.1})$$

where the matrix  $A$  propagates an error in the direction of the track at  $l$  to an error in the position of the track at  $(l + dl)$ , matrix  $B$  describes deflection caused by the magnetic field and term  $(\delta\mathbf{x}^M)_{l+dl}$  appears due to multiple scattering and energy loss straggling in the interval  $(l, l + dl)$ . Following [167] let's define

$$F_{l+dl} = (\delta\mathbf{x})_l + dl \cdot A_{l+dl} \cdot (\delta\mathbf{x})_l + dl \cdot B_{l+dl} \cdot (\delta\mathbf{x})_l \quad (\text{E.2})$$

Then dividing the total length of the track  $L$  into  $n$  small steps of size  $dl = L/n$  and applying (E.1) one obtains:

$$(\delta\mathbf{x})_L = \left( \prod_{j=n}^1 \mathbf{F}_j \right) (\delta\mathbf{x})_0 + \sum_{v=1}^{n-1} \left[ \left( \prod_{j=n}^{v+1} \mathbf{F}_j \right) (\delta\mathbf{x}^M)_v \right] + (\delta\mathbf{x}^M)_n \quad (\text{E.3})$$

Going to the limit  $n \rightarrow \infty$ :

$$(\delta\mathbf{x})_L = \mathbf{F}(0, L) \cdot (\delta\mathbf{x})_0 + \int_0^L \mathbf{F}(l, L) \cdot \left( \frac{\delta\mathbf{x}^M}{dl} \right) dl \quad (\text{E.4})$$

where

$$\mathbf{F}(l_1, l_2) = \lim_{dl \rightarrow 0} \left( \prod_{j=\mu_2}^{\mu_1} \mathbf{F}_j \right) \quad (\text{E.5})$$

The last term in the Eq.(E.4) means that each new error ( $\delta \mathbf{x}^M$ ) at point  $l$  is propagated to point  $L$  as ( $\delta \mathbf{x}_0$ ) is propagated from 0 to  $L$  in the first term. There is no correlation between the multiple scattering and energy loss errors in two different point of the track. The last term is usually calculated as a random component in the covariance matrix. Therefore this term can be omitted and one gets:

$$(\delta \mathbf{x})_L = \mathbf{F}(0, L) \cdot (\delta \mathbf{x})_0 \quad (\text{E.6})$$

This is mean for propagation the errors in an elementary tracking step the matrix  $\mathbf{F}$  must be found:

$$\mathbf{F} = I + (\mathbf{A}_{l+dl} + \mathbf{B}_{l+dl}) \cdot dl \quad (\text{E.7})$$

In existing references matrices  $\mathbf{A}$  and  $\mathbf{B}$  are given for so-called the transverse system of variables (SC system in GEANE)

$$\frac{1}{p}, \lambda, \phi, y_{\perp}, z_{\perp} \quad (\text{E.8})$$

with:

$\frac{1}{p}$  = inverse momentum

$\lambda$  = dip angle ( $= \frac{\pi}{2} - \theta$ )

$\phi$  = azimuthal angle

$y_{\perp}$  = y coordinate of the track in a local orthonormal reference frame with the  $x_{\perp}$  axis along the particle direction ( $y_{\perp}$  is parallel to  $xy$  plane)

$z_{\perp}$  = z coordinate in the reference system described above

For back propagation from the luminosity detector to interaction point (IP) so-called the detector system of variables is used (SD system in GEANE)

$$\frac{1}{p}, v', w', v, w \quad (\text{E.9})$$

where ( $u, v, w$ ) is an orthogonal reference system with the  $vw$  plane coincident with the detector one. The derivatives indicate the momentum direction variation in the new system.

From matrix  $\mathbf{R}(\mathbf{x})$  is easy to obtain matrix  $\mathbf{R}(\mathbf{y})$  if the Jacobian  $J = \frac{\partial(\mathbf{y})}{\partial(\mathbf{x})}$  is known

$$\mathbf{R}(\mathbf{y}) = \mathbf{J} \cdot \mathbf{R}(\mathbf{x}) \cdot \mathbf{J}^T \quad (\text{E.10})$$

For following discussion is important only have elements in discussed matrices zero or non-zero values. Interested in the elements itself reader can found them in [167] and [168]. Also for simplification small polar angle of propagated tracks is taking into account (tracks are almost parallel to z-axis). The Jacobian from SC to SD transformation has a form [167]:

$$J = \frac{\partial(1/p, v', w', v, w)}{\partial(1/p, \lambda, \phi, y_{\perp}, z_{\perp})} = \begin{pmatrix} J_{00} & 0 & 0 & 0 & 0 \\ 0 & 0 & J_{12} & 0 & J_{14} \\ 0 & 0 & J_{22} & 0 & J_{24} \\ 0 & 0 & 0 & J_{33} & 0 \\ 0 & 0 & 0 & J_{43} & 0 \end{pmatrix} \quad (\text{E.11})$$

$$J^T = \begin{pmatrix} J_{00} & 0 & 0 & 0 & 0 \\ 0 & 0 & 0 & 0 & 0 \\ 0 & J_{12} & J_{22} & 0 & 0 \\ 0 & 0 & 0 & J_{33} & J_{43} \\ 0 & J_{14} & J_{24} & 0 & 0 \end{pmatrix} \quad (\text{E.12})$$

Also we will need matrices A and B [168]:

$$A = \begin{pmatrix} A_{00} & 0 & 0 & 0 & 0 \\ 0 & 0 & 0 & 0 & 0 \\ 0 & 0 & 0 & 0 & 0 \\ 0 & 0 & A_{32} & 0 & 0 \\ 0 & A_{41} & 0 & 0 & 0 \end{pmatrix} \quad (\text{E.13})$$

$$B = \begin{pmatrix} 0 & 0 & 0 & 0 & 0 \\ B_{10} & 0 & B_{12} & B_{13} & B_{14} \\ B_{20} & B_{21} & B_{22} & B_{23} & B_{24} \\ 0 & 0 & 0 & 0 & B_{34} \\ 0 & 0 & 0 & B_{43} & 0 \end{pmatrix} \quad (\text{E.14})$$

The Fig. 4.24 shows field strength in x,y,z axis direction versus z coordinate of propagated track as it is seen by propagated antiprotons. One can divide propagation distance on regions according to magnetic field behavior:

1.  $H_x = H_y = H_z = 0$  (z from  $\sim 1200$  cm to  $\sim 660$  cm)
2.  $H_x = 0, H_y \neq 0, H_z = 0$  (z from  $\sim 660$  cm to  $\sim 340$  cm)
3.  $H_x \neq 0, H_y = H_z = 0$  (z from  $\sim 340$  cm to  $\sim 280$  cm)
4.  $H_x \neq 0, H_y \neq 0, H_z \neq 0$  (z from  $\sim 280$  cm to  $\sim 100$  cm)
5.  $H_x = H_y = 0, H_z \neq 0$  (z from  $\sim 100$  cm to 0 cm)

These cases can be organized in two more general groups:

- I) absence of magnetic field (1)
- II) presence of magnetic field (2-5)

For group I in Eq.(E.7) matrix  $\mathbf{B}$  is equal zero and for covariance matrix  $\mathbf{M}$  in SD system one has:

$$\mathbf{M} = \mathbf{J} \cdot \mathbf{A} \cdot \mathbf{J}^T = \mathbf{J} \cdot \underbrace{(\mathbf{A} \cdot \mathbf{J}^T)}_{\mathbf{K}} = \quad (\text{E.15})$$

$$= \mathbf{J} \cdot \begin{pmatrix} K_{00} & 0 & 0 & 0 & 0 \\ 0 & 0 & 0 & 0 & 0 \\ 0 & 0 & 0 & 0 & 0 \\ 0 & K_{31} & K_{32} & 0 & 0 \\ 0 & 0 & 0 & 0 & 0 \end{pmatrix} = \begin{pmatrix} M_{00} & 0 & 0 & 0 & 0 \\ 0 & 0 & 0 & 0 & 0 \\ 0 & 0 & 0 & 0 & 0 \\ 0 & M_{31} & M_{32} & 0 & 0 \\ 0 & M_{41} & M_{42} & 0 & 0 \end{pmatrix}$$

Then for errors at  $(l + dl)$  we have:

$$\begin{aligned}
 \begin{pmatrix} \delta(1/p) \\ \delta v' \\ \delta w' \\ \delta v \\ \delta w \end{pmatrix}_{l+dl} &= (\mathbf{I} + \mathbf{M} \cdot dl) \cdot \begin{pmatrix} \delta(1/p) \\ \delta v' \\ \delta w' \\ \delta v \\ \delta w \end{pmatrix}_l = \\
 &= \begin{pmatrix} (1 + M_{00} \cdot dl)(\delta(1/p))_l \\ (\delta v')_l \\ (\delta w')_l \\ (M_{31} \cdot (\delta v')_l + M_{32} \cdot (\delta w')_l) \cdot dl + (\delta v)_l \\ (M_{41} \cdot (\delta v')_l + M_{42} \cdot (\delta w')_l) \cdot dl + (\delta w)_l \end{pmatrix}
 \end{aligned} \tag{E.16}$$

Basically Eq.(E.17) shows that without magnetic field only  $\delta v$  and  $\delta w$  are changed, but  $\delta v'$  and  $\delta w'$  are stayed constants.

With magnetic field one has to add to Eq.(E.16) following term:

$$\begin{aligned}
 \mathbf{Y} &= \mathbf{J} \cdot \mathbf{B} \cdot \mathbf{J}^T = \mathbf{J} \cdot \underbrace{(\mathbf{B} \cdot \mathbf{J}^T)}_{\mathbf{G}} = \\
 &= \mathbf{J} \cdot \begin{pmatrix} 0 & 0 & 0 & 0 & 0 \\ G_{10} & G_{11} & G_{12} & G_{13} & G_{14} \\ G_{20} & G_{21} & G_{22} & G_{23} & G_{24} \\ 0 & G_{31} & G_{32} & 0 & 0 \\ 0 & 0 & 0 & G_{43} & G_{44} \end{pmatrix} = \begin{pmatrix} 0 & 0 & 0 & 0 & 0 \\ Y_{10} & Y_{11} & Y_{12} & Y_{13} & Y_{14} \\ Y_{20} & Y_{21} & Y_{22} & Y_{23} & Y_{24} \\ 0 & Y_{31} & Y_{32} & 0 & 0 \\ 0 & Y_{41} & Y_{42} & 0 & 0 \end{pmatrix}
 \end{aligned} \tag{E.17}$$

Then for additional errors change due to magnetic field from  $l$  to  $(l + dl)$  we have:

$$(\mathbf{Y} \cdot dl) \cdot \begin{pmatrix} \delta(1/p) \\ \delta v' \\ \delta w' \\ \delta v \\ \delta w \end{pmatrix}_l = \begin{pmatrix} 0 \\ Y_{10} \cdot \delta(1/p)_l + Y_{11} \cdot (\delta v')_l + Y_{12} \cdot (\delta w')_l + Y_{13} \cdot (\delta v)_l + Y_{14} \cdot (\delta w)_l \\ Y_{20} \cdot \delta(1/p)_l + Y_{21} \cdot (\delta v')_l + Y_{22} \cdot (\delta w')_l + Y_{23} \cdot (\delta v)_l + Y_{24} \cdot (\delta w)_l \\ Y_{31} \cdot (\delta v')_l + Y_{32} \cdot (\delta w')_l \\ Y_{41} \cdot (\delta v')_l + Y_{42} \cdot (\delta w')_l \end{pmatrix} \cdot dl \quad (\text{E.18})$$

For full errors estimation in case of presence of magnetic field one has to sum results from Eq.(E.17) and Eq.(E.18):

$$\begin{pmatrix} \delta(1/p) \\ \delta v' \\ \delta w' \\ \delta v \\ \delta w \end{pmatrix}_{l+dl} = \begin{pmatrix} (1 + M_{00} \cdot dl)(\delta(1/p))_l \\ (Y_{10} \cdot \delta(1/p)_l + Y_{11} \cdot (\delta v')_l + Y_{12} \cdot (\delta w')_l + Y_{13} \cdot (\delta v)_l + Y_{14} \cdot (\delta w)_l) \cdot dl + (\delta v')_l \\ (Y_{20} \cdot \delta(1/p)_l + Y_{21} \cdot (\delta v')_l + Y_{22} \cdot (\delta w')_l + Y_{23} \cdot (\delta v)_l + Y_{24} \cdot (\delta w)_l) \cdot dl + (\delta w')_l \\ ((M_{31} + Y_{31}) \cdot (\delta v')_l + (M_{32} + Y_{32}) \cdot (\delta w')_l) \cdot dl + (\delta v)_l \\ ((M_{41} + Y_{41}) \cdot (\delta v')_l + (M_{42} + Y_{42}) \cdot (\delta w')_l) \cdot dl + (\delta w)_l \end{pmatrix} \quad (\text{E.19})$$

Therefore with magnetic field  $v$ ,  $w$ ,  $v'$ ,  $w'$  errors are correlated.

# FTF versus DPM as a background model for the LMD

## F.1 DPM

### F.1.1 Dual Models and relativistic quantum strings



Figure F.1: Meson (left) and baryon (right) structure as relativistic strings ([169])

Dual Models (DM) are based on the regge-resonance dual approach [170]. The first approach bases on assumption that all interactions are the exchange of the quanta of the corresponding field. For example the nucleon-nucleon interaction in nucleus can be described as a  $\pi$  mesons exchange. In scattering processes at high, but not relativistic, energies the interaction goes through the more heavier  $\rho$  and  $\omega$  mesons. And at higher energies the exchanges of particle-like reggeons play the most important role. The second approach is the assumption that in hadron collisions unstable intermediate states (resonances) occur. Resonances are responsible for hadron interactions at moderate energies. These two approaches are independent, but not complementary,

because they both have common dynamic nature.

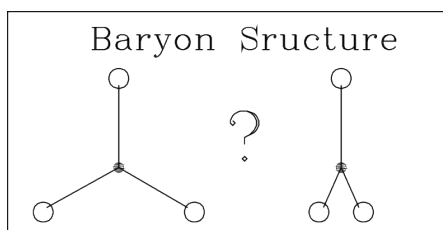


Figure F.2: A possible baryon structure ([83])

In this approach all particles can be interpreted as an one-dimensional system, which is usually called a *string*. And interactions between particles and resonances are represented as ruptures or recombinations of strings. Mesons in this picture are presented as a string with  $q$  and  $\bar{q}$  quarks on the ends and indefinite number of  $q\bar{q}$  virtual pairs as shown on left side of Fig F.1. Baryons, shown on right side of Fig F.1, have two possible interpretations in the theory of relativistic strings as indicated in Fig. F.2. The first one assumes that configuration of local maxima of the energy density in the baryon can have the "Mercedes star" form and the global maximum is associated with a string junction. The second one assumes that baryons have a compact diquark form. Depending on the assumed structure there can be various different final states in baryon-baryon interaction [83].

During the interaction the strings are glued together. This intermediate string can be excited (resonance state) or change the length due to the external field. Then the string breaks apart and the final state particles appear. This mechanism is illustrated in Fig. F.3, where meson scattering goes through colliding chains of quarks and forming a single chain, which rupture leads to mesons in the finale state.

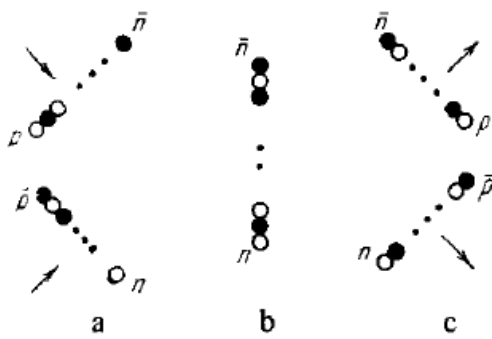


Figure F.3: Meson scattering: (a) quarks chains collide and join at their extremities; (b) the intermediate state - a single chain; (c) rupture of the chain and emission of mesons ([170])

The Dual Parton Model is a synthesis of the Regge phenomenology, quark ideas and  $1/N_f$  expansion of the QCD [83]. The energy dependence of the cross sections

of the  $p\bar{p}$ -processes is given by the Regge phenomenology. The cross sections are in a correspondence with diagrams of the  $1/N_f$  expansion of the QCD. The diagrams describe the creation of unstable intermediate states - quark-gluon strings. The string fragmentation is considered at quark level. The main problem is the description of the low mass string fragmentation and the fragmentation of massive constituent quarks. It is solved by choosing various phenomenological dependencies. As a result a good description of various inelastic reactions was reached and this approach is used in the Monte Carlo generator, called DPM, for the simulation background events at  $\bar{P}$ ANDA.

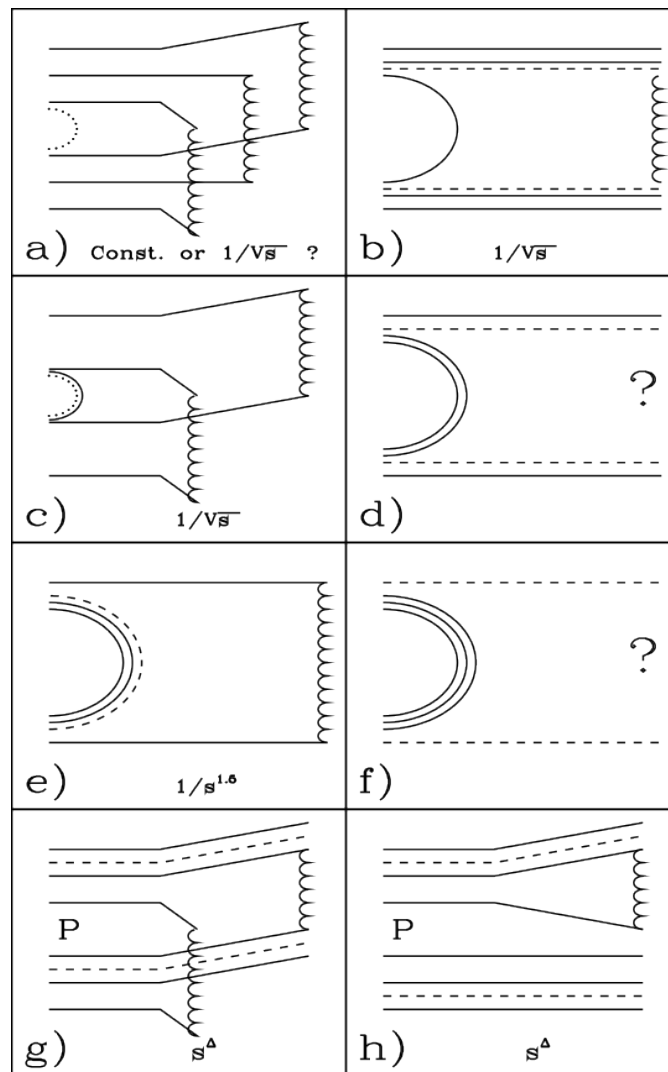


Figure F.4: Processes in  $p\bar{p}$  interactions according to DPM ([83]). The question marks mean that the corresponding estimation are absent

Some processes which are possible in baryon-antibaryon interactions are shown in Fig. F.4, where string junctions are presented by dashed lines. In the process of

Fig. F.4(a) annihilation of the string junctions from colliding baryons results in creation of three strings. Fig. F.4(b) shows processes of quark and antiquark annihilation in one string. Also one string created due to the processes shown in Fig. F.4(e). Annihilation of quark, antiquark and the string junctions represented by diagram in Fig. F.4(c). Excited strings with complicated configuration are created in processes Fig. F.4(d) and Fig. F.4(f). If the collision energy is sufficiently small, glueballs can be formed in the process Fig. F.4(f). Mesons with constituent gluons can be created in the process Fig. F.4(d). Therefore the process Fig. F.4(f) can be responsible for glueball production, and the process Fig. F.4(d) for exotic meson production. The pomeron exchange is responsible for 2 strings formation and diffraction dissociation (Fig. F.4(g) and Fig. F.4(h)). They are dominant at high energies. In the simplest approach it is assumed that the cross sections of the processes have an energy dependence given in Fig. F.4, where  $s$  is the square of the total energy in the center-of-mass system (CMS). Some of the processes (Fig. F.4(d), Fig. F.4(f)) have not a well-defined energy dependence of the cross sections. Since it is usually assumed that their cross sections are small, they were neglected.

The calculation of cross sections is a complex procedure, because there are interactions in the initial and the final state [64]. For the Monte Carlo generator the calculated cross sections for processes from Fig. F.4 are parameterized as following:

$$\begin{aligned}
 \sigma_a &= \frac{51.6}{\sqrt{s}} - \frac{58.8}{s} + \frac{16.4}{s^{1.5}} \\
 \sigma_b &= \frac{77.4}{\sqrt{s}} - \frac{88.2}{s} + \frac{24.6}{s^{1.5}} \\
 \sigma_c &= \frac{93}{s} - \frac{106}{s^{1.5}} + \frac{30}{s^2} \\
 \sigma_g &= \frac{18.6}{s^{0.08}} - \frac{33.5}{\sqrt{s}} + \frac{30.8}{s} \\
 \sigma_d &= \sigma_e = \sigma_f = \sigma_h = 0
 \end{aligned} \tag{F.1}$$

All cross sections are given in mb with  $s$  in GeV.

The parameters of the model were determined by fitting the model to the experimental data, to the total  $p\bar{p}$  and  $pp$  interaction cross sections. The model is in good agreement with data for  $P_{lab} \geq 5$  GeV/c. Therefore using the fitted parameters, the cross sections of  $p\bar{p}$  interactions can be calculated at  $P_{lab} \geq 5$  GeV/c.

The strings from the process included in the DPM model (Fig. F.4) fragment into hadrons. The fragmentation is simulated according to the Ranft-Ritter model [171]. After the string fragmentation all unstable hadrons decay. This is simulated by the help of the code DECAY [172], where unstable hadrons decay via two or three particle decays until all decay products are stable particles. For the angular distribution of decay

products two or three body phase space Monte Carlo model is used.

Finally, a connection can be provided between the processes in Fig. F.4 and channels of  $p\bar{p}$  interactions which can be registered in the detector [64], [83], [173]. Processes of Fig. F.4(a) are responsible for the multi-particle production in  $p\bar{p}$  interactions (e.g  $p\bar{p} \rightarrow 2\pi^+2\pi^-\pi^0$ ,  $p\bar{p} \rightarrow 2\pi^+2\pi^-$ ,  $p\bar{p} \rightarrow 3\pi^+3\pi^-\pi^0$ ,  $p\bar{p} \rightarrow 3\pi^+3\pi^-$  etc). Fig. F.4(b) and Fig. F.4(e) determine the cross sections of the two particle (binary) reactions such as  $p\bar{p} \rightarrow \pi^+\pi^-$ ,  $p\bar{p} \rightarrow K^+K^-$  and baryon-antibaryon pairs in the finale state (e.g  $p\bar{p} \rightarrow \Lambda\bar{\Lambda}$ ,  $p\bar{p} \rightarrow n\bar{n}$ ). Processes as in Fig. F.4(b) also include additional pion(s) radiation in the finale state with baryon-antibaryon pairs (e.g  $p\bar{p} \rightarrow \Lambda\bar{\Lambda}\pi^0$ ,  $p\bar{p} \rightarrow \Lambda\bar{\Lambda}\pi^+\pi^-$ ). And the process Fig. F.4(e) gives the main contribution to the cross section of the 3-meson final states, where the yield of the process of Fig. F.4(a) is very small at  $P_{beam} > 1$  GeV/c. Fig. F.4(c) gives 2-particle states at low energies (e.g  $p\bar{p} \rightarrow \pi^+\pi^-$ ,  $p\bar{p} \rightarrow 2\pi^0$ ,  $p\bar{p} \rightarrow K^+K^-$ , etc). Processes of Fig. F.4(g) and Fig. F.4(h) provides description of the diffraction dissociation of baryon (e.g  $p\bar{p} \rightarrow p\pi^0\bar{p}$ ,  $p\bar{p} \rightarrow p\pi^+\pi^-\bar{p}$ ,  $p\bar{p} \rightarrow p\pi^-\bar{n}$ , etc).

The advantage of the Dual Models is a direct physical picture, which together with quantum field theory leads to many reasonable results. Disadvantage is the large number of parameters which have to be tuned with experimental data. The model also lacks of an accurate description of any particular finale state, e.g its differential cross sections, angular distributions of particles in finale state, etc and provides only estimation of the total cross section for each channel.

### F.1.2 Comment on comparison between DPM and the experimental data

As shown on Fig. 6.13 there is significant discrepancy between the data and the DPM prediction for  $p\bar{p} \rightarrow \pi^+\pi^-\pi^0$  channel, which was not observed in results of [83]. The reason for this is not clear, because this process in DPM is described by diagram Fig. F.4(a), which parameterization did not changed from the publication [83]. However as it turned and pointed out in [173], contribution from diagram Fig. F.4(e) dominates for  $p\bar{p} \rightarrow \pi^+\pi^-\pi^0$ . The processes of Fig. F.4(e) were calculated within FTF generator (see Appendix F), therefore it would be interesting to cross check its results for  $p\bar{p} \rightarrow \pi^+\pi^-\pi^0$  with data and DPM estimations.

For channels with antiprotons, particularly  $p\bar{p} \rightarrow p\bar{p}\pi^0$  and  $p\bar{p} \rightarrow p\bar{p}\pi^+\pi^-$ , DPM gives similar overestimation of the cross section at low beam momenta as in [83]. And  $p\bar{p} \rightarrow \bar{p}\pi^+n$  follows this trend too. The reason for this lies in DPM structure, all of these processes are described by diagrams Fig. F.4(g) and Fig. F.4(h). It is worth to stress once again that FTF estimation for diagrams Fig. F.4(g) and Fig. F.4(h) is different from DPM one. Therefore it would be interesting to compare FTF generator results with DPM and available data for channels with the diffraction dissociation of baryons too.

## F.2 FTF

The DPM approach for estimation of inelastic interactions cross sections (see Chapter 6) was extended to low energies and new tuning of parameters was done within the FTF of GEANT4 toolkit [59]. e.g. it has different parameterization of  $\sigma_a$ ,  $\sigma_b$ ,  $\sigma_c$  are also the parameterization of  $\sigma_e$  is introduced [173]:

$$\sigma_a = \frac{25}{\sqrt{s-4m^2}} \quad (\text{F.2})$$

$$\sigma_b = \begin{cases} 15.65 + 700 \cdot (2.173 - \sqrt{s})^{2.5} & \text{if } \sqrt{s} \leq 2.172 \\ 34/\sqrt{s} & \text{if } \sqrt{s} > 2.172 \end{cases}$$

$$\sigma_c = \frac{2}{\sqrt{s-4m^2}} \left( \frac{m_p + m_t}{s} \right)^2$$

$$\sigma_e = 140/s \quad (\text{F.3})$$

where  $m_p$  and  $m_t$  are masses of projectile and target particles

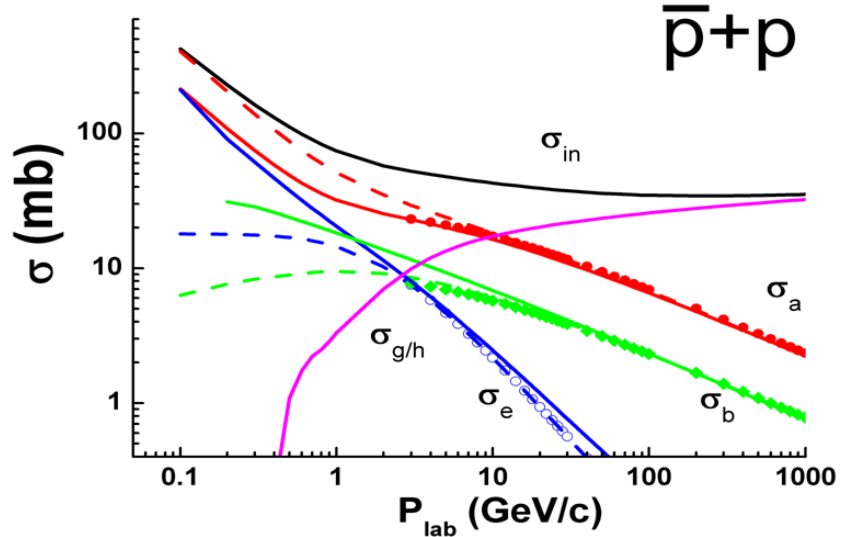


Figure F.5: Processes parameterization in DPM (dashed lines) and FTF (solid lines) models of  $p\bar{p}$  inelastic cross sections [173]

Cross-section for processes with new parameterization (FTF) and old one (DPM) are shown on Fig. F.5. As one can see on the plot at low energies there is significant difference for each particular contribution.

As the next step steps in the FTF generator, the fragmentation is simulated according to the LUND model [174]. For an angular distribution of decay products two and three body phase space Monte Carlo model is used.

Due to different parameterization (compare Eq. F.2 versus Eq. F.3) one can expect different results of the generators. Moreover in [173] good agreement between data and FTF predictions was demonstrated. Thus it is interesting to compare estimations for inelastic channels of  $p\bar{p}$  interactions from FTF and DPM.

### F.3 Simulation description

With each model  $2 \cdot 10^7$  inelastic events were generated in a stand-alone mode. Out of this  $10^5$  events were reconstructed. The geometry description of the set-up included the LMD <sup>1</sup>, the beam pipe <sup>2</sup> and the magnets, surrounded by the cave with vacuum. The point-like IP was positioned at (0,0,0). For the generation of secondary particles FTFP\_BERT physics list was used in GEANT4.

### F.4 Generator (true) level

The difference between the FTF and the DPM is already visible on the generated distributions before propagation of particles through the detector. e.g. the multiplicity of particles per event, which is shown on Fig. F.6. It is not surprising that the FTF has different prediction for two particle final states due to including the process Fig. F.4.e, which is responsible for binary reactions. Estimation of multi-particle final states production also should be different from the DPM due to improved parameterization of  $\sigma_a$ .

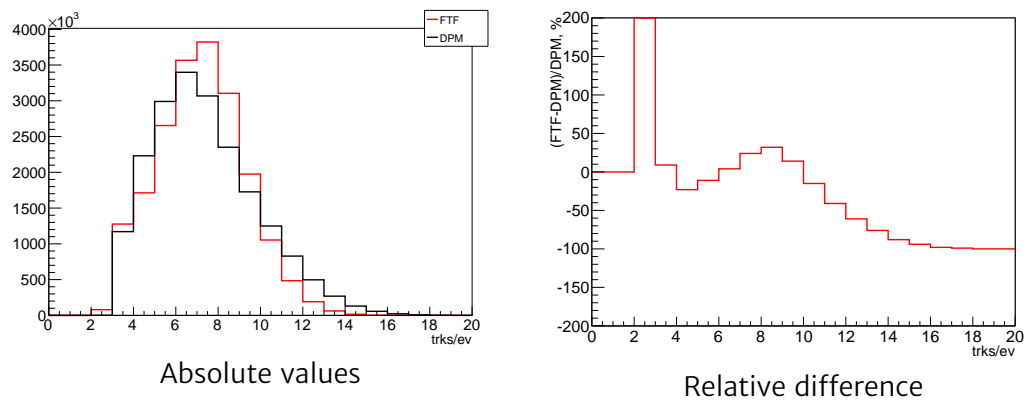


Figure F.6: Multiplicity of final state particles per event

In the background studies with the DPM (Chapter 6) it was shown that particles from inelastic interactions at the IP should have certain kinematics to leave a track

<sup>1</sup>version Sep 2014

<sup>2</sup>beampipe\_201309.root

in the LMD. e.g. only particles with  $\theta_{MC}$  angle below 150 mrad can contribute to the background. The relative difference of the total amount of particles with  $\theta_{MC} < 150$  mrad between the FTF and the DPM is not very large ( $-0.2\%$ ). However there are significant differences in angular (Fig. F.7) and momentum (Fig. F.8) distributions. The FTF predicts more particles in the most crucial for the LMD regions: at very small  $\theta$  angles (below 20 mrad) with momentum close to the beam momentum (15 GeV/c).

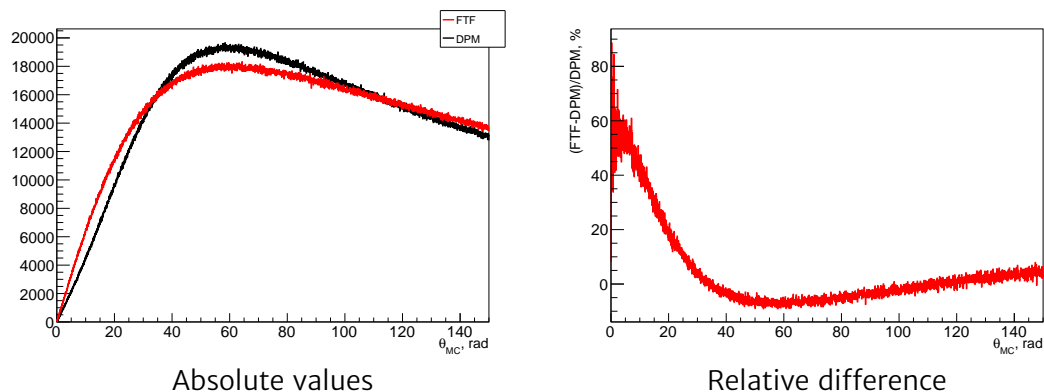


Figure F.7: Distributions of  $\theta_{MC}$  angle for particles with  $\theta_{MC} < 150$  mrad

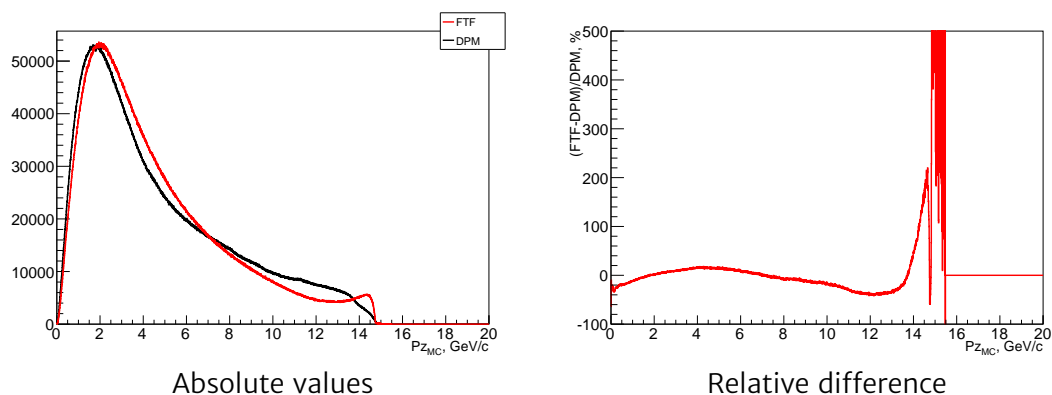


Figure F.8: Distributions of z component of the momentum vector of particles with  $\theta_{MC} < 150$  mrad

## F.5 Reconstructed tracks

Tab. F.1 shows number of reconstructed hits and tracks after different stages of the reconstruction<sup>3</sup>. Although the number of found track candidates is higher for the FTF only by 62%, more of them mimic behavior of the signal tracks and go safely through

<sup>3</sup>for the track search Cellular Automaton was used

the cuts. This is expected since many of particles, as predicted by the FTF, appear in the phase space region close to the signal one.

After ...	DPM	FTF	(FTF-DPM)/DPM, %
Hit rec	10335	12276	18.8
Track search	1017	1651	62.3
X&Y cut	39	228	485
M cut	36	224	505

Table F.1: Number of reconstructed objects for simulation with the DPM and the FTF (the beam momentum  $15 \text{ GeV}/c$ )

## F.6 Estimation of background with FTF

From the previous study with DPM, contribution from the inelastic background (after all cuts) was  $\sim 0.2\%$  (Fig. 6.36) at the beam momentum  $15 \text{ GeV}/c$ . With the FTF this number should be  $\sim 5$  times higher (Tab. F.1). Thus the inelastic background contribution could be as high as  $\sim 1\%$ . And the total amount of background becomes  $\sim 2\%$ . As was demonstrated in Tab. 6.3 in case of the background on the level of  $\sim 2\%$  the accuracy of the luminosity extraction at this beam momentum becomes  $\sim 1\%$ . However the different angular distribution of the background could change the accuracy of the luminosity extraction. Therefore the background studies with the FTF generator with higher statistic is a subject of future investigations.

<b>BDT</b>	Boosted Decision Trees	<b>TMVA</b>	Toolkit for Multivariate Data Analysis
<b>CA</b>	Cellular Automaton	<b>TOF</b>	Time of Flight System
<b>CR</b>	collector ring	<b>TS</b>	Target Spectrometer
<b>DAQ</b>	data acquisition		
<b>DCS</b>	Detector Control System		
<b>DIRC</b>	Detector of Internally Reflected Cherenkov light		
<b>DPM</b>	Dual Parton Model		
<b>EMC</b>	Electromagnetic Calorimeter		
<b>FAIR</b>	Facility for Antiproton and Ion Research		
<b>FS</b>	Forward Spectrometer		
<b>FTF</b>	Fritiof model		
<b>FTS</b>	Forward Tracker Stations		
<b>GEM</b>	Gas Electron Multiplier		
<b>GSI</b>	Helmholtzzentrum für Schwerionenforschung GmbH		
<b>HESR</b>	High Energy Storage Ring		
<b>HL</b>	high luminosity		
<b>HR</b>	high resolution		
<b>HV-MAPS</b>	high voltage monolythic active pixel sensors		
<b>IP</b>	Interaction Point		
<b>KOALA</b>	Key experiment for PANDA Luminosity determination		
<b>LMD</b>	Luminosity Detector		
<b>MVD</b>	micro vertex detector		
<b>MVD</b>	Micro Vertex Detector		
<b>PCA</b>	Point of Closest Approach		
<b>PID</b>	Particle Identification		
<b>p-LINAC</b>	proton linear accelerator		
<b>QCD</b>	Quantum Chromodynamics		
<b>QED</b>	Quantum Electrodynamics		
<b>RESR</b>	Recuperated Experimental Storage Ring		
<b>RS</b>	Range System		
<b>SciTiI</b>	Scintillating Tiles		
<b>SIS</b>	Schwerionen Synchrotron		
<b>STT</b>	Straw Tube Tracker		
<b>TF</b>	Track Following		

# Bibliography

- [1] Beringer, J. et al., “Review of Particle Physics” *Phys.Rev.* **D86** (2012)
- [2] Wigner, E., “Events, Laws of Nature, and Invariance Principles” *The Subnuclear Series* **21** (1985)
- [3] Aad, G. et al., “Observation of a new particle in the search for the Standard Model Higgs boson with the ATLAS detector at the LHC” *Phys.Lett.* **B716** (2012)
- [4] Chatrchyan, S. et al., “Observation of a new boson at a mass of 125 GeV with the CMS experiment at the LHC” *Phys.Lett.* **B716** (2012)
- [5] Ablikim, M. et al., “Observation of a Charged Charmoniumlike Structure in  $e^+e^- \rightarrow \pi^+\pi^- J/\Psi$  at  $\sqrt{s} = 4.26$  GeV” *Phys.Rev.Lett.* **110** (2013)
- [6] Roberts, C. D., “Strong QCD and Dyson–Schwinger Equations” (2012) [arXiv:nucl-th/1203.5341](#)
- [7] Raya, A., “The Origin of Mass” *AIP Conf.Proc.* **1116** (2009)
- [8] PANDA Collaboration, “Physics Performance Report for PANDA: Strong Interaction Studies with Antiprotons” (2009) [arXiv:hep-ex/0903.3905](#)
- [9] Morningstar, C. et al., “The Glueball spectrum from an anisotropic lattice study” *Phys.Rev.* **D60** (1999)
- [10] Wiedner, U., “Future Prospects for Hadron Physics at PANDA” *Prog.Part.Nucl.Phys.* **66** (2011)
- [11] Belle Collaboration, “Observation of a narrow charmonium – like state in exclusive  $B^\pm \rightarrow K^\pm \pi^+ \pi^- J/\Psi$  decays” *Phys.Rev.Lett.* **91** (2003)
- [12] Bodwin, G. et al., “Quarkonium at the Frontiers of High Energy Physics: A Snowmass White Paper” (2013) [arXiv:hep-ph/1307.7425](#)
- [13] Valcarce, A. et al., “Heavy baryon spectroscopy with relativistic kinematics” *Phys.Lett.* **B733** (2014)
- [14] Klempt, E. et al., “Baryon spectroscopy” *Rev.Mod.Phys.* **82** (2010)
- [15] Goeke, K. et al., “Hard exclusive reactions and the structure of hadrons” *Prog.Part.Nucl.Phys.* **47** (2001)

- [16] Mankind, “Wikipedia, the free encyclopedia” (2014)  
URL <http://www.wikipedia.org/>
- [17] Sudol, M. et al., “Feasibility studies of the time-like proton electromagnetic form factor measurements with PANDA at FAIR” *Eur.Phys.J.* **A44** (2010)
- [18] FAIR, “FAIR Green Paper – The Modularized Start Version” (2009)  
URL <https://www.gsi.de/documents/DOC-2009-Nov-124-1.pdf>
- [19] Gutbrod, H. et al., “FAIR – Baseline Technical Report” (2006)  
URL [www.fair-center.eu/fileadmin/fair/publications\\_FAIR/FAIR\\_BTR\\_6.pdf](http://www.fair-center.eu/fileadmin/fair/publications_FAIR/FAIR_BTR_6.pdf)
- [20] Dolinskii, A. et al., “Antiproton complex at the FAIR project” *NIM A* **629**(1) (2011)
- [21] Groening, L. et al., “The 70-MeV Proton Linac for the Facility for Antiproton and Ion Research FAIR” *Proceedings of the Linear Accelerator Conference LINAC2006* (2006)
- [22] Tahir, N. et al., “Design of a Target for Antiproton Production at the Future FAIR Facility” *GSI Annual Report* (2007)
- [23] Nolden, F. et al., “TDR – Collector Ring (CR)” (2008)
- [24] Kester, O. et al., “Status of the FAIR Facility” *Proceedings of IPAC13, Shanghai, China* (2013)
- [25] Maier, R. et al., “HESR – Normal conducting lattice with dispersion suppressors” (2008)
- [26] Maier, R., “The High-Energy Storage Ring (HESR)” *Conf.Proc.* **C110328** (2011)
- [27] Stockhorst, H. et al., “Cooling scenario for the HESR complex” *AIP Conf.Proc.* **821** (2006)
- [28] Maier, R. et al., “Status of Stochastic Cooling Predictions at the HESR” *Conf.Proc.* **C110904** (2011)
- [29] Parkhomchuk, V. et al., “An Electron Cooling System for the Proposed HESR Antiproton Storage Ring” (2004)
- [30] PANDA collaboration, “Technical Design Report for PANDA Internal Targets” (2014)
- [31] Prasuhn, D., *privat communication*
- [32] PANDA collaboration, “Technical Design Report for the PANDA Luminosity Detector” *under preparation* (2015)
- [33] Wuerschig, T., “The  $\bar{P}ANDA$  detector at FAIR” *Hyperfine Interact.* **211** (2012)
- [34] Goetzen, K. et al., “Present Status of the PANDA Software Trigger” (2014)
- [35] PANDA collaboration, “Technical Design Report for the PANDA Micro Vertex Detector” (2012) [arXiv:physics.ins-det/1207.6581](https://arxiv.org/abs/physics.ins-det/1207.6581)
- [36] PANDA Collaboration, “Technical design report for the PANDA Straw Tube Tracker” *Eur.Phys.J.* **A49** (2013)

- [37] PANDA collaboration, “Web-site of PANDA collaboration” (2014)  
URL <http://www-panda.gsi.de>
- [38] PANDA Collaboration, “Technical Design Report for PANDA Electromagnetic Calorimeter” (2008) [arXiv:physics.ins-det/0810.1216](https://arxiv.org/abs/physics.ins-det/0810.1216)
- [39] Adam, I. et al., “The DIRC particle identification system for the BaBar experiment” *Nucl.Instrum.Meth.* **A538** (2005)
- [40] Kalicy, G. et al., “Status of the PANDA Barrel DIRC” *JINST* **9** (2014)
- [41] Föhl, K. et al., “First particle identification with a Disc-DIRC detector” *Nucl.Instrum.Meth.* **A732** (2013)
- [42] Brunner, S. et al., “Time resolution below 100 ps for the SciTil detector of PANDA employing SiPM” *JINST* **9** (2014)
- [43] PANDA collaboration, “Technical Design Report for PANDA Muon System” (2012)  
URL [www-panda.gsi.de/archive/public/panda\\_tdr EMC.pdf](http://www-panda.gsi.de/archive/public/panda_tdr EMC.pdf)
- [44] Armstrong, T. and et al., *Phys. Rev.* **D47** (1993)
- [45] Stancari, G., “A New Complementary Scan Technique for Precise Measurements of Resonance Parameters in Antiproton Proton Annihilations” *Conf.Proc.* (2007)
- [46] Stein, H. et al., “Determination of target thickness and luminosity from beam energy losses” *Phys.Rev.ST Accel.Beams* **11** (2008)
- [47] Garzoglio, G. et al., “Experiment E835 at Fermilab” *Nucl.Instrum.Meth.* **A519** (2004)
- [48] Trokenheim, S. et al., “A p anti-p luminosity monitor for Fermilab experiment E760” *Nucl.Instrum.Meth.* **A355** (1995)
- [49] Galoyan, A. et al., “Parametrization of the anti-P P Elastic Scattering Differential Cross Section Between  $2\text{-GeV}/c \leq P(\text{lab}) \leq 16\text{-GeV}/c$ ” (2008) [arXiv:hep-ex/0809.3804](https://arxiv.org/abs/hep-ex/0809.3804)
- [50] Armstrong, T. et al., “Precision measurements of anti-proton proton forward elastic scattering parameters in the  $3.7\text{-GeV}/c$  to  $6.2\text{-GeV}/c$  region” *Phys.Lett.* **B385** (1996)
- [51] HepData, “The Durham HepData Project” (2014)  
URL <http://hepdata.cedar.ac.uk/>
- [52] Eisenhandler, E. et al., “Differential Cross-Sections for anti-Proton-Proton Elastic Scattering Between  $0.69\text{-GeV}/c$  and  $2.43\text{-GeV}/c$ ” *Nucl.Phys.* **B113** (1976)
- [53] Birnbaum, D. et al., “Anti-p-p elastic scattering at 8 and 16  $\text{gev}/c$ ” *Phys.Rev.Lett.* **23** (1969)
- [54] Jenni, P. et al., “Measurement of the Real Part of the Forward Amplitude in anti-p p Elastic Scattering” *Nucl.Phys.* **B94** (1975)
- [55] — — — “Anti-p p and p p Forward Elastic Scattering Between  $4\text{-GeV}/c$  and  $10\text{-GeV}/c$ ” *Nucl.Phys.* **B129** (1977)

- [56] Hu, Q. et al., “A recoil detector for the measurement of antiproton–proton elastic scattering at angles close to 90°” *Eur.Phys.J.* **A50**(10) (2014)
- [57] Spataro, S., “Event reconstruction in the PandaRoot framework” *J.Phys.Conf.Ser.* **396** (2012)
- [58] Brun, R. et al., “GEANT3” (1987)
- [59] Agostinelli, S. et al., “GEANT4: A Simulation toolkit” *Nucl.Instrum.Meth.* **A506** (2003)
- [60] Hrivnacova, I., “The Geant4 virtual Monte Carlo” *J.Phys.Conf.Ser.* **396** (2012)
- [61] The ROOT Team, “ROOT User’s Guide” (2013)  
URL <http://root.cern.ch/drupal/content/root-users-guide-534>
- [62] Sjostrand, T. et al., “A Brief Introduction to PYTHIA 8.1” *Comput.Phys.Commun.* **178** (2008)
- [63] Ryd, A. et al., “EvtGen: A Monte Carlo Generator for B–Physics” (2005)
- [64] Galoian, A. and V. Uzhinsky, “New Monte Carlo implementation of quark–gluon–string model of anti–p p interactions” *AIP Conf.Proc.* **796** (2005)
- [65] Spieler, H., “Semiconductor detector systems” *Ser.Semicond.Sci.Tech.* **12** (2005)
- [66] Michel, M., “Simulation des PANDA–Luminositätsmonitor–Systems” *Johannes–Gutenberg Universität Mainz, Diplom thesis* (2010)
- [67] Abt, I. et al., “CATS: A cellular automaton for tracking in silicon for the HERA–B vertex detector” *Nucl.Instrum.Meth.* **A489** (2002)
- [68] Gorbunov, S. et al., “ALICE HLT high speed tracking on GPU” *IEEE Trans.Nucl.Sci.* **58** (2011)
- [69] Kisel, I., “Event reconstruction in the CBM experiment” *Nucl.Instrum.Meth.* **A566** (2006)
- [70] Blobel, V., “A new fast track–fit algorithm based on broken lines” *Nucl.Instrum.Meth.* **A566** (2006)
- [71] James, F. and M. Roos, “Minuit: A System for Function Minimization and Analysis of the Parameter Errors and Correlations” *Comput.Phys.Commun.* **10** (1975)
- [72] Lutz, G., “Optimum Track Fitting in the Presence of Multiple Scattering” *Nucl.Instrum.Meth.* **A273** (1988)
- [73] Yarba, J., “Recent developments and validation of Geant4 hadronic physics” *J.Phys.Conf.Ser.* **396** (2012)
- [74] Fontana, A. et al., “Use of GEANE for tracking in virtual Monte Carlo” *J.Phys.Conf.Ser.* **119** (2008)
- [75] Hoppner, C. et al., “A Novel Generic Framework for Track Fitting in Complex Detector Systems” *Nucl.Instrum.Meth.* **A620** (2010)
- [76] Pflüger, S., “Development of the PANDA Luminosity Fit Software Package” *Johannes–Gutenberg Universität Mainz, Dissertation in preparation*

- [77] Gorbunov, S. and I. Kisel, “Analytic formula for track extrapolation in non-homogeneous magnetic field” *Nucl.Instrum.Meth.* **A559** (2006)
- [78] Calen, H., “Status of Pellet Tracking and some Vacuum system consideration” *Talk at the PANDA Collaboration Meeting* (June 2014)
- [79] Viret, S. et al., “LHCb VELO software alignment, Part I” (2005)
- [80] Blobel, V., “Millepede II. Linear Least Squares Fits with a Large Number of Parameters” (2007)  
URL [www.desy.de/~blobel/Mptwo.pdf](http://www.desy.de/~blobel/Mptwo.pdf)
- [81] Needham, M., “Knossos interface to Millepede II” (2008)  
URL <http://ppewww.ph.gla.ac.uk/LHCb/VeloAlign/StandAloneCode.html>
- [82] Gorbunov, S. and I. Kisel, “Analytic formula for track extrapolation in non-homogeneous magnetic field” *Nucl.Instrum.Meth.* **A559** (2006)
- [83] Uzhinsky, V. and A. Galoyan, “Cross-sections of various processes in anti-P P interactions” (2002) *arXiv:hep-ph/0212369*
- [84] Flaminio, V. et al., “Compilation of cross-sections” *CERN* (1984)
- [85] Dbeyssi, A. and E. Tomasi-Gustafsson, “Classification of Pbar P induced reactions” (2012)  
URL [http://www-panda.gsi.de/db/notesDBr/AD12-121213\\_report-cross-sectionsPbarp.pdf](http://www-panda.gsi.de/db/notesDBr/AD12-121213_report-cross-sectionsPbarp.pdf)
- [86] Zambrana, M., “Documentation of  $p\bar{p} \rightarrow \pi^+\pi^-$  generator” (2011)  
URL <http://panda-wiki.gsi.de/pub/PANDAMainz/EventGenerators/note.pdf>
- [87] HepData, “The Durham HepData Project” (2014)  
URL <http://hepdata.cedar.ac.uk/>
- [88] Uzhinsky, V., “Tuning of the GEANT4 FRITIOF (FTF) Model Using NA61/SHINE Experimental Data” (2011) *arXiv:hep-ph/1109.6768*
- [89] Yarba, J., “Recent developments and validation of Geant4 hadronic physics” *J.Phys.Conf.Ser.* **396** (2012)
- [90] Hocker, A. et al., “TMVA - Toolkit for Multivariate Data Analysis” *PoS ACAT* (2007)
- [91] Coadou, Y., “Boosted Decision Trees and Applications” *EPJ Web Conf.* **55** (2013)
- [92] Ioffe, B. L., “Bottomonium production in  $\bar{p}p$  annihilation” *Phys. Rev. D* **47** (1993)
- [93] Eichten, E. et al., “Quarkonia and their transitions” *Rev.Mod.Phys.* **80** (2008)
- [94] Chen, G.-Y. et al., “How to identify the structure of near-threshold states from the line shape” (2013) *arXiv:hep-ph/1309.2859*
- [95] Lange, S. et al., “Prospects for X(3872) Detection at Panda” *AIP Conf.Proc.* **1374** (2011)
- [96] Guo, F.-K. et al., “What can radiative decays of the X(3872) teach us about its nature?” *Phys.Lett.* **B742** (2015) , pp. 394–398

- [97] Appelquist, T. and H. D. Politzer, “Heavy Quarks and  $e^+e^-$  Annihilation” *Phys. Rev. Lett.* **34** (1975)
- [98] Joffe, D. N., “A Search for the singlet-P state  $h_c(1^1P_1)$  of charmonium in  $p\bar{p}$  annihilations at Fermilab experiment E835p” (2004) [arXiv:hep-ex/0505007](https://arxiv.org/abs/hep-ex/0505007)
- [99] Lange, S., “XYZ States - Results from Experiments” (2013) [arXiv:hep-ex/1311.7594](https://arxiv.org/abs/hep-ex/1311.7594)
- [100] Swanson, E. S., “The New heavy mesons: A Status report” *Phys.Rept.* **429** (2006)
- [101] Brambilla, N. et al., “Heavy quarkonium: progress, puzzles, and opportunities” *Eur.Phys.J.* **C71** (2011)
- [102] Baglin, C. et al., “Charmonium spectroscopy by antiproton annihilation with protons from an internal H2 gas jet target” *Bari Europhys.High Energy* (1985)
- [103] Ablikim, M. et al., “Measurements of  $h_c(1^1P_1)$  in  $\psi'$  Decays” *Phys. Rev. Lett.* **104** (2010)
- [104] Rubin, P. et al., “Observation of the P(1)-1 state of charmonium” *Phys.Rev.* **D72** (2005)
- [105] Rosner, J. et al., “Observation of h(c)(P(1)-1) state of charmonium” *Phys.Rev.Lett.* **95** (2005)
- [106] Andreotti, M. et al., “Results of a search for the h(c) (1)P(1) state of charmonium in the eta(c) gamma and  $J/\Psi$   $\pi^0$  decay modes” *Phys.Rev.* **D72** (2005)
- [107] Dobbs, S. et al., “Precision Measurement of the Mass of the h(c)(P-1(1)) State of Charmonium” *Phys.Rev.Lett.* **101** (2008)
- [108] Ablikim, M. et al., “Measurements of  $h_c(1^1P_1)$  in  $\psi$  Decays” *Phys.Rev.Lett.* **104** (2010)
- [109] — — — “Study of  $\psi(3686) \rightarrow \pi^0 h_c, h_c \rightarrow \gamma \eta_c$  via  $\eta_c$  exclusive decays” *Phys.Rev.* **D86** (2012)
- [110] Renard, F., “How to Produce and Observe the p Wave Singlet Charmonium State?” *Phys.Lett.* **B65** (1976)
- [111] Novikov, V. et al., “Charmonium and Gluons: Basic Experimental Facts and Theoretical Introduction” *Phys.Rept.* **41** (1978)
- [112] McClary, R. and N. Byers, “Relativistic Effects in Heavy Quarkonium Spectroscopy” *Phys.Rev.* **D28** (1983)
- [113] Kuang, Y.-P. et al., “Hadronic Transitions and P Wave Singlet States of Heavy Quarkonia” *Phys.Rev.* **D37** (1988)
- [114] Galkin, V. et al., “Radiative E1 decays of quarkonium in the framework of relativistic quark model. (In Russian)” *Sov.J.Nucl.Phys.* **51** (1990)
- [115] Chemtob, M. and H. Navelet, “Two Gluon Model of Hadronic Transitions Between S, D and P States in  $c\bar{c}$  and  $b\bar{b}$  Systems” *Phys.Rev.* **D41** (1990)
- [116] Bodwin, G. T. et al., “Rigorous QCD predictions for decays of p wave quarkonia” (1992) [arXiv:hep-ph/9211253](https://arxiv.org/abs/hep-ph/9211253)

- [117] Chen, G.-P. et al., “More on the psi (radially excited p wave singlet) production in anti-p p annihilation” *Phys.Rev.* **D46** (1992)
- [118] Chao, K.-T. et al., “Some problems on the charmonium p wave singlet state” *Phys.Lett.* **B301** (1993)
- [119] Casalbuoni, R. et al., “Effective Lagrangian for quarkonia and light mesons in a soft-exchange-approximation” *Phys.Lett.* **B302** (1993)
- [120] Ko, P., “Radiative and hadronic transitions of the charmonium p wave-singlet state” *Phys.Rev.* **D47** (1993)
- [121] Gupta, S. N. et al., “Heavy quarkonium potential model and the p wave singlet state of charmonium” *Phys.Rev.* **D49** (1994)
- [122] Adams, G. et al., “Evidence for Decays of h(c) to Multi-Pion Final States” *Phys.Rev.* **D80** (2009)
- [123] Brambilla, N. et al., “Heavy quarkonium physics” (2004) arXiv:hep-ph/0412158
- [124] Goetzen, K., “Fast Simulations” *Talk at the PANDA Collaboration Meeting* (June 2014)
- [125] Melnychuk, D., “Development of electromagnetic calorimeter detectors and simulations for spectroscopic measurements of charmonium with PANDA” arXiv:hep-ex/1003.3144
- [126] Dover, C. B. et al., “The Physics of nucleon - anti-nucleon annihilation” *Prog.Part.Nucl.Phys.* **29** (1992)
- [127] Baglin, C. et al., “ $J/\Psi$  resonant formation and mass measurement in antiproton-proton annihilations” *Nuclear Physics B* **286**(0) (1987)
- [128] Montanet, L. and S. Reucroft, “High Resolution Bubble Chambers and the Observation of Shortlived Particles” *Phys.Rept.* **83** (1982)
- [129] Mittal, V. et al., (2009) *Introduction to Nuclear and Particle Physics*
- [130] Sandweiss, J., “Hadron and photon beams for bubble chambers” *Nuclear Physics B - Proceedings Supplements* **36**(0) (1994)
- [131] Pullia, A., “Searches for Dark Matter with Superheated Liquid Techniques” *Adv.High Energy Phys.* **2014** (2014)
- [132] Steel, E., “List of Publications Covering Bubble Chamber Experiments Carried Out at CERN During the Period 1960-1974” (1976)
- [133] Carron, G. et al., “The CERN antiproton accumulator complex (AAC): current status and operation for the nineties” (CERN-PS-92-41-AR) (1992)
- [134] Baglin, C. et al., “Precision Measurements of the Anti-proton - Proton Elastic Scattering Cross-section at 90-degrees in the Incident Momentum Range Between 3.5-GeV/c and 5.7-GeV/c” *Phys.Lett.* **B225** (1989)
- [135] — — — “Antiprotons Collisions with a Gas H2 Jet and Formation of Charmonium States” (1983)
- [136] Ahmad, S. et al., “The Asterix Spectrometer at LEAR” *Nucl.Instrum.Meth.* **A286** (1990)

- [137] Aker, E. et al., “The Crystal Barrel spectrometer at LEAR” *Nucl.Instrum.Meth.* **A321** (1992)
- [138] Bressani, T., “The latest results from OBELIX” *Nuclear Physics A* **675** (2000)
- [139] Evangelista, C. et al., “Study of the reaction  $\bar{p}p \rightarrow \phi\phi$  from 1.1-2.0 GeV/c” *Phys. Rev. D* **57** (1998)
- [140] Love, W., “The BNL Multiparticle Spectrometer (MPS) Program” (1975)
- [141] Armstrong, T. et al., “Observation of the p wave singlet state of charmonium” *Phys.Rev.Lett.* **69** (1992)
- [142] Apeldoorn, G. et al., (1974) *Report of working party on antiproton interactions Tech. Rep. CERN-TCC-74-25* CERN Geneva
- [143] Harigel, G., (1985) *List of publications covering BEBC experiments* CERN, Geneva
- [144] Bertrand, G. et al., “Inclusive  $V_0$  production in pp interactions at 12 GeV/c” *Nuclear Physics B* **128**(3) (1977)
- [145] Barnes, P. et al., “Study of the reaction  $p\bar{p} \rightarrow \Lambda\bar{\Lambda}$  near threshold” *Physics Letters B* **189** (1987)
- [146] Johansson, T., “Antihyperon-hyperon production in antiproton-proton collisions” *AIP Conf.Proc.* **796** (2005)
- [147] Sculli, J. et al., “Limits on  $\Xi(2.2)$  Formation in  $\bar{P}P \rightarrow K^+K^-$ ” *Phys.Rev.Lett.* **58** (1987)
- [148] Sanford, J., “Experimental planning and support - CY 67” *Technical note* (1968)  
URL <http://www.c-ad.bnl.gov/esfd/ES&F\Tech\Notes/15.pdf>
- [149] — — — “Experimental division progress - CY 69” *Technical note* (1969)  
URL <http://www.c-ad.bnl.gov/esfd/ES&F\Tech\Notes/27.pdf>
- [150] Dao, F., J. Lach, and J. Whitmore, “Inclusive Neutral Particle Production in 14.75-GeV/c anti-Proton Interactions” *Phys.Lett.* (1974)
- [151] Foley, K., “Hadron spectroscopy in the Brookhaven Multiparticle Spectrometer” (1979)
- [152] Booth, C. et al., “Differences between anti-p p and pp interactions at 8.8-GeV/c and their relationship to anti-p p annihilations” *Phys.Rev.* **D27** (1983)
- [153] Ward, D. et al., “Exclusive annihilation processes in 8.8 GeV anti-p p interactions and comparisons between anti-p p nonannihilations and p p interactions” *Nucl.Phys.* **B172** (1980)
- [154] Barnett, B. et al., “Limits on baryonium production in anti-p p interactions at 8.3-GeV/c and 13.0-GeV/c” *Phys.Rev.* **D27** (1983)
- [155] — — — “A Study of anti-p p Annihilations Using LASS” (1976)
- [156] Armstrong, T. et al., “Measurement of the J / psi and psi-prime resonance parameters in anti-p p annihilation” *Phys.Rev.* **D47** (1993)

- [157] Crawley, H., W. Kernan, and F. Ogino, “Anti-p p elastic scattering at 2.33 gev/c” *Phys.Rev.* **D8** (1973)
- [158] Crawley, H., E. S. Hafen, and W. Kernan, “Anti-p p elastic scattering at 2.85 gev/c” *Phys.Rev.* **D8** (1973)
- [159] Ambats, I. et al., “Systematic study of  $\pi^+ - p$ ,  $k^+ - p$ ,  $p p$ , and anti-p p forward elastic scattering from 3 to 6 gev/c” *Phys.Rev.* **D9** (1974)
- [160] Baker, W. et al., “Anti-proton-proton elastic scattering at 3.55 gev/c” *Nucl.Phys.* **B12** (1969)
- [161] Eide, A. et al., “Elastic scattering and two-body annihilations at 5 gev/c” *Nucl.Phys.* **B60** (1973)
- [162] Braun, H. et al., “Analysis of Two Prong Events in anti-Proton-Proton Interactions at 5.7-GeV/c” *Nucl.Phys.* **B95** (1975)
- [163] Buran, T. et al., “Anti-Proton-Proton Elastic Scattering at 6.2-GeV/c” *Nucl.Phys.* **B97** (1975)
- [164] Russ, J. et al., “Elastic Scattering of  $\pi^-$ ,  $K^-$ , and anti-p from Hydrogen at 8-GeV/c and 16-GeV/c” *Phys.Rev.* **D15** (1977)
- [165] Berglund, A. et al., “ $K^- p$  and  $\bar{p}p$  Elastic Scattering at 10.1-GeV/c” *Nucl.Phys.* **B176** (1980)
- [166] Brandenburg, G. et al., “Measurement of Particle and anti-Particle Elastic Scattering on Protons Between 6-GeV and 14-GeV” *Phys.Lett.* **B58** (1975)
- [167] Wittek, W., “Propagation of errors along a particle trajectory in a Magnetic Fields in CMS” (1980)
- [168] Strandlie, A. and W. Wittek, “Propagation of covariance matrices of track parameters in homogeneous magnetic fields in CMS” (2006)
- [169] “Terning’s View of Physics” (2009)  
URL <http://particle.physics.ucdavis.edu/blog/>
- [170] Marinov, M., “Relativistic Strings and Dual Models of Strong Interactions” *Usp.Fiz.Nauk* **121** (1977)
- [171] Ritter, S., “Monte Carlo code bamjet to simulate the fragmentation of quark and diquark jets” *Computer Physics Communications* **31**(4) (1984)
- [172] Hänssgen, K. et al., “The Monte Carlo code decay to simulate the decay of baryon and meson resonances” *Computer Physics Communications* **31**(4) (1984)
- [173] Galoyan, A., “Physics of antiproton-proton and antiproton-nucleus annihilation processes implemented in Geant4” *Talk at the PANDA Collaboration Meeting* (September 2013)
- [174] Bengtsson, H.-U. and T. Sjostrand, “The Lund Monte Carlo for Hadronic Processes: Pythia Version 4.8” *Comput.Phys.Commun.* **46** (1987)